DOCTOR OF PHILOSOPHY

Investigations into low band-gap, semiconducting polymers

Mills, Christopher Alan

Award date:
2001

Awarding institution:
Bangor University

Prifysgol Cymru · University of Wales
BANGOR

Investigations into low band-gap, semiconducting polymers.

Thesis submitted in candidature for the degree of Doctor of Philosophy.

January 2001

Christopher Alan Mills

School of Informatics,
University of Wales, Bangor,
Dean Street,
Bangor,
Gwynedd,
LL57 1UT, UK.

To

Yvonne, my mum, and Nic, my "little" brother,
without whose support I would never have made it this far.

Chris and Leigh, the best of friends.

Abstract

The physical and electronic characteristics of the low band-gap polymers, poly(4-dicyanomethylene-4H-cyclopenta[1,2-b;3,4-b']dithiophene) (PCDM) and poly(7-benzo[1,3]dithiol-2-ylidine-7H-3,4-dithia-cyclopenta[a]pentalene) (PBDT), have been examined. The polymers were studied using microscopic and spectroscopic methods to determine the chemical and morphological properties of the polymer films. Micrographs of the polymer surfaces revealed PCDM to consist of a relatively smooth surface covered by large aggregations. PBDT had a much rougher surface with a large surface area, possibly suitable for the production of a polymeric battery. Polymer band-gaps were estimated using UV-vis spectra to be 1.38 eV and 1.29 eV respectively for PCDM and PBDT. XPS measurements allied with the PCDM and PBDT band-gaps have been used to produce preliminary band diagrams for ITO/polymer/Al diodes.

Diodes of PCDM and PBDT were fabricated to allow study of the electrical behaviour of the polymers using DC current-voltage (I-V) measurements and AC impedance spectroscopy. Equivalent RC circuits of ITO/PCDM/Al diodes have been used to model the presence of 2 dispersions in the admittance plots and to explain the effects of increasing temperature, polymer film thickness and contact material. The DC electrical measurements for PCDM reveal almost symmetrical current-voltage characteristics. A hysteresis effect dependent on the direction of the voltage sweep observed in the DC characteristics has a potential application in the production of a polymeric "memory element". For sweep voltages starting above approximately ±4 V, "high" and "low" conductance states occur when sweeping from negative to positive and positive to negative bias respectively. The "low" state is stable for many months whereas the "high" state decays exponentially with time constants of approximately 2000 s. Characteristic values for PCDM films have been estimated using the experimental results.

An investigation of the production of command surfaces using a series of ethylene homopolymers, prepared by electropolymerisation under anodic and cathodic conditions, has also been undertaken.

Acknowledgements

The author would like to thank the following people for their invaluable help in the completion of this thesis.

- **Professor D. Martin Taylor** for his faith in my abilities and for giving me a chance to study for my doctorate. His support and expert guidance throughout this project has helped me complete work in which I had little prior experience.

- **EPSRC** and **BNFL** for financial support and especially **Walter Weaver**, **Dr. Andy Alderson** and **Dr. Steve Vinton** from BNFL who guided my work with respect to BNFL's aims.

- **Dr. Paddy Murphy** and **Louise Hall** of the department of Chemistry at the University of Wales, Bangor, for their help in synthesising the CDM monomer used in this work. Also **Eddie Kavanah** of the same department for completing the X-ray diffraction measurement on PCDM used in section 5.3.5.

- **Dr. David Lacey** and **Gary Stevenson** of the University of Hull, for providing the monomers, along with spectroscopic data, used in the production of the command surface polymers used in section 7.1.

- **Dr. Bernardo Laks** and **Jordan Del Nero** of the Universidade Estudual de Campinas, São Paulo, Brazil, for the theoretical UV/vis calculations used in section 5.3.3.

- **Dr. Andy Evans** and **Joachim Steiner** of the University of Wales, Aberystwyth, who completed the X-ray photoelectron spectroscopy used in section 5.3.4.

- **Thomas Gelbrich** of the University of Southampton for completing the X-ray diffraction measurements on CDM and providing me with the crystal structure diagrams used in section 5.3.5.

- **Dr. Geraint Jones**, **Dr. Antonio Riul Jr.**, **Dr. Arwel Hughes**, **Dr. Henrique Gomes** and **Colin Dalton** for their help and discussions with respect to the work completed here and within the field of semiconducting polymers generally.

- **Albert Rees** and **John Tame** for their technical assistance in surface analysis and semiconductor preparation respectively.

- **Finally**, all my friends and colleagues in Bangor and elsewhere. You are too numerous to mention but special thanks to Colin, Geraint, Arwel, Louise D., Consuelo, Ana, Pablo, Debbie J., Toto and family, Louise H., Andy T., Eddie, Paul R., Jonny, Nick, Dewi, Paul S, Alan, Saad, Peter, Huw, Iestyn, Andy G, Jess and Debs.

Contents

List of captions

Figure captions

Scheme captions

Table captions

Symbols and abbreviations

A	= Acceptor atom
A*	= Modified Richardson constant
AC	= Alternating current
AFM	= Atomic Force Microscopy
Ag	= Silver
Al	= Aluminium
Au	= Gold
β_{PF}	= Constant (Poole-Frenkel)
β_S	= Constant (Schottky)
BDT	= 7-benzo[1,3]dithiol-2-ylidine-7H-3,4-dithia-cyclopenta[a]pentalene
BuLi	= Butyl lithium
χ_S	= semiconductor electron affinity
C	= Total capacitance
C_b	= Bulk capacitance
CCD	= Charge coupled device
C_d	= Depletion layer capacitance
CDM	= 4-dicyanomethylene-4H-cyclopenta[1,2-b;3,4-b']dithiophene
CDT	= 4H-cyclopenta[1,2-b;3,4-b']dithiophene-4-one
d	= Semiconductor thickness
DC	= Direct current
DCM	= Dichloromethane
DMF	= Dimethylformamide
ε, ε_r, κ_e	= Relative permittivity (also termed dielectric constant)
ε_0	= Vacuum permittivity
ε_∞	= High frequency permittivity
ε_S	= Static permittivity
e, q	= Electronic charge
$e\phi_m$	= Metal workfunction
$e\phi_s$	= Semiconductor workfunction

eV_{bi} = Barrier height

E = Electric field strength

E_C = Conduction band edge

E_{Fm} = Metal Fermi level

E_{Fs} = Semiconductor Fermi level

E_g = Band-gap energy

E_t = Trap depth

E_V = Valence band edge

EDAX = Energy dispersive x-ray analysis

EDOT = 3,4-Ethylenedioxide

EL = Electroluminescence

EMPA = Electron microprobe analysis

Ether = Diethylether

EtOH = Ethanol

ϕ = Potential energy

FTIR = Fourier transform infra-red

G = Conductance

HOMO = Highest occupied molecular orbital

I = Current

ITO = Indium tin oxide

j = Imaginary number

J = Current density

J_0 = Reverse saturation current density

J_F = Current density under positive bias

k = Boltzmann's constant

LB = Langmuir-Blodgett

LCR = Inductance, capacitance and resistance

LED = Light emitting diode

LUMO = Lowest unoccupied molecular orbital

μ = Mobility

MEH-PPV = poly(2-methoxy-5-(2'-ethyl-hexyloxy)-1,4-phenylene vinylene)

ν = Frequency

ν_0 = Attempt to escape frequency

n	= Ideality factor
N_0	= Effective density of delocalised states
N_A	= Density of acceptor states
N_C	= Effective density of states in the conduction band
N_t	= Trap density
N_V	= Effective density of states in the valence band
NLO	= Non-linear optics
NMR	= Nuclear magnetic resonance
π	= Bonding π-orbital
π^*	= Antibonding π-orbital
p	= probability
P3MeT	= Poly(3-methylthiophene)
PBDT	= Poly(7-benzo[1,3]dithiol-2-ylidine-7H-3,4-dithia-cyclopenta[a]pentalene)
PCC	= Pyridinium chlorochromate
PCDM	= Poly(4-dicyanomethylene-4H-cyclopenta[1,2-b;3,4-b']dithiophene)
PL	= Photoluminescence
PS	= Porous silicon
PTFE	= Poly(tetrafluoroethylene)
PZT	= Lead zirconium titanate
ρ	= Electric charge density
R_b	= Bulk resistance
R_d	= Depletion layer resistance
R_s	= Series contact resistance
RMS	= Root mean square
σ	= Bonding σ-orbital
σ^*	= Antibonding σ-orbital
S	= Entropy
SCL	= Space charge limited
SCLC	= Space charge limited current
SEM	= Scanning electron microscope
Si	= Silicon
SPM	= Scanning probe microscope

τ = Circuit relaxation time

T = Absolute temperature

TBAHFP = Tetrabutylammonium hexafluorophosphate

TBATFB = Tetrabutylammonium tetrafluoroborate

THF = Tetrahydrofuran

TSA = Toluene sulphonic acid

trans-Pac = Trans-polyacetylene

UV-vis = Ultraviolet-visible

V = Bias voltage

V_A = Applied bias voltage

V_F = Forward bias

V_R = Reverse bias

V_{SO} = Extent of band bending at 0V

V_{TFL} = Trap filled limit voltage

ω = Angular frequency

W = Depletion layer width

x = Distance

XPS = X-ray photoelectron spectroscopy

XRD = X-ray diffraction

Y = Admittance

Z = Impedance

1. Introduction

Since the discovery of semiconducting polymers in 1977, with the fabrication of films of polyacetylene [1], interest in the use of this type of semiconductor has grown to the point where they are expected to display properties that rival their inorganic counterparts. Indeed, reports of research involving the use of these organic semiconductors in everyday electronic applications have reached the level of popular scientific publications, such as Physics World [2, 3] and New Scientist [4], and even national newspapers [5]. These applications include illuminated warning signs and mobile telephone displays, as well as the electronics required to drive them.

Polymers could be an integral part of the next generation of low cost, "throw away" electronic devices [3]. The large number of polymer systems available, due to the diversity of organic molecules, would mean that a number of appropriate materials could be developed. The advantages of organic semiconducting polymers, including mechanical durability and ease of processing, make them attractive for use in the field of electronics. Also, these species potentially have low fabrication costs compared to their inorganic counterparts.

The motivation for scientists and engineers in this field is, therefore, to identify new semiconducting organic materials and to develop devices, such as thin-film transistors with high conductivities and fast switching speeds, which incorporate these materials. The ability of some of these materials to luminesce also opens up the possibility of producing large area displays incorporating diodes that emit light covering the entire UV-visible-IR portion of the electromagnetic spectrum. Another fruitful area of research is to gain an understanding of the properties of these polymers and the mechanisms occurring within them.

There is a large volume of research into polymers based on one of the original polymers identified as having a low band-gap, poly(phenylene vinylene). Except for poly(3-alkylthiophenes), polythiophene-based polymers have yet to attain the same levels of interest although they have as much potential as their phenylene vinylene counterparts. The possibility of rivalling the properties displayed by the phenylene vinylene polymers, allied to the promising low band-gap characteristics of constrained,

thiophene-based polymers, is expected to lead to another group of polymeric semiconductors useful for electronic applications.

The aim of this project is to characterise the physical and electronic properties of two relatively novel low band-gap polymer systems that utilise constrained thiophenes, namely PCDM and PBDT. The justification for examining these polymers depends on the low band-gap property arising from the constrained molecular configurations. Unconstrained polymers, such as polythiophenes, tend to have higher band gaps. However, diodes incorporating polythiophene-based polymers have been reported to display good stability under normal operating conditions. It is expected that the chemical stability will transfer to diodes containing the polymers studied here and that this stability allied with the low band-gap properties of the PCDM and PBDT will produce devices with useful electronic properties.

PCDM and PBDT are expected to display minority carrier behaviour, a requirement for the development of devices such as diodes and thin film transistors. The electrical characteristics of diodes produced from thin polymer films, which were previously subjected to physical characterisation, has been undertaken in this thesis to determine the potential of using these polymers in electronic applications.

An introduction into the background of semiconduction in polymers and a review of the reported literature on low band-gap polymers and their applications is provided. This leads to an explanation of the methods used to characterise these polymers and the results gained. The properties of command surfaces based on ethylene homopolymers is also presented with the future possibility of combining command surface and low band-gap polymers in sensor applications..

Thesis organisation:

Chapter 2: Introduction to semiconduction in polymers, including the theory behind polymeric semiconductors and diodes.

Chapter 3: Reported literature on the definition of low band-gap polymers and possible methods of customisation of the polymers and their applications. Includes the reported literature involving PCDM and PBDT.

Chapter 4: Experimental methods for the production and characterisation of polymeric, thin film diodes.

Chapter 5: The results and discussion of physical characterisation of polymeric thin films, split into sections covering microscopic and spectroscopic characterisation.

Chapter 6: The results and discussion of electrical characterisation of diodes incorporating PCDM and PBDT, including admittance measurements and DC characteristics.

Chapter 7: An investigation into the production of command surfaces using a series of ethylene homopolymers.

Chapter 8: Conclusions arising from the experimental work and suggestions for furthering the project.

Appendix 1: Chemical synthesis of CDM monomer and NMR characterisation of the synthesis steps.

Appendix 2: Mathematical modelling of the polymer diode circuit proposed in chapter 2.

Appendix 3: An investigation into the displacement of PCDM upon exposure to laser light.

Papers: Samples of the journal papers arising during the course of this project.

2. Semiconduction in polymers

This chapter provides an explanation of semiconduction in polymers by initially describing the structure of inorganic semiconductors and introducing the definitions of intrinsic and extrinsic semiconductors, and n- and p-type character. These simple inorganic semiconductor concepts are then developed for polymeric semiconductors with a description of polymer structure and band formation. The occurrence of conduction and valence bands, with the consequent formation of the band gap, is explained using a molecular orbital description of the monomer as a starting point. The origin of the various charged species, including solitons, polarons, bipolarons and excitons, found in semiconducting polymers are also explained.

The nature of ohmic and rectifying (or Schottky) contacts are explained in terms of inorganic semiconductor band theory. From these considerations, the DC and AC electrical behaviour of a Schottky diode incorporating a depletion layer, and a diode containing a depletion layer and a small series resistance, are modelled. Finally, a number of current controlling mechanisms in Schottky diodes are discussed, including electrode limitation by Schottky emission and Fowler-Nordheim tunnelling and bulk limitation by the Poole-Frenkel mechanism and space-charge accumulation.

2.1 Basic semiconductor theory

2.1.1 Inorganic semiconductors

Before describing the origin of semiconduction in polymeric materials, it is helpful to look at the basic theory of inorganic semiconductors in order to introduce some of the established semiconductor concepts.

The simplified structure of inorganic semiconducting materials usually involves a crystalline lattice consisting of atoms of a single element or elements with the same valency [6]. The valence electrons of these atoms form the covalent bonds between the atoms that make up the lattice. In an intrinsic semiconductor, the valence electrons are tightly bound in the covalent bonds but thermal vibrations in the lattice can cause

electrons to escape from their neighbouring atoms and form holes. The probability of this occurring at or below room temperature is low because the thermal energy available is lower than the internal ionisation energy of the semiconductor atoms. However, as the number of valence electrons available in the material is high (approximately 10^{23} cm^{-3}) the concentration of carriers produced is non-zero. In an intrinsic semiconductor, the concentrations of free holes and electrons are equal.

It is necessary to modify the chemical structure of an intrinsic semiconductor to significantly increase the number of mobile charge carriers. Replacement of some of the atoms in the crystal lattice of the semiconductor with atoms of elements with higher (or lower) valency achieves this. This doping of the intrinsic semiconductor leads to the formation of the doped, extrinsic semiconductor in which one free charge carrier dominates. The dominant free charge carrier, whether it be electrons or holes, is called the majority carrier and consequently the carrier of lower concentration is the minority carrier.

If the dopant has a higher valency than the semiconductor atoms, the unbonded electron on the dopant is loosely bound to the nucleus. Interactions between this electron and the surrounding atoms reduces this Coulomb interaction further causing the ionisation energy to be reduced. This allows the electron to be removed at low temperatures. In this case, free electrons dominate and the material is said to be n-type. If the dopant has a lower vacancy than the lattice atoms, the dopant atom has an empty orbital which can accept an electron from the lattice of the semiconductor. This causes a mobile hole to be left behind on the semiconductor lattice. Where such free holes dominate, the semiconductor is p-type.

However, in both cases the extrinsic semiconductor is electrically neutral under ambient conditions due to the balancing charge of the dopant atoms. Upon application of an electric field, the free carriers are mobile in the direction of the field but the dopant ions remain static within the semiconductor lattice.

2.1.2 Polymeric semiconductors

2.1.2.1 Polymer structure

The electrical properties of polymeric semiconductors are best explained by considering initially the simplest of semiconducting polymers, trans-polyactylene (trans-PAc) [7]. This unsaturated polymer consists of C–H groups alternately single and double bonded to their neighbours by overlapping σ and π-orbitals respectively. This conjugated system is interchangeable across the carbon atoms forming the polymer backbone, producing conformations of the polymer with identical energies (Figure 2.1(a)). The discrete bonding model is actually a simplification in that the bonds between carbon atoms are hybrids rather than the discrete bonds shown. The sp^2 hybrid orbitals on the carbon atoms involved in the π-bonding overlap with their neighbours to form a continuous system through which electrons can easily travel (Figure 2.1(b)). Hence, polymers of this type are said to be quasi-metallic.

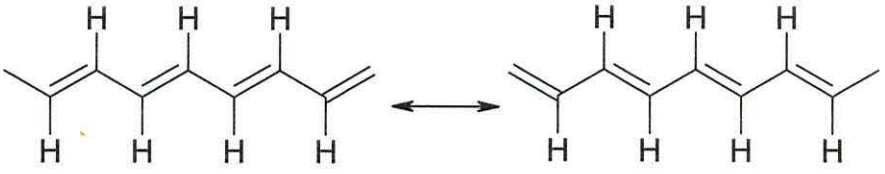

(a)

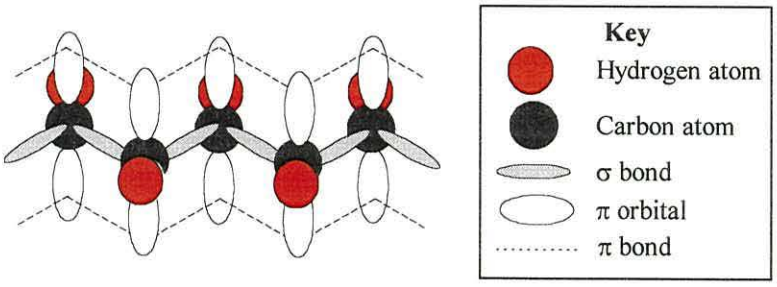

(b)

Figure 2.1 *(a) Kekulé type structures showing energetically identical conformers and (b) orbital structure showing the π-bonding orbitals of trans-polyacetylene.*

This simplified model of trans-PAc is useful for describing the formation and movement of charged species along the polymer backbone since, it can be used to illustrate the conduction mechanisms occurring in the polymer. The delocalised charge

carriers in the π-bonds distribute charge along a length of the polymer and if an external source is applied to the polymer, such as an electric field or a temperature gradient, charge can be moved along the polymer chain in the field direction.

2.1.2.2 Band formation

In the monomer, the energy levels in a bond are described by molecular orbital theory [8]. The discrete energy levels between atoms separate into lower energy, bonding (σ and π) and higher energy, antibonding (σ* and π*) levels (Figure 2.2(a)). The number of atoms in the repeat unit of the conjugated polymer determines the number of π-energy levels available for bonding. Initially, the σ energy level fills following Pauli's exclusion principle [8]. If there are 8 carbon atoms in the monomer unit, such as in poly(phenylene vinylene) (PPV), there are 8 π-energy levels each of which can be occupied by 2 electrons. However, as the carbon atoms only supply 1 electron each to the π-bond, the four lower energy, π-levels fill and the four higher energy, π*-levels remain empty.

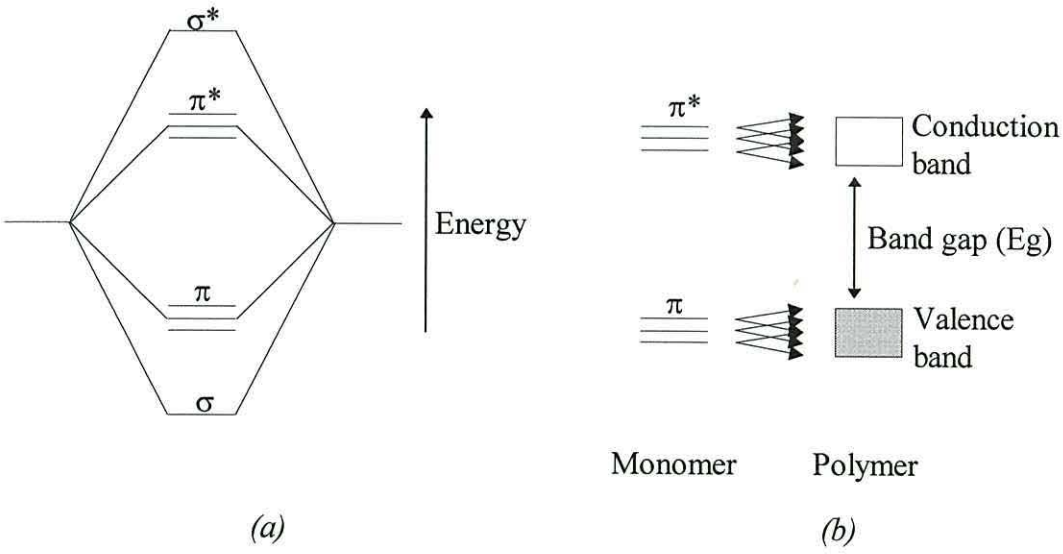

Figure 2.2 *(a) Molecular orbital model showing the discrete energy levels in a monomer bond and (b) diffusion and overlap of the energy levels into bands upon polymerisation.*

The difference between saturated and unsaturated monomers is the lack of π-bonds in the saturated analogue. Promotion of an electron in a saturated monomer,

from an electron rich, bonding σ-orbital to an electron deficient, antibonding σ*-orbital is energetically unfavourable. If the promotion does occur, because the σ-electron is promoted to an anti-bonding orbital, the monomer falls apart. Unsaturated monomers, on the other hand, contain π-bonds which are not necessary for the fundamental structure allowing promotion of electrons from a π-orbital to a π*-orbital without causing monomer decomposition.

Polymerisation gives rise to a high concentration of such π-bonds causing the discrete atomic energy levels in the monomer to split, forming energy bands. When Peierls instability [9] occurs in the polymer these bands split, to form a filled valence band and an empty conduction band (Figure 2.2(b)).

This model of bonding and antibonding energy levels forming bands applies to all polymers. In the molecular orbital model, electrons are confined to discrete energies in the molecule and excitation of an electron occurs from the highest occupied molecular orbital (HOMO) to the lowest unoccupied molecular orbital (LUMO). In the polymer, because the energy levels form a quasi continuous band, the charge carriers are excited from the valence band edge to the conduction band edge, across a forbidden region of energies called the π-π* band gap (Figure 2.2(b)) [10]. Conduction depends on promotion of electrons to the conduction band and therefore, the difference between insulating and semiconducting polymers depends on the magnitude of the band gap.

For insulators, the band gap is greater than 6 eV and therefore large enough to ensure that the probability of electron excitation from the valence band to the conduction band is negligible. Semiconducting polymers have band gaps with energies less than those of insulators, commonly about 2 eV or less. In an ideal, intrinsic conducting polymer the conduction and valence bands overlap allowing free transfer of electrons from the valence band into the conduction band (Figure 2.3). In an extrinsic, conducting polymer excited (polaron) states in the band gap overlap allowing transfer of these excited species. Formation of these excited species is covered further in section 2.1.2.4.

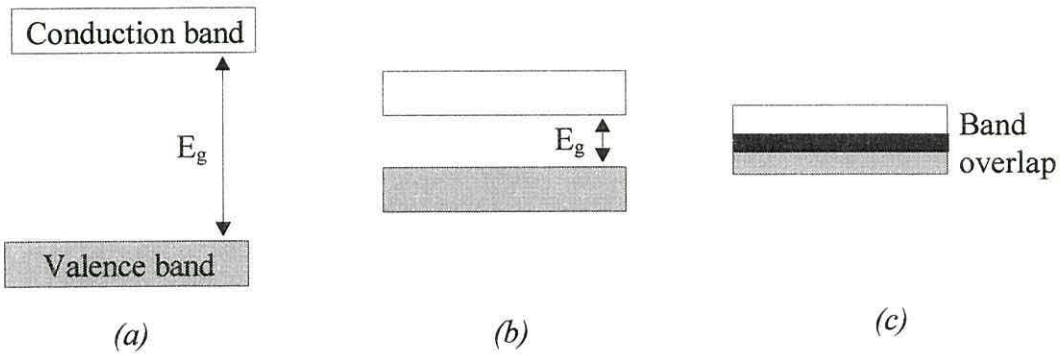

Figure 2.3 *Schematic diagram of the energy bands of (a) insulating, (b) semiconducting and (c) conducting polymer systems.*

2.1.2.3 Application of inorganic theory to organic systems

The nature of free charge carriers in semiconducting polymers is more complex than described earlier for inorganic semiconductors due to a number of reasons [11].

- Macromolecular polymer systems are disordered causing even heavily doped polymers to be insulating rather than metallic.
- Any alteration of the electronic structure of the atoms in the polymer causes a change in the structural configuration of the polymer around that atom. Therefore, excitations such as the production of electrons and holes, cause chain distortions to occur in the surrounding polymer leading to the formation of solitons, polarons and bipolarons.
- The formation of excitons due to Coulomb interactions between electrons in the π-bands and holes in the π*-bands are ignored.

The lattice distortions and the Coulomb interactions should be included in any description of the structure of conjugated polymers.

2.1.2.4 Solitons, polarons, bipolarons and excitons

Solitons [12] occur on polymers with degenerate ground states such as trans-PAc which has two molecular configurations of equal energy as depicted in figure 2.1(a). A defect in the conjugation of the polymer backbone at one carbon atom, produced by the removal of an electron upon doping, causes the orientation of the bonding on either side of this domain boundary to be the mirror of each other (Figure 2.4). The soliton

produces a discrete energy level at the mid-point of the band gap which can be occupied by up to two electrons. If the soliton level is unoccupied, it is positively charged and has a spin of zero. If it contains one electron it is neutral and has a spin of ½, and if it contains two electrons it is negatively charged and has zero spin. Experiments have shown that the boundary is not as sharp as shown in figure 2.4 but actually exists over approximately 7 carbon atoms [12].

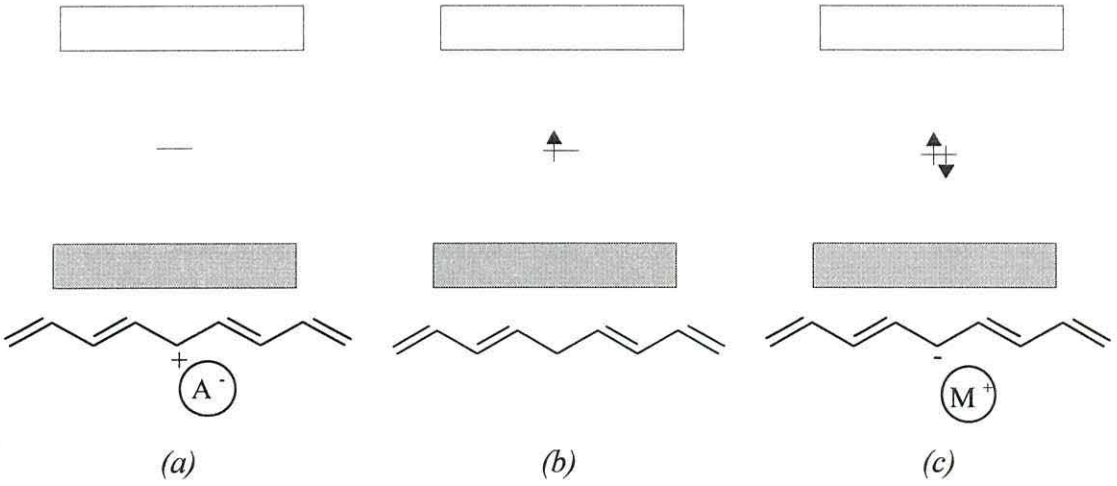

Figure 2.4 *Schematic diagram and band structure of a soliton showing the (a) positively charged, (b) neutral and (c) negatively charged species.*

Solitons do not occur in non-degenerate polymers such as polyanaline and the polythiophenes but similar mechanisms for conduction are found. The simplest way to produce conduction within a semiconducting polymer, which has a completely filled valence band, is to introduce charge carriers into the conduction band, or remove charge from the valence band, by the introduction of electron donors or acceptors respectively into the system. Doping of the polymer with electron acceptors, which provide an empty energy level in the band-gap of the polymer near to the valence band edge, increases the probability of an electron from the valence band being promoted to the higher level (Figure 2.5(a)). The polymer becomes cationic resulting in the formation of an ionic complex between itself and the anionic dopant. Transfer of an electron to the acceptor leaves behind a hole in the valence band (Figure 2.5(b)).

The presence of the positively charged hole on the polymer chain modifies the geometry of the polymer around the hole. This distortion, or polarisation, reduces the energy of the hole, which now occupies a localised energy level, in the band-gap,

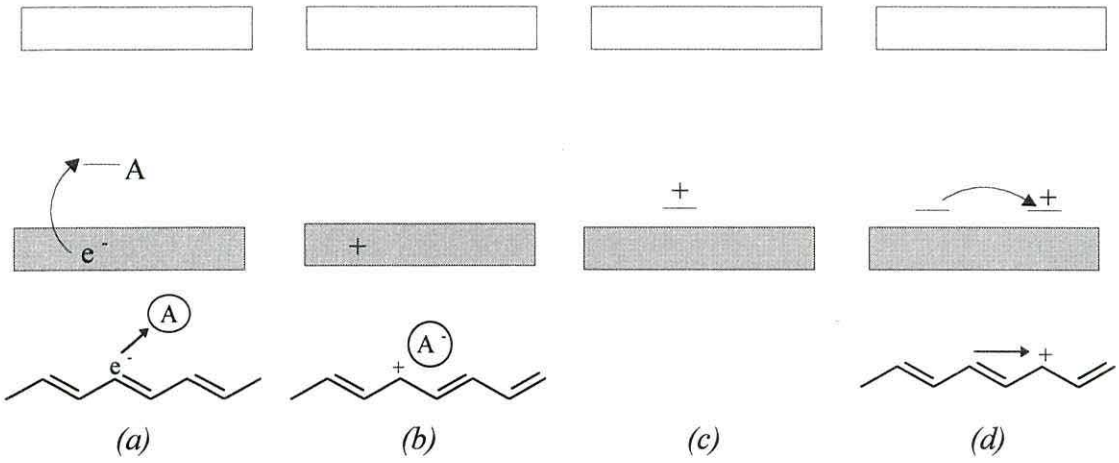

Figure 2.5 *Polaron formation and conduction. (a) An electron is promoted to an acceptor energy level, A, forming a hole in the valence band (b). The hole polaron is formed by movement of the hole to a band-gap state (c) which can propagate along a polymer chain when sufficient band-gap states exist (d).*

above the valence band edge (Figure 2.5(c)). The hole and associated polarisation is known as a polaron [13]. A number of these localised energy levels can be formed along the length of the polymer and when the density is high enough, for example by introducing a sufficiently high concentration of the dopant, enough levels exist for the hole to move from one to the next under the influence of an applied field (Figure 2.5(d)). This is the basis of the "hopping" theory of conduction [13].

If the polymer is oxidised further, a second charge can be introduced onto the polymer in the vicinity of the first. Now, either two separate lattice distortions are produced in the form of two polarons or the distortions can combine to form a single entity called a bipolaron [14]. A bipolaron has zero spin and binds together two charges of the same sign in close proximity. The bipolaron is energetically favourable compared to the polaron but both produce localised electronic states within the band gap. High doping concentrations in the polymer cause the polaron states to form a band, within the band-gap of the polymer, which yields quasi-metallic conduction. In polymers with non-degenerate ground states solitons are forbidden and conduction is confined to polaron and bipolaron mechanisms.

For further, more detailed, explanations of conduction mechanisms involving solitons, polarons and bipolarons the reader is refereed to McGehee and co-workers [15].

The excitation of an electron into the conduction band and consequent formation of a hole in the valence band can lead to the formation of an exciton [16]. In this case, both the electron and the hole produce distortions in the polymer causing localised states to be formed for both in the band-gap, near to the conduction band for the electron and near to the valence band for the hole. The polymer distortion confines the charges in the vicinity of each other and again, high doping levels in the polymer cause the localised states to form bands. The excitons can be long lived which allows conduction through the bands in a similar manner to the polarons and bipolarons.

2.2 Diode theory

To measure the electrical properties of polymers it is usual to form a polymeric diode structure by depositing the polymer onto a metallic substrate and adding a metallic counter-electrode to the top surface of the polymer. Ideally the electrodes are ohmic so that the results of experiments carried out on the diode reflect the electrical properties of the polymer. However, electrodes often inadvertently make rectifying contacts to the polymer and in some instances these rectifying contacts are used to investigate the band structure in the polymer.

The origin of ohmic contacts and rectification in a Schottky diode may be understood by considering the junction between a metal of workfunction $e\phi_m$ and a semiconductor of workfunction $e\phi_s$. The relevant band diagrams for each material prior to contact are shown in figure 2.6.

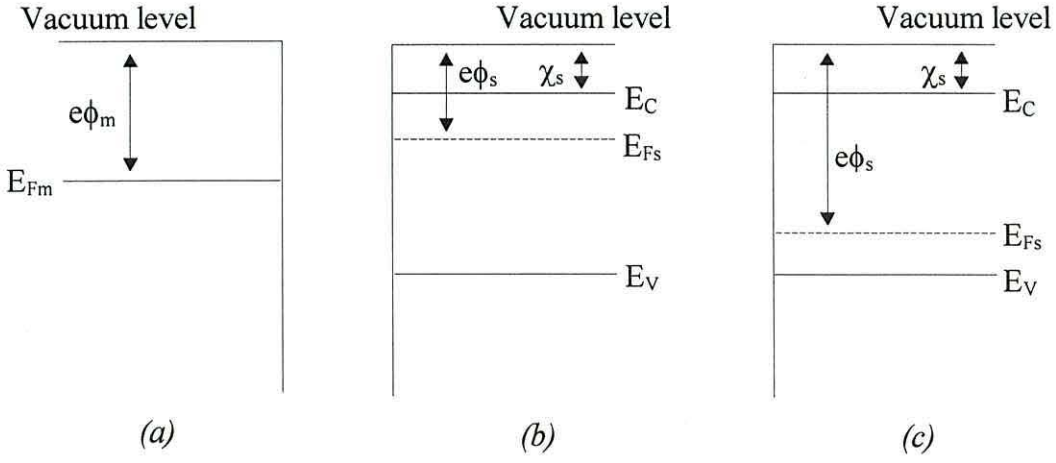

Figure 2.6 *Energy levels in (a) a metal, and (b) an n-type and (c) a p-type semiconducting polymer, prior to contact.*

2.2.1 Ohmic contacts

Ohmic contacts [17] can be formed which produce symmetrical current-voltage characteristics, the flow of carriers from the metal into the semiconductor and vice versa being equal. Minority carriers in the vicinity of the ohmic contact readily recombine with the majority carriers provided by the contact. The ohmic contact therefore acts as a virtual sink for minority carriers.

Ohmic contacts are produced using two methods. In the first case, if a metal with a workfunction greater than that for a p-type semiconductor (or less than that for a n-type semiconductor) is in contact with the semiconductor, and the barrier is small compared to kT, then carriers flow in either direction (metal to semiconductor and vice versa) without impediment. The second case, reducing the barrier thickness by heavy doping of the semiconductor causes a high field to be formed in the thin barrier. The barrier height is consequently reduced due to image force effects and the barrier becomes transparent in both directions. Formation of n^- or p^+ region near to the metal contact by heavy doping causes the junction to have high leakage currents. In both cases, there is very low resistance to current flow in both directions and the current-voltage characteristics are very symmetrical.

2.2.2 Schottky barrier diodes

Schottky barrier diodes [17] are based on the rectifying characteristics of a Schottky barrier, formed upon contacting a metal and a semiconductor. The Schottky diode consists of a sandwich structure incorporating the polymer and two electrodes, which are usually metals, one forming a rectifying contact and the other an ohmic contact (Figure 2.7). A large number of semiconducting materials are used in polymeric diodes, such as paraphenylenes, poly(phenylene vinylene)s, polythiophenes and polyanalines. Marsitzky and Mullen [18] have compiled a review of the synthesis of such materials.

Upon contacting the metal with the n-type semiconductor, majority electrons diffuse into the metal which consequently charges negatively with respect to the

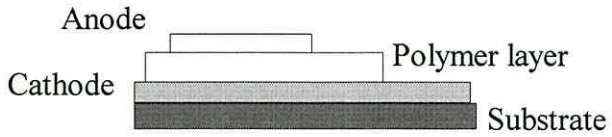

Figure 2.7 *Schematic diagram of a polymeric Schottky diode.*

semiconductor, thus, raising the potential energy of all the electrons in the metal. This process continues until the Fermi levels coincide, at which point a potential, $eV_{bi} = e\phi_m - e\phi_s$ is developed across the junction. This potential acts to prevent the further diffusion of electrons from the semiconductor. Indeed, majority carriers are driven from the junction under the action of the associated electric field. The parabolic potential distribution appearing in the surface space charge layer (depletion layer) of positively charged donors causes the bands of the semiconductor to bend as shown in figure 2.8. Similar considerations lead to the band diagram in figure 2.8(b) after contacting a metal and a p-type semiconductor where $\phi_s > \phi_m$.

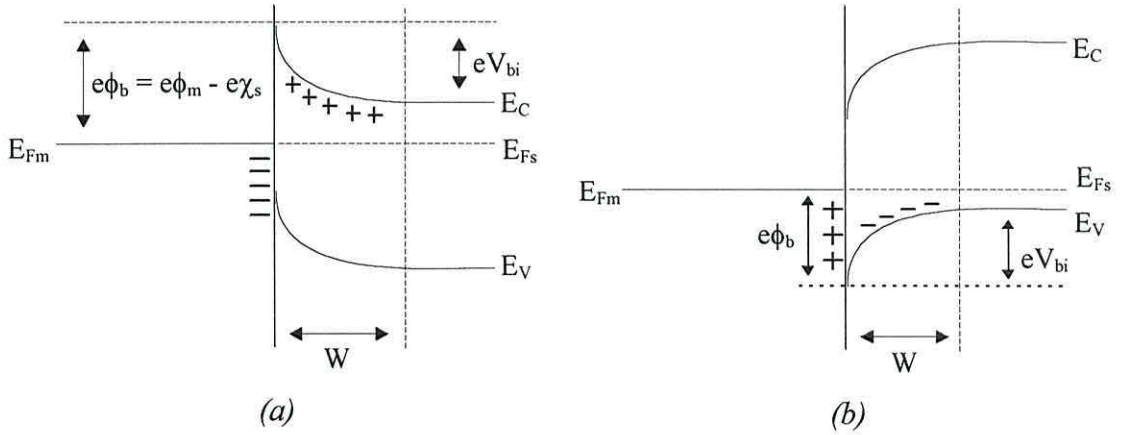

Figure 2.8 *Rectifying metal/semiconducting polymer contacts for (a) n-type and (b) p-type polymers.*

2.2.2.1 Electron and hole injection

The sandwich structure of the Schottky diode is such that the diode can be tailored preferentially to inject electrons or holes into the polymer by the suitable choice of electrode materials on either side. Also, the introduction of further organic layers at the electrode surfaces can be used to facilitate or block the flow of one charge carrier or the other into the bulk of the diode. The tailoring can then be used preferentially to

increase the concentration of one charge carrier in the polymer or to localise recombination of the charge carriers in one area of the diode, such as at an interface between the polymer and an electrode, thus increasing the probability of recombination. This aspect is covered further in section 3.2.1.

2.2.3 DC behaviour of an ideal Schottky barrier

The current at a metal/semiconductor interface can be described by the flow of charge carriers from the semiconductor to the metal and the metal to the semiconductor. For an n-type semiconductor-metal contact, when no bias is applied to the system, holes diffuse from the valence band, over the barrier and into the metal contact. Meanwhile, electrons from the contact and from the conduction band in the polymer migrate into the depletion region. The carrier diffusion from metal to semiconductor is exactly balanced by carrier diffusion from semiconductor to metal, as shown in figure 2.9(a).

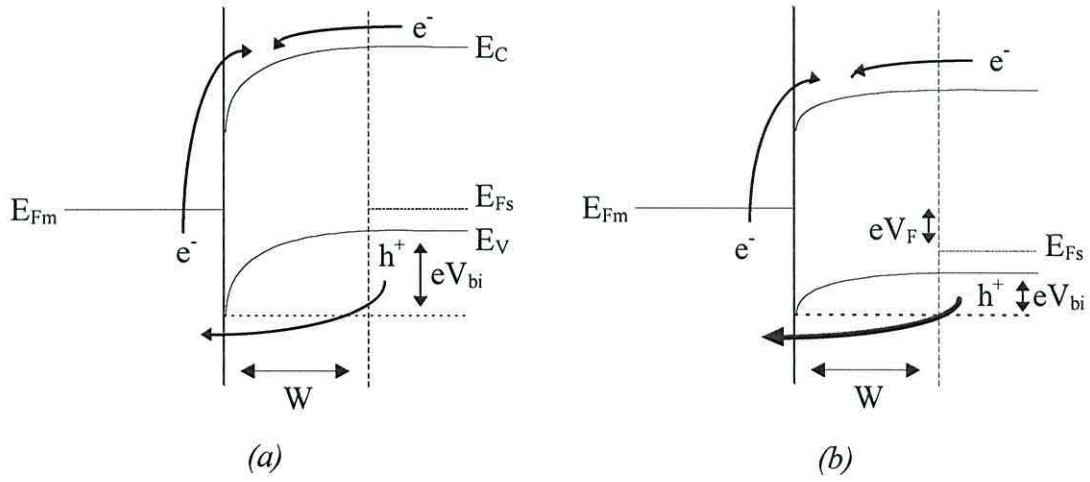

Figure 2.9 *Schottky barrier formed at the interface between a metal and a p-type semiconductor at (a) zero bias and (b) positive bias.*

Upon application of a positive bias, V_F, to the semiconductor (Figure 2.9(b)) (or negative to the electrode) the barrier to hole injection is reduced, increasing the rate of diffusion of holes into the metal. The rate of migration of electrons from the metal is also increased by the reduction in barrier height, however the increase is smaller than that for the holes as the barrier to electron injection is still significantly large. Migration from the conduction band remains constant due to the small number of

electrons in the conduction band being constant. Therefore, the hole diffusion dominates and the resulting current, denoted J_F [19], is given by,

$$J_F = J_0 \exp\left(\frac{qV_F}{nkT}\right) \qquad (2.1)$$

where, q is the electronic charge, T is the absolute temperature and J_0 is the reverse saturation current density. n is an ideality factor included to account for deviations from ideal single carrier theories.

The ideality factor of a good rectifier is close to 1. Ideality factors greater than unity have been explained by effects such as barrier tunnelling, the presence of an interfacial layer and interface states. For polymeric diodes the major effect would arise from the bulk resistance of the polymer or the presence of interfacial layers in the device, which reduces the fraction of the applied voltage appearing across the depletion layer.

In reverse bias, the barrier height increases and therefore the rate of hole diffusion decreases. The electron injection from the electrode is also reduced due to the higher barrier, but the electron migration from the conduction band again remains constant. In this case, as the majority carrier diffusion is reduced, the measured current is a net electron flow from the semiconductor to the metal.

For a majority hole charge in the bulk of the semiconductor to enter the metal, it must diffuse across the depletion region until it reaches the interface where it must enter the metal before being rapidly removed. The two processes (i) diffusion through the semiconductor and (ii) transfer to the metal, determine the current flow depending on which presents the greater impediment [7]. Diffusion theory assumes that the current limiting process is diffusion through the semiconductor whereas thermionic emission theory assumes that transfer of the charge carrier into the metal limits the current.

As the barrier height from the metal to the semiconductor remains constant the reverse current is independent of the applied voltage [20] and therefore,

$$J_0 = A^* T^2 \exp\left(\frac{-q\phi_b}{kT}\right) \qquad (2.2)$$

where, A* is the modified Richardson constant and ϕ_b is the difference between the Fermi level in the metal and the valence band in the semiconductor. Again, in practice the current actually increases slightly due to the bias dependence of the barrier height.

When the current is limited by diffusion [21] then,

$$J_0 = qN_V \mu E_{max} \exp\left(\frac{-q\phi_b}{kT}\right) \qquad (2.3)$$

where N_V is the effective density of states in the valence band and E_{max} is the maximum field strength in the space charge layer occurring at the interface. E_{max} is proportional to $(V_{SO}-V)^{1/2}$ where V_{SO} is the extent of the band bending in the semiconductor at zero applied bias, i.e. the contact potential difference. At high reverse bias the diode current increases as $V^{1/2}$.

When image force lowering effects are taken into account the reverse current is modified [19] and given by,

$$J_R = J_0 \exp\left\{\left(\frac{q}{kT}\right)\left(\frac{q^3 N_A (V_C - V_A)}{8\pi^2 \varepsilon_\infty^2 \varepsilon_S \varepsilon_0^3}\right)^{1/2}\right\} \qquad (2.4)$$

where, N_A is the acceptor density, V_A is the applied voltage and ε_∞, ε_S, and ε_0 are the high frequency, static and vacuum permittivities respectively and $V_C = V_{SO} - (kT/q)$. The reverse current now varies as $(V_C - V_A)^{1/4}$.

2.2.4 AC behaviour of an ideal Schottky diode

In an ideal Schottky diode formed from a p-type semiconductor, the depletion region contains a fixed, uniformly distributed space charge (Q_{SC}) arising from the presence of ionised acceptor impurities [22]. Upon incremental change of the voltage, dV, applied to the semiconductor the depletion width changes and causes an incremental change in the space charge, dQ_{SC}. The small signal capacitance of the depletion region is then defined as $C_d = dQ_{SC}/dV$ which leads to the Mott-Schottky relation [23] between the depletion capacitance and the applied voltage i.e.,

$$C_d^{-2} = \frac{2}{q\varepsilon\varepsilon_0 N_A}(V_{SO} + V), \qquad (2.5)$$

where N_A is the density of acceptor states, and V_{SO} is the degree of band bending. Applying equation 2.5 to experimental data enables N_A and V_{SO} to be determined.

For a polymeric diode, the equivalent circuit can be described by two parallel RC circuits in series [19, 24]. C_d and R_d represent the high-resistivity, depletion layer

while C_b and R_b represent the low resistivity, bulk polymer region in the diode (Figure 2.10). Therefore, the capacitance of the diode cannot be assumed to be solely due to the depletion region alone.

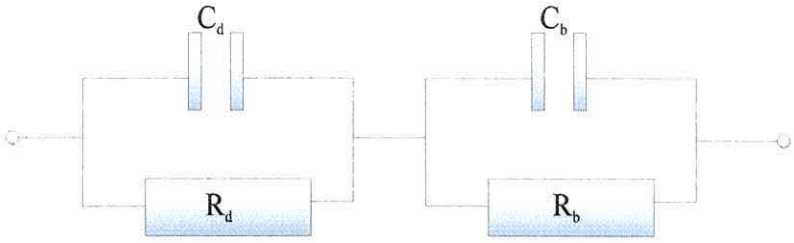

Figure 2.10 *Equivalent circuit for a polymeric diode compromising of a depletion layer and a bulk region. R_b, R_d, C_b and C_d are the resistances and capacitances of the bulk and depletion regions respectively.*

The total admittance, Y_P, of the circuit in figure 2.10 is given by [19],

$$Y_P = G_P + j\omega C_P, \tag{2.6}$$

where,

$$C_P = C_g + \frac{C_{LF} - C_g}{1 + (\omega\tau)^2}, \tag{2.7}$$

and,

$$G_P = G_{LF} + \frac{G_a}{1 + (\omega\tau_R)^2}. \tag{2.8}$$

C_g is the series sum of the bulk and depletion layer capacitances, $C_d C_b / (C_d + C_b)$, and C_{LF} is the effective low frequency capacitance defined by,

$$C_{LF} = \frac{C_d R_d^2 + C_b R_b^2}{(R_d + R_b)^2}. \tag{2.9}$$

G_{LF} is the low frequency, or DC, conductance $(R_d + R_b)^{-1}$, and G_a is the AC conductance given by,

$$G_a = \omega^2 \frac{R_d R_b (R_d C_d - R_b C_b)^2}{(R_d + R_b)^3}, \tag{2.10}$$

and τ_R is the circuit relaxation time given by,

$$\tau_R = \frac{R_d R_b}{R_d + R_b}(C_d + C_b). \tag{2.11}$$

Thus, the effective capacitance of the circuit undergoes a Debye-like dispersion with a single relaxation time. Figure 2.11 describes the capacitance and loss of the circuit as a function of frequency. At low frequencies, R_b short circuits C_b so only C_d is measured (region A). At sufficiently high frequencies above the relaxation frequency (B), the measurement bridge "observes" the circuit as the series sum of C_b and C_d and since $C_b << C_d$ the measured capacitance is approximately C_b (region C). Also, at very low frequencies in figure 2.11(b), that part of the loss (G/ω) contributed by the DC component of conduction ($= G_{DC}/\omega$) rises rapidly as frequency decreases (region A).

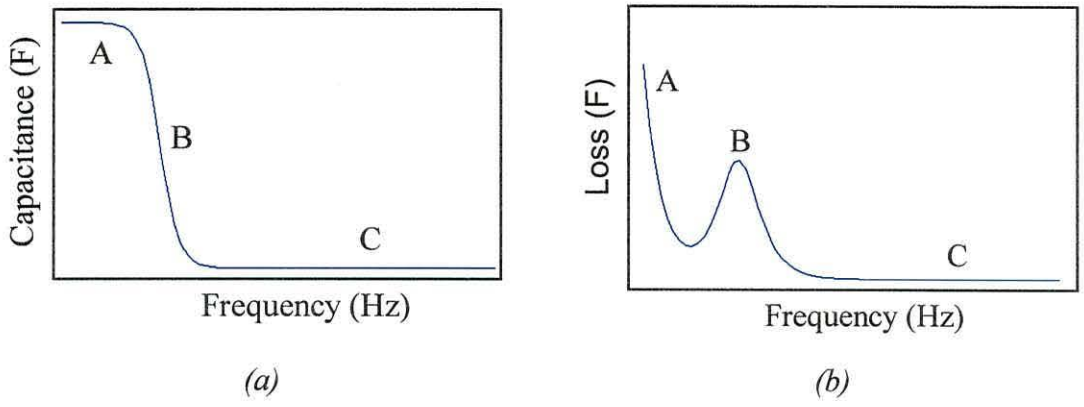

Figure 2.11 *Theoretical plots of (a) capacitance and (b) loss (G/ω) versus frequency using the circuit described in figure 2.10.*

For a diode in which the electrode introduces a small series resistance, the circuit diagram is modified as shown in figure 2.12 to include the series resistance, R_s [25, 26].

The impedance of this circuit can be expressed as,

$$Z = \frac{1}{\frac{1}{R_d} + j\omega C_d} + \frac{1}{\frac{1}{R_b} + j\omega C_b} + R_s \qquad (2.12)$$

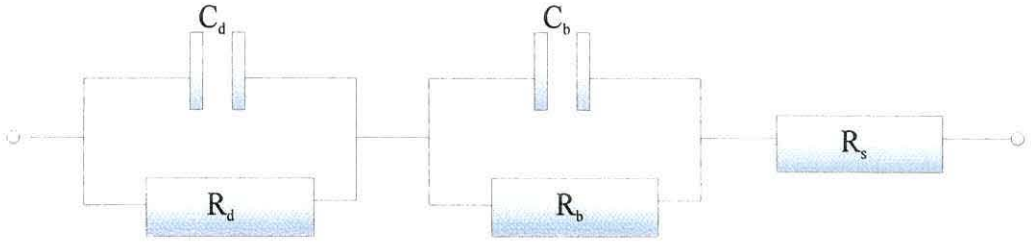

Figure 2.12 *Equivalent circuit for a polymeric diode comprising of a depletion layer and a bulk region, and incorporating a small series resistance, R_s.*

The admittance may again be determined and again the capacitance, C_p, and conductance, G_p, found. The mathematical treatment is given in Appendix 2. From equation A2.11 it is seen that as $\omega \rightarrow 0$,

$$G_p = \frac{1}{R_b + R_d + R_s}, \tag{2.13}$$

and,

$$C_p = \frac{C_d R_d^2 + C_b R_b^2}{R_d^2 + R_b^2 + R_s^2 + 2R_d R_b + 2R_d R_s + 2R_b R_s}. \tag{2.14}$$

As R_d tends to ∞, $G_p \approx 0$ and $C_p \approx C_d$. Rearranging the equations for the capacitance and conductance (Appendix 2) and allowing ω to tend to ∞ then, $G_p \approx 1/R_s$ and $C_p \approx 0$. Figure 2.13 shows the theoretical plots of the capacitance and loss curves due to this modification to the equivalent circuit.

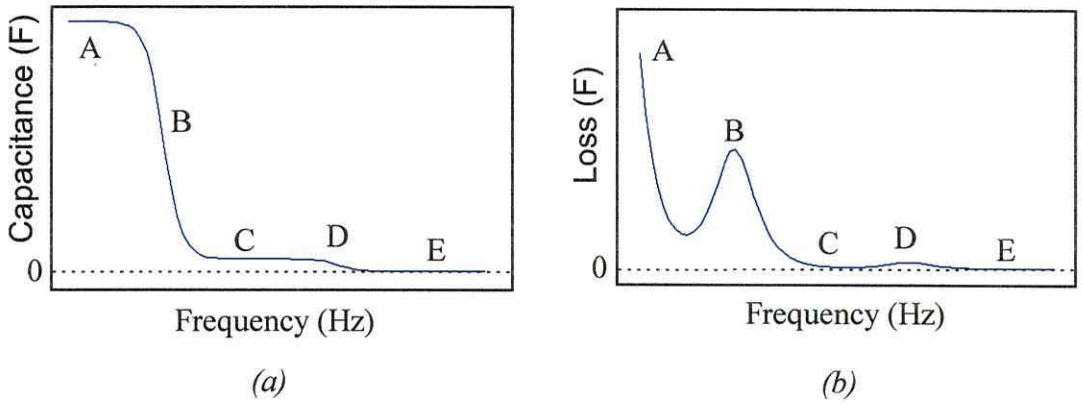

Figure 2.13 *Theoretical plots of (a) capacitance and (b) loss (G/ω) versus frequency using the circuit described in figure 2.12.*

Again, at low frequencies, only C_d is measured (region A). As frequency rises the dispersion due to the depletion layer (region B) is observed. At higher frequencies, the susceptances of the bulk and depletion layer capacitances decrease sufficiently so that R_d and R_b may be ignored. Thus, the total capacitance, C_T, is the series sum of C_b and C_d, i.e. ,

$$C_T = \frac{C_b C_d}{C_b + C_d}, \tag{2.15}$$

and is charged through R_s. As C_d is large compared to C_b, then $C \approx C_b$ (region C). Following the second dispersion (region D), at higher frequencies, due to the presence of the series resistance the capacitance falls to zero (region E).

2.2.5 Conduction mechanisms

Application of an electric field, E, to a polymeric semiconductor causes charged species in the polymer to move giving rise to a current density, J, which depends on E. To enter the polymer, electrons/holes must overcome a potential energy barrier at the interface and once in the polymer may fall into potential energy wells, called traps. To contribute to the current, the electrons/holes then must surmount further potential energy barriers to escape from the traps.

2.2.5.1 Potential energy wells

The potential energy wells in the polymer may be described as areas where the potential energy falls dramatically and into which a charged particle can become trapped (Figure 2.14(a)). An electron or hole in the well with charge q must gain energy, ϕ_w, to surmount the energy barrier. The probability, p, of gaining this energy is given by the Eyring rate equation [27], $p = \nu \exp\left(-\frac{\phi_b}{kT}\right)$. Upon application of a uniform applied field, E_x, the potential energy is modified (Figure 2.14(b)) with an increase in the height of the barrier on one side and a reduction on the other. The probability of a charge carrier at the same energy as in Figure 2.14(a) leaving the potential well is now increased in the direction of the net electric field. A number of types of barrier lowering can occur on the application of the field.

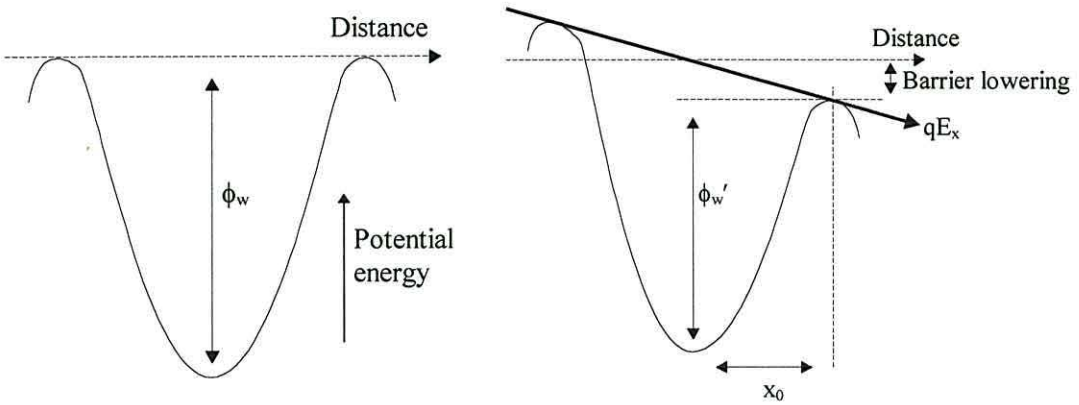

Figure 2.14 *Potential energy well in a semiconducting polymer with (a) no applied field and (b) an applied field, E.*

2.2.5.2 The Poole-Frenkel model

The Poole-Frenkel effect is a bulk dielectric effect. If an electron is removed from a localised state in the semiconductor, leaving behind a bound positive charge, the Poole-Frenkel model, based on the work by Frenkel [28], is obeyed. In the absence of an electric field the potential energy depends on the coulombic attraction between the electron and the positive site left behind. The potential energy can then be defined as,

$$\phi_{(x)} = \frac{-e^2}{4\pi\varepsilon_0\varepsilon_r|x|}, \tag{2.16}$$

where x is the distance of the electron from the positive site and ε_0 and ε_r are the permittivity of free space and the relative permittivity respectively. Upon application of a field, the potential becomes,

$$\phi_{(x)} = \frac{-e^2}{4\pi\varepsilon_0\varepsilon_r|x|} - eEx. \tag{2.17}$$

The potential energy barrier has a maximum at x_0 (Figure 2.14(b)) where,

$$x_0 = \left(\frac{e}{4\pi\varepsilon_0\varepsilon_r E}\right)^{1/2}, \tag{2.18}$$

which results in a total lowering of the barrier of $e\left(\frac{eE}{\pi\varepsilon_0\varepsilon_r}\right)^{1/2}$. The flow of charge carriers over the barrier in the direction opposing the field is halted when considering a

single site. However, for fields in excess of approximately 10^5 Vcm^{-1}, if another potential energy well is nearby the current in the direction of the field, over the lower barrier, dominates over the current in the opposite direction so that [29],

$$J = A\exp\left(-\frac{\left(\phi_w - e\beta_{PF}E^{1/2}\right)}{kT}\right), \tag{2.19}$$

where $\beta_{PF} = \left(\frac{e}{\pi\varepsilon_0\varepsilon_r}\right)^{1/2}$.

The Poole-Frenkel mechanism has been used to explain conduction based on polaron hopping in an Al/Acid-doped PANI/Al device at high fields [30].

2.2.5.3 The Schottky effect

Emission of electrons from a metal electrode, over a potential barrier which is lowered by the application of an applied field, into a semiconductor is known as the Schottky effect. The potential energy of the electron is governed by an image-force law and takes the form [31],

$$\phi_{(x)} = \frac{-e^2}{16\pi\varepsilon_0\varepsilon_r x}, \tag{2.20}$$

where x is the distance of the electron from the metal/polymer interface ($x > 0$ so that the electron is positioned in the semiconductor, not in the metal). Upon application of the field [32] (Figure 2.15) the expression for the potential is modified to,

$$\phi_{(x)} = \frac{-e^2}{16\pi\varepsilon_0\varepsilon_r x} - eEx\,. \tag{2.21}$$

This produces a maximum for the lowered barrier at x_0 where,

$$x_0 = \left(\frac{e}{16\pi\varepsilon_0\varepsilon_r E}\right)^{1/2}, \tag{2.22}$$

causing a total lowering of the barrier in the direction of the field of $e\left(\frac{eE}{4\pi\varepsilon_0\varepsilon_r}\right)^{1/2}$ and, therefore, the current is,

$$J = A\exp\left(-\frac{\left(\phi_w - e\beta_S E^{1/2}\right)}{kT}\right), \tag{2.23}$$

where $\beta_S = \left(\frac{e}{4\pi\varepsilon_0\varepsilon_r}\right)^{1/2}$.

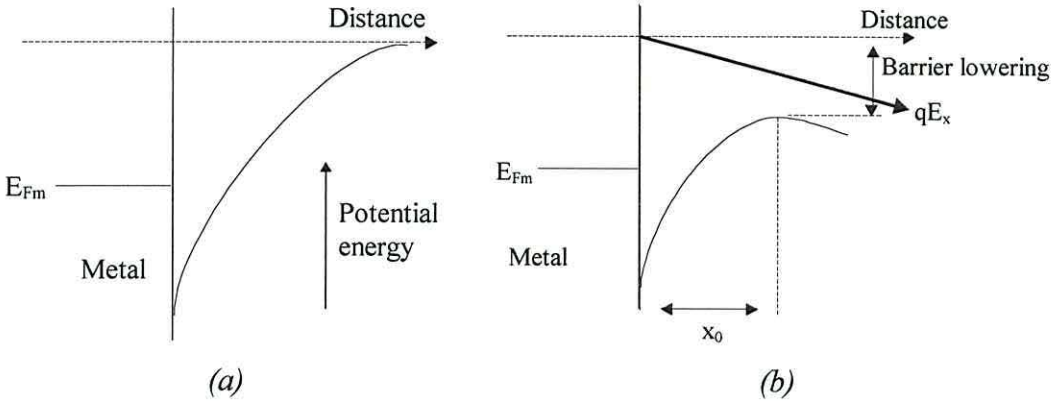

Figure 2.15 *Potential energy diagram showing the origin of the Schottky effect. (a) No applied field and (b) field, E, applied in the positive direction.*

2.2.5.4 Fowler-Nordheim tunnelling theory

In classical physics the electron is considered to be a particle so that the presence of a potential energy barrier, prevents electrons from surmounting the barrier unless they are thermally or optically excited to a sufficiently high energy. In a polymeric diode such barriers can occur at the polymer/electrode interface or at trap sites. Quantum mechanical concepts, on the other hand, allow electrons with seemingly too little thermal energy to "tunnel" through a potential barrier. This is especially favourable at the top of the barrier where it is at its thinnest. Using the electron in the potential well in figure 2.14(b) as an example, if the field was increased further (> 10^7 Vcm^{-1}) the barrier would be further lowered thus becoming sufficiently thin (< 10 nm) for tunnelling to occur.

Consider a potential barrier under forward bias (Figure 2.16) where ϕ is the barrier height, W is the thickness of the barrier and n is the number of charge carriers available for tunnelling. The tunnelling current, I_t, can be described by Fowler-Nordheim tunnelling theory, and is defined as [7, 31],

$$I_t = qA\nu_t nT_t, \tag{2.24}$$

where, ν_t is the velocity of the tunnelling electrons and T_t is the tunnelling probability, defined as,

$$T_t = \exp\left(\frac{-8\pi\sqrt{2qm^*}}{3hE_x}\phi^{3/2}\right). \qquad (2.25)$$

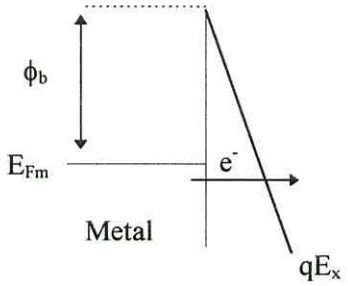

Figure 2.16 *Fowler-Nordheim tunnelling through a potential barrier.*

Equation 2.24 can be rewritten to show that the current relates to the applied electric field so that,

$$I\alpha E^2 \exp\left(-\frac{\kappa}{E}\right), \qquad (2.26)$$

where κ is a parameter based on the barrier shape. From the slope of a plot of J/E^2 versus E^{-1} at high fields, κ may be estimated and hence the barrier height, ϕ, since,

$$\kappa = \frac{8\pi(2m^*)^{1/2}}{3qh}\phi^{3/2}, \qquad (2.27)$$

where, m* is the effective mass of the hole, e is the charge on an electron and h is Planck's constant.

Parker applies the Fowler-Nordheim tunnelling model to hole injection in an ITO/MEH-PPV/Ca diode [32]. At low fields the current in the device was dominated by thermionic emission but as the field was increased Fowler-Nordheim tunnelling took over. Using a variety of cathode materials, with workfunctions that increased from 4.2 eV (In) to 5.2 eV (Au), Parker concluded that, as the barrier height deduced for each device remained unchanged, the barrier in each was at the ITO/polymer interface. By replacing the ITO anode with a thin PANI layer [33] the barrier to hole injection was thought to decrease making the tunnelling diodes more efficient.

2.2.5.5 Space-charge-limited current

If one carrier dominates conduction in the polymer, or one carrier is significantly more mobile than the other, a charge imbalance occurs and the current is space charge modified. An extreme, but simple, case is the one-carrier, space-charge- limited current (SCLC) model [13]. Mott and Gurney [34] used Poisson's equation, $\frac{d^2V}{dx^2} = -\frac{\rho(x)}{\varepsilon_0 \varepsilon_r}$, where ρ(x) is the electric charge density, in conjunction with the current flow equation for a trap free semiconductor with a single mobile carrier, $J = ne\mu E$, where J is the current density, n is the electron concentration, e is the charge on an electron, μ is the mobility and E is the electric field strength, and, by neglecting the diffusive contribution, showed that the current obeyed Child's law,

$$J = \frac{9\mu\varepsilon_0\varepsilon_r V^2}{8d^3}, \qquad (2.28)$$

where d is the thickness of the semiconductor and V is the applied voltage. The presence of traps in the polymer, shallow or deep depending on whether they are above or below the Fermi level (Figure 2.17), was found to lower the SCLC.

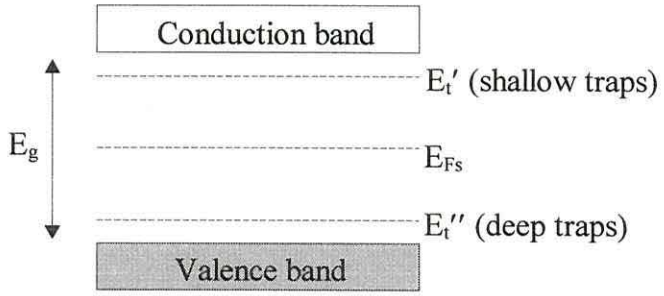

Figure 2.17 *Position of shallow and deep electron traps in the semiconductor band-gap.*

Lampert [35] described the current-voltage characteristic for a dielectric with a single set of shallow traps (Figure 2.18). Ohm's law, $J \propto V$, is obeyed at low voltages, region **A**, where the injected charge density is lower than the thermally generated carrier density. At higher voltages, the current becomes space-charge-limited with the modification due to the presence of the traps, region **B**. At the trap filled limit, V_{TFL}

(**C**), the current increases rapidly over a small voltage range until all the traps are filled, **D**, and the current returns to the trap-free curve, $J \propto V^2$.

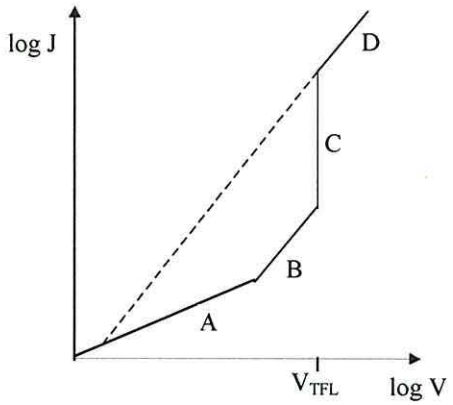

Figure 2.18 *Current density versus voltage plot for a dielectric with a single set of shallow traps, trap free law (-----) and trap modified square law (——).*

Mark and Helfrich [36] extended Lampert's theory by assuming that traps are distributed in energy. They showed that in such cases,

$$J = N_c \mu e^{1-l} \left[\frac{\varepsilon l}{N_t (l+1)} \right]^l \left[\frac{2l+1}{l+1} \right]^{l+1} \frac{V^{l+1}}{d^{2l+1}} \qquad (2.29)$$

where N_c is the effective density of states in the conduction band and $l = \frac{T_c}{T}$, where T_c is a parameter describing the trap distribution. A number of polymer films [37], including thiophene based polymers, have been found to be space charge limited using ITO substrates as hole injectors.

2.3 Summary

The basic theoretical concepts applied to semiconducting polymers and the Schottky diode devices that can be formed using those polymers have been reviewed. A short introduction into inorganic semiconductors was used to introduce such ideas as hole formation, intrinsic and extrinsic properties, including doping, and also the idea of minority and majority carriers. This then led to the theoretical ideas underlying polymeric semiconductors, by initially describing the structure of the simplest polymer of this type, polyacetylene.

Band formation was then introduced by first describing the molecular orbital model of energy levels in the monomer and how polymerisation led to the formation of the conduction and valence bands in the polymer, with the subsequent formation of the band gap due to Peierls instability in the C=C bonds. The difference between insulating, semiconducting and conducting polymers was then explained in terms of the magnitude of the band gap. The inorganic semiconductor approach to the formation of free charge carriers was seen to be too simplistic for the polymeric semiconductor due to the formation of lattice distortions and Coulomb interactions in the polymer.

Thus it was necessary to introduce new charge species, namely solitons, polarons, bipolarons and excitons, in polymeric systems. The solitons were found to occur exclusively in polymers with degenerate ground state configurations whereas non-degenerate polymers could form the other types of polarised states.

Diode theory was then covered with a description of ohmic contacts and Schottky barrier diodes. The origin of rectification and the formation of a depletion region in these diodes was examined based on the band structure of the contacting materials. The AC and DC behaviour of an ideal Schottky barrier was investigated with theoretical descriptions produced for each. The AC description considered that the polymeric diode could be represented by an equivalent circuit consisting of two RC circuits in parallel, describing the bulk and depletion layers in the polymer, yielding a single dispersion. Modification of this model to include a small series resistance caused the appearance of a second dispersion, assigned to the presence of the resistance.

The conduction mechanisms in the bulk material of these diodes was then considered in terms of the potential energy wells and barriers found in these systems. Four mechanisms for conduction were discussed, namely, the Poole-Frenkel model, the Schottky effect, Fowler-Nordheim tunnelling theory and space charge limited current theory. These models will be used to analyse the experimental AC and DC electrical results obtained for the polymers used in this project.

3. Low band-gap polymeric diodes

3.1 Low band gap polymers

The goal of a number of researchers [38] has been the design of a low band gap polymer for use in electronic components as a replacement for their inorganic counterparts. The large number of possible organic polymers available by chemical "tuning" of the polymeric structure means that there is a good possibility that materials of this type could be found that can compete with inorganic-based electronics, at least in niche markets. Polymeric electronics would have the advantages of low cost, easy processability and good mechanical properties, while still having electronic properties on a par with inorganic-based devices.

For example, organic LEDs are predicted to have a maximum luminescent efficiency, and hence emitted light intensity, equivalent to a external quantum efficiency of 5% photons per electron (ph/el) [39]. Already, LEDs incorporating MEH-PPV [40] are approaching 3% ph/el external efficiency with luminescent intensity of 100 cd/m^2 (the brightness of a computer screen) at 2.5 V bias, and 4000 cd/m^2 (the brightness of a fluorescent light bulb) at less than 4 V bias. A blue DO-PPP LED [41] has also been found to produce 3% ph/el external efficiency, comparable to inorganic LEDs.

Although short operating lifetimes ranging from a few minutes to a few hundred hours at 100 cd/m^2, compared to 10,000 hours for an equivalent inorganic LED, are common, a PPV LED has been found to produce lifetimes in excess of 3,000 hours at approximately 25 cd/m^3 [42].

The following sections review the low band-gap polymers reported at the present time in the literature. A definition of low band-gap polymers leads to a review the background to basic monomer units used for the production of these polymers. The methods for customising polymers is also reviewed, using examples for polymers in general rather than just low band-gap polymers. Finally, an examination of the polymers, PCDM and PBDT, used in this project is undertaken. A short review is included of the various device customisation methods and applications utilising such

polymers. The applications concentrate on three major areas, optical devices, electrical components and sensors. The reader is also directed to a number of comprehensive review articles in the "Handbook of Conducting Polymers" which expand on much of the literature presented here [7].

3.1.1 Background

Low band-gap polymers can be defined as polymers with band-gaps lower than or equal to 2 eV. A number of polymers reported in the literature, examples of which are given in table 3.1, fall into this category, including polymers based on phenylene vinylene, heterocycle and acetylene monomers. These basic monomers, and often their homologues, are typically used for the production of polymers found in devices such as LEDs.

Table 3.1 *Examples of polymers reported in the literature with band-gaps ≤ 2 eV.*

Polymer	Reported band-gap (eV)
MEH-PPV [43]	2
CN-PPV [44]	1.8
CN-PPV/PPV [45]	1.7
poly(thiophene-phenylenevinylene) [46]	1.68 - 1.24
poly(thiophene phenylenevinylene) [47]	1.8
poly(thiophene vinylene) [47]	1.55
POPT [48]	1.55
PCDT [49]	1.2
PCDM [49]	0.8
PDTT [50]	1.2
Ppy-based [51]	1.1
donor/acceptor [52]	1.15 - 0.5
PTT [53]	1.02
poly(iso-thianaphthalene) [53]	0.54
PMP [54]	1.75 - 1.24

Each of the monomer units (Figure 3.1) displays a high degree of conjugation which, upon polymerisation, produces polymers with similar degrees of conjugation. These polymers are then especially suited, due to this conjugation, for applications where a semiconductor is required. Although polymers, produced using these starting monomers alone, tend not to have low band-gap properties, for example poly(phenylene vinylene) has been reported to have a band gap of approximately 2.2 eV, a large amount of literature is available regarding polymers with low band-gaps *based on* poly(phenylene vinylenes) and poly(heterocycles).

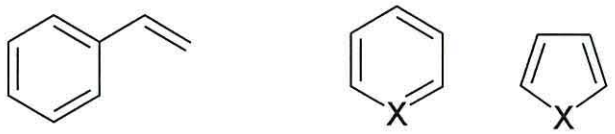

(a) *(b)*

Figure 3.1 *(a) Phenylene vinylene and (b) heterocycle (where X is the heteroatom) monomer units.*

The simplest conjugated polymer is polyacetylene. It was the first polymer to be artificially doped, in 1977, producing higher conductivities upon achieving a quasi-metallic state [1, 55]. This discovery led to the award of the 2000 Nobel Prize for Chemistry to the principle researchers, Heeger, Shirakawa and MacDiarmaid. Polyacetylene has been found to be insoluble in all organic solvents and is prone to oxidation of its double bonds under ambient conditions, but it has been used successfully in devices [56] even in its free standing, flexible state [57]. The conductivity of polyacetylene has been improved from 10^{-5} S cm^{-1} when initially reported in 1970 to approximately 10^{5} S cm^{-1} currently [58]. However, it is unsuitable for the production of low band-gap materials.

The first polymer to be shown to electroluminesce [59], poly(phenylene vinylene) (PPV), is also one of the most extensively studied. Yellow/green light emission from a PPV diode was produced but the efficiency of light emission was calculated to be low, about 0.01%. However, due to the ease of processing PPV from precursor monomers [62] further work has concentrated on customisation of the basic polymer in a number of ways to produce low band-gap materials. Copolymerisation [61], the use of acceptor moieties, such as cyano groups [62], or donor moieties, such as

heteroatoms [46, 63], and the use of non-conjugated fractions of the polymer [64] have all been attempted to try to improve on the polymer characteristics. As indicated earlier, diodes based on derivatives of PPV with a high luminescence yield [65], comparable to their inorganic counterparts [66], have been produced.

As the work presented here is based on materials incorporating thiophene, the production of heterocyclic polymers and especially poly(thiophene)-based polymers will be concentrated on. Heterocyclic monomers based on 5- or 6-membered rings of carbon, and incorporating sulphur, nitrogen or oxygen, have all been studied [67]. The term heterocycle can be used to describe both aromatic molecules, such as pyridine, and non-aromatic molecules, saturated or otherwise, such as piperidine (Figure 3.2). However, only the aromatic homologues can be used to produce the highly conjugated polymer systems required for semiconducting materials and therefore, the non-aromatic molecules will be disregarded.

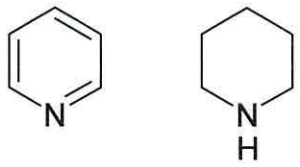

(a) *(b)*

Figure 3.2 *(a) Aromatic pyridine and (b) non-aromatic piperidine molecules.*

Aromatic molecules obey the Hückel criterion, containing $4n + 2$ electrons in π-orbitals, where n is a positive integer (or zero in special cases). The most well known aromatic molecule, benzene, consists of a ring of 6 carbon atoms with alternating single and double bonds. In pyridine, a 6-atom cyclic molecule, a CH unit from the benzene molecule is simply replaced with an sp^2 hybridised nitrogen atom. Therefore, pyridine has a lone pair of electrons, rather than the hydrogen present on the benzene carbon, but it is still aromatic by virtue of having 6 electrons in the π-orbitals of the ring system donated by the carbons and the nitrogen. Five membered heterocycles, such as pyrrole, are also aromatic as the lone pair of electrons on the nitrogen contributes to the π-system as shown in figure 3.3. This completes the six electrons required to satisfy the Hückel rule.

This explanation shows that there are two types of systems. Molecules such as pyridine are inherently aromatic, whereas, molecules like pyrrole are aromatic only by

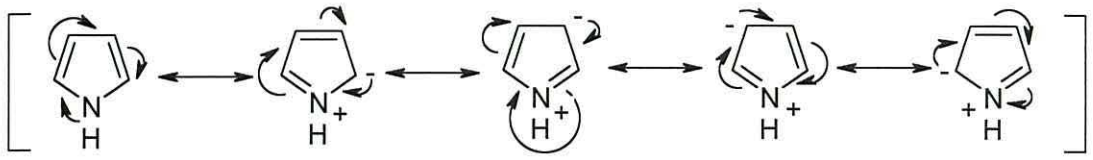

Figure 3.3 *Contribution of the lone pair of electrons on the heteroatom of pyrrole to its aromatic system, satisfying the Hückel criterion.*

delocalisation of the heteroatom lone pair of electrons. As this delocalisation requires removal of the lone pair from the heteroatom, the aromaticity of the 5-membered heterocycle depends on the electronegativity of the heteroatom. Therefore, as oxygen is more electronegative than nitrogen or sulphur, furan is considered to be almost non-aromatic. Thiophene is the most aromatic, sulphur being the least electronegative atom, and nitrogen less so (Figure 3.4). Synthesis reactions for such 5- and 6-membered heterocycles have been reviewed by Davies [67].

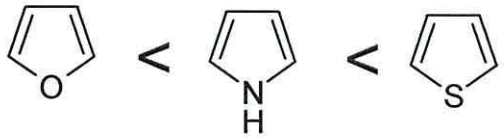

Figure 3.4 *Aromaticity of 5-membered heterocycles, furan < pyrrole < thiophene.*

The first low band-gap polymer to be identified as such was poly(isothianaphthalene) (PITN) in 1984 [68], which was found to have a band-gap of approximately 1.1 eV [69] although this figure has now been reduced [54]. The low value was thought to be due to the high quinoid character and maximum coplanarity in the structure [70].

Similarly, poly(3-alkylthiophenes) (P3AT's) have been found to be low band-gap polymers with a wide range of side groups available for substituting at the 3-position. The addition of long-chain alkyl side groups helps to improve the solubility, and hence the processability, of the monomers and good electrical conductivity is achieved from the polymers, up to 10^5 S cm^{-1} [68]. Careful chemical control of the polymerisation step has also allowed regioregular PAT's to be produced which has also improved device characteristics [71]. Again a number of derivatives of PITN and PAT's, including bridged dithiophenes such as PCDM and PBDT, are available and are covered in review articles [7].

3.1.2 Polymer customisation

Customisation of the polymer is sometimes required to achieve optimum characteristics. This section describes methods for "tailoring" the polymer structure, such as constraint of the conjugated polymer backbone to increase π-orbital overlap. The examples of the polymers used here are not necessarily low band-gap polymers but the customisation methods used can be modified for use with most systems.

Only a small number of polymers have been synthesised to date which are used as the precursors for low-band gap polymers. These polymers include PPVs, thiophene-based polymers and polyanaline-based polymers. Consideration should, therefore, be given to methods for customising existing polymers and the possible tailoring of new polymers from first principles. Known guidelines can be followed to ensure the polymer displays a low-band gap character. This can be done by considering a number of factors concerning the make up of the polymer, including its structural and electronic properties.

The alignment and overlap of the π-bonds in the polymer are facilitated by the conformation of the polymer backbone. If the carbon chain is twisted the amount of π-overlap is reduced and hence the polymer displays a more insulating character. Therefore, some of the most efficient semiconducting organic materials are constrained to reduce the amount of twisting that can occur in the backbone. This is usually achieved by the introduction of aromatic moieties into the polymer chain. These moieties do not interrupt the conjugation in the polymer due to the aromaticity present within the moieties themselves and can be used to introduce further polymer modifications, such as electron withdrawing groups, heteroatoms or solubilising groups, making the polymers more versatile.

For semiconducting polymers, one of the most important prerequisites is that conjugation occurs along the carbon backbone to facilitate charge carrier movement. The degree of conjugation present can affect the optical and electrical properties of the polymer by altering the band-gap. Therefore, by engineering the conjugation length or the degree of aromatic versus quinoid character in the polymer the band gap can be altered.

By designing a high degree of quinoid character into the polymer the C-C bond length is decreased and the polymer band-gap is decreased [54, 72], indeed polymers with band gaps approaching 1 eV have been designed using this approach. The average length of the conjugation in the polymer chain can be controlled in the polymerisation stage. Comparison of PPV polymer films produced by spin coating and self assembly has shown that the self assembly technique produces a shorter average conjugation length and a blue shift in the photoluminescence spectrum indicating a change in the band-gap [73].

In a theoretical study, Boudreaux and co-workers [74] showed that starting from polyacetylene (band-gap of 1.5 eV) a series of poly(arenemethide) polymers could be designed with successively smaller band-gaps. The band-gap was reduced by addition of aromatic rings (1.17 eV), rigidification of the polymer (0.97 eV) and finally addition of a nitrogen heteroatom into the rings (0.6 eV). Addition of a heteroatom into a polymer chain is a common feature of designing semiconducting polymers with atoms of nitrogen [51, 75] and sulphur [76] commonly used, normally as part of a heterocycle moiety.

Rigidification of the polymer using bulky constituents has been tried on a number of polymers [77] to reduce the amount of twisting in the polymer backbone and hence, increasing the π-orbital overlap and reducing the band-gap. This method can be used to produce regioregularity in a polymer such as 3-substituted poly(alkylthiophenes), where the substituent groups align in a head to tail fashion (Figure 3.5) [71, 78]. The use of long carbon chain substituents can also be used to increase the solubility of polymers.

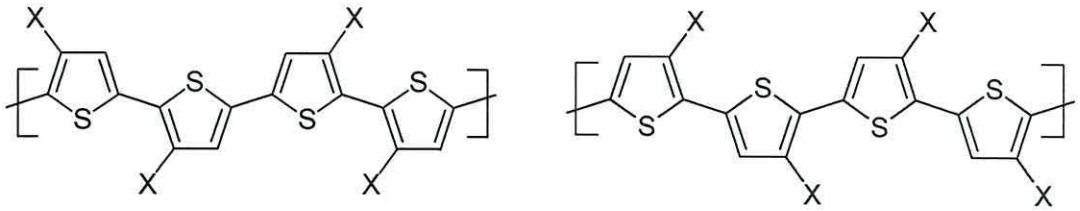

Figure 3.5 *Chemical structure of (a) regiorandom and (b) regioregular poly(alkylthiophene).*

PCDM and PBDT, two polymer structures which utilise electron withdrawing groups, heteroatoms and rigidification using bridged thiophene groups, have been studied in this project.

3.1.3 PCDM

The monomer, 4-dicyanomethylene-4H-cyclopenta[2,1-b:3,4-b']dithiophene (CDM) consists of a bridged dithiophene molecule with a dicyanomethylene moiety attached at the bridging carbon atom (Figure 3.6). The monomer is an aromatic molecule, having a planar structure and $4n+2$ π-electrons (n=5), in agreement with the Huckel rule [79]. The π-bonding system of the compound extends across the thiophene rings of the carbon backbone and the cyano-groups on the substituent moiety. Polymerisation occurs through the 2-position of the thiophene rings to produce the conjugated polymer, poly(4-dicyanomethylene-4H-cyclopenta[2,1-b:3,4-b']dithiophene) (PCDM). PCDM was initially polymerised by Ferraris and Lambert [80] in 1991 and reported to have a band gap of less than 0.8 eV, estimated from the energy difference between hole and electron injection in cyclic voltammetric measurements.

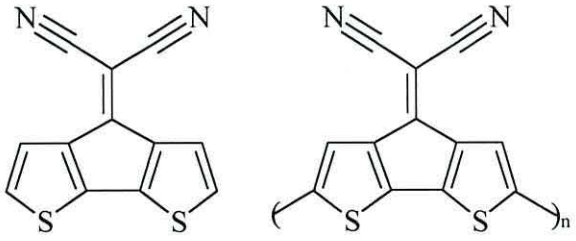

(a) *(b)*

Figure 3.6 *Chemical structure of (a) CDM monomer and (b) PCDM.*

Ferraris and Lambert further explained why the introduction of electron withdrawing groups at the carbon bridge lowers the band-gap. The HOMO and LUMO frontier molecular orbitals for CDM (Figure 3.7) are interesting. In the diagram, the radius of the circles representing the atomic orbitals are approximately proportional to the magnitude of the atomic orbital coefficient and the colour of the circles (black or white) represents the arbitrary sign of the lobe of each orbital.

The HOMO is asymmetric with respect to a vertical mirror plane resulting in a node (* in figure 3.7) at the bridging carbon atom. The node is a point at which the

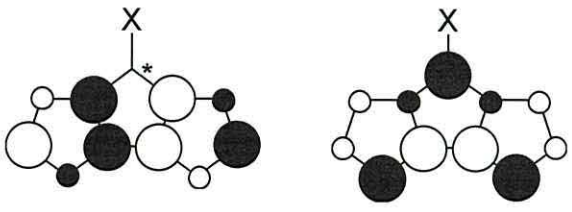

(a) *(b)*

Figure 3.7 *Atomic orbital diagrams showing the (a) HOMO and (b) LUMO frontier orbital models of the bridged dithiophene, where X indicates the position of the electron withdrawing group.*

probability of occupation by an electron is zero, due to a change in sign of the wavefunction at this point. Therefore, electron withdrawing moieties positioned at this bridging atom have little effect on the energy of the HOMO. However, the LUMO is symmetrical and electron withdrawing groups at the bridging carbon significantly lower the LUMO, consequently the band-gap is reduced. The band-gap reduction can be controlled by appropriate choice of the electron withdrawing group.

The aromaticity of the monomer is also seen in the polymer units and a quinoid conformer of PCDM can be found by movement of the π-electrons around the thiophene backbone (Figure 3.8).

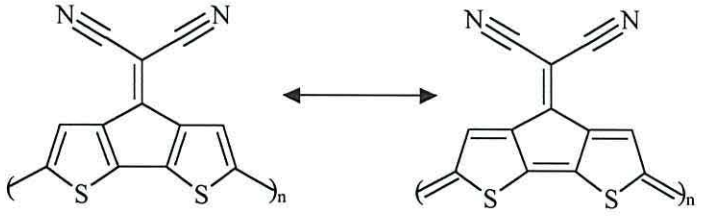

Aromatic Quinoid

Figure 3.8 *Chemical structure of aromatic and quinoid conformers of PCDM.*

From in-situ conductivity measurements [81], Huang and Pickup have confirmed that the optical band-gap of the pure polymer is approximately 0.8 eV. This value was estimated from the intrinsic conductivity, $1x10^{-8}$ S cm^{-1}. The conductivity was measured using Pt/PCDM/Au devices immersed in acetonitrile solution, containing tetrabutylammonium hexafluorophosphate (TBAHFP, Bu_4NPF_6, 0.1M) as an electrolyte.

They then proceeded to co-polymerise CDM monomer with 3,4-ethylenedioxythiophene (EDOT), to produce an electropolymerised copolymer with a vanishingly small band-gap [82]. Confirmation of controllable copolymerisation, rather than polymer blend formation, was obtained using Raman spectroscopy and cyclic voltammetry. Copolymers with differing compositional ratios were synthesised by varying the polymerisation potential. The copolymer band-gap decreased from approximately 0.33 eV to less than 0.16 eV as the polymers changed from CDM rich copolymers (compositional ratio of 2.5:1) to EDOT rich copolymers (less than 1:1). The conductivity measurements showed that the copolymers have higher intrinsic conductivities than polymers formed using the pure reactant monomer units.

Huang and Pickup also employed spectroscopic, electrochemical and conductivity measurements to investigate structural modifications of the, ex-situ electrochemically n-doped, polymer following reaction with oxygen [83]. Controlled modification of the polymer was achieved during immersion of the polymer in the acetonitrile solution, described previously, by saturating the solution with dry air. This modification led to a reduction in the polymer band-gap through substitution of carbonyl/hydroxyl groups at free β-positions within the polymer.

Gunatunga and co-workers [84] reported a preliminary analysis of the polymer using SEM and UV-vis spectroscopy as well as initial AC and DC electrical characteristics of a Au/PCDM/Al diode. The DC characteristics were found to be offset from 0 V and displayed little rectification.

Electroluminescence from a polymeric LED incorporating PCDM has been investigated by Dong and co-workers [85]. A Au/PCDM/porous silicon/Si/Al diode was fabricated using n-type silicon substrates and deposition of the reported polymer was from nitrobenzene solution by a monolayer assembly technique. However, PCDM is insoluble in nitrobenzene. It is possible that the authors simply deposited monomer onto the silicon substrate. Unfortunately, since they do not provide any spectroscopic data which could be compared to the Raman, IR and UV-vis spectra presented here no conclusions can be drawn. Visible orange light emission occurred upon biasing the LED at a current density of 0.5 Acm^{-2} and the EL spectrum was found to peak at 650 nm, red-shifted by 40 nm compared to the PL spectrum.

Riul and co-workers [86] have produced Langmuir-Blodgett (LB) films of CDM monomer on hydrophilic glass, gold coated glass and indium tin oxide glass. The CDM monomer was rendered soluble in solutions of common organic solvents with acetonitrile and the completed films characterised by UV-vis and Raman spectroscopy, AFM and DC electrical conductivity.

3.1.4 PBDT

Poly(7-benzo[1,3]dithiol-2-ylidine-7H-3,4-dithia-cyclopenta[a]pentalene), PBDT, was first synthesised by Kozaki and co-workers in 1992 [87] using electrochemical oxidation of the corresponding monomer, BDT. BDT is another dithiophene-based molecule similar to CDM (Figure 3.9) but having a dithiol moiety positioned on the carbon bridge rather than the dicyanomethylene on CDM. The BDT was found to have a melting point of 212-213 °C and an absorbtion maximum at 400 nm (in ethanol). The authors also provided x-ray structural analysis of the monomer crystals [88] and revealed that there was a short range S-S intermolecular interaction between the benzodithiol moieties on neighbouring monomer atoms.

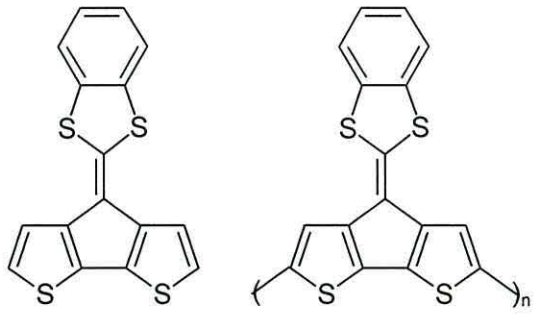

(a) *(b)*

Figure 3.9 *Chemical structure of (a) BDT monomer and (b) PBDT.*

MNDO calculations of the LUMO, HOMO and HOMO -1 states of a hydrogen substituted analogue of the BDT monomer (Figure 3.10) were made to show the magnitudes of the atomic orbital coefficients. The small atomic orbital coefficients at the 2-position on the HOMO, and the larger coefficients in the same position on the HOMO -1, suggested that polymerisation would selectively occur at this position. The small coefficients at the 2-positions of the dithiol moiety on the HOMO state mean that

the molecule has a low oxidation potential, 0.7 V (vs. SCE) compared to 1.03 V (vs. SCE) for polythiophene, and is easily oxidised at these positions. Addition of substituents (such as the benzene ring in BDT) at the 3-position of the dithiol was also found to affect the electrical properties [88].

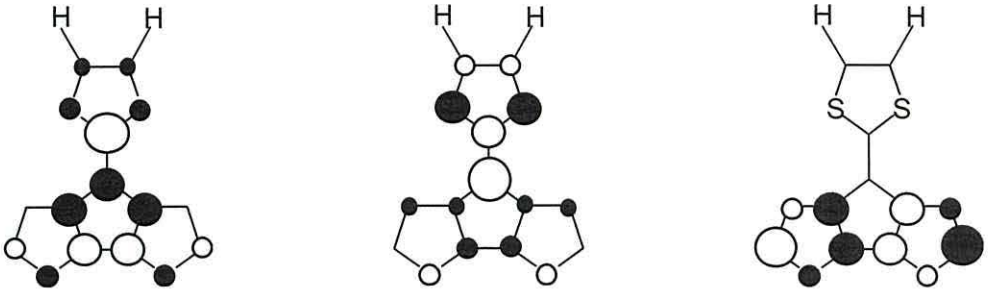

Figure 3.10 *Atomic orbital diagrams of the (a) LUMO, (b) HOMO and (c) HOMO -1 states of BDT-like monomer.*

The undoped polymer was found to have major absorptions at 610-690 nm and 420-590 nm in the UV/vis spectrum and peaks at 1572, 1546, 1202, 1102 and 666 cm^{-1} were found in the infra-red spectrum. The conductivity of the PF_6^--doped polymer was 33 S cm^{-1}. UV/visible spectroscopy of a similar polymer (Figure 3.11) allowed a band-gap of approximately 1.4 eV to be estimated.

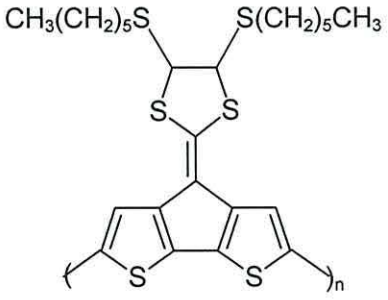

Figure 3.11 *PBDT-like polymer used for band-gap estimation.*

3.2 Device customisation and applications

The polymers described in the previous section can be used for a variety of applications. This discussion reviews the customisation of polymeric devices and includes topics, such as the selection of electrode materials, addition of blocking and injecting layers and the formation of flexible devices. The review then concentrates on

three main application areas, namely optical devices, electronic components and sensors, and covers devices such as light emitting diodes (LEDs), photodiodes, batteries, electrochemical sensors and nuclear radiation sensors. This is not a definitive review but is designed to provide an insight into the wide range of possible uses for these polymers. In this section, the focus does not concentrate on the low band-gap polymers exclusively allowing the broad range of customisation techniques and device applications to be explored.

3.2.1 Device customisation

Contact materials for polymeric devices include, gold [89], silver [90], calcium [47, 91], aluminium [47] and blends of these metals [92]. Transparent anodes such as tin oxide films, doped with indium (ITO) or fluorine (FTO) on a glass or plastic substrate [93], and a bilayer ITO/polyaniline (PANI) electrode where the PANI is protonated with camphor-sulphonic acid (PANI-CSA) are also available. The PANI-ITO electrode [94] takes advantage of the high work function of PANI and the low surface resistance of ITO. Other electrodes include protonated PPy [95] which acts as a semi - transparent anode with a work function similar to ITO, and p and n doped silicon electrodes. Experimental testing of the different electrode materials has been carried out to produce optimum performance, depending on the characteristics required of the device.

Multilayer devices can consist of polymer layers which tune the emission wavelength in an LED or act as charge carrier injectors or blocking layers in polymeric LED and electronic devices. This technique is particularly common for the production of LEDs which can emit more than one colour and, indeed, colours throughout the spectrum have been obtained [96].

An example of a 3 - layer LED with 'hole - blocking' and 'hole - injecting' layers uses a PDPV emitting layer giving green emissions [97]. In the ITO/PPV/PVK/PDPV/metal configuration, the ITO injects electrons and emission occurs from the PDPV layer. The PPV hole - injecting layer actually acts as a bridge between the ITO and the PVK by having a work function intermediate between that of its neighbours, allowing more efficient hole transfer. In this example, PVK acts as the hole - blocking layer. In an ITO/PPV/But-BPD/metal LED [98], the hole blocking layer

is 2-(4-biphenylyl)-5-(4-tert-butylphenyl)-1,3,4-octadiazole (But-BPD). The devices give 1 % ph/el and 0.8 % ph/el external quantum efficiency respectively, compared to 0.2 % ph/el [45] for single layer PPV devices.

A flexible LED [99] and other flexible electronic devices [100] have been fabricated. The LED was made of MEH-PPV using poly(ethylene terephthalate) (PET) as the substrate. Calcium was used as the electron injecting electrode and soluble PANI-CSA as the hole injecting electrode. The LED was found to be insensitive to flexing.

Spin coating [101] is probably the most common way of fabricating small area polymeric films mainly due to the simplicity of the method, and a number of polymers have been made using this method. Unfortunately, spin coating methods suffer from some drawbacks [102]. It is hard to produce contaminant free and pin-hole free films using this technique. Also, the production of multi-layer polymer devices is difficult because mutually exclusive solvents are required to stop deposited polymers from redissolving.

Chemical vapour deposition (CVD) [103] and thermal deposition techniques [104] are also common fabrication methods which have the advantages of being solvent free, thus minimising contamination. A major advantage of this approach is that polymer and electrodes can be deposited using the same apparatus. The films tend to be smooth and uniform but both require the use of high vacuum.

Other forms of deposition techniques have advantages and disadvantages, and many are tailored to the needs of the polymer growth. Electropolymerisation [105] is simple and can, with care, produce pin-hole free films (see section 5.2) but they are susceptible to contamination. Self assembly and precursor routes [106] require careful chemical control and can involve complicated multi-step processes involving several chemical reagents. Plasma deposition [107, 108] is probably the most versatile method allowing the polymerisation of almost any monomer onto most substrates but, due to the high energies involved, the polymers are usually cross-linked and structurally inhomogeneous.

3.2.2 Optical devices

3.2.2.1 Light emitting diodes (LED), lasers and flat screen displays

The fabrication of a yellow/green light emitting poly(phenylene vinylene) (PPV) polymer LED by Burroughs and co-workers [59] has led to interest in the possibility of producing cheap, large area displays. Since then, a large amount of literature has accumulated on LED fabrication and testing using polymers with light emissions covering the visible [59, 109] portion, and to a lesser extent the infrared (IR) [110] and ultraviolet (UV) [111] portions, of the electromagnetic spectrum. Improvements have also been made in efficiency, luminescent intensity, and fabrication of the LED devices. Indeed flexible [99] and multiple layer devices [112] are now common. Organic electroluminescent displays have been produced which show potential for flat panel display applications [113] with three colour light emitting polymers deposited on thin film transistors using ink jet print patterning. Kido [1] reports that the global market for electronic displays in 1999 is worth $50 billion. The progress towards the commercialisation of flat screen displays is reviewed by Neale [114].

Light emission from polymers has also been used in the production of solid state lasers. A review by Kranzelbinder and Leising [115] describes the application of highly luminescent materials, in the form of conjugated, semiconducting polymers, as laser active media and includes technological developments towards electrically driven organic devices. Polymers which have been used in these laser applications include PPV [116] and its derivatives [117], poly(paraphenylenes) [118] and poly(methyl methacrylate) [119]. A variety of configurations, such as planar, microring and microdisc, have been used for lasers incorporating these organic materials [120] and utilisation of a flexible plastic substrates has allowed the fabrication of a robust, flexible laser [121].

3.2.2.2 Photodiodes and dual function devices

Some polymer LEDs have also been found to operate as light detectors (photodiodes) under reverse bias. Using MEH-PPV in a simple one-layer device, using ITO and

calcium as the electrical contacts, a LED/photodiode was produced [122]. In reverse bias (- 10V) the photodiode has an external quantum yield of approximately 20% electrons per photon (el/ph), whereas in forward bias the LED emits a red/orange light.

Photosensitivity in polymers is improved by using blends of the polymer and an excited-state charge transfer acceptor such as fullerene (C_{60}) [123]. The C_{60} prevents charge carrier recombination, thereby enhancing the carrier quantum yield and charge separation, which is then detected through an external circuit. Using MEH-PPV and C_{60} external quantum yields of 50 to 80% el/ph have been achieved at -2 to -5V reverse bias with photosensitivity comparable to silicon photodiodes.

Polymer photodiodes [124] have also been found to be more sensitive to blue and UV radiation (below 550 nm) than silicon photodiodes which have been UV enhanced.

3.2.2.3 Optocouplers

The simplest optocoupler consists of an LED, with an input current (I), and a photodiode, with an output current (I_0), which are optically coupled but electrically isolated (Figure 3.12). A polymer optocoupler using an MEH-PPV LED (external EL quantum efficiency > 1 % ph/el) and a poly(3-octylthiophene) (P3OT) photodiode (quantum yield > 20 % el/ph) [125] produced a current transfer ratio comparable to devices made using inorganic semiconductors (~ 2 x 10^{-3} at -10 V bias).

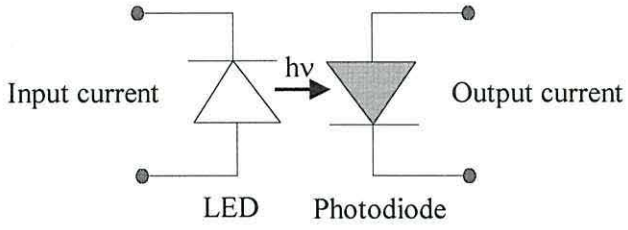

Figure 3.12 *Basic optocoupler diagram.*

3.2.2.4 Electrochemical cells (LEC)

An electrochemical cell is a light emitting device using a conjugated polymer/solid electrolyte as the active layer [126]. Upon application of a voltage to the system, simultaneous electrochemical p- and n-doping occurs at the anode and cathode respectively, a p-n junction is then formed in-situ, and radiative recombination occurs

at the junction. MEH-PPV and an ion transport polymer, poly(ethylene oxide) (PEO), have been used to produce an orange light emitting device [127].

Light emitting electrochemical cells have some advantages over polymer LEDs.

1) As the in-situ p-n junction is formed by electrochemical doping, the 'turn on' voltage, V_{on}, approximately equals the energy gap of the semiconducting polymers. For example, $V_{on} < 3$ V for visible light emission.
2) Environmentally stable metals, such as gold, can be used as electrical contacts because carrier injection occurs through ohmic contacts into the n- and p-type semiconductor regions. Whereas for polymer LEDs, reactive, low work function metals, such as calcium, are required for efficient carrier injection.
3) The cathode and anode work functions do not need to match the HOMO and LUMO energy levels of the semiconductor, therefore the same electrode material can be used for both wide and low band gap semiconductors.

3.2.2.5 Photovoltaic cells

Photovoltaic cells utilise photoinduced electron transfer between composite materials of conducting polymers, termed donors, and acceptor molecules such as fullerene (C_{60}) [125]. Photoinduced transfer occurs in time spans faster than radiative and non - radiative decay mechanisms (~10^3 seconds faster), therefore the transfer is highly efficient and emission response can be improved compared to non - composite polymers. For example, the addition of only 1 % C_{60} increased the photoconductivity of MEH-PPV polymer by one order of magnitude [128]. Other examples of conducting polymers and molecular acceptors have been suggested by Yoshino and co-workers [129].

3.2.2.6 Polymer grid triodes (PGT)

Polymer grid triodes are light emitting devices analogous in construction to a n-p-n (or p-n-p) transistor. A PGT is a multilayer device consisting of a cathode and an anode `sandwiching` layers of semiconducting material which themselves `sandwich` a layer

called the common grid network which is formed from another semiconducting polymer. The PGT can be thought of as 2 diodes coupled back to back.

Yang and Heeger [130] fabricated a PGT using PANI-CSA as the common grid network, MEH-PPV as the semiconducting polymer and aluminium and calcium as the cathode and anode respectively. Under positive bias, the PANI-CSA / MEH-PPV / Ca diode emitted light. The PANI-CSA layer acted as a `hole injector` and `electron extractor` for the MEH-PPV layers on either side and also as a third electrode controlling the current flow between the anode and cathode, thereby controlling the luminescent intensity.

Arrays of PGT's [131] using pixelated electrodes connected by a common grid network electrode were used to produce a `plastic retina` providing gain control for image enhancement. The retina was able to control local contrast on a display allowing a detailed image to be observed. The PGT array could be used to process images after analogue to digital conversion. Integrated into the device display, information would arrive digitally at the PGT array where it was processed. The output of the PGT pixels then served as the input for the display pixels.

3.2.2.7 Polarisers

An interesting use of conjugated polymer materials involves the production of an IR radiation polariser [132]. In this application, uniaxially orientated PANI / copolymer strands act as a polariser over the range 400 to 4000 cm^{-1}, which is comparable to commercial wire grid polarisers.

3.2.3 Electrical components

3.2.3.1 Batteries

Polymeric electrodes for secondary (rechargeable) batteries are electrochemically doped when the battery is charged, electrons are provided from an external source, and un-doped on discharge. The imbalance of electrons in the polymer is then counteracted by ions from the electrolyte diffusing into the polymer, (Figure 3.13)

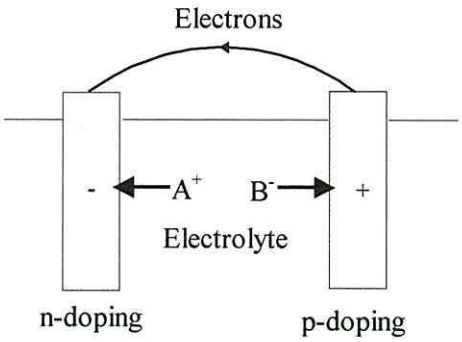

Figure 3.13 *Polymer electrode charging with electrons provided from an external current source.*

Comparison of PAc and PPP polymer electrode batteries with a lead-acid battery [133] shows that the energy density within the battery is comparable (~30 Wh/kg) but that the power density of the polymer electrodes was a factor of ten greater than the lead-acid battery. The higher current density is due to the electrolyte ions being able to diffuse into and out of the polymer quickly. The fibrous nature of the polymer also means the polymer has a large surface area with which to interact with the electrolyte ions. An advantage of polymer electrodes would be that the charging mechanisms in the battery are reversible, physical processes with no polymer consuming reactions.

The battery electrolyte may also be a polymeric material such as poly(ethylene oxide) (PEO) or poly(propylene oxide) (PPO) which form ion complexes with inorganic compounds. Polymeric electrolytes are advantageous in having good electrochemical stability and fast ion-transfer kinetics between the electrolyte and the electrode.

Kalaji and co-workers [134] have attempted to use a series of bridged dithienyl polymers, including PCDM, in redox supercapacitors which were expected to posses a combination of high energy and power density (typically 15 Wh/kg and 1500 W/kg respectively) for used in high power applications, such as accelerating an electric car. The ability to n- and p-dope these materials makes them suitable as the active material in polymeric batteries. Analysis of their properties was undertaken using cyclic volammetry and electrochemical spectroscopy. Further spectroelectrochemistry on the same polymers [135] was completed, studying the IR spectrum of the polymers with respect to the band shift (and hence bond strength) of the electron withdrawing groups

upon n- and p-doping. The experiments confirmed the feasibility of n-doping the polymers.

3.2.3.2 Field effect transistors (FET)

Polymer films have been used as the active element in metal - insulator - semiconductor field effect transistors (MISFET), due to the attractions of large area deposition and ease of processing. The charge carrier mobilities of the polymer need to improve to compete with inorganic material based devices and this is achieved by careful control of the device architecture and to a lesser extent the doping of the polymer. MISFETs using pentacene [136], poly(3-methylthiophene) (P3MT) [137], and poly(thiophene vinylene) (PTV) [138] have been produced using similar device configurations, (Figure 3.14).

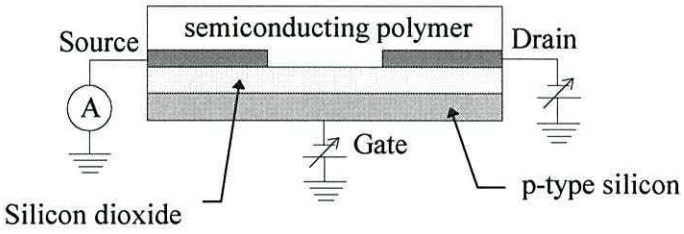

Figure 3.14 *General MISFET construction.*

The pentacene MISFET gave carrier mobilities of 9 x 10^{-3} cm^2 V^{-1} s^{-1} which was two orders of magnitude lower than inorganic α - silicon devices (~ 1 cm^2 V^{-1} s^{-1}) but the polymer MISFET could still be used for inverter and NOR gates. The electropolymerised P3MT films give mobilities of 8.5 x 10^{-4} cm^2 V^{-1} s^{-1}.

Sirringhaus and co-workers [139] have improved the mobility of polymeric TFTs by introducing alignment of the polymer in the direction of conduction. Charge carrier mobilities of 0.01 to 0.02 $cm^2V^{-1}s^{-1}$ and good operating stability have been achieved for TFT devices utilising aligned chains of a polyfluorene copolymer. Current flow perpendicular to the polymer chain alignment has been found to be 5-8 times lower than that parallel to the alignment. These mobilities are only a factor of 5 lower than those reported for a TFT based on poly(3-hexylthiophene) (P3HT). A mobility of 0.1 $cm^2V^{-1}s^{-1}$ for the P3HT TFT is attributed to strong π-π^* interchain interactions.

A flexible MISFET has been produced [140] which is insensitive to flexing and bending, using the semiconductor, α, ω -di(hexyl)sexithiophene. The source, drain and gate electrodes were made from a conducting, graphite-based polymer ink, and the substrate was a strip of adhesive tape with electrical contact to the gate electrode made using the same ink. The insulator was poly(ethylene terephthalate) (PET).

3.2.4 Sensors

One of the basic requirements of analytical work is the ability to detect and monitor levels of analyte, whether through the detection of molecular or atomic species or through the detection of various forms of emitted radiation. Many useful sensors convert a non-electrical physical or chemical quantity into an electrical signal.

Due to the wide range of hydrocarbon-based materials available for polymer design, a variety of properties, such as fluorescence, conductivity and molecular recognition, are available for exploitation. Polymeric materials for use in sensors are appealing due to characteristics such as low cost, flexibility and relative simplicity of the fabrication processes which are common to most polymers.

3.2.4.1 Electrochemical sensors

Transfer of electric charge occurs readily from bulk conducting polymers to certain analytes or *vice versa.* The transfer may then be monitored by observing changes in the properties of the polymer, such as electrochemical potential or conductivity. Jasowicz [141] has reviewed applications of conducting polymers for use in potentiometric chemical microsensors. Interest in these polymers concentrates on the electronic and ionic charge transport in the bulk of the polymer and at the polymer/electrode or polymer/analyte interfaces. The charge transport is dependent on the partitioning of the analyte between its bulk state (gaseous or solution) and the polymer. The charge transfer then occurs by rearrangement of the π electrons in the polymer due to polarisation of the polymer units.

For detection of solution ions, the ion exchange properties of a conducting polymer are utilised. Anions within the polymer matrix are exchanged for anions, of similar size or smaller, from the solution without any loss of polymer electronegativity.

Size exclusion can be controlled, in principle, by altering the growing conditions to produce a denser or more open polymer structure. Derivatives of polypyrrole polymers and poly 3-methylthiophene have been described as anion selective membranes for acidic anions or chromium oxyanions respectively [141]. Polythiophene has been found to display a cationic response to monovalent cations and some divalent cations.

In one type of gas/vapour sensor, changes in the work function at a polymer/electrode interface is detected using a field effect transistor. The detector incorporates two electrodes, one of which is insensitive to the analyte and hence used as a control. Changes in electron affinity or surface dipole at the detector electrode causes a change in the electrode work function and the difference between this and the workfunction of the control is measured. A high electron affinity for the polymer will cause electrons to be transferred from the analyte causing oxidation of the analyte. If the electron affinity is low, the reverse happens and the analyte is reduced.

Examples of polymers used in potentiometric gas sensors include polypyrrole [142] and polyanaline [143]. Gas partition into the polymer is not vital with these sensors because electron transfer can occur at the polymer surface, so that dense polymers produced by methods such as plasma polymerisation can be used. A polythiophene-based metal insulator semiconductor field effect transistor (MISFET) has been used as an oxygen sensor [137] and electrochemically prepared polyfuran [144] as a humidity sensor.

3.2.4.2 Absorption-based mass sensors

A common type of polymeric sensor is an absorption based mass sensor. The polymer is normally deposited onto an acoustic wave device such as a quartz crystal microbalance. For these devices, a change in resonance frequency is proportional to the mass of the analyte deposited onto the microbalance. The polymer layer is used to collect and concentrate the vapour molecules from the gas phase, and usually requires good permeability for analyte partitioning and a thin film to reduce the possibility of polymer resonance.

A review of the acoustic wave devices used for these sensors has been published by Grate, Martin and White [145] and a review of the background to acoustic

wave vapour sensors has been reported by Grate, Patrash and Abraham [146]. Examples of different sensors , such as surface acoustic wave (SAW), flexural plate wave (FPW) and thickness shear mode (TSM or quartz microbalance) devices, and some non-conjugated sorbent polymers are presented. Plasma deposition techniques have been used to polymerise both amino acid/fluoropolymer [147], ethylenediamine [148] and 4-vinylpyridene [148] polymers, normally on quartz crystal microbalances, for the measurement of analytes such as chloromethanes, primary alcohols and other organic vapours.

3.2.4.3 Luminescence-based sensors

Most luminescence based sensors use a fluorophore suspended in a polymer as the underlying design of the detector. Ruthenium and osmium complexes [149], suspended in polymers such as poly(methylmethacrylate) (PMMA) and polydimethylsiloxane (PDMS) have been used as sensors for methanol vapours and oxygen, including the possibility of an in-vivo oxygen sensor.

3.2.4.4 Surface plasmon resonance sensors

Surface plasmon resonance (SPR) sensors use a non-propagating light wave, formed at a metal-coated surface when the angle of the incident light is set at a specific value. The evanescent wave extends from the interface into the analyte solution, decaying with increasing distance. Changes in the refractive index close to the metal-coated surface perturb the light wave and alter the propagation characteristics of the surface plasmon. This causes the resonance angle of the light to change, which can be monitored and the results correlated to the mechanisms causing the refractive index change. The use of polymers in these systems allows the analyte to be concentrated in the region close to the interface to produce an optimum signal [150]. A common use for SPR techniques is for biological immunoassays [151]. Immunosensors using polymers have been found to have a better sensor response and a lower detection limit than conventional SPR sensors due to the dense, 2-dimensional immobilisation of antibodies on the polymer surface.

3.2.4.5 Nuclear radiation detectors

Nuclear radiation counters may be based on a number of device designs, such as ionisation chambers and scintillation detectors, where radiative decay processes can take place. Ionisation chambers, such as the Geiger counter, consisting of a detector material between electrodes, use the production of ions and electrons to detect the presence of ionising radiation. Scintillation counters detect the emission of light from atoms which are excited, directly or otherwise, by the radiation. Both types of detector could be adapted to use polymeric materials as the detector material. Semiconducting solids having been found to have advantages over gases for use in ionisation chambers. Complete absorption of the more penetrating radiations can occur in a shorter distance in solid detectors than gaseous detectors, thus making the detector smaller. Also, measurements of the penetration depth of the radiation into a solid can also be made.

Yoshino and co-workers [152] have used hexafluorosulphate, SF_6, doped polythiophene which could be used as an electromagnetic radiation or neutron flux detector. As well as changes in properties, the colour of the doped polymer changed upon irradiation from red to blue allowing physical checks to be made on the penetration depth. Radiation scintillator detectors based on polymers [153] have been described including a poly(methylphenylsiloxane) (PMPS)-based sensor which was resistant to damage by irradiation of up to 10 Mrad.

3.3 Summary

After defining a low band-gap polymer as a polymer with a band-gap lower than or equal to 2 eV and presenting a number of examples, a review of low band-gap polymers has been presented. A short introduction to conjugated polymers has been presented starting with the first polymer to be artificially doped, poly(acetylene), and leading to PPV- and thiophene-based polymers. The review then concentrates on polyheterocycles by, initially, looking at the aromatic structure of benzene and developing this to introduce heterocyclic molecules that obey the Huckel criteria. An explanation of how 5-membered heterocycles delocalise electrons from the heteroatom

to contribute to π-bonding completes the picture of conjugation in heterocyclic polymers.

The properties of a few heterocyclic polymers were then given, before polymer customisation is reviewed. The basic polymer can be tailored to produce the required low band-gap state. This usually involves increasing the amount of overlap of the orbitals along the polymer backbone, designing in a high degree of quinoid character into the polymer and the addition of electron withdrawing and donating substituents. The polymers used in this project, PCDM and PBDT, have been shown to utilise electron withdrawing groups, heteroatomic donating atoms and rigidification using bridged thiophene groups.

The background literature regarding PCDM and PBDT has also been reviewed. The initial fabrication of PCDM by Ferraris and Lambert produced a polymer with a band-gap of approximately 0.8 eV. Atomic orbital diagrams were used to explain how the presence of the electron withdrawing group on the bridging carbon reduced the energy of the LUMO and hence reduced the band-gap. Work by Huang and Pickup has confirmed the low band-gap of PCDM using in-situ conductivity measurements. They have also studied PCDM in a copolymer with EDOT, which produced a polymer with a vanishingly small band-gap, and an oxygen-modified analogue of PCDM, also leading to a reduction in the band-gap. Preliminary electrical characterisation, light emission by electroluminescence from a PCDM LED and the deposition of CDM onto various substrates are also reported.

PBDT was first synthesised in 1992 and since then there has been little further work on this polymer. The authors produced x-ray structural data and atomic orbital diagrams for the monomer revealing that PBDT is susceptible to oxidation at the 2-position of the dithiol moiety. UV/visible spectra were used to estimate a band-gap of 1.4 eV.

Approaches to device customisation have been considered and applications described which utilise low band-gap semiconducting polymers. Customisation techniques such as the selection of electrode materials, addition of blocking and injecting layers and the formation of flexible devices is covered and the review of applications concentrates on three main areas, optical devices, electronic components and sensors.

4. Experimental methods

A range of techniques were used in this investigation from chemical synthesis through to device characterisation. In the following sections, therefore, details of the methods used for monomer synthesis, preparation and characterisation of the polymers and the testing of the devices are described.

4.1 Monomer synthesis

The synthesis of CDM monomer **7** was carried out using a multi-step synthetic process previously outlined by Jordans and co-workers [154] (Scheme 4.1,). 4H-cyclopenta[1,2-b;3,4-b']dithiophene-4-one (**6**, CDT) was synthesised from two equivalents of 3-bromothiophene (**1**, 97%, Aldrich Chemicals, UK) via a ring-closing method utilising methyl formate to form the methylene bridge between thiophene rings, and ethylene glycol as a protecting group during ring closure. CDM monomer was then synthesised from **6** via a piperidine catalysed Knoevenagel condensation reaction using malonitrile [45]. The synthesis is described in greater detail in appendix 1 together with the results of NMR analysis which was used to monitor the progress of the synthesis.

BDT monomer was synthesised from **6** by reaction with lithiated 2-diethoxyphosphinyl-1,3-benzodithiole **8** (Scheme 4.2,) following a procedure reported by Kozaki and co-workers [87, 88]. BDT monomer was used as supplied from the Chemistry department at the University of Wales, Bangor, and 3MeT monomer was purchased from the Aldrich Chemical Company.

4.2 Polymer synthesis

All substrate preparation, electropolymerisation and diode production was carried out in a class 10,000 clean room to minimise atmospheric contamination of the polymer samples during fabrication.

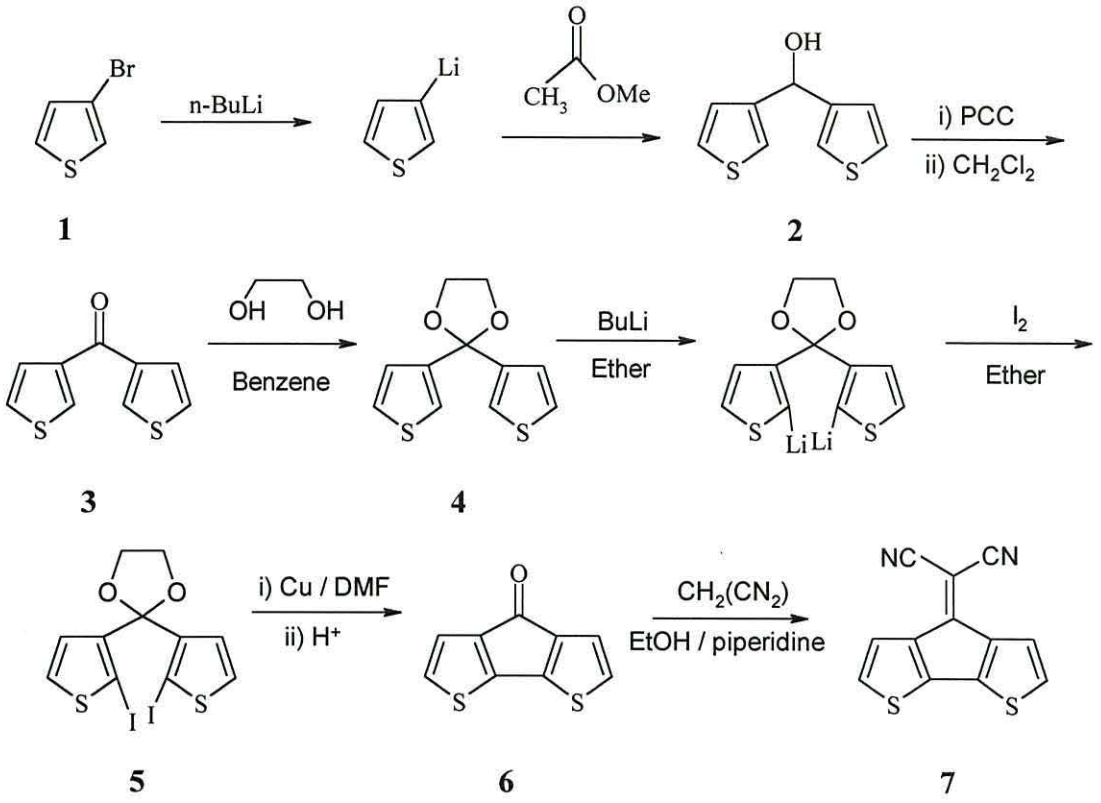

Scheme 4.1 *Reaction scheme for the synthesis of CDM monomer* **7**.

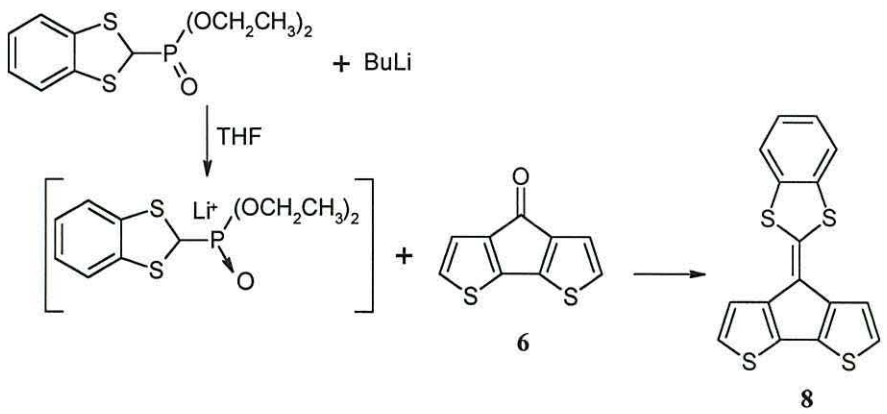

Scheme 4.2 *Reaction scheme for the synthesis of BDT monomer* ***8*** *from CDT* ***6***

4.2.1 Substrate preparation

The substrates used for the electropolymerisation step included metal-coated glass slides prepared by vacuum deposition, or ITO-coated glass. The glass onto which metal films were vacuum deposited were soda lime float glass microscope slides (Whitehart Scientific Lens, UK) with approximate dimensions of 25 x 75 mm. The slides were

first scored with a diamond scribe into halves on the reverse side, for later separation, so that the electrode produced would fit in the electrochemical cell. The substrate was then washed thoroughly with, sequentially, cold, hot and ultrapure water (Milipore Q system). Decon 90 (Scientific Services Ltd.), a bleach replacement, was rubbed onto the slide to remove traces of organic material and then the slide was again rinsed with the hot, cold and ultrapure water. A stream of warmed air was then used to dry the glass after which it was examined in a bright, white light. This operation was repeated until the slide was clear of dust and contaminants.

Metal deposition was performed in a Balzers TSH170 turbo pump vacuum system. The microscope slide was held above a removable tungsten boat and a chromium-coated tungsten filament, both held between a pair of electrodes. Depending on the later experimental requirements, either 0.7 mm of gold (99.99%, 0.5 mm diameter, Heraeus Silica and Metals, UK) or silver (99.9%, 0.5 mm diameter, Advent Research, UK) wire was placed into the tungsten boat. The system was pumped down to 10^{-5} Torr and a thin layer of chromium was deposited onto the substrate by passing approximately 40 A through the chromium-coated filament for 2-3 seconds. After the vacuum had recovered, the gold/silver was deposited by passing approximately 40 A through the metal-containing tungsten boat for 40 seconds. The vacuum was again allowed to recover to 10^{-5} Torr while the substrate cooled, after which the vacuum was released and the slide removed. The substrates were either used immediately or placed into an air-tight container to limit contamination.

The ITO-coated glass (20 Ω/□, Pilkington, UK) was supplied in 350 x 350 mm sheets which were cut to approximate microscope slide dimensions by hand. The substrates were then scored and washed in a similar fashion to the glass microscope slides.

4.2.2 Electropolymerisation

All solutions were made up within a fume cupboard using clean, dry glassware. PCDM and PBDT were electropolymerised from a solution of the monomer (0.01 mol dm^{-3}) and tetrabutylammonium tetrafluoroborate electrolyte (TBATFB, 0.1 mol dm^{-3}, 99%, Aldrich chemicals, UK) dissolved in nitrobenzene (99%, Aldrich chemicals, UK).

P3MeT was electropolymerised from monomer (0.5 mol dm^{-3}) and TBATFB (0.1 mol dm^{-3}) in propylene carbonate solvent (99%, Aldrich chemicals. UK). The solution was degassed using nitrogen for 20 minutes immediately before and after polymerisation and then stored in the dark at 4 °C to minimise photo-oxidation effects.

Potentiostatic polymerisation was performed in a three electrode cell controlled using a Princeton Applied Research EG&G model 273 potentiostat/galvanostat connected to a differential electrometer cell model 273 (Figure 4.1).

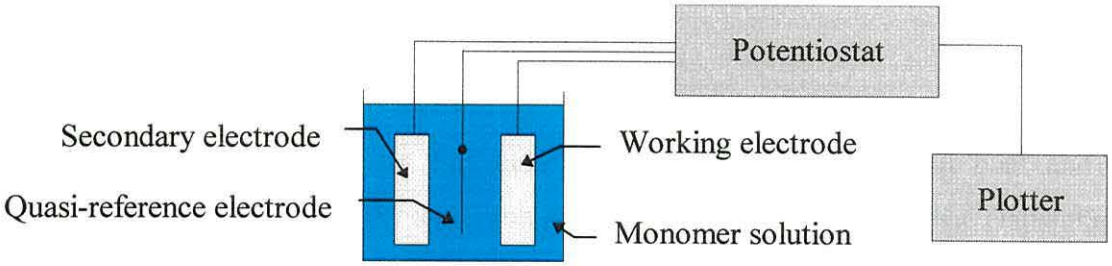

Figure 4.1 *Schematic diagram of the apparatus used for electropolymerisation of semiconducting polymers.*

The cell consisted of a 50 ml beaker in which the electrodes were dipped into the monomer solution to a depth of approximately 3 cm. The beaker was washed with ultrapure water and acetone then dried in an oven prior to use. The electrodes were suspended in the solution using a PTFE cap to the beaker which housed a copper contact for the working electrode and openings for the reference and secondary electrodes. The working electrode consisted of the previously metallised microscope slide or ITO-coated glass. The reference electrode consisted of a length of clean silver wire (99.9%, 0.5 mm diameter, Advent chemicals, UK). Silver wire is not recognised as a standard electrode but it was used in this work for convenience. As long as it was cleaned prior to use it can be considered to be a reproducible "quasi-reference" electrode. The secondary electrode was platinum foil (dimensions of 7 mm x 6 mm).

The polymerisation followed that reported by Roncali and co-workers [155] and modified by Taylor, and co-workers [125] consisting of three steps controlled by the potentiostat. Firstly, a nucleation step was performed using a slightly higher potential than the growing step to create a high density of nucleation sites on the substrates. The potential was then stepped down to the growing potential where polymerisation occurred over a period of time. The potential was then stepped down to 0V to dedope

the polymer. This step generally required the dedoping current to fall below approximately 20μA and then to continue dedoping for a fixed period of time. An example of typical growing conditions is given in table 4.1.

Table 4.1 *Typical polymerisation conditions for the polymerisation of PCDM, PBDT and P3MeT.*

Polymerisation condition	Value		
	PCDM	**PBDT**	**P3MeT**
Nucleation potential (V)	2	2	2.3
Nucleation time (s)	10	20	5
Step potential (mV/s)	50	50	50
Growing potential (V)	1.8	1.2	1.8
Growing time (s)	600	200	30
Step potential (mV/s)	50	50	50
Dedoping potential (V)	0	0	0
Dedoping time upon reaching 20 μA (s)	300	300	600

After preparation, the sample was removed from the monomer solution and rinsed with acetone for 10-15 seconds to remove excess monomer and solvent and then dried under a stream of nitrogen. The sample was then immediately removed for Schottky diode formation (Section 4.2.3) or to storage under vacuum.

Cyclic voltammetric analysis was performed in preliminary polymerisation experiments to determine the potential values required for the nucleation and polymerisation steps. An x-y plotter was used to confirm that polymer growth had occurred at these potentials by observing the decrease in current as the voltammogram was cycled.

4.2.3 Schottky diode production

Schottky diodes were prepared by placing the polymer sample in the turbopump vacuum system with a mask consisting of an array of circular holes of 2.5 mm^2 area placed over the top as described previously [156, 107]. Approximately 20 mm of

aluminium wire (BDH, UK) was wrapped around a tungsten filament connected between the electrodes of the vacuum system which was then pumped down to 10^{-5} Torr. A current of approximately 40 A was passed through the filament for approximately 30 seconds to deposit onto the polymer the electrode array. The devices formed were removed from the vacuum chamber and electrical characteristics investigated immediately, or they were stored under vacuum.

4.3 Compound and device characterisation

4.3.1 Film morphology

4.3.1.1 Atomic Force Microscopy

A Digital Instruments Nanoscope 3A Multimode Scanning Probe Microscope (SPM) was used to produce raster-scanned, electronic renderings of sample polymer surfaces using the Atomic Force Microscope (AFM) mode of operation. The apparatus consisted of the SPM with controlling electronics, an interfaced personal computer and two monitors, one used to display control settings and the other for image display. The SPM contained a lead zirconium titanate (PZT) piezoelectric scanner, an imaging laser, the probe holder and sample support and a position sensitive, quadrant photodiode detector. The maximum scan size possible with the piezoelectric scanner was 200 μm by 200 μm with a maximum vertical range of 8 μm.

The polymer samples on their glass or ITO substrates were cut to fit into the sample holder and fixed to 15 mm diameter steel disks using the adhesive tabs provided. The disk was then placed onto the magnetic sample holder within the SPM. Depending on the sample roughness and the analysis method used, one of a variety of cantilevered probes incorporating a pyramidal tip was used. These included silicon nitride and crystal silicon probes.

The sample surface can be imaged using a number of methods, e.g. contact mode, non-contact mode and tapping mode. Contact and non-contact modes use the cantilever as a spring, allowing the tip to react to different surface forces near to the sample molecules. The detector then records any perturbation in the position of the

cantilever. In contact mode, repulsive forces between the tip and the sample atoms are used to image the surface. The tip is said to be in contact when the atoms of the tip and sample experience repulsive, Coulombic forces at about 0.1 to 1 nm distances.

In non-contact mode, the tip is held further away from the sample where the attractive and repulsive forces are weaker, allowing analysis of soft, deformable samples. The tapping mode uses a cantilever vibrating at its resonant frequency. As the tip is brought close to the surface, it makes intermittent contact (taps) causing the oscillation amplitude to decrease. This method has the advantage of minimising damage caused by the lateral forces exerted in contact mode.

The control mechanism for precise tip-sample interaction utilises an electronic feedback loop to control the tip's position with respect to the sample surface. The raw images were enhanced and analysed using off-line software (Nanoscope version 4.1 software). The maximum resolution of the AFM is a few nanometers.

4.3.1.2 Scanning Electron Microscopy

An International Scientific Instruments ISI-40 scanning electron microscope (SEM) was also used to image the polymer surface. The SEM used an electrically heated tungsten filament (Agar Scientific Ltd., UK) to produce the beam of electrons. The 0.1 mm diameter, v-shaped filament was maintained at between -2 and -30 kV and was surrounded by a grounded Wehnelt cylinder which accelerated the electrons through the condenser and aperture lenses. The beam was raster scanned across the sample surface using electromagnetic coils which move the electrons in the x and y directions. The analysis chamber and electron gun were held at a vacuum of approximately 10^{-6} Torr.

Samples were mounted in a similar manner to the AFM samples, on steel disks using adhesive tabs, with a conductive path of quick drying silver paint between the conductive surface of the sample, the gold or ITO, and the surface of the disk. The disks were placed on a stage which could be moved in the x, y and z directions and rotated about each axis allowing images to be obtained from all angles. A scintillation detector (Thornley-Everhart) was used to detect low energy secondary electrons emitted from the sample which consisted of a Naton® surface coated with an

aluminium film biased to 12 kV. Emitted light was then fed down a light guide to a photomultiplier tube linked via a video amplifier to a cathode ray tube (CRT) display. The CRT was slaved to the scan pattern of the electron beam which allowed the formation of the surface image. The images were then captured using a personal computer frame grabber with the SEM scanning at slow speeds.

4.3.2 Spectroscopic analysis

4.3.2.1 Fourier transform infra-red spectroscopy

Infra-red analysis was undertaken using a Bomem Michelson MB-100 Fourier transform infra-red (FTIR) spectrometer incorporating a P/N 19650 series monolayer/grazing angle accessory (Graseby Specac Ltd., UK). The spectrometer used Win-Bomem Easy (version 3.04, level II) software to control a double pendulum-design interferometer with potassium bromide corner cube mirrors. The excitation laser was a red emitting (633 nm) helium/neon laser, producing a spectral precision of 0.01 cm^{-1}, and the emitted light was detected using a deuterated triglycine sulphate pyro-electric detector giving a spectral range of 6000 to 350 cm^{-1}. The sample was placed onto the spectrometer stage within the grazing angle accessory and the spectrum recorded at different grazing angles between 70° and 80° to produce the most intense spectrum. Spectra were normally recorded between 500 and 4000 cm^{-1} where it was found that all of the sample's spectral peaks were positioned.

4.3.2.2 Raman spectroscopy

Raman spectroscopy was carried out using a Renishaw Ramascope 1000 Raman microscope with two possible excitation lasers, a red emitting (633 nm) helium/neon laser and a green emitting (514 nm) argon ion laser. The spectrometer consisted of the lasers, a microscope with motorised stage for sample support and laser focusing, a CCD array-based spectrophotometer and a controlling personal computer.

The computer contained Galactic GRAMS 32 software (version 4.11, level II) and Renishaw WIRE software (version 3.1). The GRAMS software was a 32 bit data

processor and database, designed to handle and analyse spectroscopic data, whereas the WIRE software was used for instrument control including system calibration, data capture, video image capture and control of the motorised stage allowing mapping to be undertaken. The microscope was an Olympus BH-2 microscope with a magnification, using the video-capture, of 2000x using the 50x microscope objective. A motorised Prior Instruments microscope stage was used to allow computer controlled stage movement to a resolution of 1 μm in the x, y and z directions.

The motorised stage was used for mapping the signal produced across a polymer film by moving the sample in small, incremental steps and recording the Raman spectrum. A single wavelength could then be chosen and the signal intensity at that wavelength plotted as a 2-D plot. This method was also used for mapping the signal from a polymer sample which had undergone laser ablation. For such an experiment the polymer was exposed to the helium/neon laser on full power for varying amounts of time, between 5 and 7200 seconds, using the motorised stage to move the beam known distances between exposed areas. Once the ablation was complete, the polymer spectrum was mapped along a straight line through the ablated areas, at smaller increments than the separation distances between the laser exposed areas. This allowed a comparison of the spectra for the ablated areas with the pristine polymer on either side.

4.3.2.3 Ultra-violet/visible spectroscopy

A Hitachi model U-2000 double beam, ultra-violet/visible (UV/vis) spectrophotometer was used for UV/vis analysis of monomer and polymer samples. This apparatus consisted of a deuterium discharge lamp for UV light emission and a tungsten iodide lamp for visible light emission, with an automatic switch-over adjustable within the range 325 to 370 nm. The primary beam was then passed through a half-silvered mirror beamsplitter which transmitted approximately 50% of the light to produce a sample beam, the 50% reflected light forming a reference beam. Silicon photodiode detectors were used for detection of the transmitted and reflected beams over a wavelength range from 190 to 1100 nm.

Both solid and solution spectra could be recorded using different sample holders. Solutions were analysed using quartz cuvettes with a path length of 10 mm and solid film samples were analysed using a sample holder which held the polymer films vertically in the path of the light beam. Both methods required the use of a reference. In the case of the solutions this was the identical solution but without the analyte, whereas for the solid samples the substrate material (normally a section of a glass microscope slide or ITO glass) was placed in the reference beam. The sample chamber remained light-tight during the analysis to avoid contamination of the sample spectrum. Normally, a spectrum would be run in absorption mode with a scan speed of 800 nm/min and a data capture setting of one data point every 2 nm.

4.3.2.4 X-ray diffraction spectroscopy

X-ray diffraction experiments were carried out on monomer crystals of CDM by the Department of Chemistry at the University of Southampton and attempts were made to analyse PCDM by the Department of Chemistry, Bangor, using a Philips Analytical x-ray diffractometer in a grazing angle configuration.

4.3.2.5 Energy dispersive x-ray analysis

Interfaced with the SEM was a Link Systems 860 series 2 X-ray analyser which allowed energy dispersive X-ray analysis (EDAX) emitted by the atoms in the polymer when they were subjected to the electron beam of the SEM. The EDAX analysis required an electron beam of greater current than that used for the SEM topographic imaging in order to produce the required X-ray intensity for analysis. A beryllium window covered a lithium-doped silicon semiconductor detector which absorbs the X-rays emitted from the sample, exciting K-shell electrons in the silicon. The detector is liquid nitrogen-cooled to reduce dark current noise.

4.3.2.6 X-ray photoelectron spectroscopy

X-ray photoelectron spectroscopy (XPS) was undertaken by the Department of Physics at the University of Wales, Aberystwyth. The analysis of PCDM on a gold-coated glass substrate was achieved using an AEI/Kratos ES200A spectrometer which has an overall instrumental resolution of 0.9 eV. Measurements were carried out at 300 W, using x-rays from the Mg (Kα) line at 1253.6 eV, and using a "fixed-retarding-ratio" so that the sensitivity was proportional to the kinetic energy.

For further information on the background to the spectroscopic techniques used here the reader is referred to the text books by Skoog, West and Holler [157] and Skoog and Leary [158].

4.3.3 Electrical characterisation

The Schottky diodes were mounted on a copper stage in an earthed, steel vacuum chamber allowing electrical characterisation at pressures between ambient and 10^{-5} Torr (Figure 4.2). The temperature was controlled using a Eurotherm 91e temperature controller and a chromel-alumel thermocouple which was placed in close contact with the sample. The sample was heated using electrical resistance heating blocks, controlled by the temperature controller, or cooled by liquid nitrogen cooling of the copper stage. All experiments at low pressures were carried out in the dark. Both the DC and AC measurements were controlled using visual basic software programs.

4.3.3.1 DC characterisation

DC characterisation was performed using a Hewlett Packard 4140B pA meter/DC voltage source which can apply a range of negative and positive voltages to the device. The currents were allowed to stabilise prior to the measurement reading being taken by incorporating a delay between the change in the voltage and the measurement. Common measurement settings are shown in table 4.2 and any differences in later measurements will be highlighted in the text. Extended current-voltage plots were achieved by manual

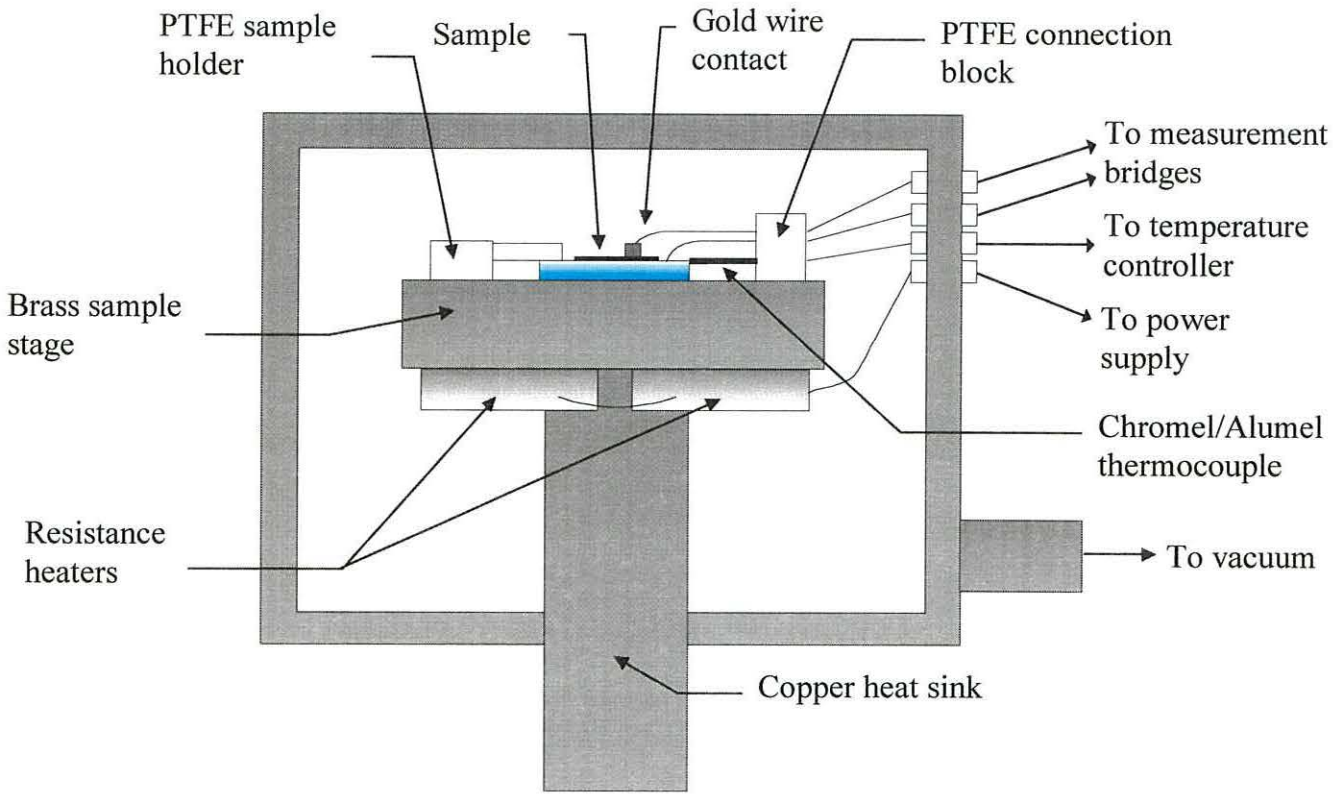

Figure 4.2 *Schematic diagram of the sample chamber used for electrical characterisation of metal/polymer/ITO diodes.*

voltage control using a DC power supply (Farnell 30V, 2A power supply) and a digital electrometer and multimeter. The results were then analysed using previously reported methods in an effort to identify the conduction mechanisms occurring in the thin polymer films.

Table 4.2 *Measurement settings for DC analysis of the semiconducting polymer diodes.*

Measurement setting	Value
Start voltage (V)	-2
Stop voltage (V)	+2
Step voltage (V)	0.1
Step delay time (s)	60

4.3.3.2 Admittance measurements

A Hewlett Packard 4284A 20 Hz - 1 MHz precision LCR meter was used for AC electrical characterisation. Capacitance and loss were measured as a function of frequency from 20 Hz to 1 MHz using a test signal of 50 mV. Capacitance-voltage measurements were also carried out at fixed frequencies over a range of voltages, between -5 V and +5 V at increments of 0.1 V. The AC characteristics of a PCDM diode were recorded for temperatures at and above room temperature. The temperature was initially increased to 80 °C with AC measurements recorded at 5 °C steps, allowing 30 minutes between measurements for the temperature to stabilise. The sample was then cooled to room temperature with measurements repeated in the reverse direction. To complete the temperature measurements, liquid nitrogen was used to cool the PCDM sample to below room temperature.

A sample which consisted of a range of polymer thicknesses on the same ITO substrate, the thicknesses of which were checked using the AFM, had AC characteristics recorded for each layer to investigate polymer thickness effects. AC characteristics were also measured for polymeric diodes using ITO substrate electrodes with aluminium, gold and silver top electrodes at temperatures between –50 °C and

+60 °C to compare the effect of different top electrodes and data was also collected for an ITO/PCDM/Al diode in positive and negative bias.

4.4 Summary

The synthetic routes followed in the preparation of CDM and BDT monomers have been described in this chapter together with the methods employed for preparing their respective polymers by electropolymerisation. A brief description of the various analytical and characterisation techniques used in the work has also been provided. The results obtained using these techniques will be presented and discussed in the following chapters.

5. Results and discussion: Microscopy and spectroscopy

The techniques described in chapter 4 were used to characterise the polymers poly(4-dicyanomethylene-4H-cyclopenta[1,2-b;3,4-b']dithiophene) (PCDM), poly(7-benzo[1,3]dithiol-2-ylidine-7H-3,4-dithia-cyclopenta[a]pentalene) (PBDT), and their respective monomers, and their properties compared with poly(3-methylthiophene) (P3MeT). The results in this chapter concentrate on microscopic and spectroscopic analysis of the sample materials; electrical characterisation is covered separately in the next chapter. Microscopy was used to characterise the surface roughness of the polymers and to ensure that the polymer films were pin-hole free, and hence suitable for later electrical characterisation. The chemical and structural composition of the polymers were studied using spectroscopy techniques to ensure that the polymers were as contaminant-free as possible.

5.1 Substrate choice

The use of gold-coated glass substrates during the polymerisation was found to be problematic. Chromium loss from the chromium keying layer of the working electrodes was found to occur readily at high potentials, albeit less readily at potentials lower than 2 V. This loss of chromium caused the gold to lose adherence to the glass and hence the electrode and the polymer became detached from the glass substrate and disintegrate. It was thought that the chromium was being drawn off the glass surface and into solution by the potential difference across the electrodes.

With this in mind, an experiment was carried out using a solution of nitrobenzene and TBATFB salt at potentials between 0 and 3V. The chromium was found to be removed from the electrode even in the absence of the monomer and, at the same time, a red precipitate formed at the platinum electrode. The formation of this compound had not been noticed previously due to the dark blue coloration of the CDM monomer solution. This experiment was repeated using a different electrolyte, tetrabutylammonium hexaflourophosphate (TBAHFP), but the same results occurred.

Analysis of a gold coated slide was performed using EDAX before and after electropolymerisation (Figure 5.1). As the lighter elements, such as carbon and hydrogen, were undetectable by the EDAX spectrometer, no peaks due to the atoms in the polymer are observed in the spectra. This allows the heavier atoms which constitute the electrode and substrate to be studied. The spectral interpretation is given in table 5.1.

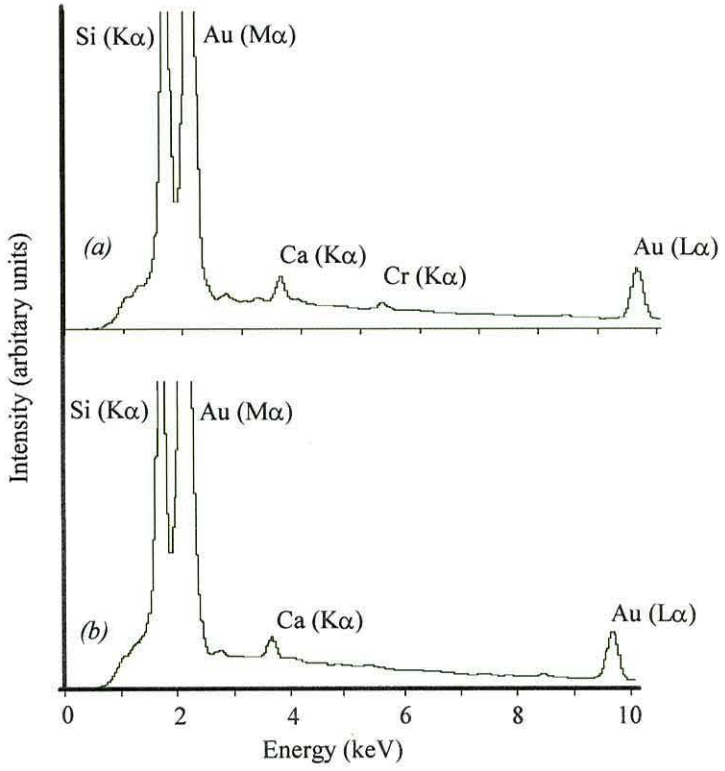

Figure 5.1 *EDAX analysis of the surface of a gold-coated glass slide substrate (a) prior to and (b) after electropolymerisation of PCDM showing the reduction of the chromium peak after polymerisation.*

The peaks due to the silicon and calcium atoms in the glass substrate, and the peaks for the gold top layer, have similar intensities prior to and after the polymerisation but the chromium peak at 5.4 keV reduces in intensity after polymerisation. This indicates a reduction in the amount of chromium on the substrate. Analysis of the platinum electrode after polymerisation showed that no chromium was present on the platinum which suggests that the chromium leeched from the working electrode remained in solution, possibly complexed within the red precipitate.

Table 5.1 *EDAX spectral assignments for a gold coated glass slide.*

Energy (keV)	Spectral assignment [159]
1.74	Silicon (Kα)
2.12	Gold (Mα)
3.70	Calcium (Kα)
5.41	Chromium (Kα)
9.72	Gold (Lα)

Further experiments showed that using 1.6 to 1.8 V as the growing potential reduced the problem of chromium leeching and gave more reproducible polymer films. However, it was decided to concentrate on using ITO substrates to eliminate this problem entirely. The ITO-coated glass was analysed using EDAX revealing a contaminant free sample with peaks due to the indium (3.29 keV) and tin (3.44 keV) in the coating, and silicon (1.74 keV) and calcium (3.69 keV) due to the glass substrate (Figure 5.2).

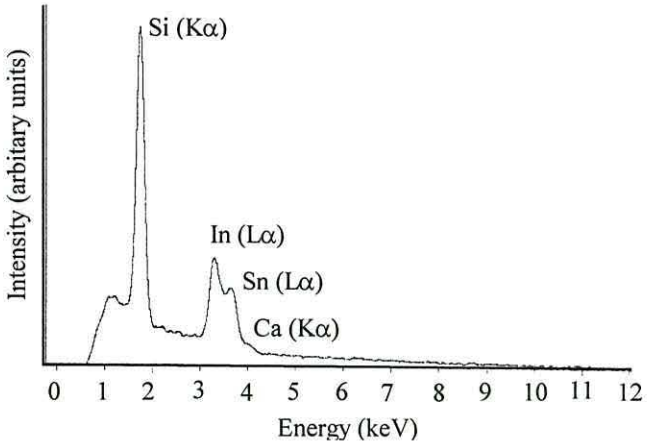

Figure 5.2 *EDAX analysis of ITO-coated glass.*

5.2 Microscopic analysis

5.2.1 Atomic force microscopy

For comparison, AFM images of pristine glass, prior to cleaning and after coating with gold, and ITO-coated glass are shown in figures 5.3 to 5.5.

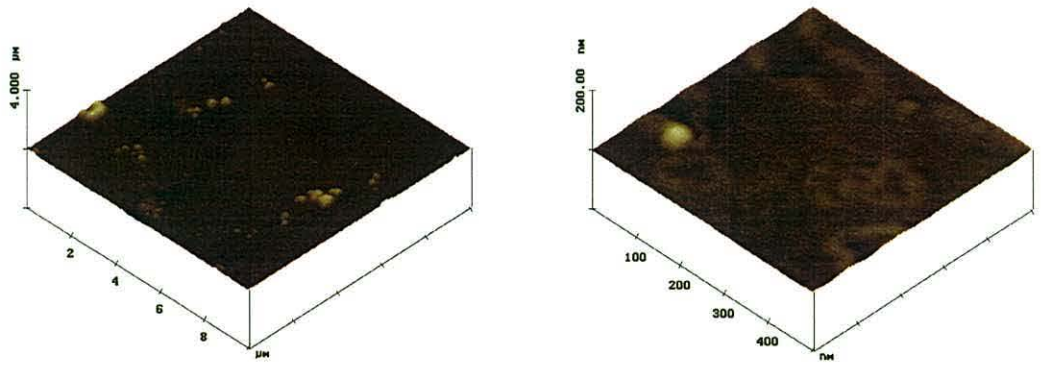

(a) *(b)*

Figure 5.3 *AFM images of a pristine glass substrate prior to cleaning, (a) 10 µm x 10 µm and (b) 500 nm x 500 nm.*

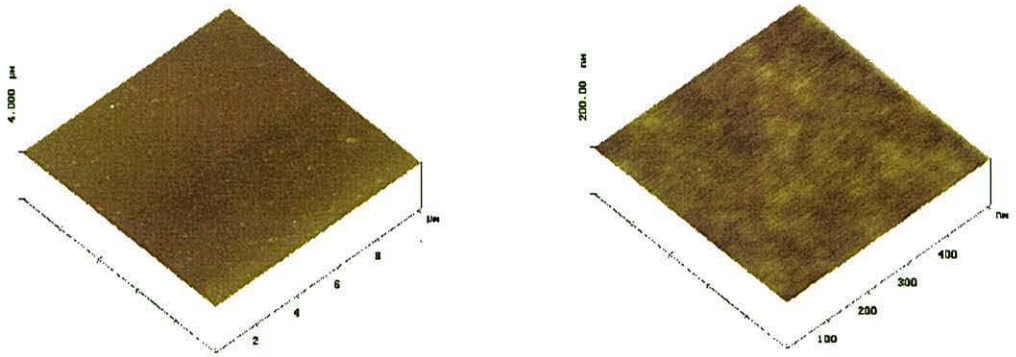

(a) *(b)*

Figure 5.4 *AFM images of a gold-coated glass substrate, (a) 10 µm x 10 µm and (b) 500 nm x 500 nm.*

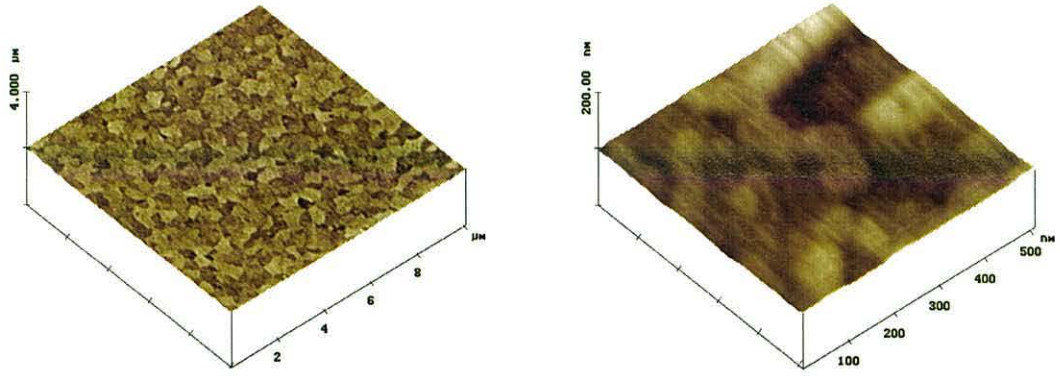

(a) *(b)*

Figure 5.5 *AFM images of an ITO-coated glass substrate, (a) 10 µm x 10 µm and (b) 500 nm x 500 nm.*

The P3MeT and PCDM films grown on gold and ITO substrates have also been analysed using AFM and the thickness of the polymers measured using sectional analysis. Images of P3MeT films electropolymerised onto gold-coated glass (Figure 5.6) and ITO (Figure 5.7) substrates show similar surface types for both, i.e. smooth, pin-hole free surfaces with a few large aggregates. The polymer protuberances seen in figures 5.6*(b)* and 5.7*(b)* cover an area of approximately 200 nm x 200 nm for both samples.

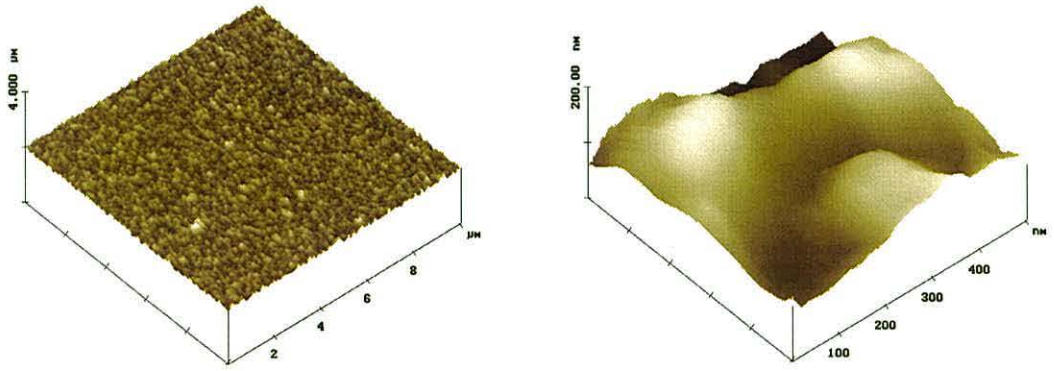

(a) *(b)*

Figure 5.6 *AFM images of P3MeT on gold-coated glass substrate, (a) 10 µm x 10 µm and (b) 500 nm x 500 nm.*

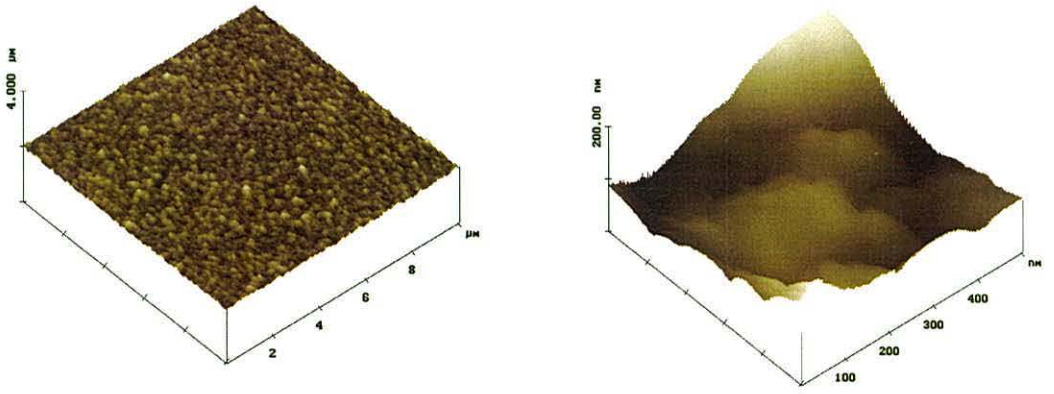

(a) *(b)*

Figure 5.7 *AFM images of P3MeT on ITO substrate, (a) 10 µm x 10 µm and (b) 500 nm x 500 nm.*

Similar images for PCDM on gold-coated glass and ITO-coated glass (Figures 5.8 and 5.9) show a different morphology. The polymer compromises a smooth, pin-hole free film with a number of larger aggregations of polymer on the surface as seen in figure 5.8*(a)* and 5.9*(a)*. The size of the polymer protuberances in figures 5.8*(b)* and

5.9*(b)* are approximately 200 x 200 nm whereas the larger aggregations in the 10 x 10 μm image are approximately 400 x 400 nm. However, despite the presence of these large aggregations, the PCDM has a similar RMS roughness to the P3MeT samples. This suggests that the polymer layer under the larger aggregations is smoother than the P3MeT surface. However, the presence of these larger aggregates could affect the electrical characteristics of the PCDM.

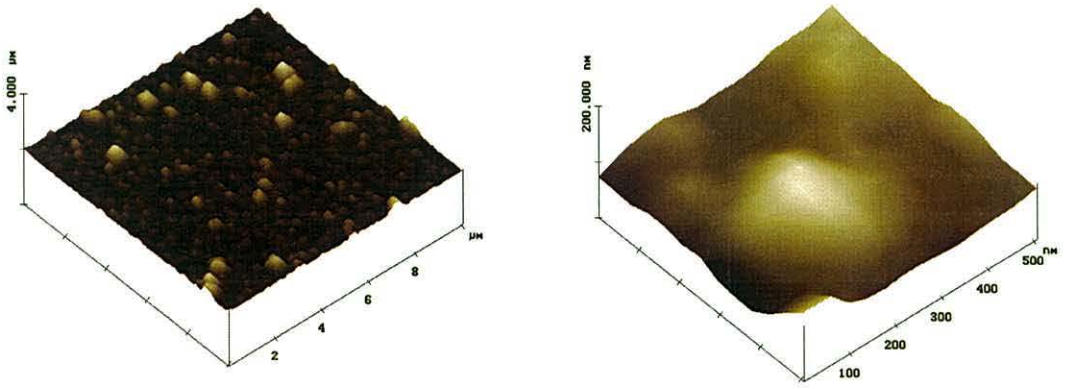

(a) *(b)*

Figure 5.8 *AFM images of PCDM on gold-coated glass substrate, (a) 10 μm x 10 μm and (b) 500 nm x 500 nm.*

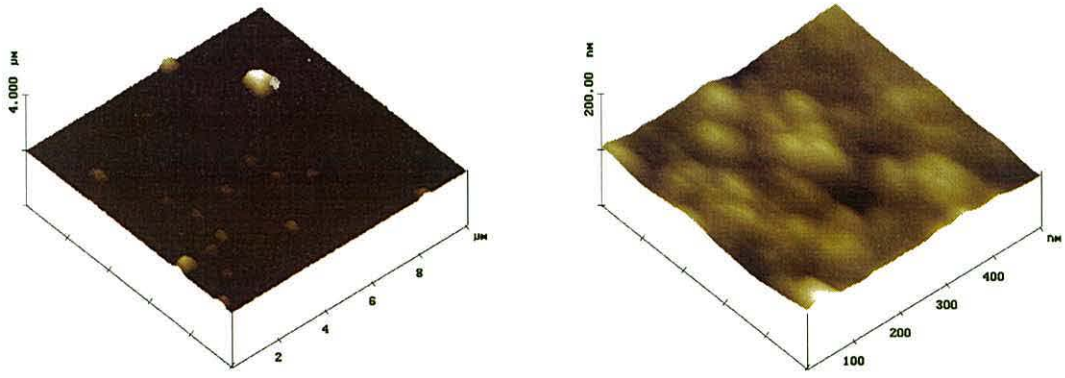

(a) *(b)*

Figure 5.9 *AFM images of PCDM on ITO substrate, (a) 10 μm x 10 μm and (b) 500 nm x 500 nm.*

From the 10 μm x 10 μm images, the RMS roughness values and maximum height of the surfaces of both the substrates and the polymer films are given in table 5.2. The gold and ITO coated glasses have similar roughness', much smoother than the pristine glass. The PCDM and P3MeT samples also have similar rms roughness, with the samples grown on ITO having a lower surface roughness than those grown on gold.

Interestingly, the maximum heights of the polymers show that all the polymer films had large, localised "mounds" of material, with heights approximately twice the measured film thickness in the case of PCDM. This suggests that although the film surfaces are smooth, localised areas of the surface are uneven and it must be assumed that diodes produced using these polymers will have uneven field distributions due to this variation in film thickness.

Table 5.2 *RMS roughness and maximum heights of substrate and polymer surfaces over the 10 μm x 10 μm AFM images .*

Material surface	RMS roughness (nm)	Maximum height (nm)	Average polymer thickness (nm)
Pristine glass	13.81	42.70	n/a
Gold-coated glass	1.45	27.77	n/a
ITO-coated glass	2.46	19.42	n/a
P3MeT on gold	42.07	351.79	290
P3MeT on ITO	28.87	249.93	210
PCDM on gold	51.79	406.60	170
PCDM on ITO	28.28	412.67	220

AFM was also used to measure the thicknesses of PCDM films grown on the same ITO substrate (Table 5.3) by raising the substrate in a step-wise fashion out of the electrolyte solution. The thickness is not linearly proportional to the growing time as might be expected empirically. As the thickness of the semiconducting polymer film increased, the currents measured during the polymerisation fell, so that the polymer deposited more slowly.

Unfortunately, the surface of the PBDT sample was too rough for the AFM to engage and produce an image. Therefore the morphology was investigated using scanning electron microscopy (SEM) and contrasted with SEM images of PCDM.

Table 5.3 *Thickness of PCDM films for different growing times on a single ITO substrate.*

Growing time (s)	Polymer thickness (nm)
60	63.7
300	107.6
600	120.1

5.2.2 Scanning electron microscopy

SEM micrographs of PCDM (Figure 5.10) revealed a smooth, pin-hole free polymer morphology dotted with larger aggregations of polymer on the surface. The polymer aggregations range in size up to approximately 2 μm and are of different shapes, including spherical, elongated spheroids and irregular, nodular groupings.

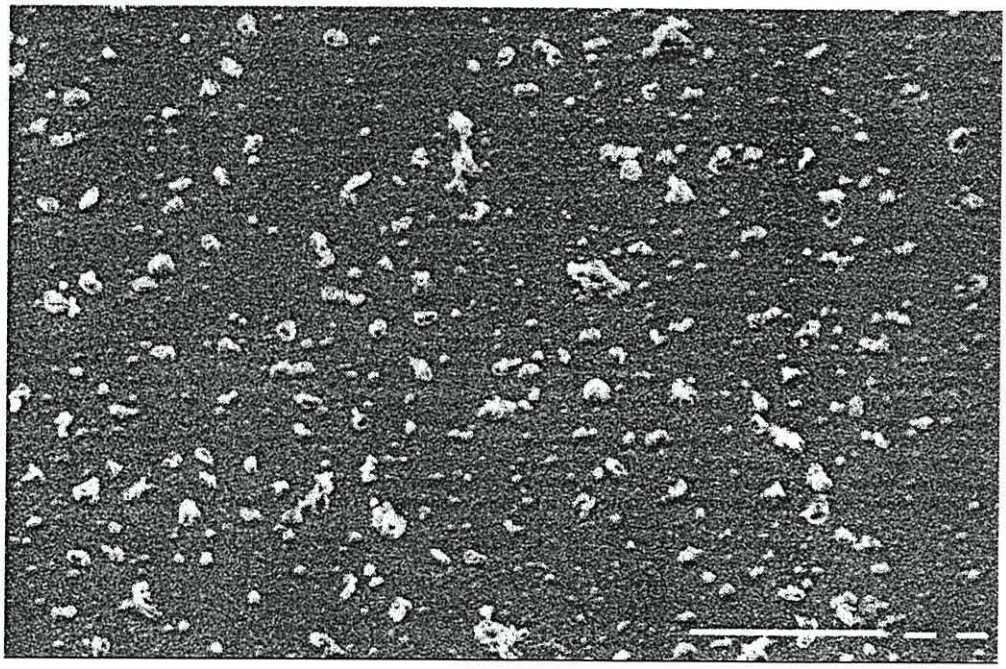

Figure 5.10 *SEM image of PCDM film on ITO (long bar = 10 μm).*

The morphology of PBDT on the other hand (Figures 5.11) was very different. The surface of the PBDT was much rougher than that for the PCDM with aggregations of polymer clumped together. The expanded area of the surface shown in figure 5.11*(b)* indicates that the PBDT could contain pin holes through to the substrate.

Figure 5.12 shows the polymer aggregations to be approximately 1 μm across. Assuming that the polymer is of similar thickness to the others grown in this work, i.e.

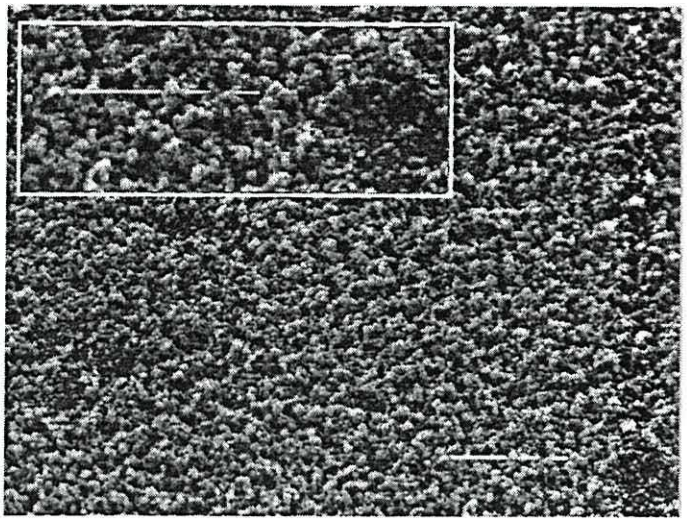

Figure 5.11 *SEM image of a PBDT film on an ITO substrate, inset is expanded area showing a hole in the bottom right- hand corner revealing the underlying substrate (long bar = 10 μm).*

approximately 200 nm, then the polymer aggregates seem to be much larger than the thickness of the film. This roughness in the film structure could be due to the speed at which the polymer film grows. The PBDT grows much faster than both the PCDM and P3MeT so there is less time available for the polymer to grow in an orderly fashion and yield a smooth surface morphology. A reduction in the polymerisation potential could correct this by slowing the rate of growth, and produce a film which would be more suitable for electrical characterisation.

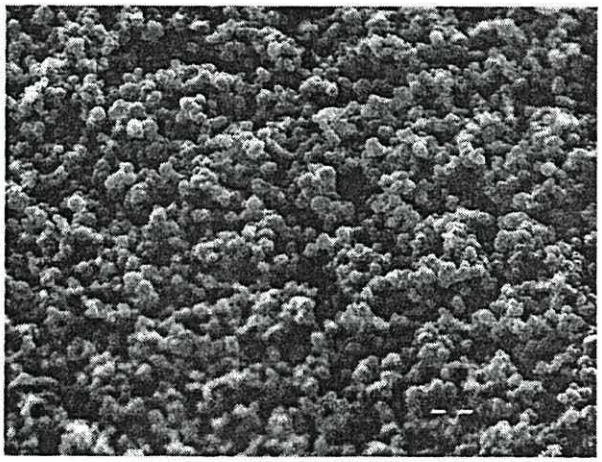

Figure 5.12 *Magnified image of PBDT on ITO highlighting the polymers roughness (bar = 1 μm).*

Although the PBDT films were very rough compared to the PCDM, and therefore less suitable for electrical characterisation, PBDT could be useful in the production of polymeric supercapacitors, or batteries, where a large surface area is an advantage. Bithienyl polymers, including PCDM, have been studied with respect to the possibility of forming these capacitors [134] by charging two adjacent polymer films to their n- and p- doped states respectively and then discharging them at constant current. PCDM was found to be suitable as a material for this type of supercapacitor. If PBDT is found to be stable to p- and n-doping, allied to its large surface area, it could be useful for supercapacitor production.

Comparison of PCDM films grown previously in this department and reported in the literature show that the films grown here are smooth and pin-hole free. Beyer and co-workers [162] present an image of a PCDM film which was grown potentiodynamically on gold, and is smooth but shows signs of pin-holes in the polymer, unfortunately it is difficult to tell whether these holes penetrate the full extent of the film. A film grown potentiostatically on gold by Gunatunga and co-workers [86] had similar morphology to that shown here, with a relatively smooth, pin-hole free surface.

5.3 Spectroscopic analysis

A range of spectroscopies, including FTIR, Raman, UV-visible and XRD were used to investigate the chemical structures of both the monomers and the polymers used in this project. This allowed a comparison to be made between the pristine polymer and the material subjected to different experimental conditions. Some consideration has been given to possible modification of the polymer under normal storage and experimental conditions and a Raman mapping method has been used to map the surface of PCDM. The crystal structure and packing of monomer units of CDM have been modelled using computer packages to analyse XRD data. Monomer dimensions and possible polymerisation routes have been deduced using this data.

5.3.1 Fourier transform infra-red spectroscopy (FTIR)

Figure 5.13 is an FTIR spectrum of PCDM electrodeposited onto a gold-coated glass substrate. The spectrum displays well defined spectral peaks, although there is some "noise" due to atmospheric water, between 1800 and 1500 cm^{-1}, superimposed on the polymer spectrum. Based on the Raman spectral assignments proposed by Huang and Pickup [82, 83], the spectral vibrations in the PCDM FTIR spectrum were deduced and are given in table 5.4.

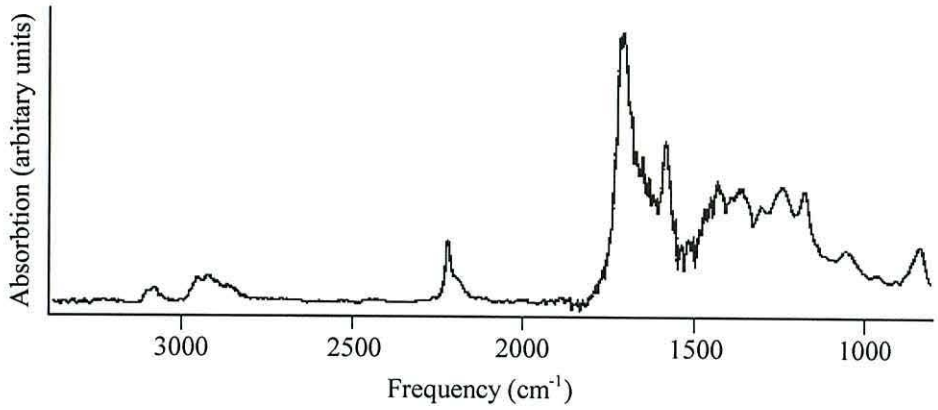

Figure 5.13 *FTIR spectrum for a PCDM film.*

Table 5.4 *FTIR spectral assignments for a PCDM film.*

Wavelength (cm^{-1})	Spectral assignment
3082	C=C-H
2924	C-C-H
2228	C≡N
1710	C=O
1587	C=C-$(CN)_2$
1438	C_α=C_β
1369	C_β-C_β
1182	Inter-ring C_α-C_α'

The presence of the C=C and C-C bonds at 1438 and 1369 cm^{-1} as well as the inter-ring C-C at 1182 cm^{-1} confirms that polymerisation has occurred. However, the C=O group signal at 1710 cm^{-1} suggests the presence of a contaminant in the polymer

film, for example acetone, or that some modification of the polymer has occurred. The possibility that the polymer film contains contaminants and the possibility of modification of the polymer, by oxygen attack of the thiophene rings or nitrile hydrolysis of the C-$(CN)_2$ group, are considered in section 5.3.6.

5.3.2 Raman spectroscopy

The Raman spectra of the substrate materials were first recorded as references for comparison with the polymer spectra. The spectra for pristine and ITO-coated glass substrates (Figure 5.14) are very similar, but both show significant fluorescence with a maximum at approximately 2700 cm^{-1} and 2900 cm^{-1} respectively. The introduction of the ITO coating could be modifying the spectrum of the underlying glass causing it to be shifted towards the blue end of the electromagnetic spectrum.

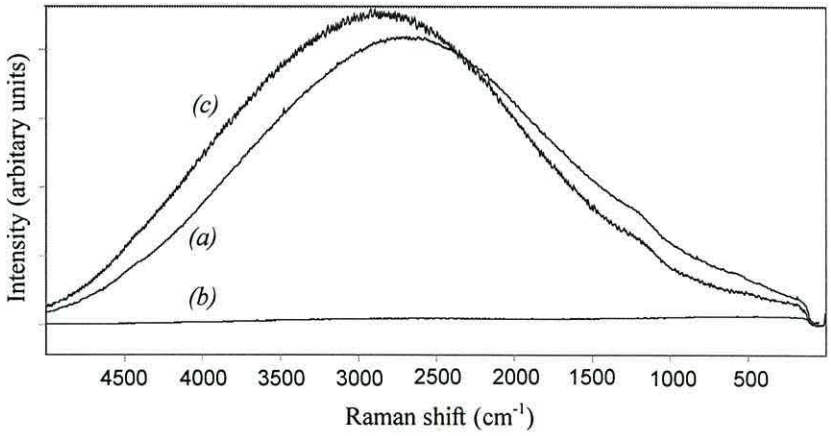

Figure 5.14 *Raman spectra of (a) pristine glass, (b) gold-coated glass and (c) ITO-coated glass substrates.*

The fluorescence could be due to the glass itself or to impurities in the glass which can also fluoresce. This phenomenon can be problematic due to the low efficiency of the Raman scattering compared to the fluorescence process. If the fluorescent intensity is sufficiently high it becomes difficult to obtain the Raman spectrum. However, the introduction of a gold layer on the surface of the glass reduces the fluorescence detected by the spectrometer, provided the laser is focused correctly. This process also occurs if the sample polymer is sufficiently thick and opaque to stop the laser light from penetrating to the glass.

Analysis of the CDM monomer, spectrum *(a)* in figure 5.15, was completed by focusing the laser on a monomer crystal on the spectrometer stage. The major spectral vibrations occur at 2228 cm^{-1}, due to the C≡N stretch, and at 1587 cm^{-1}, due to the C=C-$(CN)_2$ group. The very simple spectrum with discrete peaks suggests that the monomer is contaminant-free and that little, if any, polymerisation occurs during the synthesis. Figure 5.15*(b)* was obtained for a 1 year old sample of the monomer which, after storage in the dark under vacuum, was used to determine whether any chemical changes occurred over time.

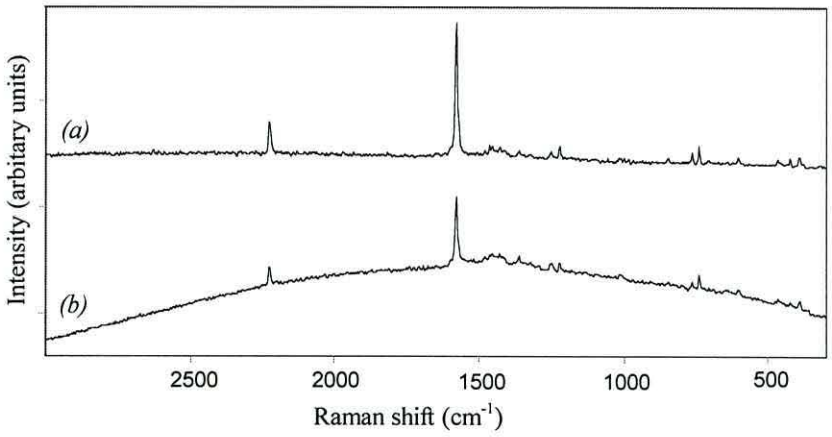

Figure 5.15 *Comparison of Raman spectra of (a) a new and (b) a 1 year old sample of CDM monomer.*

There is no change in the positions of the spectral peaks nor is there any change in the appearance of the spectrum apart from a greater degree of background fluorescence, centred at approximately 1600 cm^{-1}, in the older sample (see the explanation of figure 5.17 for suspected reason for monomer fluorescence). The lack of change in the Raman spectra, as well as a lack of change in the NMR data (Appendix 1) over a similar period, suggest that the monomer compound is *chemically* stable for periods up to 1 year.

Upon polymerisation, the Raman spectrum of PCDM displayed a number of new spectral peaks (Figure 5.16) but many of the features characteristic of the monomer spectrum remain. Comparison of the monomer and polymer show that the polymer retains the C≡N peak at 2228 cm^{-1}, the C=C$(CN)_2$ peak at 1587 cm^{-1} and some of the smaller peaks below 1000 cm^{-1}. However, the appearance of broad peaks at approximately 1500 cm^{-1} are due to the change in π-bonding owing to the formation of

the inter-monomer C_α-C_α bond during polymerisation. The vibrations of the coupled C-C and C=C bonds across a large number of repeat units in the polymer cause the peaks to broaden.

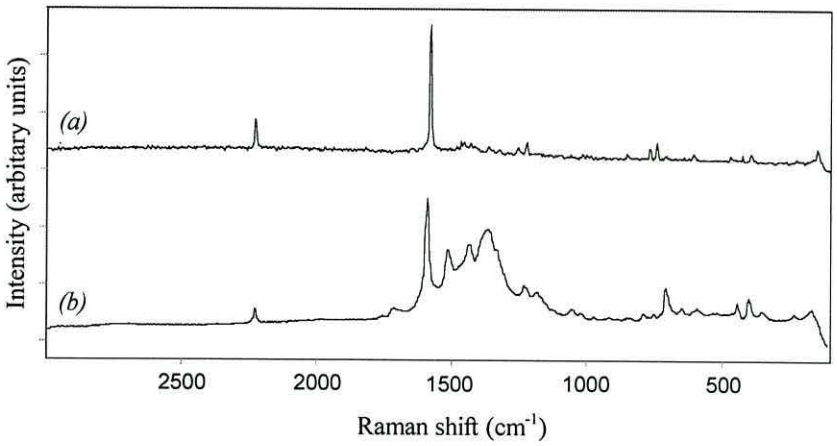

Figure 5.16 *Raman spectra of (a) CDM monomer and (b) PCDM.*

Similar to the spectra for the monomer seen in figure 5.15, the spectrum of PCDM recorded immediately post polymerisation is comparable to that for a one year old sample (Figure 5.17). The spectra are identical, but the background fluorescence is greater in the spectrum of the older sample. The spectrum for PCDM in figure 5.16*(b)* does not show any of this fluorescence as the polymer sample investigated was different.

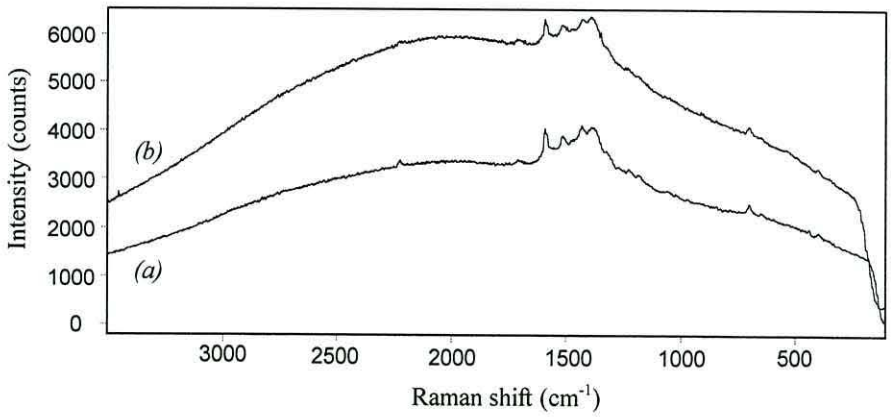

Figure 5.17 *Raman spectra of PCDM (a) recorded immediately post-polymerisation and (b) recorded after a period of approximately 1 year storage in the dark, under vacuum.*

The fluorescence occurring in polymers, such as PCDM, has been attributed to the crystallinity of the molecule [157]. As the polymer becomes more disordered over time, the rate of non-radiative relaxation is lowered sufficiently to allow time for fluorescence to occur. The attachment of the polymer to a substrate surface is also thought to have an effect. For the monomer, this increase in fluorescence could be due to an decrease in crystallinity in the monomer crystal over time.

The Raman spectrum is similar to the FTIR spectrum (Figure 5.18) with respect to the peaks at 2228 cm^{-1} and 1587 cm^{-1}, as expected due to the complementarity of the methods, although the Raman spectrum does not have the "noise" due to water vapour interference seen in the FTIR spectrum. Differences in the FTIR and Raman spectra include,

1. the absence of C-H peaks in the Raman spectrum.
2. the different intensities in the peaks due to the C=C and C-C bond vibrations at about 1500 cm^{-1}.
3. the lesser intensity of the peak at 1712 cm^{-1} in the Raman spectrum.

These differences are mainly due to the fact that different spectral vibrations are more active or inactive depending on the method employed for the measurement.

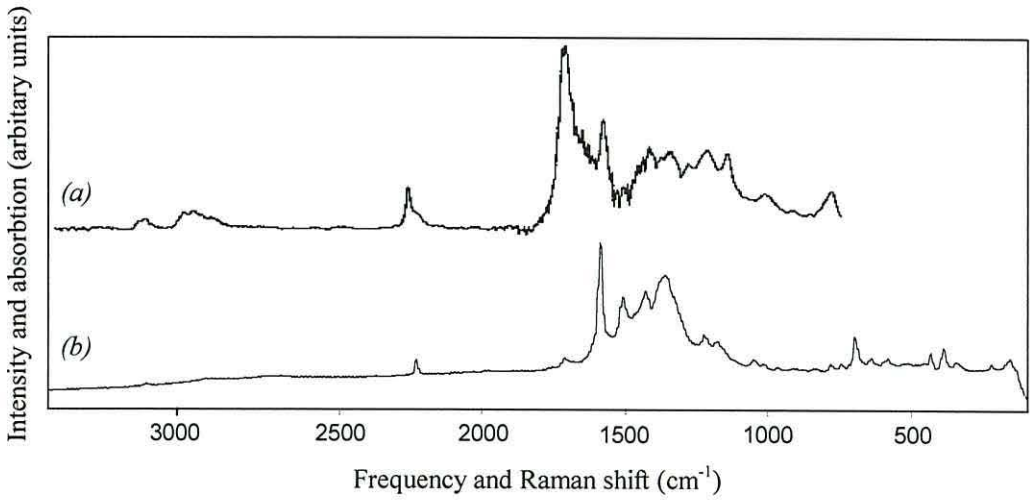

Figure 5.18 *(a) FTIR and (b) Raman spectra of PCDM presented together for comparison.*

Comparison of the monomer and polymer spectra for BDT (Figure 5.19) reveals a similar effect occurring as in the CDM analogues. The smaller range, from 1700 to 500 cm^{-1}, was used to highlight the peaks in the monomer spectrum which all

occurred below 2000 cm^{-1}. Unfortunately, the BDT monomer is highly fluorescent, with a maximum occurring at approximately 2000 cm^{-1}, making it difficult to obtain well defined spectra. The polymer spectrum displayed broad peaks, similar to those in PCDM, at approximately 1500 cm^{-1}. Indeed it seems that the appearance of these peaks is an indication that polymerisation has occurred in polythiophene-based polymers as similar features are seen in spectra for P3MeT [161] and homopolymers of acrylonitrile [90].

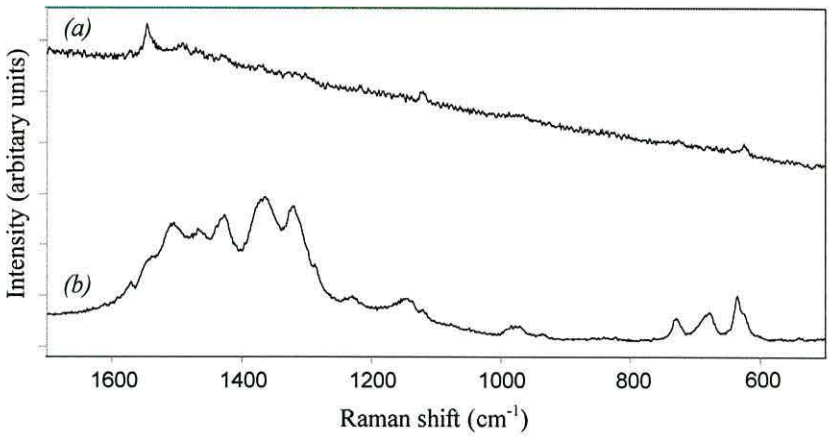

Figure 5.19 *Raman spectra of (a) BDT monomer and (b) PBDT.*

Plotting the respective monomer and polymer spectra for BDT and CDM together highlights the similarities between the two compounds (Figure 5.20). Again, the monomer spectra are truncated to show the detail in the BDT spectrum. The common features are to be expected due to the common carbon-bridged dithienyl moiety present in each. However in the case of the PBDT there is no C=C-$(CN)_2$ peak, as expected due to the different chemical structure, but there is also a lack of a peak at 1712 cm^{-1} which has been attributed to C=O. The appearance of a broad peak at 2700 cm^{-1} in the PBDT spectrum does however suggest that there is a contribution due to the glass substrate appearing in the spectrum. Observation of fluorescence with a peak maximum at approximately 2000 cm^{-1} in other Raman spectra of PBDT films suggests that the appearance of the small, broad peak at 2000 cm^{-1} in the spectrum for PBDT in figure 20(b) indicates that there is some sample fluorescence.

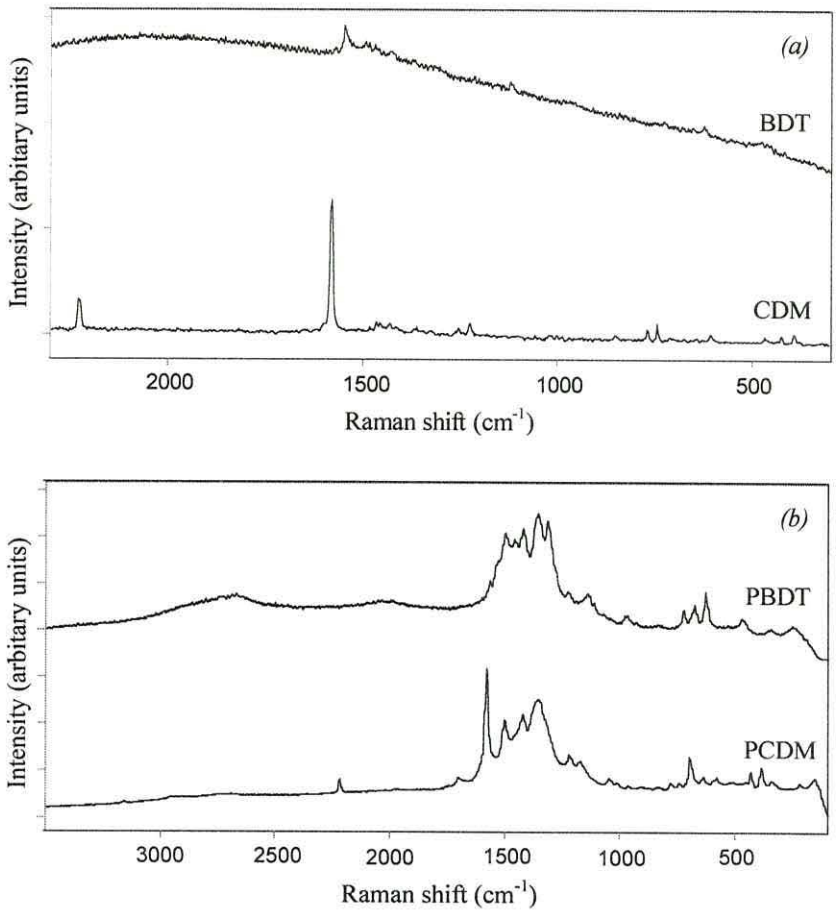

Figure 5.20 *Raman spectra of BDT and CDM, (a) monomer spectra and (b) polymer spectra presented together for comparison.*

5.3.2.1 Raman mapping of fluorescence

The fluorescence occurring in the Raman spectrum of PCDM samples was measured to check the uniformity of the film. Two samples of PCDM were analysed by mapping the intensity of the Raman signal at 2000 cm^{-1} (Figure 5.21). 2000 cm^{-1} was chosen since it was well away from the characteristic polymer peaks and would, therefore give a direct measure of the fluorescence in the sample. The two samples were grown using identical polymerisation conditions except for the growing times, which were 300 seconds for sample 1 and 600 seconds for sample 2. The samples were then mapped at 2 mm and 4 mm intervals in the x and y directions respectively across the whole surface of the sample.

The low signal up to approximately 3 mm is from the gold substrate. From 3 mm to the bottom edge of the slide is the signal obtained from the polymer. The

triangular area between 23 and 26 mm in *(b)* coincided with a broken corner of the slide.

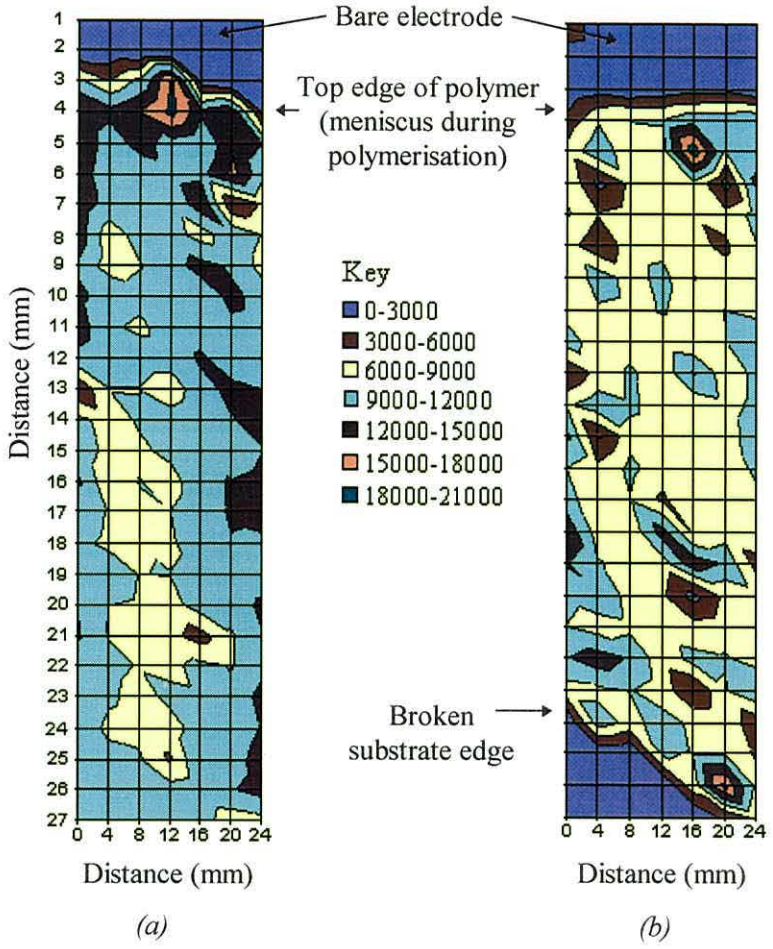

Figure 5.21 *Raman map of fluorescence intensity from a PCDM film grown, on a gold-coated glass substrate, for (a) 600 seconds and (b) 300 seconds.*

The polymers show a central region of approximately constant fluorescence intensity with areas of greater or lesser intensity. Reductions in the spectral intensity have been found to be due to changes in the polymer morphology and in the use of the autofocus facility on the Raman spectrometer. For example, aggregations of polymer on the smoother polymer surface seen in the AFM micrographs (Figure 5.9) caused a reduction in the intensity of the Raman signal produced. Also, the focusing of the laser spot on the polymer surface was not always consistent when using autofocus option on the spectrometer. This caused the laser spot to defocus during some spectral measurements resulting in a lower intensity than expected. However these reductions occurred infrequently.

It can be seen that areas of higher fluorescence were found around the edges of the sample, along the edges of the substrate electrode, and also at the upper edge of the growing area where the meniscus is situated during polymerisation. The intensity of the fluorescence over most of sample *(b)* corresponded to 6000 to 9000 counts whereas that for *(a)* was found to be between 9000 and 12000 counts. This increased fluorescence intensity is consistent with *(a)* being thicker, i.e. having grown for a longer time. From the difference in the fluorescence intensities, *(a)* is between 30% and 50% thicker than sample *(b)*. This is confirmed by atomic force microscopy, where *(a)* and *(b)* were shown to be 190 nm and 140 nm thick respectively at the centre of the sample, making *(a)* approximately 36% thicker.

Another map, of the fluorescent intensity across the top (meniscus) edge of the polymer (Figure 5.22), was produced by scanning at 200 μm intervals across the surface of the gold-coated glass substrate (spectrum number 1), over the boundary between the polymer and the substrate and into the bulk of the polymer (spectrum number 8). This showed that the fluorescence increased upon crossing the boundary between the electrode and the polymer, but the peaks in the spectra due to the polymer vibrations remained unchanged.

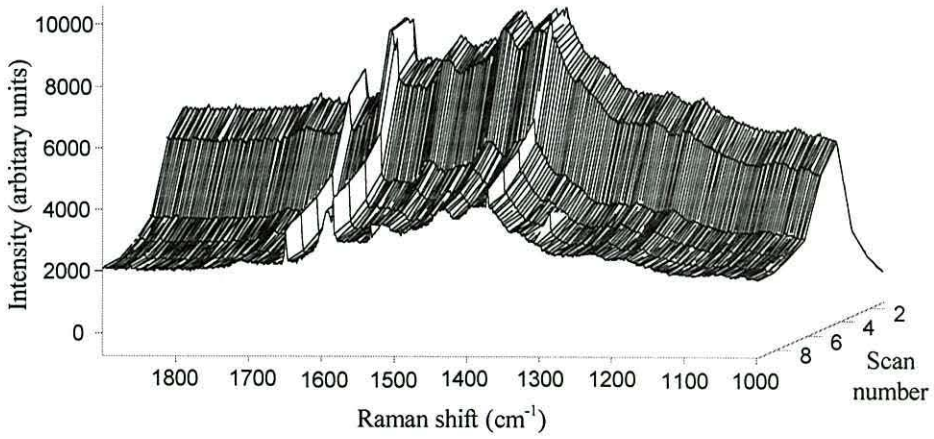

Figure 5.22 *Raman map across a gold-coated glass substrate/PCDM boundary.*

Assuming that the fluorescence maps reflect the local film thickness, then devices fabricated towards the middle of each substrate should be formed on film of uniform thickness. Any electrical characterisation performed on diodes fabricated on a single substrate should concentrate on the devices in the centre of the film to minimise any variability arising from the variable film thickness at the sample edges.

Exposure of the PCDM to high laser powers in the Raman microscope was found to discolour the polymer in the laser exposed regions, as shown in figure 5.23. The figure shows discoloured, exposed polymer as well as the polymer aggregations seen in the AFM micrographs (Figure 5.9). This interesting phenomenon is covered further in appendix 3. It is assumed that the pristine PCDM is originally semi-crystalline and that the polymer exposed to the laser melts and forms a more disordered polymer causing the fluorescence seen in the Raman spectrum to be blue shifted. The lack of change in the Raman spectra does confirms that the polymer does not decompose - new compounds detectable by the spectrometer would have been created. The shift in fluorescence could be due to a change in the degree of crystallisation or concentration of impurities in the ablated areas.

Figure 5.23 *Optical microscope image of a PCDM film showing the effect of laser exposure (light, circular areas) and polymer aggregations (irregular, dark areas).*

5.3.3 Ultra-violet/visible spectroscopy

UV-vis spectra were recorded for samples electropolymerised onto ITO. The ITO had a spectral cut-off at approximately 300 nm and was found to be transparent to the UV-vis radiation at wavelengths above this (Figure 5.24). The main absorption bands of PCDM deposited on ITO were found to fall in this transparent region but a baseline blank was run with ITO in both the sample and reference beams as a control. Discrepancies between the ITO used in the control and the ITO used for the sample as well as differences in the local atmosphere could cause the differences seen at wavelengths lower than 300 nm in the PCDM measurement. The UV-vis spectrum for PCDM is similar to that reported by Ferarris and Lambert [80].

The UV-vis spectra of CDM monomer solution, monomer deposited onto ITO using the Langmuir-Blodgett technique and the corresponding spectra of PCDM electropolymerised on an ITO substrate are presented in figure 5.25. The spectrum recorded for the monomer in solution *(a)* displays two main absorption bands as

reported by Riul and co-workers [86]. At approximately 300 to 400 nm a broad band occurs arising from the overlap of the π-π* transitions in the molecule. At 600 nm is the charge transfer band, arising from the interaction of the electron donating sulphur groups and the electron accepting cyano groups and giving rise to the blue colour of the monomer solution.

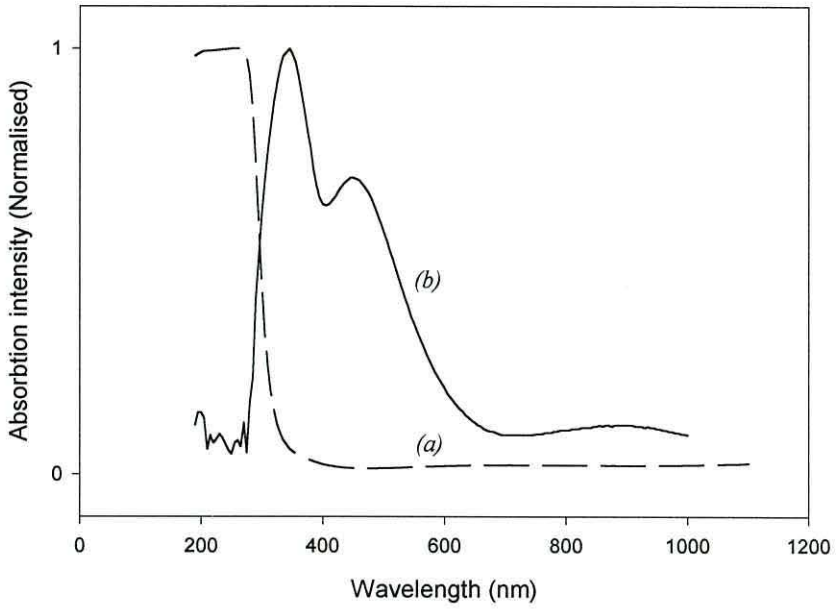

Figure 5.24 *UV-Vis spectra of (a) ITO and (b) PCDM electropolymerised on ITO showing the spectral cut-off at approximately 300 nm.*

In the spectrum for the monomer LB film *(b)*, the molecular π-π* transition band is still present but the charge transfer band is absent. This could be due to the alignment of the monomer units in the film. If the dipoles of the monomer units are aligned antiparallel to one another, the effective dipole of the film is zero and hence the charge transfer band does not occur. This antiparallel arrangement of dipoles could occur as the monomer molecules in the unit cell of the monomer crystal (see section 5.3.5) are seen to be antiparallel with their neighbours within the same plane. In the polymer spectrum *(c)*, molecular π-π* transitions are present at approximately 300 nm and 450 nm. Also, centred at approximately 900 nm is the π-π* transition band of the extended polymer which corresponds to the band gap.

Similarly, a spectrum of an LB film of BDT monomer has molecular π-π* transitions at 200 nm and 420 nm whereas, a PBDT thin film (Figure 5.26) contains an extra molecular transition at 600 nm, and the π-π* transition of the polymer at

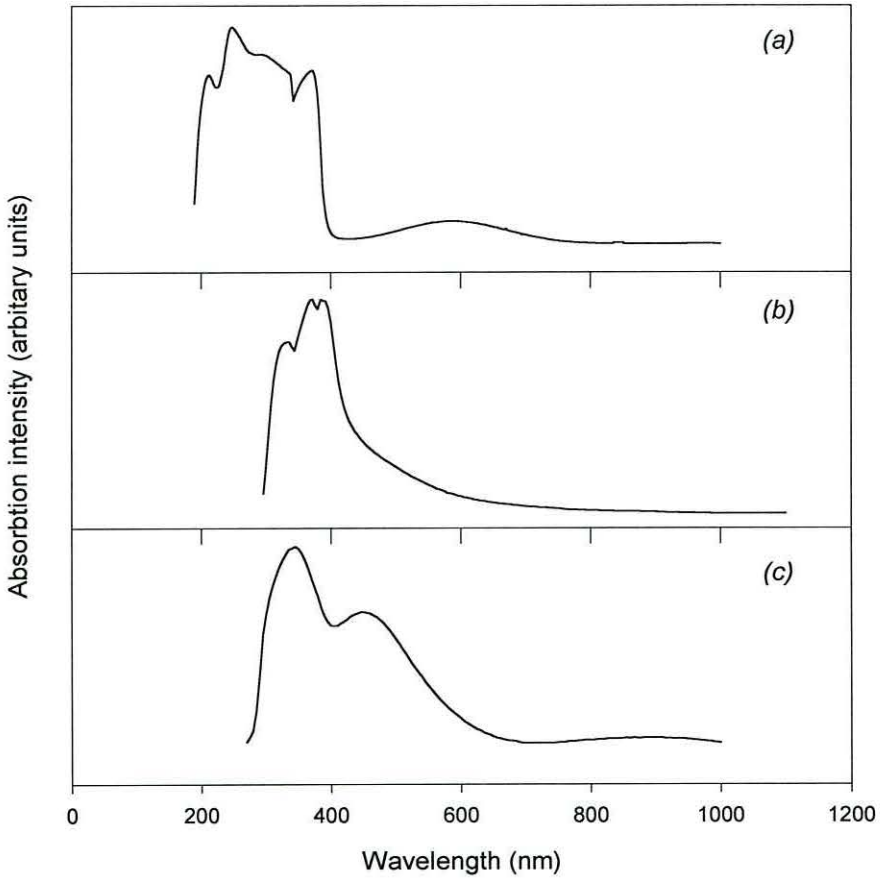

Figure 5.25 *UV-vis spectra of (a) CDM monomer solution, (b) an LB film of CDM monomer and (c) a PCDM film on ITO substrates.*

approximately 1000 nm. The molecular transitions have been previously reported by Kozaki and co-workers (see section 3.1.4). Similarity in the spectra for the PCDM and the PBDT is not unexpected due to the similarity in the polymer structure, where both polymers possess the conjugated polymer backbone incorporating the carbon bridged dithiophene unit. The polymers also produce similar dipoles arising from the electron donating sulphur atoms and the electron withdrawing moiety on the carbon bridge.

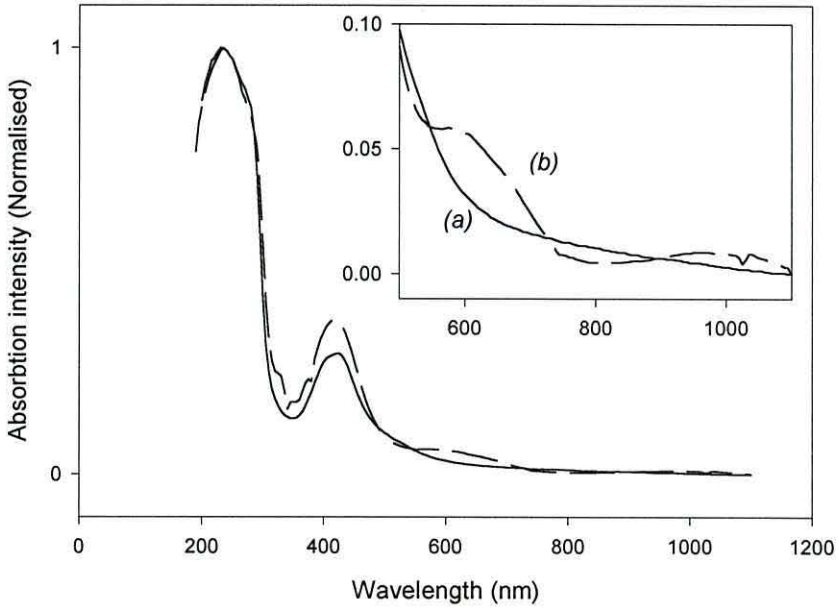

Figure 5.26 *UV-vis spectra of (a) an LB film of BDT monomer and (b) a PBDT film on ITO substrates.*

Semi-empirical calculations completed by Jones and co-workers [162] on CDM monomer, dimer and trimer structures in the ground state, have been used to produce theoretical UV-vis spectra for comparison with experimental results. A fully optimised geometry was obtained using a MOPAC computational package [163] and absorbtion spectrum calculations were made using the ZINDO computational package [164]. The most probable geometry for the dimer and trimer was found to be essentially planar in a parallel or anti-parallel configuration when external forces, such as dipole alignment with neighbouring polymer chains, were neglected. The molecular dipole moment for the anti-parallel dimer system was found to approach zero, considerably lower than that for any other configuration.

Comparison of the theoretical spectra of the monomer and the dimer with experimental spectra for the polymer showed good agreement in the positioning of the

absorbtion peaks. Major contributions to the absorbtions in the theoretical spectra of the CDM monomer and dimer are shown in table 5.5 where H denotes the highest occupied molecular orbital (HOMO) and L is the lowest unoccupied molecular orbital (LUMO).

Table 5.5 *Principle contributions to the absorption peaks in theoretical UV-vis spectra of CDM and BDT monomers and dimers.*

Molecular geometry	Absorption peak maximum (nm)	Principle contributions
CDM monomer	183.7	H-2 ⇒ L+1
		H-3 ⇒ L+2
	306.9	H-1 ⇒ L
		H ⇒ L+4
CDM dimer	296.2	H ⇒ L+3
		H-3 ⇒ L
	406.3	H ⇒ L+2
		H-1 ⇒ L+1
BDT monomer	180.7	H ⇒ L+2
		H-3 ⇒ L
	298.9	H-1 ⇒ L
		H ⇒ L+2
BDT dimer	310.2	H ⇒ L
		H-1 ⇒ L+1
	639.6	H-3 ⇒ L
		H-2 ⇒ L

The experimental results for the monomer were found to be slightly red-shifted compared to the theoretical results, which could be due to the presence of a small amount of polymer, possibly in the form of dimers and trimers, in the monomer sample or by organic contaminants. As the conjugation length increased from monomer to dimer, the spectral peaks shifted to longer wavelengths. A further shift was seen in the experimental spectrum for the polymer consequent on the increase in conjugation length.

The absorption wavelengths for the experimental spectra of PCDM and CDM monomer (Figure 5.25) are readily converted into absorption energy (eV) since,

$$E(eV) = \frac{hc}{\lambda e} \qquad (5.1)$$

where, λ is the wavelength in metres, h is Planck's constant (6.626×10^{-34} Js), c is the speed of light (2.998×10^{8} ms^{-1}) and e is the elementary charge (1.602×10^{-19} C).

Plotting the absorption spectra as a function of energy, the band gap can be estimated. As expected, the energies for the band gap transition decrease from the theoretical monomer and dimer spectra to the experimental polymer spectrum (Table 5.6). Ferraris and Lambert [80] assign the low energy edge of the polymer π-π^* absorption band at approximately 0.8 eV as the band-gap of PCDM through analogy with the monomer spectra of CDT [165] and CDM. In the experimental calculations of the band-gap for PCDM and PBDT here, the peak maximum of the band has been used because the spectrum does not show the low energy edge of the band. The theoretical calculations also use this value for completeness. This causes the calculated band gap for each material to be higher than those reported previously, but comparison of the PCDM UV-vis spectra with that presented by Ferraris and Lambert also show the peak maximum to occur at approximately 1.4 eV.

Table 5.6 *Theoretically calculated energies of the π–π^* transitions in monomers and dimers of CDM and BDT compared with those estimated from experimental UV-visible absorption spectra.*

Material	**Low energy π–π^* transition energy (eV)**		
	Calculated		**Experimental**
	Monomer	**Dimer**	**Polymer**
CDM	1.70	1.44	1.38
BDT	2.38	1.95	1.29

It has been stated [166] that as the valence and conduction bands in a polymer are broad, producing a broad absorption in UV-vis spectra, that the band gap can be interpreted as either the absorbtion maximum or the commencement of the absorption

band at the low energy end. However it is a matter of convention and at this time it seems that either method can be argued as valid. The peak maximum can be said to correspond to a transition between the highest density of states in the valence and conduction bands whereas the absorbtion band edge corresponds to a transition of the final electrons, presumably from the band edge of the valence band.

The band-gap energy for PCDM estimated from the UV/vis data was compared with that estimated from in-situ conductivity measurements completed by Huang and Pickup [82]. The authors measured a minimum in a conductivity versus voltage plot, between the formal potentials for p- and n-doping, corresponding to an intrinsic conductivity of $1x10^{-8}$ Scm^{-1}, consistent with an optical band-gap of approximately 0.8 eV. Similar measurements for an oxygen modified PCDM sample made by the same authors [83] produced intrinsic conductivities of $8x10^{-7}$ and $1.3x10^{-6}$ Scm^{-1} corresponding to band-gap values of 0.52 and 0.22 eV respectively.

In summary, the emergence of the low energy, band gap transition in the polymer spectra provides evidence that polymerisation has occurred. Comparison of theoretical and experimental values of the low energy π-π^* transition band show that the energy decreases upon progressing from the monomer, through the dimer to the polymer.

5.3.4 X-ray photoelectron spectroscopy

The XPS spectrum of the surface of a PCDM sample is given in figure 5.27. The peaks due to carbon, nitrogen and sulphur are those expected for the polymer while that for the oxygen is thought to be due to surface adsorbed oxygen or oxidation of the polymer. The concentration of oxygen present is greater than that of carbon suggesting that the former case is occurring. The absence of any peak due to the presence of gold confirms that the irradiating beam does not penetrate the full extent of the polymer film.

Figure 5.28 expands the areas in the spectrum containing the peaks for oxygen, carbon, nitrogen and sulphur. The presence of shoulders to the main peaks for carbon, nitrogen and sulphur indicate that each of these elements is present in two states in the polymer, whereas the oxygen, which has only a single peak, is present in one state.

The two forms of carbon can be explained by the presence of sp^2-hybrid carbon atoms in R=C–(R')$_2$, where R and R' = C or S, and sp^3-hybrid carbon atoms in C–C≡N groups within the PCDM structure. The two forms of sulphur and nitrogen are harder to explain. The sulphur is seen to be present as R–S–R in PCDM, and the nitrogen as R≡N. The other forms of these elements could be due to oxidation of the atoms to give R–SO_2–R and R–NO_2 respectively.

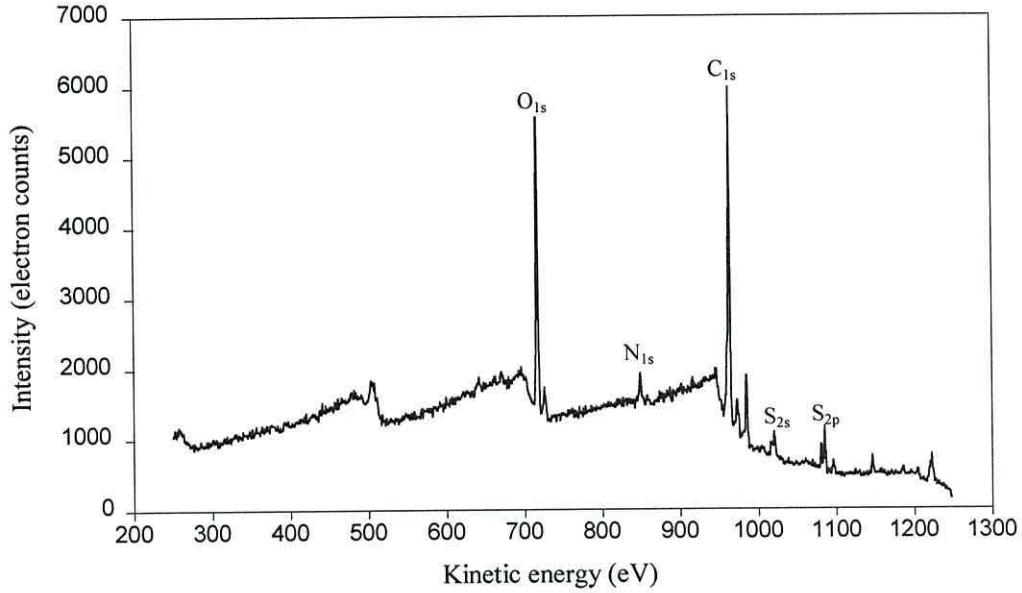

Figure 5.27 *XPS spectrum of PCDM.*

These species if present, should give rise to signatures in the Raman and FTIR spectra for PCDM (Figure 5.18). The peaks due to the vibrations of the R–SO_2–R group occur at ν_s = 1120 to 1160 cm^{-1} and ν_a = 1310 to 1350 cm^{-1} and are both strong in the FTIR spectrum but only the ν_s vibration is strong in the Raman spectrum. For the R–NO_2 group the vibrations occur at ν_s = 1340 to 1380 cm^{-1} and ν_a = 1530 to 1590 cm^{-1}, ν_a being strong in FTIR and ν_s being very strong in Raman.

Examination of the respective spectra shows that the ν_s and ν_a peaks for the R-SO_2-R group could be present in the FTIR spectrum but the Raman spectrum lacks a strong peak for ν_s. For the R-NO_2 group there is the possibility that there is a peak due to the ν_s vibration, although it is not as strong as expected, but the ν_a peak is absent from the FTIR spectrum. These results suggest that the alternative forms of sulphur and

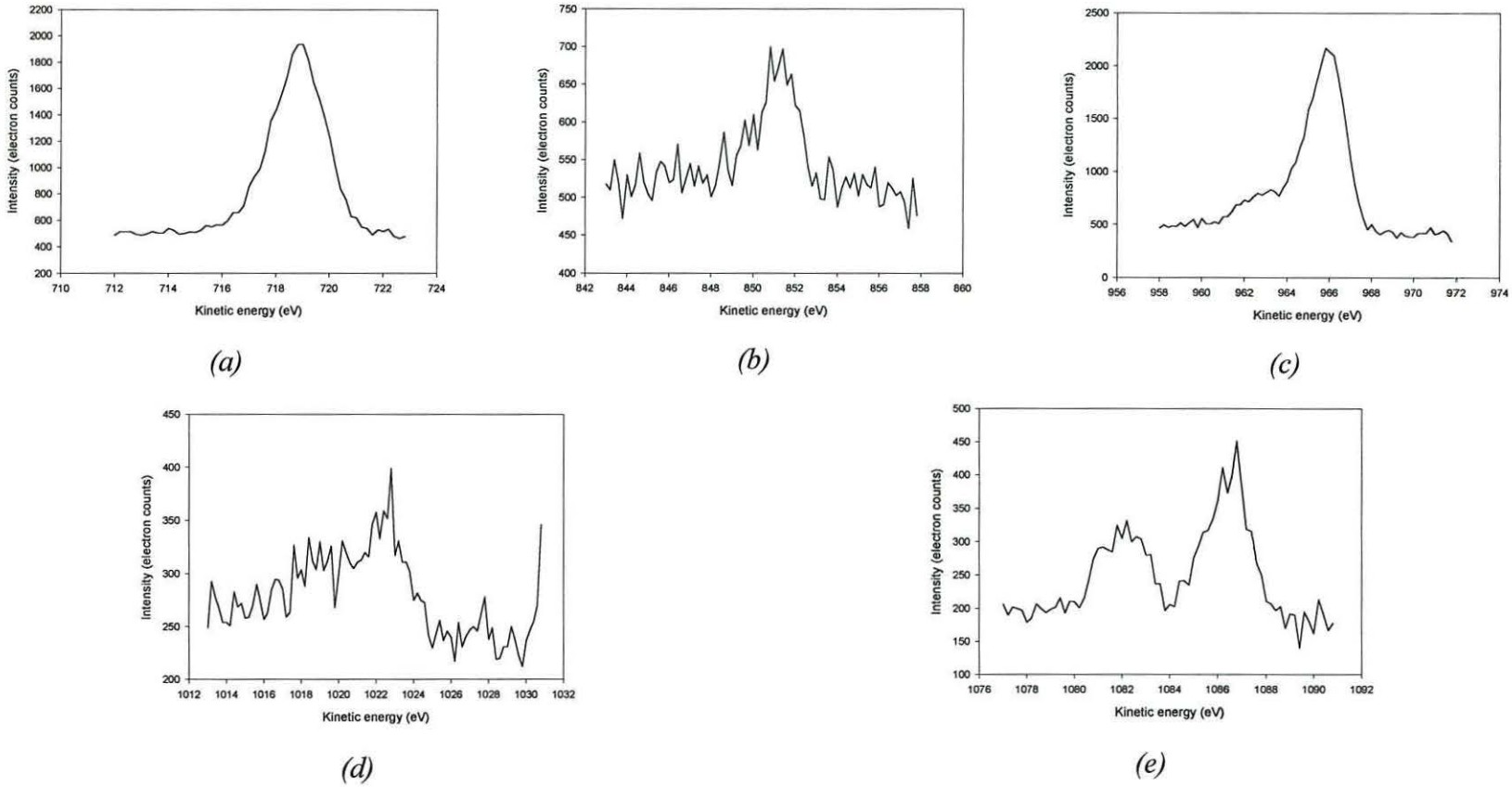

Figure 5.28 *Expanded XPS spectra of (a) O_{1s}, (b) N_{1s}, (c) C_{1s}, (d) S_{2s} and (f) S_{2p} atoms in PCDM to show the double peaks occurring for the N, C and S.*

nitrogen are either not present, or in insufficient quantity to be detected using the Raman and FTIR methods. It could be that the forms of sulphur and nitrogen are not in different chemical environments, rather that they are in different electronic environments which would not be differentiated by the Raman and FTIR spectrometers. This could occur due to the possibility of the presence of aromatic and quinoid conformers in the polymer. It could also be possible that the extra form of nitrogen is due to atmospheric nitrogen recorded during the measurement.

Figure 5.29 shows sections of the XPS spectra of platinum and PCDM used for calculating the Fermi level and the valence band edge of the polymer, (surface not the bulk) respectively [167]. The platinum spectrum is measured using a standard platinum sample for valence band calibration of the polymer. The Fermi energy is calculated to be 1252.11 eV, defined as the symmetry point of the measured curve. The valence band edge energy is 1252.00 eV which has been measured as the intercept of the slope with the value at which the electron counts return to a constant value. Measurement of this kinetic energy for the valence band is a matter of convention but as the XPS measures the energy of the electrons removed from the valence band, it appears sensible that the energy of the electrons detected at this point correspond to the final (highest energy) electrons to be removed from the valence band and hence, this energy corresponds to the valence band edge. From these values it is seen that the valence band edge of the polymer surface is situated approximately 0.1 eV below the Fermi level of the platinum.

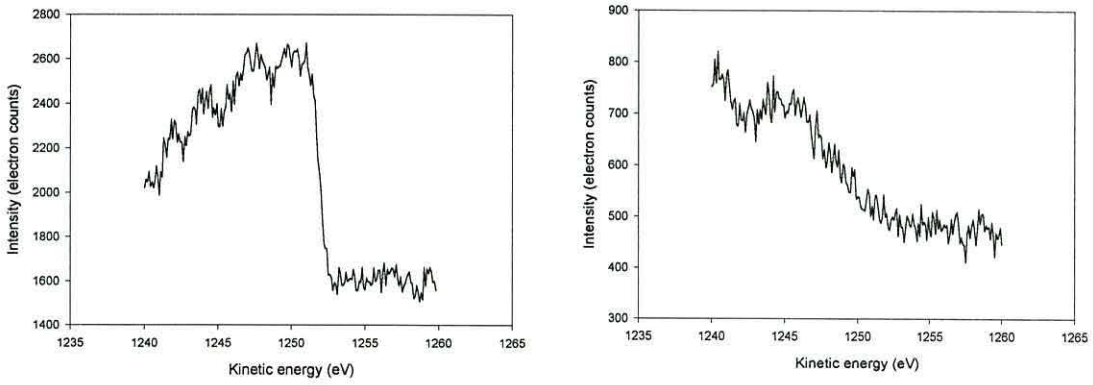

(a) *(b)*

Figure 5.29 *XPS spectra of (a) platinum and (b) PCDM for the calculation of Fermi level and valence band edge energies respectively.*

Using the platinum workfunction of 5.65 eV [168], the valence band edge can then be placed in a band diagram at 5.55 eV (Figure 5.30). As the band gap for PCDM has been previously estimated, using UV-vis measurements, to be 1.38 eV, the conduction band can also be placed in the diagram at 4.17 eV. The workfunctions of the metals used in the diodes for this work can also be found [168], and a range of possible workfunctions (4.2 to 4.75) used for ITO [169]. Values of 4.26, 4.28 and 5.1 eV have been used for silver, aluminium and gold respectively. Also, if the HOMO is unaffected by the substitution of the moiety on the carbon bridge as suggested by Ferraris and Lambert [80] (see section 3.1.3) then the XPS measurement of the valence band energy of PCDM could be equally valid for PBDT. This allows a similar band diagram to be constructed for PBDT using the band gap (1.29 eV) estimated from UV-vis spectroscopy.

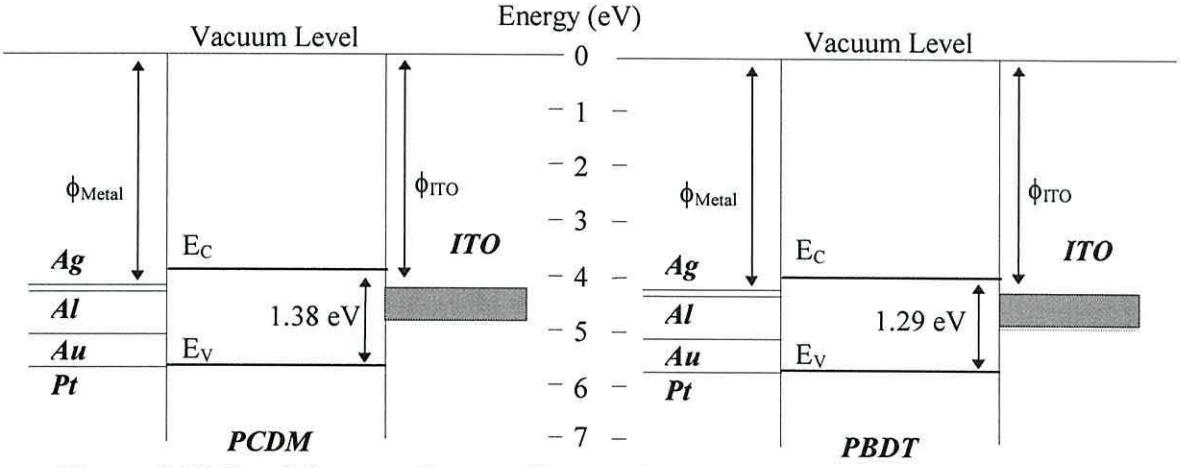

Figure 5.30 *Band diagram for metal/PCDM/ITO and metal/PBDT/ITO diodes constructed using the data for the platinum Fermi level and the PCDM valence band edge, calculated from XPS measurements, and the PCDM and PBDT band gaps, from UV-vis measurements.*

The band diagram suggests that PCDM and PBDT should produce rectifying contacts with the electrodes shown. The position of the conduction and valence bands in the polymers relative to the metal workfunctions allows band bending to occur depending on the position of the Fermi level in the polymer. However, as the XPS measurement only examines the surface of the polymer sample, and as there is the suspected presence of large amounts of adsorbed oxygen, the calculated value for the polymer valence band could be different to that of the bulk polymer. Also, the

sensitivity of the XPS apparatus, approximately 0.9 eV [167], does not allow conclusive positioning of the polymer band edges in the band diagram. However, the results do provide a tentative explanation as to why the polymer should form rectifying contacts with either the cathode or anode electrodes (or both).

5.3.5 Crystal structure

In PCDM it would be expected that a low energy configuration would be adopted with the unit dipoles aligned in a plane. A stabilising π-bond overlap between polymer chains in different layers would also be expected as the polymer units align in a graphite-like arrangement. To investigate this possibility, the crystal structures of the monomer crystal and the polymer film have been investigated using x-ray diffraction and computer modelling packages.

Within the department, CDM monomer has also been used for Langmuir-Blodgett film fabrication for which the dimensions of the CDM monomer unit were required. Using the Cerius 2 computer package, the bond lengths and angles were calculated for the CDM monomer (Figure 5.31). As the monomer is planar, the volume

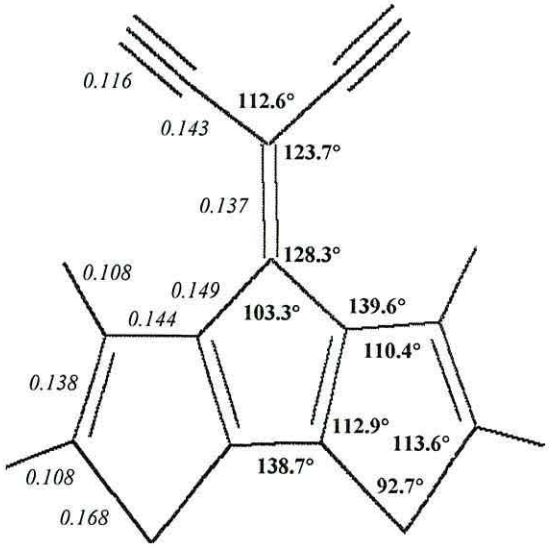

Figure 5.31 *Chemical structure diagram showing bond lengths (nm, italics) and bond angles (°, bold) in a CDM monomer unit as calculated using a computational modelling package.*

of the monomer was approximated using a space filled diagram and the atomic size of the largest atom, sulphur (Table 5.7). The approximate dimensions of the monomer were found to be 1.056 nm and 0.85 nm in the x- (from hydrogen to hydrogen) and y- (from sulphur to nitrogen) directions respectively and the volume calculated to be approximately 2.28 x 10^{-28} m^3 (0.228 nm^3).

Table 5.7 *Atomic sizes of atoms in CDM.*

Atom	Atomic size (nm) [172]
Sulphur (-S-)	0.254
Nitrogen (≡N)	0.216
sp Carbon (-C≡)	0.235
Hydrogen (-H)	0.168
sp^2 Carbon (>C=)	0.235

The crystal structure of CDM monomer was analysed using x-ray diffraction. Unfortunately a similar analysis could not be made on the BDT monomer due to its powdery nature, making it unsuitable for these measurements. The CDM monomer structure was modelled as the lowest energy conformation (Figure 5.32) and the

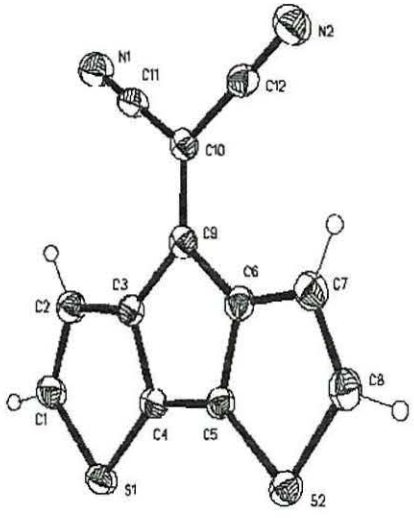

Figure 5.32 *Diagram of the lowest energy conformation of CDM. (Note: π-bonds are not shown)*

packing structure presented so it could be viewed from a number of angles (Figure 5.33). The crystal was found to consist of layers of CDM molecules in a similar arrangement to that found in graphite. From the different views it can be seen that the angles of the unit cell are different, $\alpha \neq \beta \neq \gamma$, and that the dimensions of the cell also differ, oa ≠ ob ≠ oc, suggesting the presence of a triclinic crystal structure. This was confirmed by the lack of symmetry in the cell, indicative of the triclinic system.

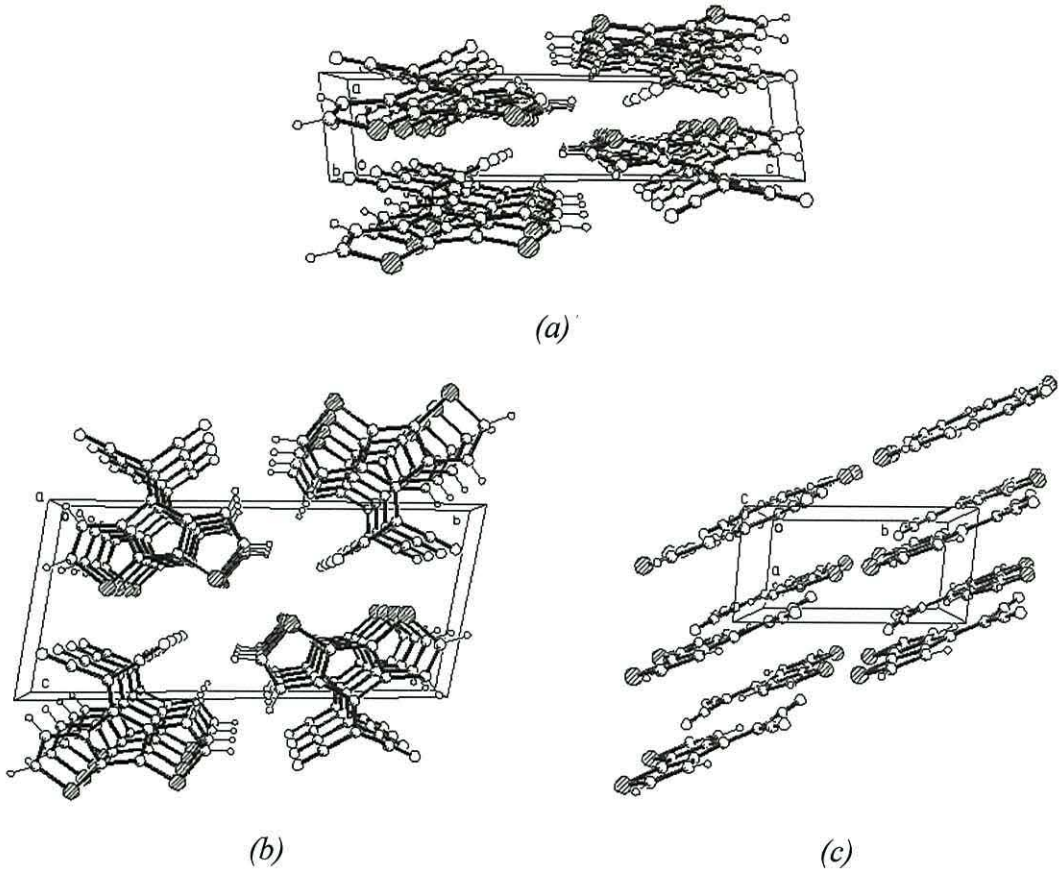

Figure 5.33 *3-D packing diagram of a CDM monomer unit cell viewed perpendicular to the (a) oac plane, (b) obc plane, (c) oab plane.*

Cerius 2 software was used to determine the length of the C_4-C_5 bond (0.144 nm) from which approximate unit cell dimensions were estimated (Table 5.8) The inter-layer distance was also found using these values and basic trigonometry functions to be 0.546 nm which could be compared with that of graphite (0.34 nm [79]).

Although the inter-layer distance for CDM is greater, it does suggest some π-overlap does occur in the CDM monomer, similar to that in graphite, giving rise to the possibility of planar electrical conductivity. The dipole moment of any particular

Table 5.8 *Unit cell dimensions for a CDM monomer unit.*

Dimension	Distance (nm)
oa	0.648
ob	0.816
oc	1.776

molecule can be seen to be aligned parallel with those directly above and below and almost parallel or anti-parallel with those in the same plane (Figure 5.33*(b)*). The parallel alignment of dipoles in the oa direction allows the maximum possible overlap of the π-orbitals in the crystal.

Due to the close positioning of the carbon atoms which would be involved in forming the intermolecular bond during polymerisation, it is possible that a similar configuration can be inferred for the polymer to that shown here for the monomer. The carbon atoms C1 and C8 from figure 5.32, shown in close proximity to each other on neighbouring molecules in the oab plane in figure 5.33*(b)*, are involved in forming the intermolecular C-C bond in PCDM. In the polymer it would again be expected that a low energy configuration would be adopted with the unit dipoles aligned in the obc plane. The stabilising π-bond overlap between polymer chains in different layers would also be reformed although it is more likely that there would be more distance between polymer chains.

In an attempt to confirm this, x-ray diffraction spectroscopy was carried out on a PCDM sample on gold-coated glass and a gold-coated glass blank. Gold-coated glass was preferred over ITO-coated glass to reduce any signal produced by the glass substrate. Figure 5.34 shows the spectrum for the polymer on the substrate. This was identical to that of the blank substrate.

The major signal occurring in both spectra at about 44.5° corresponded to a d-spacing of approximately 2.3 nm. Although the substrate was covered by polymer and gold, the signal produced is thought to be due to the glass substrate. This compares with Quartz (Pure SiO_2) with a d-spacing of approximately 2.4 nm [168]. The lack of features corresponding to the polymer or the gold in the diffraction spectrum was probably due to the sample being too thin (approximately 300 nm) therefore, the irradiating beam passed through it and detected only the glass. Normally, x-ray

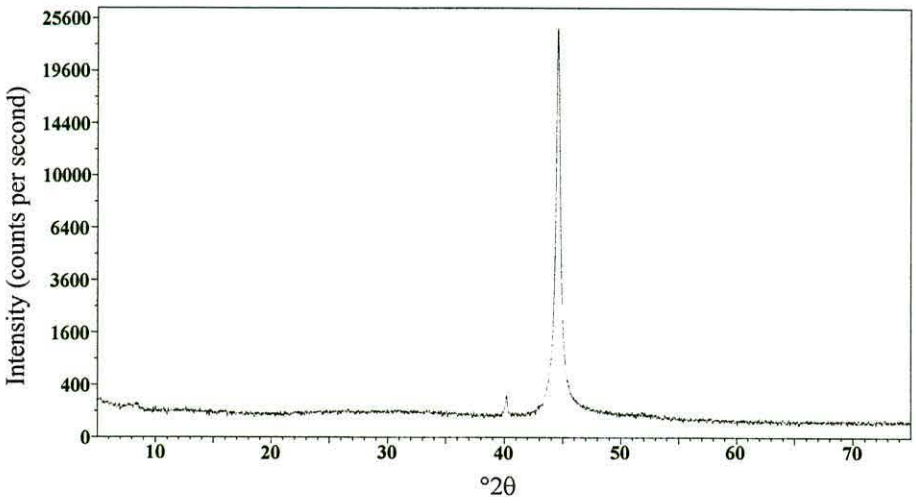

Figure 5.34 *X-ray diffraction spectra of a PCDM film on a gold-coated glass substrate.*

diffraction experiments are performed using this instrument with samples some 2 to 3 mm thick.

5.3.6 Polymer modification

The Raman results in section 5.3.2, allied to the large concentration of oxygen observed in the XPS spectrum (section 5.3.4), suggests the possibility that the monomer becomes oxidised during polymerisation. Oxygen modification at the 4-position of the thiophene rings of PCDM ,**1**, has been suggested by Huang and Pickup [83]. Substitution by oxygen electrophilic attack is shown in scheme 5.1 where the intermediates are stabilised by delocalisation of the charge over a number of monomer units. Huang and Pickup suggest that the substitution is extensive and that it could occur at both 4-positions on the thiophenes of a single monomer unit.

The authors state that the loss of conjugation due to the presence of the carbonyl group in the keto-tautomer reduces the conductivity due to both n- and p-type doping. The presence of the electron-donating alcohol group in the enol-tautomer was also thought to decrease the band gap expected for the PCDM. The authors suggest that overoxidation during the polymerisation of PCDM could also cause the formation of the oxygen-modified polymer, **2**. In this case however, it was thought that the modification would occur at a different position in the polymer structure, possibly at the sulphur in the thiophene ring.

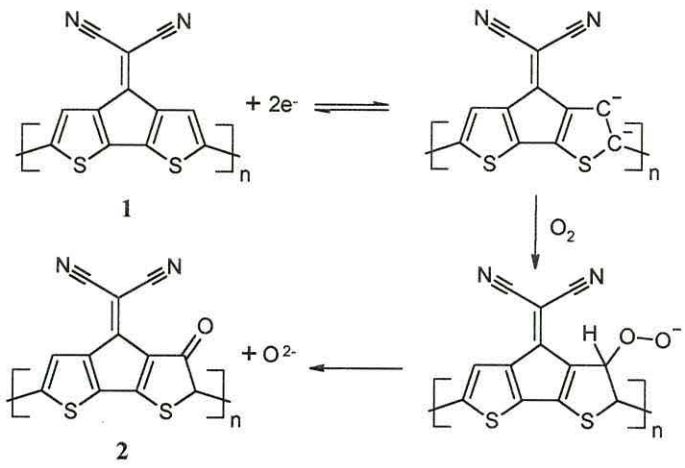

Scheme 5.1 *Electrophilic attack of PCDM, **1**, by oxygen* [81].

The absence of the 1712 cm^{-1} peak, indicative of a C=O group, in the Raman spectrum of the CDM monomer but its subsequent presence in the polymer (Figure 5.18), provides evidence that oxygen modification could be occurring during the polymerisation. The lack of modification in the monomer is confirmed by the presence of peaks due to the proton at the 4-position of the thiophenes in the NMR spectrum (Appendix 1). These would be absent if modification had occurred. The appearance of signals in the FTIR spectrum due to C-C-H and C=O groups, at 2924 cm^{-1} and 1712 cm^{-1} respectively, could also be evidence of oxygen modification in the polymer or equally, they could be due to residual amounts of acetone used to remove excess monomer solution from the polymer surface, after film polymerisation. Figure 5.35(b) shows the Raman spectra of acetone and compares it to PCDM, spectrum (a).

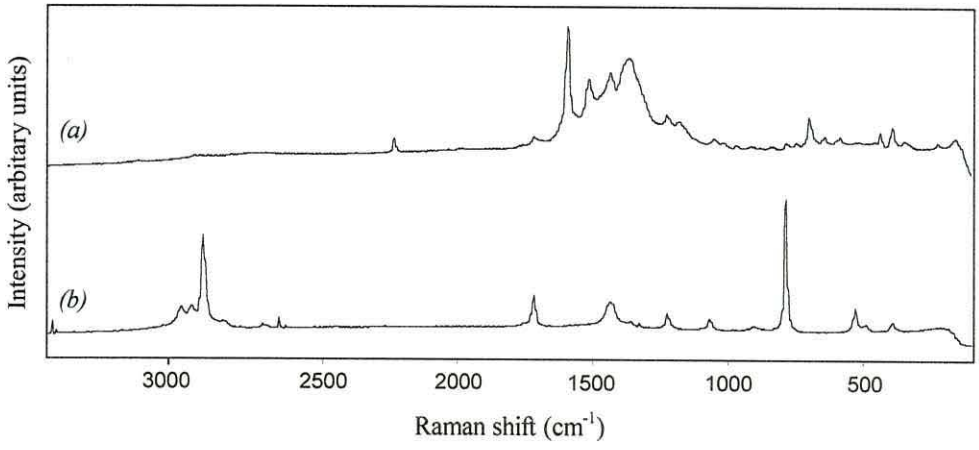

Figure 5.35 *Comparison of the Raman spectra of (a) PCDM and (b) acetone showing the position of the C-O peak at 1710 cm^{-1} in both spectra.*

The C-O peak at 1710 cm^{-1}, due to the ketone moiety on the acetone, is clearly seen in the acetone spectrum and it has the same position as a peak in the PCDM spectrum. The presence of C-H peaks at approximately 2900 cm^{-1} could also explain the C-H peaks in the same region found in the FTIR spectrum of PCDM (Figure 5.13), suggesting that acetone is present when these spectra were recorded.

The comparison of the Raman spectra of the newly polymerised PCDM and the one year old sample, shown in figure 5.17, can be used to determine if acetone is present in the polymer. The one year old sample was stored under a vacuum of approximately 10^{-2} Torr. Over that period of time, any acetone should have been removed from the surface of the polymer by evaporation. However, the 1710 cm^{-1} peak is still present in the spectrum for the old sample. This suggests that the peak is due either to a species, such as acetone, tightly bound in the polymer matrix or to modification of the polymer.

Laser ablation of the polymer surface (see Appendix 3) was found to remove the surface of the polymer, exposing the bulk of the polymer film. Raman analysis of these laser exposed depressions revealed that the Raman spectrum remained similar to that for the pristine polymer (Figure 5.36) but the background fluorescence increases, similar to that for the stored polymer sample. The magnitude of the peak at 1710 cm^{-1} is seen to decrease as the laser exposure time increases. This may be indicative of a decrease in the amount of C-O bond vibration occurring, but similar reductions in the other peaks suggests that the spectrum is being swamped by the presence of the increased fluorescence.

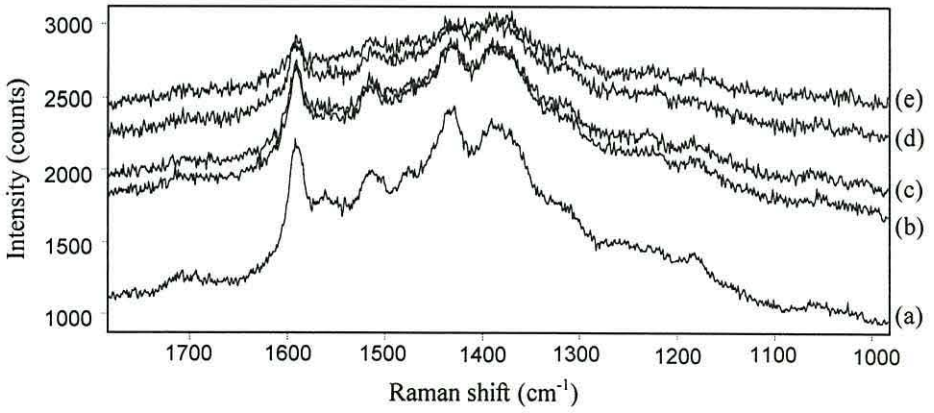

Figure 5.36 *Raman spectra of (a) pristine and (b - e) ablated PCDM surfaces after exposure to the Raman laser for (b) 60, (c) 120, (d) 300 and (e) 600 s.*

Huang and Pickup [82] describe the presence of a peak due to an OH bond vibration at 2759 cm^{-1} in the Raman spectrum which would further confirm the presence of reaction intermediates involving the modified polymer. The authors suggest that the appearance of this peak at lower Raman shift values is due to hydrogen bonding of the enol -OH groups with neighbouring -CN groups, which also leads to a splitting of the peak due to the -CN group.

However, infrared correlation charts [168] normally place the OH stretching vibration at 3000 to 3650 cm^{-1} which is a broad, weak signal in Raman spectroscopy and a broad, strong signal in infrared spectroscopy. In the present work, figure 5.18 shows that no peaks were seen in this spectral region for either type of spectroscopy. Huang and Pickup describe how they used an ITO substrate onto which the polymer was deposited and which was consequently analysed using Raman spectroscopy. Figure 5.13 shows that ITO has a maximum fluorescent intensity at approximately 2700 cm^{-1}. This suggests that the broad peak seen by Huang and Pickup in this area could be due to the substrate and not an OH moiety.

The possibility of hydrolysis of the nitrile moiety on the CDM monomer over time by exposure to atmospheric moisture has also been considered. To this end, both acid and base (Scheme 5.2) catalysed hydrolyses of the monomer were investigated. The given scheme [171] is for aliphatic nitriles but it is possible that the aromatic nature of the CDM may make it more susceptible to hydrolysis. The aromatic system could stabilise the reaction intermediates facilitating the course of the reactions shown.

However, the conditions required for the mechanisms shown are severe (concentrated acid/base and approximately 200 °C) and unlikely to occur under normal atmospheric conditions. If these mechanisms did occur, the appearance of an N-H peak, due to the intermediate amide (R-CO-NH_2), and an O-H peak, due to the final acid product (R-COOH), would be visible in the Raman spectra for PCDM (Figure 5.16). Since no such features have been found in the Raman spectra taken at different times it can be assumed with a high degree of certainty that hydrolysis of the cyano groups on the CDM did not occur.

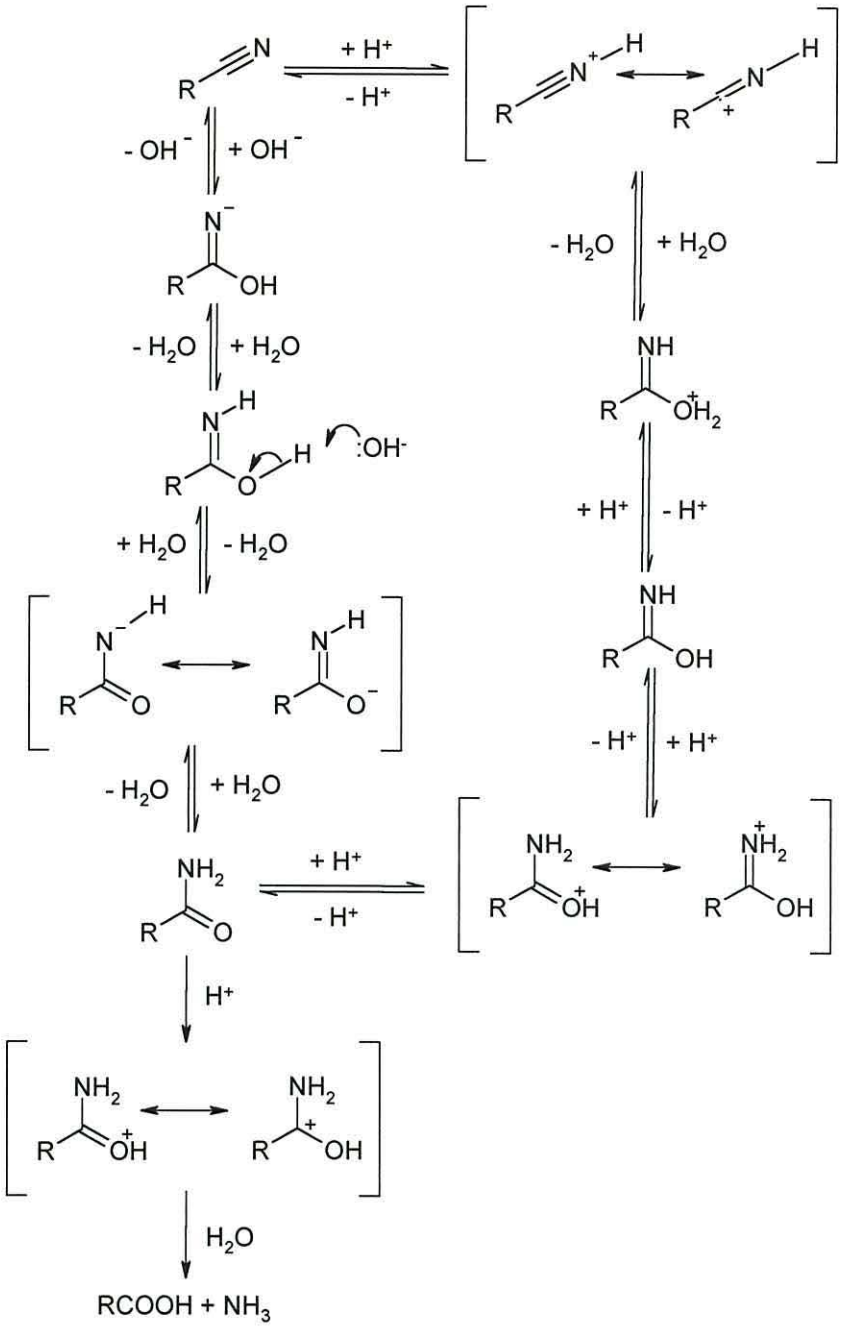

Scheme 5.2 *Acid and base catalysed, aliphatic nitrile hydrolysis* [171].

5.4 Summary

Chromium removal from gold-coated glass slides has been confirmed using EDAX analysis and was thought to cause a loss of adherence of the gold electrode from the glass substrate. The subsequent formation of a red compound upon polymerisation has suggested that the chromium is removed into solution causing contamination of the

final polymer film. To overcome this problem, ITO substrates were used for subsequent polymer film growth.

Microscopic analysis of the substrate and polymer morphologies has been carried out using AFM and SEM microscopy. The P3MeT and PCDM films were found to be pin-hole free but with different morphologies, the PCDM having a discernible number of protuberances. The substrates used all have RMS roughnesses less than 10 nm. The P3MeT and PCDM are generally smooth with similar RMS roughnesses for a 500 x 500 nm sample area. However, on a larger scale (10 x 10 μm) the PCDM is seen to have more aggregations on the surface of which may affect later electrical measurements. Sectional analysis shows that both polymers are approximately 200 to 300 nm thick, and the thickness and the roughness of each is dependent on the growing conditions. The PBDT sample was difficult to image by AFM owing to its very significant roughness, a fact confirmed by scanning electron microscopy, which showed that the film consisted of aggregations approximately 1 μm across. The image of the PBDT film also revealed evidence of hole formation, which again could be due to the speed at which the polymer grows.

The results of a spectroscopic analysis of the polymers and monomers used here has been reported. FTIR and Raman spectroscopy was used to confirm the polymerisation of the monomers and to check the chemical structures of both the monomers and the polymers. The appearance of broad peaks at approximately 1500 cm^{-1} in both the Raman and FTIR spectra for PCDM and in the Raman spectra for PBDT are indicative of polymerisation. These peaks, not seen in the monomer spectra, are due to coupling of C-C and C=C bonds in the polymer chain. The PCDM and PBDT spectra are seen to be similar in this spectral region.

One year old samples of CDM crystals and PCDM films show no spectral changes apart from an increase in fluorescence which is due to the monomer crystal and the polymer film becoming more amorphous over time. Mapping of the fluorescence seen in the Raman spectrum of a PCDM sample has been used to assess the uniformity of the polymer film. No differences are seen in the spectrum of the polymer in different areas but mapping of the fluorescence at 2000 cm^{-1} revealed a central region of almost constant fluorescence and higher fluorescence levels at the substrate edges and the position of the meniscus of the monomer solution during

polymerisation. The fluorescence was assumed to reflect the local film thickness, and hence the current density present in these areas during polymerisation, a fact supported by checking the thickness of two polymer samples using AFM. The fluorescent intensity for a 140 nm thick sample was in the range 6000 - 9000 counts while that for a 190 nm sample was in the range 9000 - 12000 counts.

XPS revealed the presence of a large amount of oxygen in PCDM, as well as two forms each of carbon, nitrogen and sulphur. The two forms of carbon are explained by the presence of hybrid sp^2 and sp^3 carbon atoms in the polymer. The presence of two forms of sulphur and nitrogen have been investigated with respect to the possibility of oxidation to NO_2 and SO_2. This could also explain the high concentration of oxygen. However, the absence of peaks due to these species in the Raman and FTIR spectra have ruled out this suggestion. It is thought that the extra forms of the nitrogen and sulphur could be due to electronic or structural differences in the polymer rather than chemical differences, such as the presence of aromatic and quinoid species, or in the case of nitrogen, detection of atmospheric nitrogen..

The possibility of oxygen modification of the carbon in the thiophene rings has also been investigated due to the presence of C-O and -C-H groups in the Raman spectra which would not be expected in the polymer. The lack of extra forms of carbon in the XPS spectra suggest that this had not occurred and the appearance of these peaks was thought to be due to the presence of residual acetone, used to wash the polymer films, tightly bound in the polymer matrix. The presence of a peak in the Raman spectrum of PCDM at 2700 cm^{-1}, reported by Huang and Pickup as being due to the presence of an OH moiety, was thought to arise from the ITO substrate due to the lack of a similar, strong OH peak expected in the FTIR spectrum. Therefore, it is unlikely that the PCDM used here is oxygen modified and that the large amount of atmospheric oxygen present on the surface of the sample, seen in the XPS spectrum, is due to adsorbed oxygen. Further, modification by hydrolysis of the nitrile moiety on the polymer was investigated but it was found that this process would require very forceful conditions. Indeed, the lack of product peaks in the Raman spectra suggested that this was also unlikely to be occurring.

Comparison of the PCDM Raman spectra with that of acetone, which is used to wash the polymer post-polymerisation, suggests that the extra peaks due to C-H and C-

O moieties could be due to residual amounts of the solvent. However, the presence of these peaks in the Raman spectrum of a sample stored under vacuum for one year suggests that the peaks may not be due to the acetone, which should have evaporated over this time. Unless the acetone is tightly bound in the polymer matrix, this suggests that the polymer could contain other contaminants.

XPS experiments to calculate the valence band edge in PCDM have also been used, in conjunction with the band gap estimated from UV-visible spectra, to produce a preliminary band diagram for the metal/PCDM/ITO diodes used later for electrical characterisation of the polymer. The band diagram places the PCDM band-gap in the same general energy region as the electrodes used to make the diodes and therefore suggests that the polymer should form rectifying contacts with either the cathode or anode materials. Unfortunately, due to the sensitivity of the XPS apparatus and the fact that the measurement is on the surface of the polymer and not the bulk, the positioning of the polymer bands may be erroneous. However, it does suggest that the diodes produced should show some rectification.

UV-visible spectra for PCDM and PBDT are seen to be similar, with absorption bands due to the molecular π-π^* transitions and the polymer π-π^* transition, arising from the similar aromatic conformations of the polymers. Comparison of the UV-vis spectra with that reported by Ferarris and Lambert confirms the presence of a polymer π-π^* transition at long wavelengths. From this transition, the band-gaps of PCDM and PBDT were found to be 1.38 eV and 1.29 eV respectively which are lower than the corresponding values determined theoretically for monomers and dimers. The higher than expected band-gap values were found to be due to measurement convention. Here, the band-gap energy was taken as the peak maximum of the polymer π-π^* transition due to limitations on the upper measurement range of the wavelength. In the work by Ferraris and Lambert, the low energy edge of the transition was used leading to a lower band gap value.

Crystals of CDM monomer were determined, by XRD spectroscopy, to be triclinic, with the monomer units layered in a similar way to graphite where the possibility of π-orbital overlap exists between units in adjacent layers. The volume of an individual monomer unit, in its lowest energy conformation as described using a computational molecular modelling package, was shown to be $\sim 2.28 \times 10^{-28}$ m^3.

Unfortunately, XRD analysis of a PCDM film was unsuccessful due to the polymer film being too thin.

6. Results and discussion: Electrical characterisation

In this chapter are presented the results of the AC and DC electrical characterisation of PCDM films for different experimental conditions. Preliminary DC characteristics for PBDT diodes are also presented.

6.1 Admittance measurements

The AC admittance plot (Figure 6.1) for a PCDM diode device shows a clear dispersion centred at about 100 Hz. In earlier studies [19] of poly(3-methylthiophene) diodes, such a dispersion was shown to arise from the formation of a rectifying contact at the junction between the aluminium contact and the electrodeposited film. The data in figure 6.1 also provides evidence for a second, much smaller dispersion at approximately 1 MHz (see inset diagram). Capacitance and loss (G/ω) curves obtained for temperatures increasing from room temperature to 80 °C were found to be identical to curves obtained when cooling the device to room temperature (Figure 6.2).

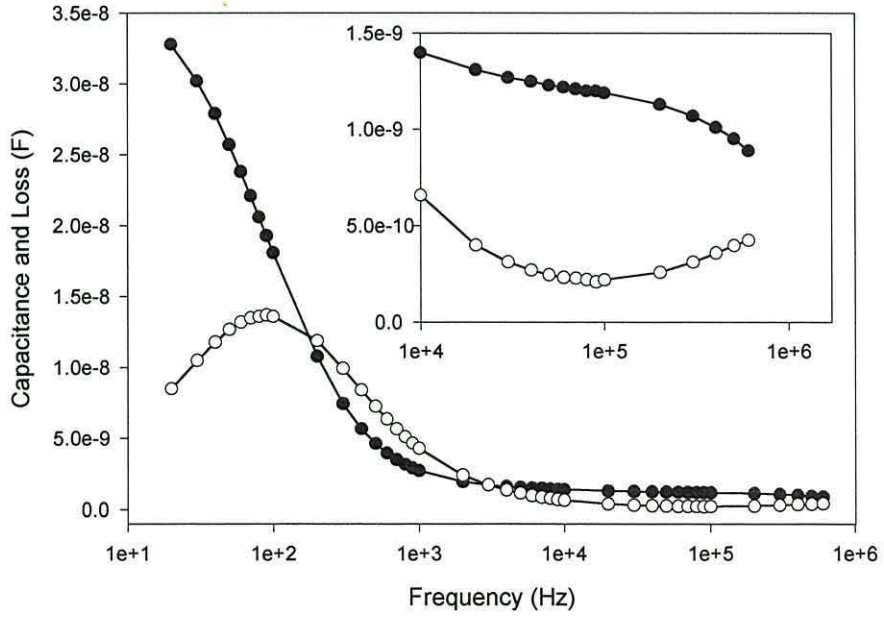

Figure 6.1 *Frequency dependence of the capacitance (●) and loss (G/ω) (○) of an ITO/polymer/Al diode at room temperature revealing the presence of two dispersions, one at ~ 100 Hz the other at ~ 1 MHz (see inset).*

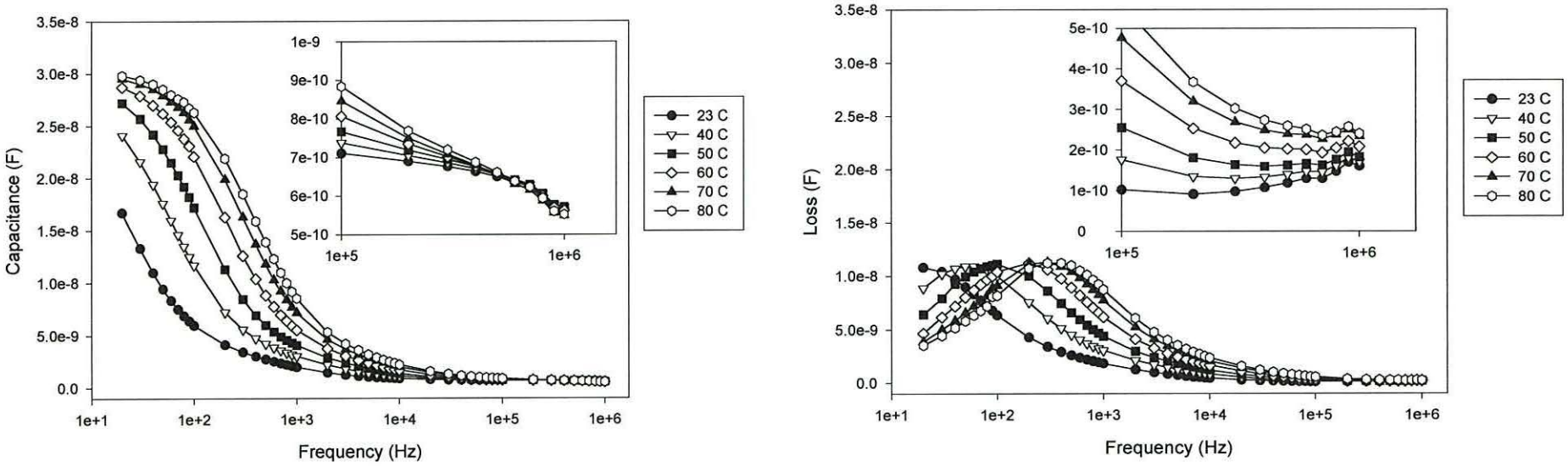

Figure 6.2 *Effect of temperature on (a) the capacitance and (b) the loss (G / ω) of an ITO/polymer/Al diode.*

Figure 6.3 shows the capacitance and loss curves obtained from films of three different thickness' produced on the same ITO substrate. As the film thickness increased (longer growing time), the main differences observed experimentally were (i) an apparent shift of the low-frequency dispersion to lower frequencies, (ii) a reduction in the frequency-independent capacitance in the mid-frequency range and (iii) a shift of the high frequency dispersion to higher frequencies.

If the low-frequency dispersion in figures 6.1 and 6.2 does arise from the presence of a depletion region at one or other of the contacts, then confirmation for this may be obtained by measuring the admittance as a function of applied voltage. In figure 6.4 it is seen that, except for a small range from 0 to -1 V, the effect of increasing the magnitude of the applied bias is to reduce the capacitance and increase the loss of the diodes at low-frequency. This is seen more clearly in figure 6.5(a) where the capacitances at 20 Hz in figure 6.4 are replotted directly as a function of applied bias. In a separate experiment, the bias dependence of the capacitance was also measured at a fixed frequency of 100 Hz. The results, figure 6.5(b), follow a similar trend to those in figure 6.5(a) but with lower capacitances because the measurement frequency was higher than the relaxation frequency of the dispersion.

The admittance data may be modelled using the model for the Schottky diode described in section 2.2.4. Values for the components of the equivalent circuit in Figure 2.12 may be determined by plotting the data in the complex plane, the so-called Cole-Cole plot [172]. The data from figure 6.2 is replotted in this form in figure 6.6 from which it is readily seen that the main dispersion follows a semicircle whose centre lies slightly below the horizontal axis. This suggests that the dispersion is slightly broader than predicted by a single relaxation time which is not unexpected in the present diodes. Local variations in film thickness (see AFM images, Figure 5.7) will lead to local variations in R_b the bulk resistance of the film.

From the inset diagram in figure 6.6 it is seen that at high frequencies the main dispersion asymptotes to a capacitance of $\sim 7 \times 10^{-10}$ F before the curve rises again as the high frequency dispersion manifests itself. This capacitance, which represents the high frequency limit of equation 2.8, corresponds to the bulk capacitance, C_b, of the diode. Thus, with $C_b = 7 \times 10^{-10}$ F, a film thickness of 220 nm and a sample area of 2.5 mm^2, the relative permittivity, ε, of the polymer is estimated to be ~7, a value typical for

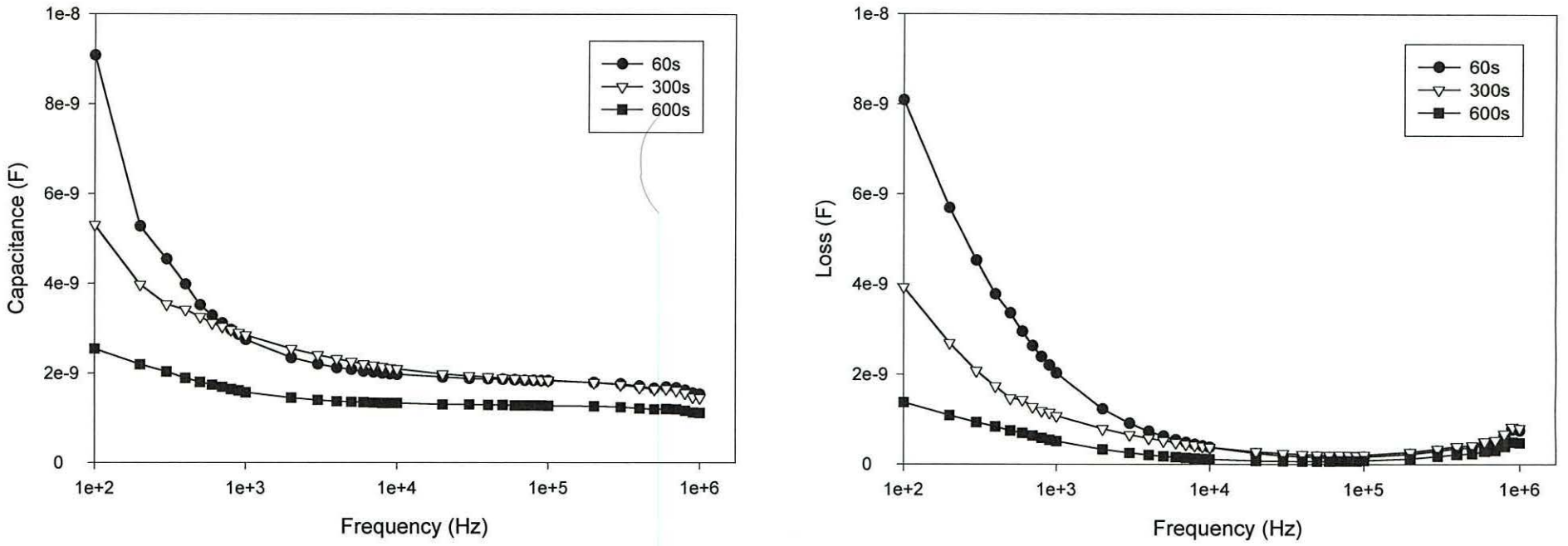

(a) *(b)*

Figure 6.3 *(a) Capacitance and (b) loss (G / ω) curves showing the effect of increasing the film thickness by increasing the film growing time.*

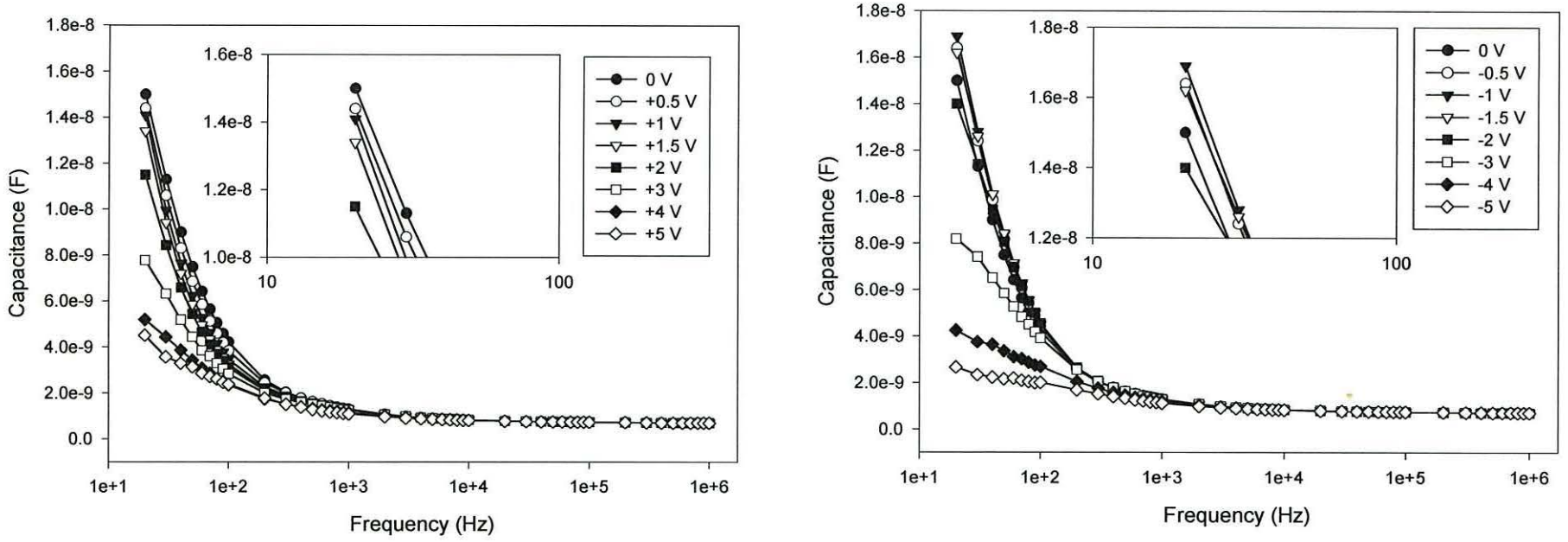

(a) *(b)*

Figure 6.4(a) *Room temperature capacitance curves for (a) positive and (b) negative voltages applied to the ITO substrate.*

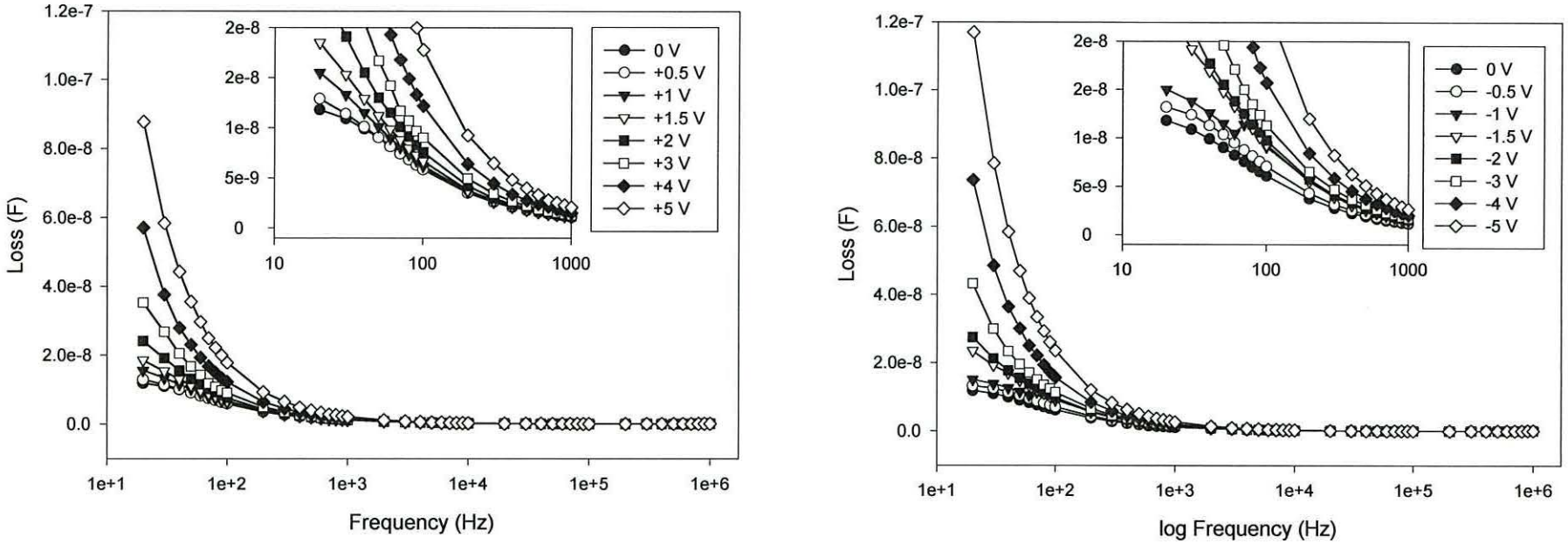

Figure 6.4(b) *Room temperature loss (G / ω) curves for (a) positive and (b) negative voltages applied to the ITO substrate.*

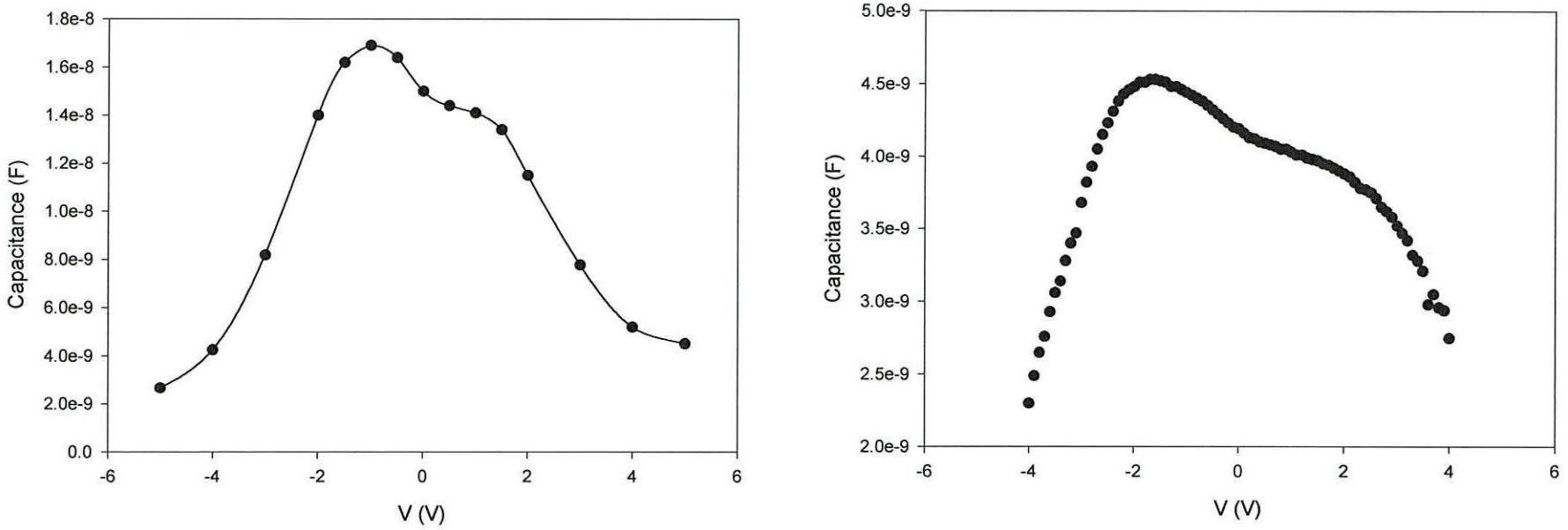

(a) *(b)*

Figure 6.5 *Capacitance-voltage (C-V) curves obtained at room temperature (a) by replotting the 20 Hz data from figure 8 and (b) by direct measurement using a 100 Hz signal.*

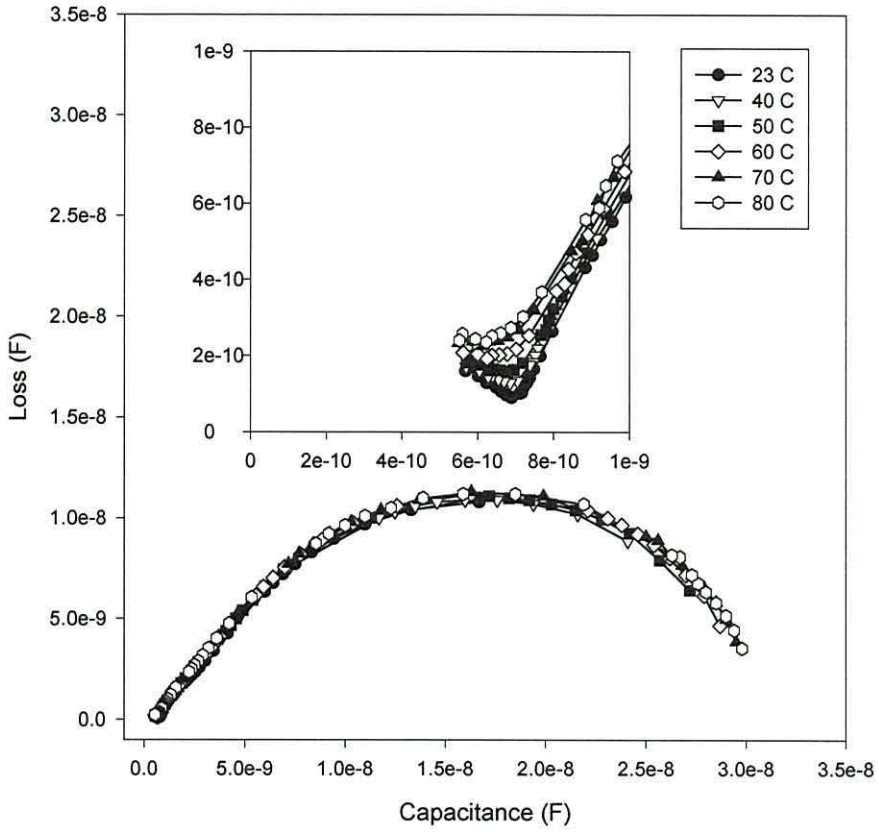

Figure 6.6 *The data presented in figure 6.2 replotted in the complex admittance plane (Cole-Cole plot). The onset of the high frequency dispersion is clearly seen in the inset diagram.*

conjugated polymers e.g. for PMeT $\varepsilon \sim 5$ [19].

The capacitance, C_d, of the depletion region may be deduced from figure 6.6 by extrapolating the low frequency data to the horizontal axis. Thus, $C_d \sim 3.2 \times 10^{-8}$ F and is independent of temperature between 23 °C and 80 °C. In this range, therefore, it may be deduced that all dopant species in the depletion region are ionised. Furthermore, assuming that the relative permittivity of the polymer estimated above applies, the width of the depletion layer is calculated to be ~ 5 nm.

To obtain values for the resistive elements of the equivalent circuit it is necessary to calculate the corresponding impedances by replotting the data in the complex impedance plane using the equations in appendix 2. In figure 6.7, the high-frequency dispersion asymptotes to a temperature-independent series resistance of ~400 Ω.

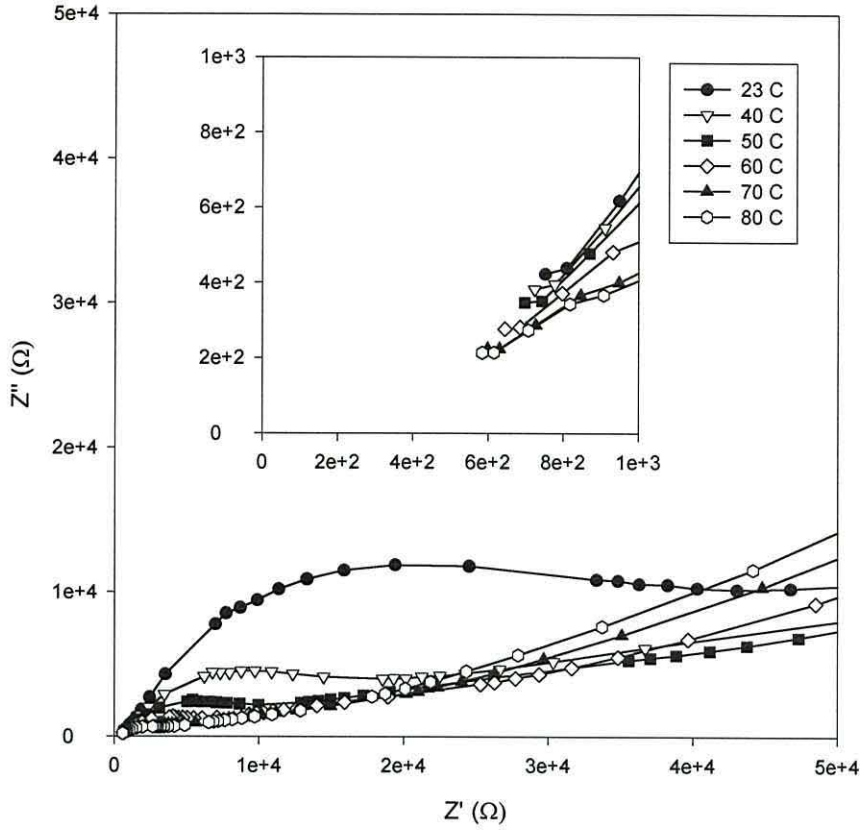

Figure 6.7 *The data of figure 6.2 replotted in the complex impedance plane to enable R_S and R_b to be estimated.*

As the device temperature increases from room temperature to 80°C the bulk resistance, R_b, (estimated by extrapolating the semicircular dispersion to the Z' axis) is seen to decrease by about an order of magnitude from ~ 45 KΩ to ~ 4 KΩ, corresponding to an activation energy of ~ 0.36 eV for the ac conductivity of the bulk polymer.

From equation 2.11 it is readily deduced that when $R_d >> R_b$ and $C_d >> C_b$, then $\tau_{LF} \sim R_b C_d$ and since C_d was temperature independent (figure 6.6) then any temperature variation of τ must arise from R_b. Figure 6.8 is an Arrhenius plot of the frequency ν_m ($= 1/2\pi\tau_{LF}$) at which the loss reaches a maximum. The linear slope yields an activation energy of 0.45 eV which is in reasonable agreement with the initial estimate from the complex impedance plots but significantly greater than the value of 0.25 eV observed in poly(3-methylthiophene) [19].

Interestingly, from the UV-visible absorption spectrum (Figure 5.29), the band-

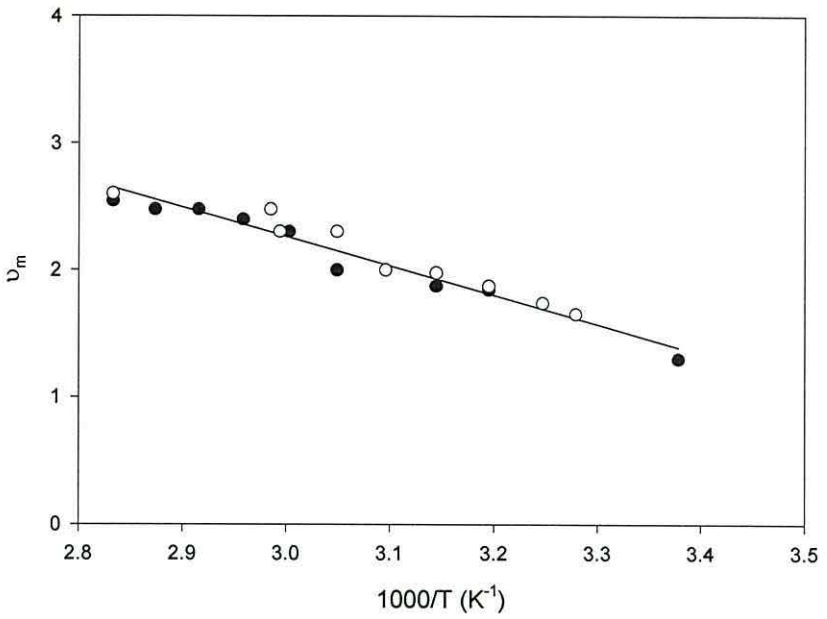

Figure 6.8 *Arrhenius plot of the frequency, v_m, at which the loss reaches a maximum for increasing (●) and decreasing (○) temperatures.*

gap of the undoped PCDM polymer investigated here is estimated to be ~ 1.4 eV. Therefore, the activation energy for ac transport in the bulk polymer is likely to be associated with the hopping mobility of the charge carriers.

The model presented in figure 2.12 readily explains the results presented in figure 6.3. As film thickness increases, then the bulk capacitance, C_b, is expected to decrease hence decreasing the time constant, $\tau_{HF} \sim C_bR_S$, of the high frequency dispersion. Furthermore, an increase in film thickness is expected to increase the bulk resistance, R_b, and hence increase the time constant, $\tau_{LF} \sim C_dR_b$, of the low frequency dispersion.

The effect of temperature was also investigated for diodes incorporating gold and silver top electrodes for comparison with those prepared using aluminium. Figure 6.9 shows that both the diodes incorporating gold and silver are characterised by a large DC loss. The high capacitance and loss values, of approximately 10^{-7} and 10^{-4} F respectively, swamp any signal from a possible depletion layer in the devices which would be expected to occur at similar values to those in figure 6.1 for aluminium-based diodes, i.e. $2x10^{-8}$ F. It is possible that the gold and silver used in these diodes form microfilaments through the polymer film and contact the ITO substrate causing the polymer film to be short circuited.

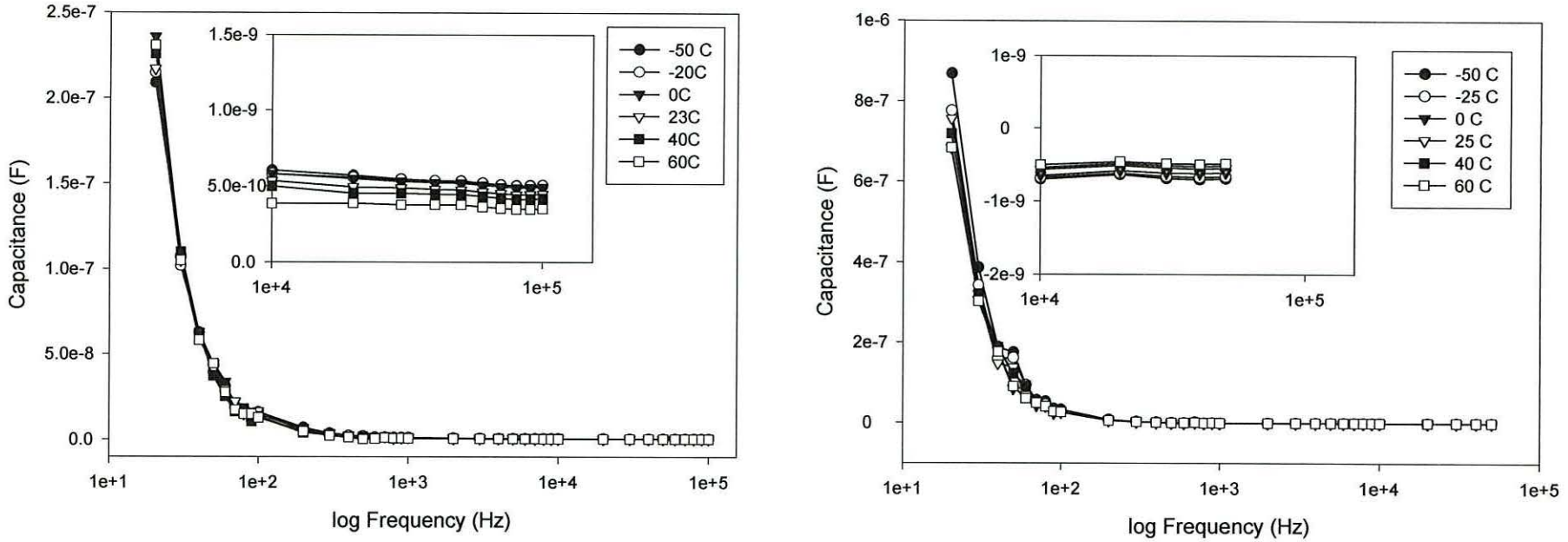

(a) *(b)*

Figure 6.9(a) *Effect of temperature on the capacitance of (a) an ITO/PCDM/Au diode and (b) an ITO/PCDM/Ag diode.*

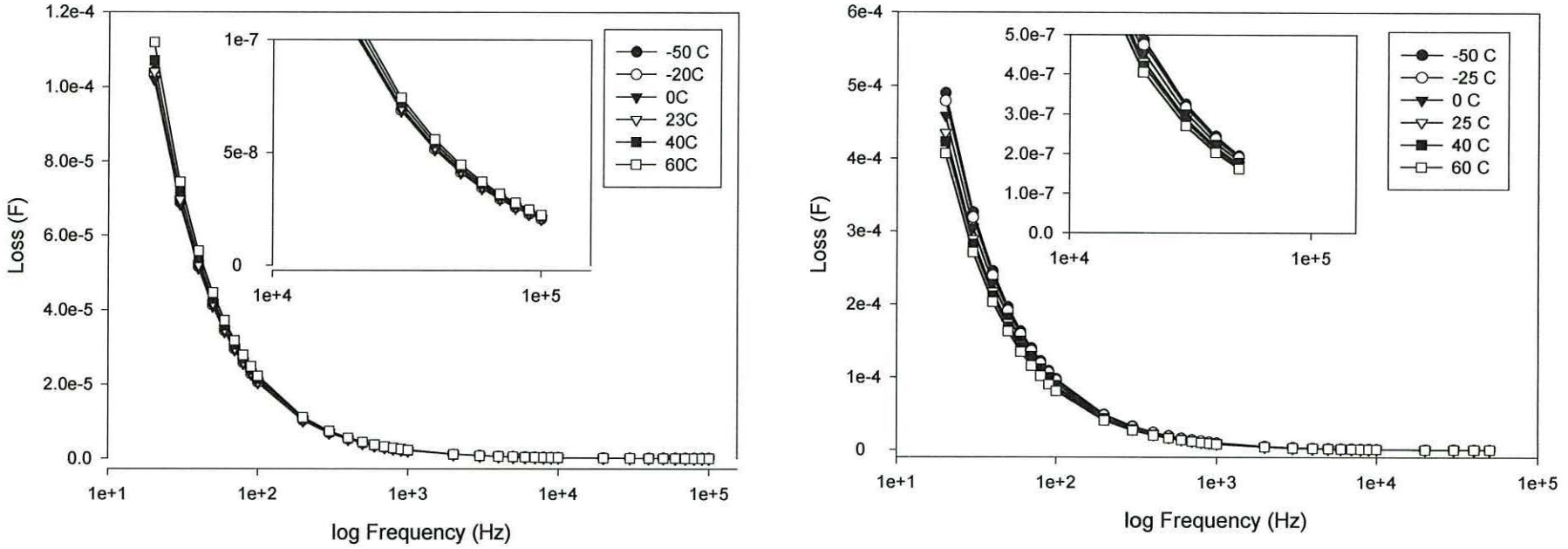

Figure 6.9(b) *Effect of temperature on the capacitance of (a) an ITO/PCDM/Au diode and (b) an ITO/PCDM/Ag diode.*

6.2 DC characteristics

6.2.1 Capacitance-voltage characteristics

Assuming the polymer is p-type, the observed dependence of the capacitance, C_d, on applied voltage in the range ±2 V, (Figure 6.5) suggests the presence of a depletion region at the polymer-ITO junction rather than at the polymer-Al junction. In principle, replotting this data as C_d^{-2} versus V should enable both the doping density and the height of the potential barrier at the junction to be determined [173]. However, the measured capacitances, even in this limited range around 0 V are unlikely to reflect correctly the actual change in depletion capacitance with applied bias as expected due to the following reasons.

Firstly, the rapid fall-off in capacitance above ±2 V, caused by the reduction in the depletion resistance, R_d, as the magnitude of the applied voltage increases, is likely also to manifest itself at the lower applied voltages. This is confirmed in figure 6.10 where the data of figure 6.4 is replotted in the complex plane (Cole-Cole plot). As can be seen, above about ±1 V the Debye-like behaviour is completely swamped making it impossible to obtain accurate estimates of C_d. For forward (negative) bias across the junction R_d is expected to decrease owing to a reduction in the depletion region width. In reverse (positive) bias the electric field at the ITO-polymer interface will increase as the depletion region expands. This will reduce R_d either through a field-enhanced carrier generation rate in the depletion region or through increased field-assisted thermal emission over the potential barrier at the junction. Equation 2.9 shows that when R_d becomes small, the capacitance measured at low frequency is reduced and for sufficiently small values of R_d ($<< 1/\omega C_d$) will tend towards C_b the bulk capacitance of the diode. The change in slope of the C-V plot (Figure 6.5) around 0 V probably reflects the different mechanisms controlling R_d in forward and reverse bias.

Secondly, in no device were we able to obtain capacitance measurements at a sufficiently low frequency (ideally at least an order of magnitude below the relaxation frequency of the device [19]) to prevent the effects of the low-frequency dispersion from interfering with the true measurement of C_d. In an effort to overcome this problem, measurements were carried out at 60 °C (Figure 6.11) with the expectation

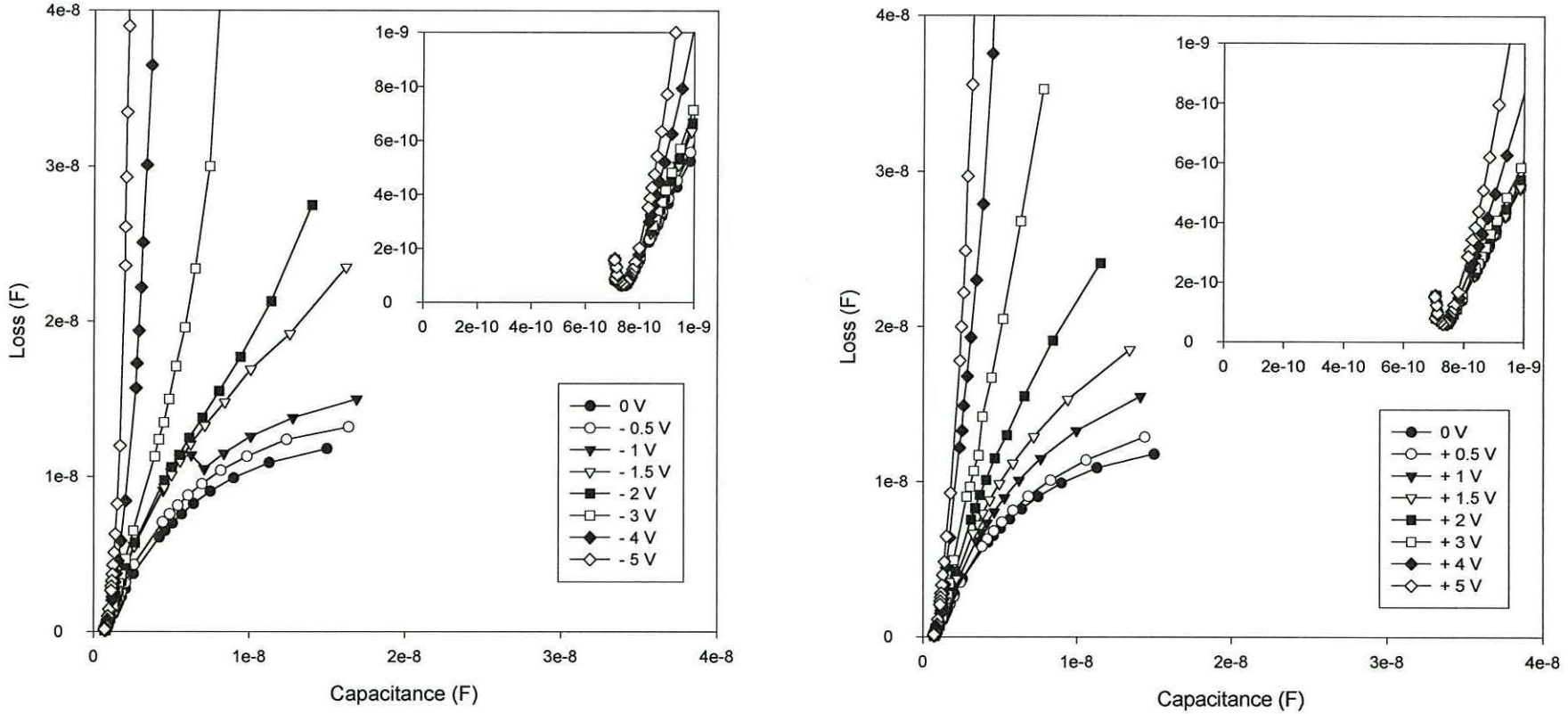

Figure 6.10 *Room temperature Cole-Cole plots showing the effect of applying (a) positive and (b) negative bias to the ITO electrode.*

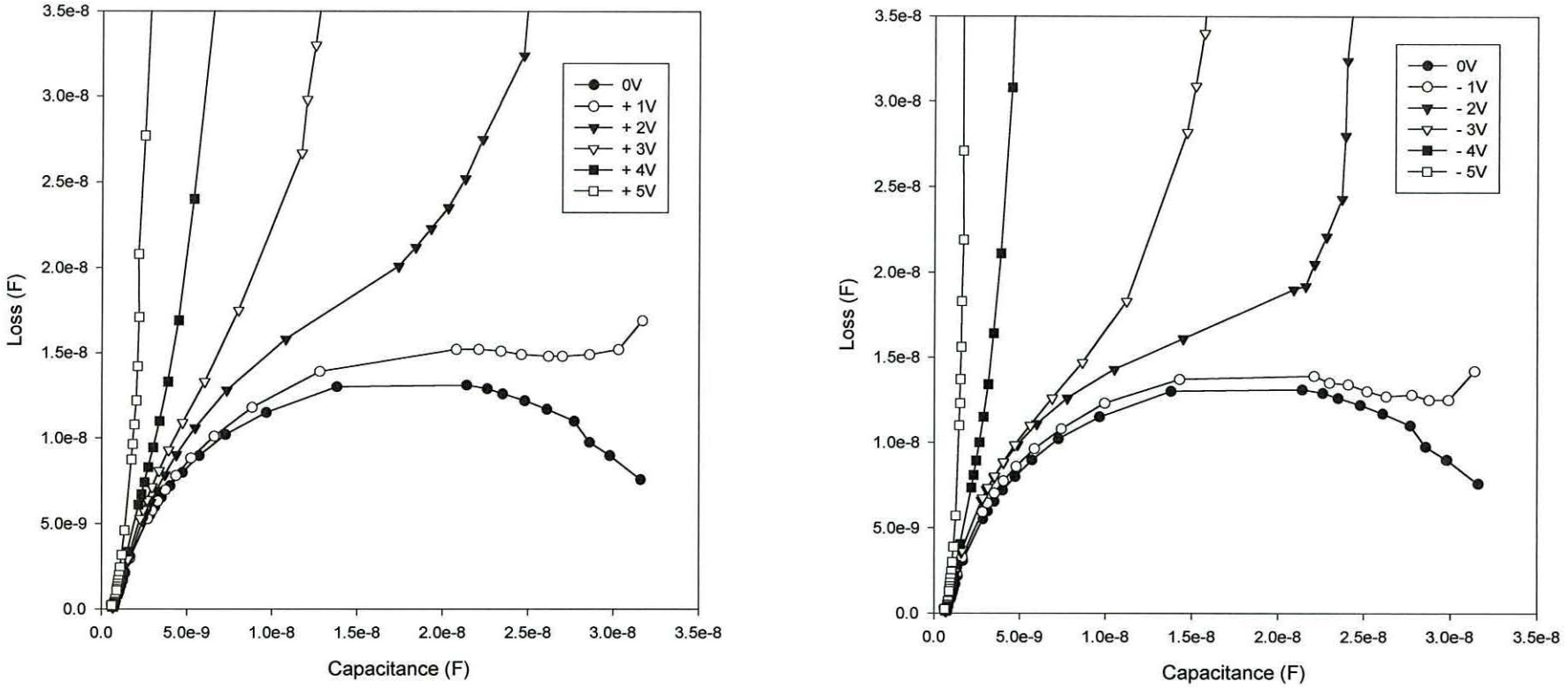

Figure 6.11 *Cole-Cole plot showing the effect of (a) positive and (b) negative applied voltages at 60°C.*

that the increase in the relaxation frequency of the low-frequency dispersion (see Figure 6.2) would more than counteract the effects of a reduction in R_d. While this approach certainly allows more of the dispersion to be observed the conductive losses in the device still dominate.

6.2.2 Current-voltage characteristics: Results

Since aluminium makes a rectifying contact to many conjugated polymers including thiophene-based polymers [139], the DC characteristics of the present diodes were expected to show some rectification, especially in view of the low frequency dispersion present in the AC admittance measurements and the band diagram derived from XPS measurements. A plot of current versus voltage, figure 6.12, shows that this is clearly not the case. Weak rectification is apparently present for applied voltages less than ~0.5 V otherwise the characteristics are almost identical for both polarities.

A closer look at the currents in the range ±0.5 V (Figure 6.13) reveals the presence of a displacement current which is greater when scanning from +5 V to -5 V than when scanning in the opposite direction.

To correct for the displacement current in the -5 V to +5 V scan, the current value at 0 V, 1.43×10^{-11} A, was subtracted from all the current values. For the +5 V to -5 V scan the 0 V value, 4.44×10^{-11} A, was added to all the current values. This had the effect of lowering the current values at low voltages for the -5 V to +5 V scan and raising the currents in the opposite scan direction. The difference in the displacement currents for either scan direction suggests a change in the interface capacitance, possibly due to a small amount of drift by the dopant ions. Figure 6.14 shows the data for the ±5 V scans from figure 6.12 replotted with the displacement current removed.

The DC characteristics are also replotted to investigate the possible conduction mechanisms described in section 2.2.5 occurring in the ITO/PCDM/Al diode. Assuming that the models fit the data a number of parameters, such as relative permittivity, can be deduced. Figure 6.14 tests for the feasibility of a space-charge-limited current mechanism (equation 2.28). A plot $\ln(J/E^2)$ versus E^{-1} (Equation 2.26, Figure 6.15) tests for the possibility of Fowler-Nordheim field emission tunnelling theory. From these plots, the barrier heights at the electrode/polymer interface can be

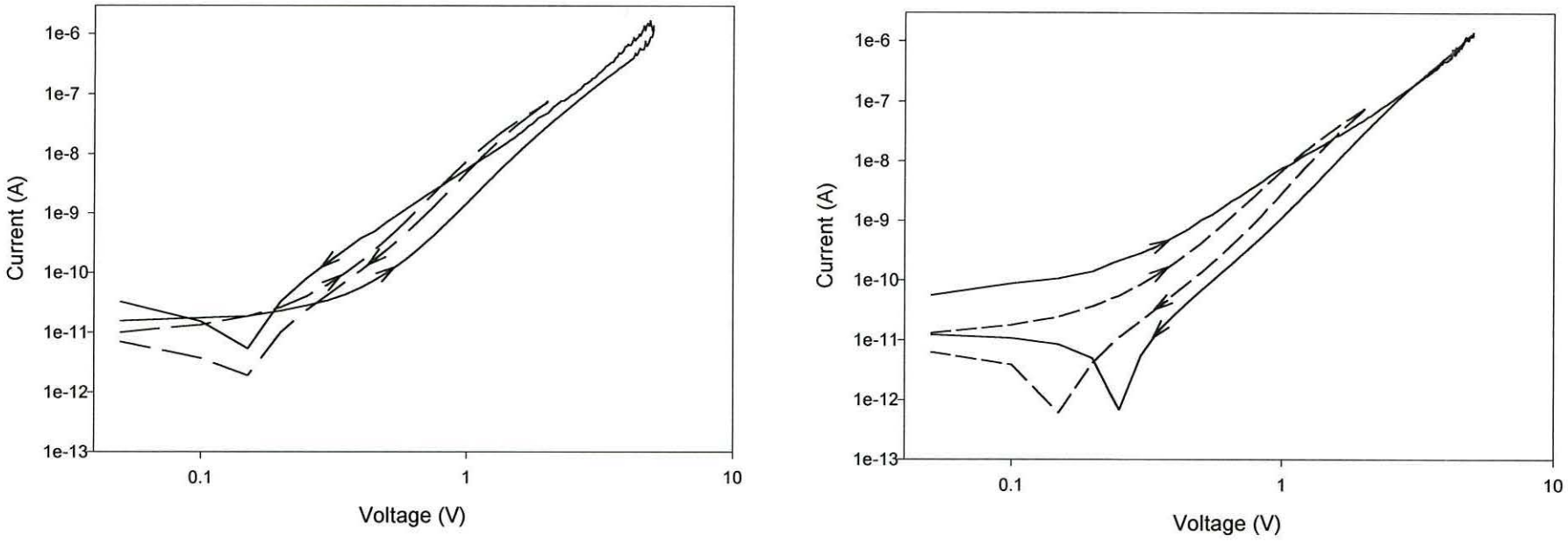

Figure 6.12 *Current-voltage (I-V) characteristics of an ITO/polymer/Al diode with (a) positive and (b) negative voltages applied to the ITO substrate. The characteristics were obtained by ramping the voltage through the ranges ±5 V or ±2 V. The directions of the voltage sweeps are indicated by the arrows. Sweep rate = 0.1 V per minute.*

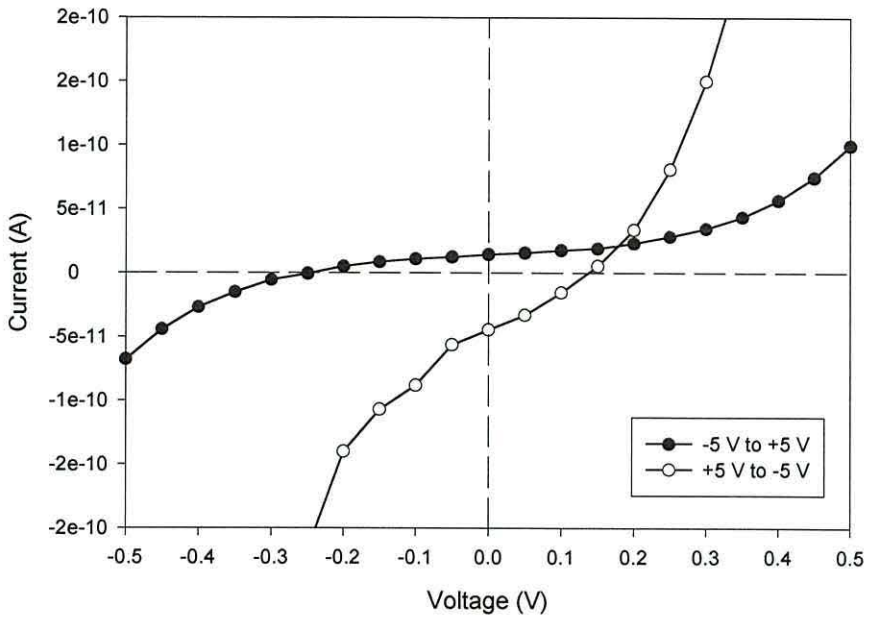

Figure 6.13 *The data in figure 3.12 replotted to show the displacement current at 0 V.*

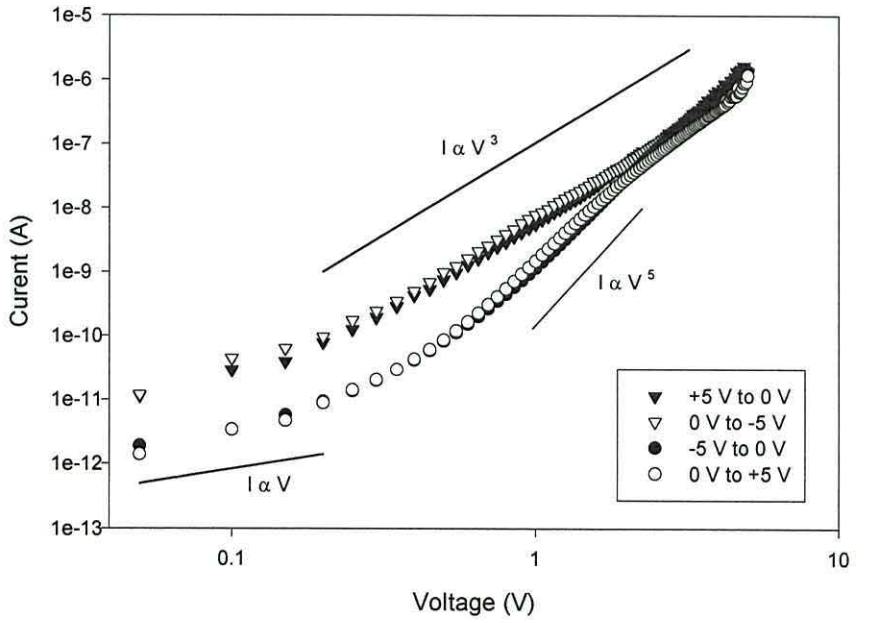

Figure 6.14 *The data for the ±5V scans from figure 6.12 replotted and corrected to remove the displacement current.*

found using equation 2.26 and 2.27, where κ is found from the slope of the linear portion of the graph at low E^{-1} values. This is then related to the barrier height (ϕ) using equation 2.27, giving a value of 0.023 eV.

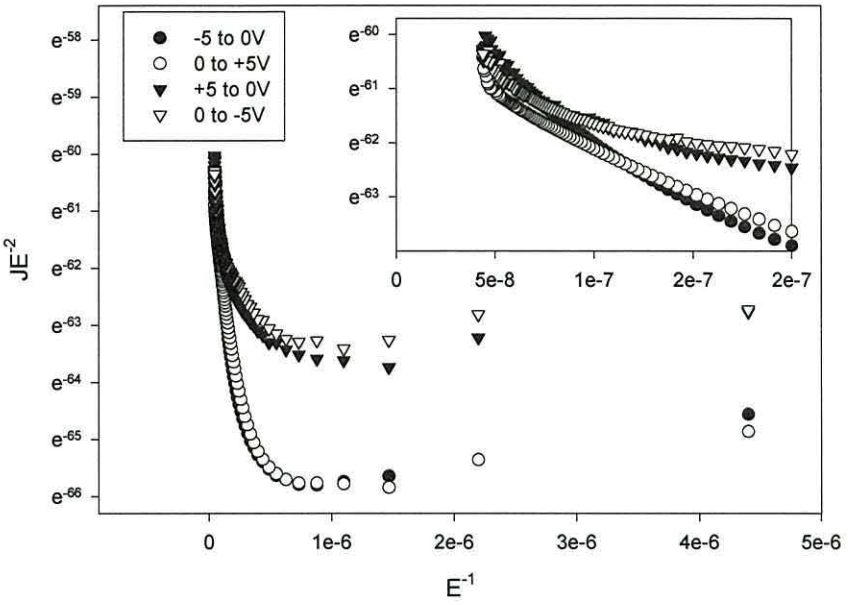

Figure 6.15 *Fowler-Nordheim plot for an ITO/PCDM/Al diode produced by replotting the data in figure 6.14.*

A plot of ln J versus $E^{0.5}$ (Figure 6.16) allows the Schottky model to be tested (Equation 2.23), the result of which gives an indication of whether the conduction mechanism occurring in the polymer is electrode limited. The slope of the graph was used to find the constant β_S, which was then related to the relative permittivity, ε_r. However, for the Schottky model to be applicable, the applied field must be large enough to make the $\exp\left(\frac{e\beta_S E^{1/2}}{kT}\right)$ term from equation 2.23 significant. Therefore, if,

$$E^{1/2} > \frac{kT}{e\beta_S},$$

where,

$$\beta_S = \left(\frac{e}{4\pi\varepsilon_0\varepsilon_r}\right)^{1/2},$$

then,

$$E > \left(\frac{kT}{e}\right)^2 \left(\frac{4\pi\varepsilon_0\varepsilon_r}{e}\right). \qquad (6.1)$$

Using the value of ε_r estimated from the admittance data (~7) in equation 6.1, the applied field needs to be greater than $3.2\text{x}10^6$ Vm^{-1} or values of $E^{0.5} > 1778$ in figure 6.16. The average permittivities of the polymer was calculated separately for the

+5 to -5 V and -5 to +5 V directions in the ranges $1778 < E^{0.5} > 3000$ and $E^{0.5} > 3000$ and the results are presented in table 6.1.

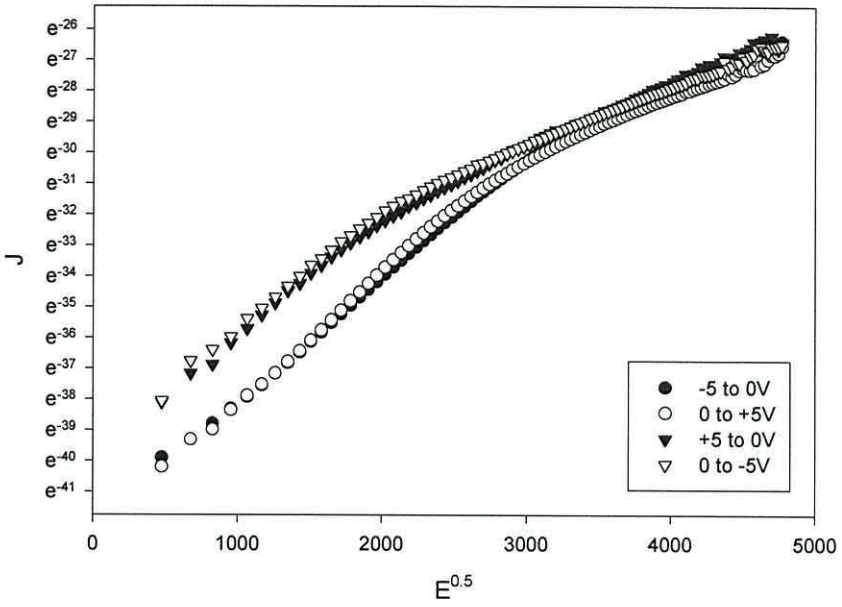

Figure 6.16 *Schottky plot for an ITO/PCDM/Al diode produced by replotting the data in figure 6.14.*

Table 6.1 *Average relative permitivities calculated upon attempting to fit the Schottky model to the current-voltage data for a PCDM thin film.*

Voltage scan direction	Applied Field	
	$1778 < E^{0.5} > 3000$	$E^{0.5} > 3000$
+5 V to -5 V	0.15	1.14
-5 V to +5 V	0.13	1.01

Similarly, a plot of J/V against $E^{0.5}$ (Figure 6.17) could be used to test for the Poole-Frenkel mechanism. Using equation 2.19, the constant, β_{PF}, can be calculated from the slope of the curve and, hence, related to the relative permittivity, ε_r. The Poole-Frenkel effect will confirm the presence of traps in the bulk of the polymer but, similar to the Schottky model, for the Poole-Frenkel model to be applicable the applied field must be large enough to make the $\exp\left(\frac{e\beta_{PF}E^{1/2}}{kT}\right)$ term from equation 2.19 significant. Therefore,

$$E > \left(\frac{kT}{e}\right)^2 \left(\frac{\pi\varepsilon_0\varepsilon_r}{e}\right). \qquad (6.2)$$

Again, using the value of ε_r estimated from the admittance data in equation 6.2, the applied field needs to be greater than $7.9\text{x}10^5$ Vm^{-1}, i.e. values of $E^{0.5} > 889$ in figure 6.17. The average permitivities of the polymer was calculated separately for the +5 to -5 V and -5 to +5 V directions in the ranges $889 < E^{0.5} > 3000$ and $E^{0.5} > 3000$ and the results are presented in table 6.2.

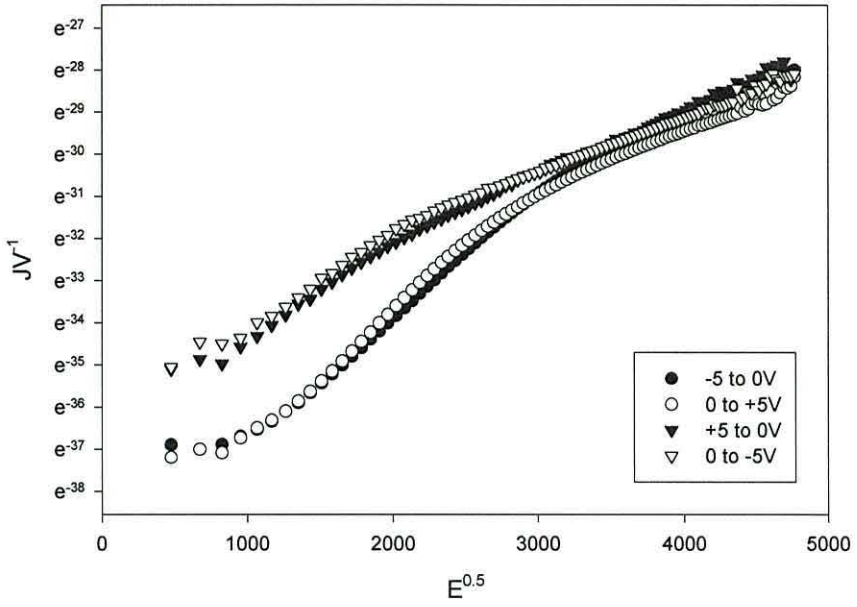

Figure 6.17 *Poole-Frenkel plot for an ITO/PCDM/Al diode produced by replotting the data in figure 6.14.*

Table 6.2 *Average relative permitivities calculated upon attempting to fit the Poole-Frenkel model to the current-voltage data for a PCDM thin film.*

Voltage scan direction	Applied Field	
	$889 < E^{0.5} > 3000$	$E^{0.5} > 3000$
+5 V to -5 V	2.44	2.43
-5 V to +5 V	0.95	2.22

The 'low' conductance state of the polymer diodes has been found to be stable for many months. Additionally, the stability of the high conductance state has been investigated. Plotting current against time (figure 6.18) allows the time constants for

the current decay at ±0.5 V to be calculated from the slopes of the plots using the equation,

$$I = I_0 \exp\frac{-t}{\tau} \qquad (6.3)$$

After applying +3 V to the diode to induce the 'high' state and decrementing to +0.5V or -0.5V, it is seen that the device currents decay exponentially with time constants of 2600s and 1500s respectively. Thus the application of negative voltages, encourages the relaxation of the 'high' conductance state. Clearly by -5 V this process is complete.

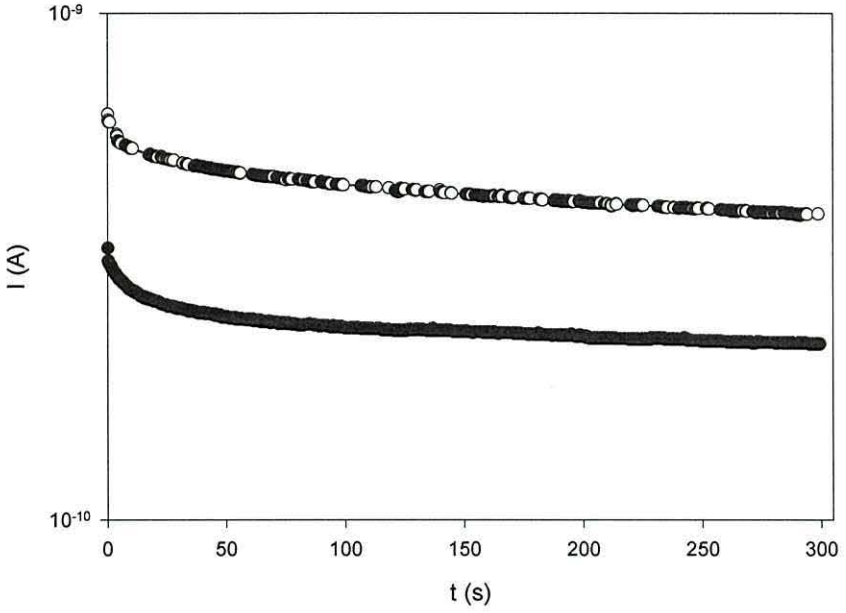

Figure 6.18 *Temporal relaxation of the 'high' conductance state at +0.5 V (●) and -0.5 V (○).*

6.2.3 Current-voltage characteristics: Discussion

Interestingly, the current-voltage plots (Figure 6.14) are sensitive to the direction of the voltage scan. When scanning from +5 V to -5 V the measured current varies as V^3 over most of the range. When scanning in the opposite sense, however, the currents measured at low voltages are approximately an order of magnitude lower but from ~ 0.8 V to ~ 2.5 V rise as V^5 until they merge with the V^3 curve. This same general pattern of behaviour was found in all devices tested. Interestingly, the 'hysteresis' between the two scan directions was much less when the range was reduced to ±2 V. Now the I-V characteristic is intermediate between the two states at lower voltages but

asymptotes to the V^3 dependence again when $|V|$ is greater than about 1 V.

Work by Riel and co-workers [174] has also examined the influence of sweep direction on the current-voltage characteristics of multilayer organic LEDs. The authors set the acquisition time for a single data point to depend on the magnitude of the current, producing an acquisition time of about 100 ms for currents below 10 nA. The lowest current recorded was 0.1 nA. The authors state that a "pronounced hysteresis" occurs in the range from -5 to 2 V but do not describe taking a displacement current into account.

The current-voltage characteristics show a displacement of the minimum current on the voltage axis of approximately 1 V. This produces a displacement current at 0 V of approximately $2x10^{-9}$ Acm^{-2} when sweeping from negative to positive and $1x10^{-8}$ Acm^{-2} when sweeping in the opposite direction. By removing this current the amount of hysteresis in the curves is reduced and possibly removed.

The displacement currents produced seem to be due to the speed of the measurement sweep. Indeed, the authors produced current-voltage curves when sweeping from negative to positive at fast, medium and slow sweep rates, which showed the displacement current being removed as the sweep rate is slowed. However, there is no data for the opposite sweep at the slow sweep rate and therefore no indication whether the hysteresis remains. Similar hysteresis has been observed by Beck and co-workers in inorganic thin films with perovskite type structures [175]. In these devices there is no displacement current present and the diodes display reproducible switching between high and low impedance states with switching times lower than 100 ns. A possible memory element has been suggested as an application for the device.

A barrier height of 0.023 eV, calculated from the Fowler-Nordheim plot, and relative permittivities below 2.5 upon application of a Schottky model and a Poole-Frenkel model, for fields above that at which $E^{0.5}$ becomes significant, have been estimated. The permittivity values were low when compared to that found using AC data (~7) and that for a similar polymer, P3MeT (~5) [19]. The low values for relative permittivity and barrier height suggest that the current-voltage data does not follow these models.

From the AC behaviour of the devices it is clear that an interfacial capacitance exists somewhere in the diode. The C-V measurements provide some evidence that this

capacitance is related to the presence of a thin depletion region at the polymer/ITO interface. It is further seen that when the applied voltage exceeds about ±2 V, then the associated parallel resistance falls sufficiently that any barrier to carrier flow presented by this depletion region is insignificant. Thus if any rectification does occur in the device it would only be observed for applied voltages less than about ±1 V. Figure 6.12 shows that differences do occur in the currents flowing under positive and negative bias in this voltage range. The differences fall into two categories:

(i) *Displacement Current:* Although 60 s is allowed between each 0.1 V step change in the applied voltage to allow the device current to reach equilibrium, the resulting pseudo-constant voltage ramp generates a displacement current, $C\frac{dV}{dt} \approx \pm 5 \times 10^{-11}$ A which charges the interfacial capacitance (~30 nF). The polarity of this current depends on the *direction* of the voltage ramp rather than the *polarity* of the voltage and can, therefore, give rise to an apparent rectification at the lowest applied voltages. This is readily identified with the currents flowing in the range ±0.3 V. Figure 6.14 shows the current-voltage characteristics after the displacement current has been removed. The small difference in the displacement current in either sweep direction seen in figure 6.13, suggests that there could be some drift of dopant ions, thus changing the depletion capacitance.

(ii) *Charge Trapping:* Once the displacement current effects have been accounted for, the I-V characteristics in Figure 6.14 display two stable states, depending on whether the voltage ramp begins with positive or with negative applied voltages. When starting at +5 V the currents follow an identical V^3 dependence on applied voltage irrespective of the voltage polarity. On the other hand, when the voltage ramp is started from -5 V, the V^3 dependence is followed initially, but as the voltage decremented below about -2 V the current fell by an order of magnitude in a manner reminiscent of a trap-modulated space-charge-limited current (SCLC) with trap emptying. Below about -1V, a V^3 dependence was again observed albeit with smaller currents flowing. As the applied voltage then incremented through positive voltages, at about +1 V the current grew more rapidly (~V^5), this time reminiscent of trap filling, before asymptoting to the original V^3 dependence above about +2 V. The region identified with the trap-free SCL current regime, however, is characterised by a V^3 dependence rather than the square law predicted by Lampert [35] (equation 2.28).

Mark and Helfrich [36] have shown, however, that a V^3 dependence is possible when traps are distributed in energy. Furthermore, in a number of conjugated polymers the carrier mobility is a function of applied field, E, the mobility generally increasing with field following a Poole-Frenkel [176] dependence (μ proportional to $\exp(E/E_o)^{1/2}$). It is conceivable that such an effect could lead to a V^3 dependence over a limited range of applied voltages.

Identifying then the steep rise in current at ~ ±1 V with the trap-filled limit voltage, V_{TFL}, the trap density, N_t, is given by [35]

$$V_{TFL} = \frac{qd^2}{\varepsilon\varepsilon_0} N_t . \qquad (6.4)$$

With d = 220 nm and $\varepsilon \sim 7$, then N_t is estimated to be ~ 8 x 10^{21} m^{-3}. Lampert [35] further shows that the ratio of the current below V_{TFL} to that flowing above is equal to θ, a parameter reflecting the distribution of charges between delocalised and trapping states. This parameter is given by

$$\theta = \frac{N_0}{N_t} \exp - \frac{E_t}{kT} \qquad (6.3)$$

where N_0 is the effective density of delocalised states at the band edge and E_t the depth of the trap relative to the edge of the delocalised band. With $\theta \sim 0.1$, $N_t \sim 10^{22}$ m^{-3}, N_0 ~ 10^{26} m^{-3} and T ~ 300 K then E_t is estimated to be ~ 0.3 eV. This is in reasonable agreement with the activation energy for the bulk resistance of the polymer as deduced from AC measurements since the average field in the polymer at V_{TFL} is sufficiently great that the discrepancy of 0.1 eV is readily accounted for by the field-lowering of the trap depth (Poole-Frenkel effect) in the DC measurement.

While the above argument appears to be reasonable it does not explain the existence of the apparent trap-free SCL current for *both* polarities when ramping from +5 V to -5 V. It seems that under a high positive electric field, traps in the polymer are filled and remain filled until an opposite field of similar magnitude is applied. However, when the voltage ramp is restricted to the range +2 V to -2 V, the I-V characteristics were essentially independent of voltage polarity and ramp direction - the plots followed the trap-controlled characteristic at low voltages and asymptoted to the trap-free plot at ±2 V. It appears, therefore that when the highest applied voltages are restricted to ±2 V carriers interact reversibly with traps. Above +2 V a quasi-

irreversibility sets in. An explanation based on interactions with deeper traps (θ values would be significantly different) can be discounted. One possibility is that when the applied voltage is raised to +5 V, changes (possibly configurational) occur in the environment of the filled trap such that the release of the carrier now requires a change in the entropy term in the Gibbs energy function i.e. the pre-exponential term is modified in the escape frequency, ν, which is now given by an expression of the form [177]

$$\nu = \nu_0 \exp\frac{\Delta S}{k} \exp-\frac{E_t}{kT} \qquad (6.5)$$

where ν_0 is the attempt-to-escape frequency and ΔS the change in entropy required to effect an escape from a trap of depth E_t. The effect of a positive ΔS would be to increase the residence time of carriers in the traps. Application of -5 V to the device appears to provide the necessary change in entropy to effect a rapid release of the carriers during the subsequent decrement to 0 V.

The rapid increase in current in the 'low' conductance state could also be explained by the onset of double injection into the device i.e. the injection of a second species with a significantly greater mobility [178]. To explain the persistence of the high conductance state it would now be necessary to postulate changes at or near the electrode/polymer interfaces which are reversed at sufficiently high negative voltages. These changes could be electrochemical in origin such as the slow drift of dopant ions [179] (reversible). On the other hand, in the case of the thin perovskite structures investigated by Beck and co-workers [175] the controlling factor could be the reversal in polarisation on cycling round the ferroelectric hysteresis loop of the oxide. If this is the correct interpretation, then it implies that PCDM may be also be ferroelectric. In view of the strong CN....S dipole in the monomer, this may well be a possibility and the less well-defined threshold for switching in the polymer compared with the crystalline oxide would certainly be expected from such a model.

6.2.4 Electrical characterisation of PBDT

Despite the poor film structure of PBDT, preliminary DC characteristics for ITO/PBDT/Al diodes are obtained in the range ±2 V (Figure 6.19). The characteristics were limited to this range as, unsurprisingly, the diodes tested tended to break down above 2 V.

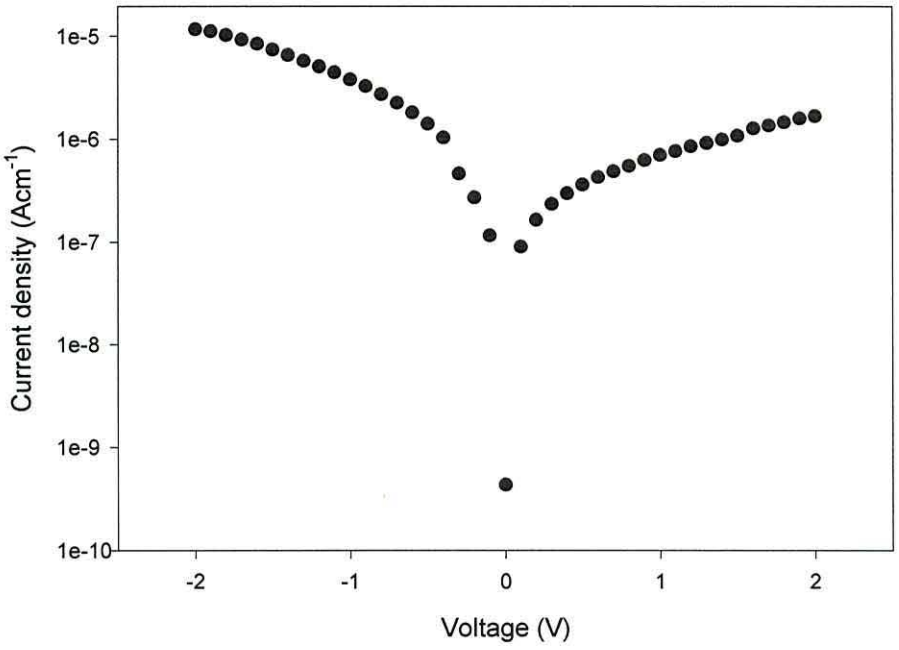

Figure 6.19 *Current density versus applied bias plots for an ITO/PBDT/Al diode.*

The PBDT diode displays similar current levels to that for the PCDM diode and it is also noticeable that the PBDT diode displays a small amount of rectification at ± 1 V although no effort was made to optimise this phenomenon. The PBDT diode seems to have rectification "reversed" from the normal sense as seen in diodes incorporating P3MeT [180, 156]. A similar phenomenon, where rectification is reversed, has seen for diodes incorporating poly(3-octylthiophene) (P3OT) [181]. Depending on the top contact an ITO/P3OT/metal diode can be made to reverse its rectification. Using an aluminium top contact, the diode rectifies in the normal direction, that is to say with higher currents upon application of a positive bias to the ITO electrode. However, upon changing the aluminium to gold the rectification is reversed, with higher currents flowing upon biasing the ITO negatively.

Removal of a displacement current of 2.01×10^{-11} A had little effect on the shape of the current-voltage curve due to the small size of this current compared to the currents at higher voltages. Similar to those for PCDM, attempts were made to fit the DC characteristics for the PBDT diode to various conduction models to determine whether the conduction was bulk limited or electrode limited. As the PBDT was too rough for AFM imaging, it is assumed that its film thickness is similar to those found for PCDM and P3MeT, i.e. 200 nm.

An attempt was made to fit Fowler-Nordheim field emission tunnelling theory to the results to calculate the barrier height at the electrode/polymer interface. Plotting J/E^2 versus 1/E revealed that there were not enough points at low 1/E values to complete the calculation of the barrier height and at these fields, therefore, no tunnelling was thought to be occurring. However, the plot follows the general shape of that shown in the comparative plot for PCDM (Figure 6.20) at higher 1/E values.

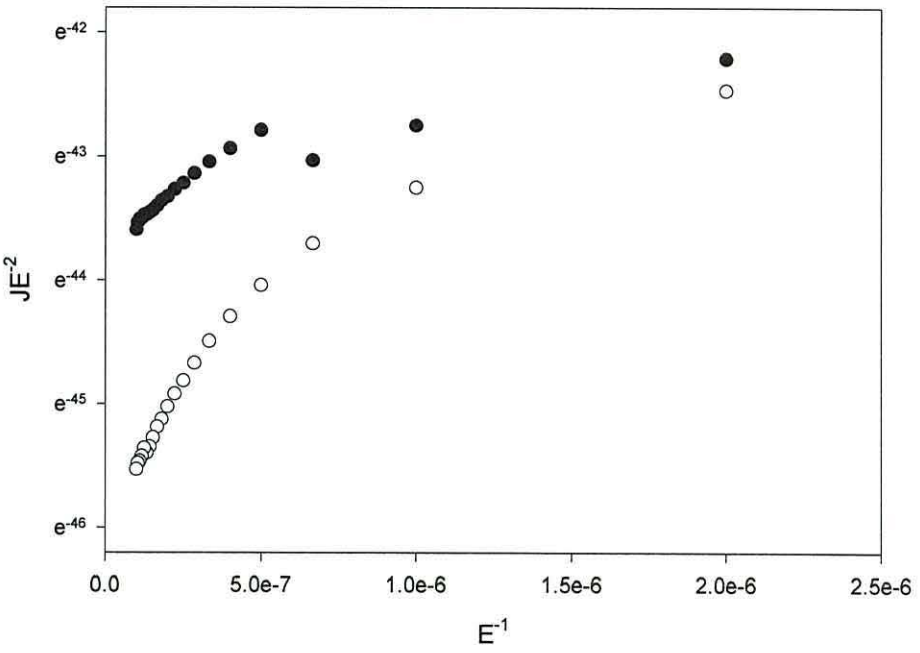

Figure 6.20 *Fowler-Nordheim plot for an ITO/PBDT/Al diode with positive (●) and negative (○) voltages applied to the ITO.*

By fitting the current-voltage results to the Schottky model (Figure 6.21), values for the relative permativity of the PBDT diode could be found, 0.77 in forward bias and 1.85 in reverse bias. Similarly, values for the relative permitivity could be calculated by attempting to fit to the Poole-Frenkel model (Figure 6.22), however there are not enough points at fields above 10 MVm^{-1} to make this measurement valid.

A plot of log I versus log V can be constructed to try to fit the space charge limited conduction (SCLC) model (Figure 6.23). The plots produce slopes of 1.58 and 0.97 in forward and reverse bias respectively up to ±2 V.

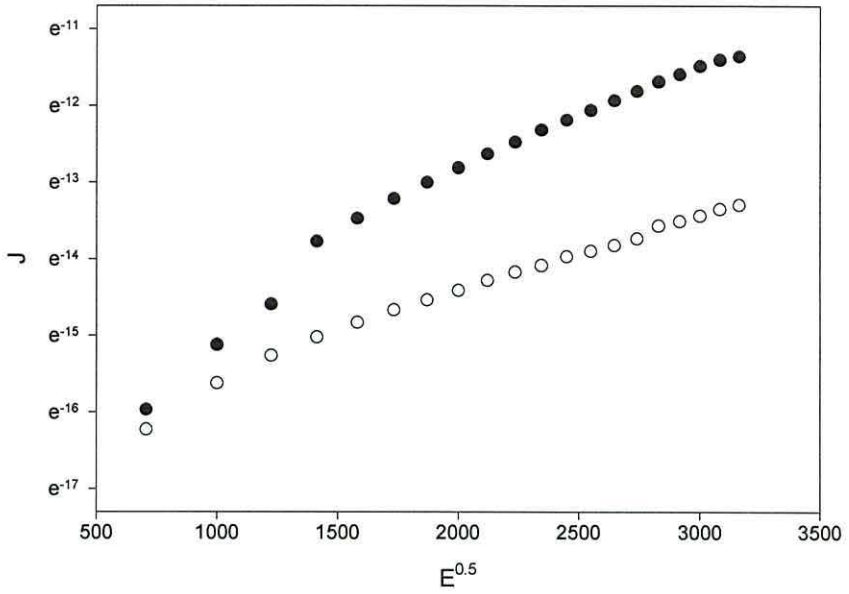

Figure 6.21 *Schottky plot for and ITO/PBDT/Al diode with positive (●) and negative (○) voltages applied to the ITO.*

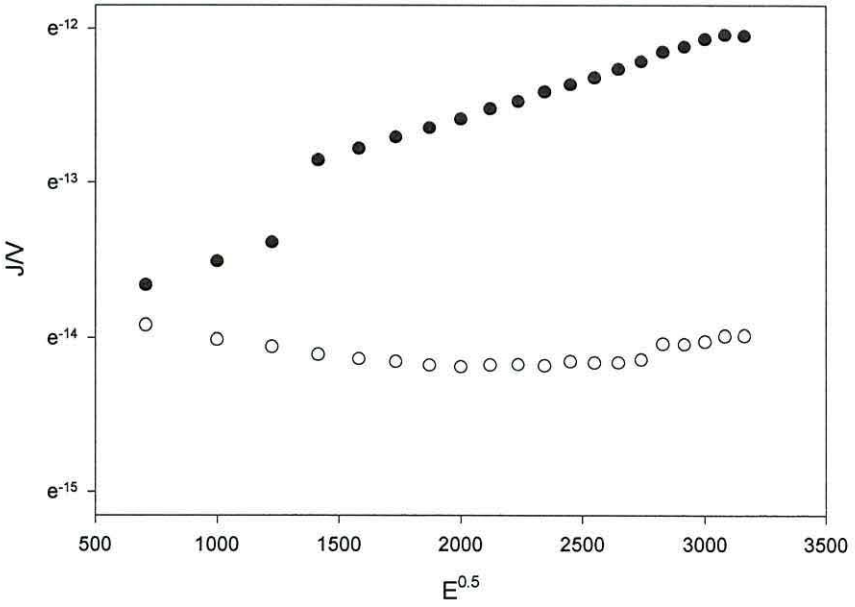

Figure 6.22 *Poole-Frenkel plot for an ITO/PBDT/Al diode with positive (●) and negative (○) voltages applied to the ITO.*

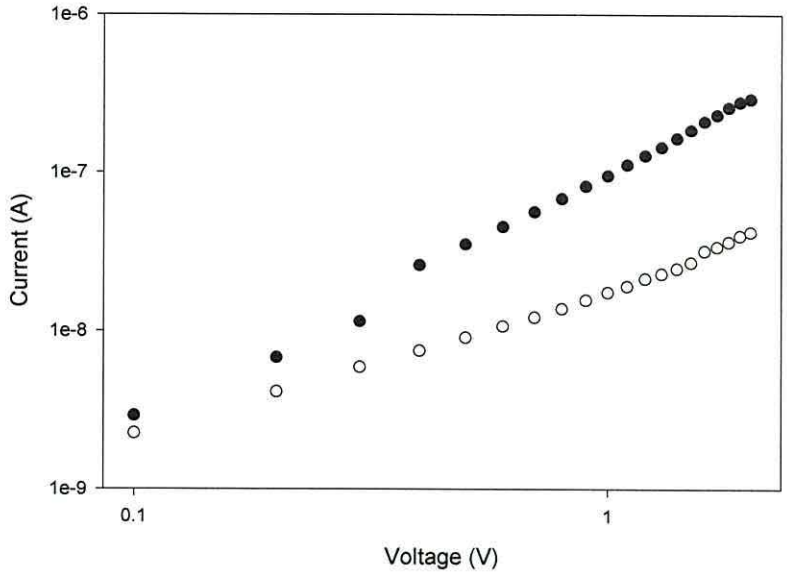

Figure 6.23 *Space charge limited conduction plot for a PBDT diode with positive (●) and negative (○) voltages applied to the ITO.*

6.3 Summary

The AC behaviour of ITO/PCDM/Al diodes reveal the presence of two dispersions, at approximately 100 Hz and 1 MHz respectively, due to the presence of a depletion layer in the polymer and a small series resistance from the ITO electrode. Assuming that PCDM is p-type, capacitance-voltage measurements in the range ±2 V suggest that the depletion region occurs at the PCDM-ITO junction. Unfortunately, the lack of capacitance measurements at sufficiently low frequency to prevent interference of the low frequency dispersion when measuring C_d and the rapid fall off in capacitance above ±2 V prevents the doping density and the height of the potential barrier at the junction from being calculated.

An increase in temperature causes the depletion layer dispersion to shift to higher frequencies, whereas, an increase in film thickness is seen to (i) shift of the low-frequency dispersion to lower frequencies, (ii) reduce the frequency-independent capacitance in the mid-frequency range and (iii) shift the high frequency dispersion to higher frequencies. The dependence of device capacitance on applied voltage suggested the presence of a depletion region at the polymer/ITO interface but DC conduction through the device was too great to allow a definitive conclusion to be drawn.

Capacitance and resistance values which could be used in the series-parallel RC circuit model described in section 2.2.4 were calculated from Cole-Cole and impedance plots. A temperature independent resistance of approximately 400 Ω was calculated for the ITO series resistance. The relative permitivity of a 220 nm thick PCDM film, with a bulk capacitance of $7x10^{-10}$ F and a sample area of 2.5 mm^2, was calculated to be approximately 7. Using this value and the depletion layer capacitance, $\sim 3.2x10^{-8}$, the same film was found to have a depletion layer ~5 nm thick.

Admittance data for PCDM diodes with gold and silver top electrodes, instead of aluminium, revealed large DC loss characteristics swamping any possible signal due to the depletion layer.

Examination of the current-voltage characteristics for ITO/PCDM/Al diodes has failed to show an expected rectification, and weak rectification is only observed below approximately 0.5 V even after removal of the displacement current.. However, the plots are sensitive to the scanned direction of the voltage, where the currents measured upon scanning from -5 V to +5 V are, at low voltages, approximately an order of magnitude lower than those measured when scanning from +5 V to -5 V.

Application of various conduction models to the current-voltage data has been attempted. A barrier height calculated from the Fowler-Nordheim plot and relative permittivities found upon application of Schottky and Poole-Frenkel models were low when compared to that found using AC data and that for a similar polymer, P3MeT. The low values for relative permittivity and barrier height suggest that the current-voltage data does not follow these models.

A V^3 dependence is followed for the +5 V to -5 V voltage ramp. For the -5 V to +5 V direction, the current also follows a V^3 dependence until the voltage decrements below ±2 V. The current then falls with approximately a V^5 dependence before returning to a V^3 dependence below about ±1 V and then an ohmic behaviour at low voltages. Therefore, it seems as though the data fits a space charge limited current model with traps with a distribution of energies leading to the V^3 dependence. Indeed the similar results presented by Beck and co-workers on perovskite films also fit a space charge limited current model with shallow traps.

If the steep rise at ±1 V is the trap-filled limit, the trap density is found to be approximately $8x10^{21}$ m^{-3} when the PCDM is 220 nm thick and has a permittivity of ~7. Further, an estimate of the trap depth relative to the edge of the delocalised band

has been found to be in reasonable agreement with the activation energy for the bulk resistance of the polymer as deduced from the AC measurements.

The curves seen in the SCLC plots seem to suggest that under a high positive electric field, traps in the polymer become filled and remain filled until an opposite field of similar magnitude is applied. Configurational changes in the polymer, where a change in the entropy term of the Gibbs energy function is required to escape from a trap, and the possible onset of double injection into the diode, by injection of a second species with greater mobility, have been suggested to explain this behaviour.

The effect appears to be identical in most respects to recent observations in diodes formed from thin films of chromium-doped $SrZrO_3$ sandwiched between a $SrRuO_3$ bottom electrode and a gold top electrode. It is suggested that residual dopant (tetrabutylammonium tetrafluoroborate) incorporated in the film during electrodeposition of the polymer may play a similar role to the chromium dopant in the oxides.

To explain the persistence of the high conductance state , changes at or near the electrode/polymer interface is necessary which are reversed at high negative voltages. These changes could be electrochemical or ferroelectric in nature. The low conductance state has been found to be stable for many months and the high conductance state displays currents that decay exponentially with time constants of 2600 and 1500 seconds at +0.5 V or -0.5 V respectively after inducing the high state at +5 V.

Preliminary examination of the DC characteristics of ITO/PBDT/Al diodes reveal that the diodes are likely to break down above ±2 V but that they do display a small amount of rectification, approximately 6.5 at ±1 V, which is not removed upon correcting for the displacement current. Rectification was in the reverse sense to that found for diodes formed from P3MeT. Attempts to fit conduction mechanism models to the DC results have proven difficult due to insufficient data points in the case of the Fowler-Nordheim and Poole-Frenkel models.

Low relative permittivity values suggest that the data does not follow a Schottky model, and application of the SCLC model produced slopes of approximately 1.6 and 1 in forward and reverse bias respectively suggesting that in reverse bias the diode follows an ohmic behaviour up to 2 V. The results presented here are not conclusive and would benefit from repeat experimentation, preferably over a larger

voltage range. However, the main drawback to electrical characterisation of these samples is the poor surface quality of the PBDT films which would, if possible, need to be improved to produce useful electrical characterisation results.

7. Command surface polymers

In 1981, Lecayon and co-workers showed that certain polymers can be grafted electrochemically onto a metal surface [182], for example, the electropolymerisation of acrylonitrile led to the formation of a thin film of poly(acrylonitrile) on nickel [183, 184], platinum [183] and copper [185, 186] surfaces. Of particular interest is the difference in the nature of the metal/polymer interface depending on whether cathodic or anodic polymerisation is used. When the substrate metal (nickel or platinum) acts as a cathode it behaves as a basic initiator for anionic polymerisation through a 1,4 Michael-type addition from the metallic surface to the vinylic carbons to form a polymeric structure as shown in figure 7.1(a). However, when the metal substrate is made an anode, it acts as a Lewis acid towards the acrylonitrile molecules, resulting in either (i) a 1,2 nucleophilic addition on the nitrile groups which affords a 'conjugated' structure (figure 7.1(b)) or (ii) through the 1,4-addition of the nitrile group to the vinyl carbon, the formation of a cumulene type structure (figure 7.1(c)). Therefore, by changing the nature of the metallic surface either end of the acrylonitrile (and also the methacrylonitrile [187]) molecule may be chemically bonded to the metal surface.

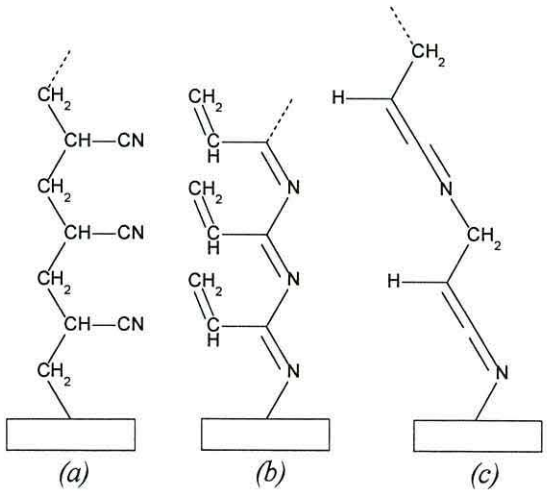

Figure 7.1 *Polymer structure when synthesised by (a) Michael-type addition, (b) 1,2 nucleophilic addition on the nitrile group and (c) 1,4 addition through the nitrile group and the vinyl carbon.*

Recent work by Jerome and co-workers [184, 188] has shown that it is also possible to 'debond' the grafted poly(acrylonitrile) by increasing the cathodic potential beyond that required for bonding, suggesting a means of producing thin, free-standing polymeric membranes. Furthermore, the work by Jerome and co-workers to date indicates that acrylonitrile-based polymer may well be suited to the preparation of functionalised macrostructures or command surfaces which could be useful in sensor or optical applications.

Although much is already known about the electropolymerisation process, there is still some doubt as to the actual mechanism of polymerisation and little is known about either (a) the tacticity of the polymer or (b) the effects of functional groups on the polymerisation process. Previous analysis of poly(acrylonitrile) grown on copper surfaces and in solution suggest that the "grafted" polymer is amorphous and isotactic, whereas the "ungrafted" chains are polycrystalline [186].

Preliminary results of an investigation into the cathodic and anodic polymerisation of the three monomers shown in figure 7.2 are presented. Electropolymerisation of monomers **2** and **3** will result in a command surface, i.e. a surface functionalised polymeric macrostructure. In a subsequent step (not investigated here) such a surface should allow the attachment of different types of active moieties for example, a sensor unit, NLO chromophore [189] or a liquid crystal unit, as shown in figure 7.3.

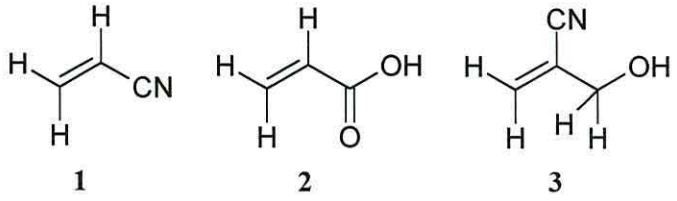

Figure 7.2 *Monomers used for polymerisation of command surfaces, acrylonitrile **1**, acrylic acid **2** and 2-cyanoprop-1-en-3-ol **3**.*

Indeed poly(acrylic acid) has been used as a chemical sensor by functionalising with β-cyclodextrin and poly(acrylonitrile) has been used to immobilise uranium and neptunium for α-spectroscopy [190]. Similar simple polymers have been used as the basis for biosensors [191].

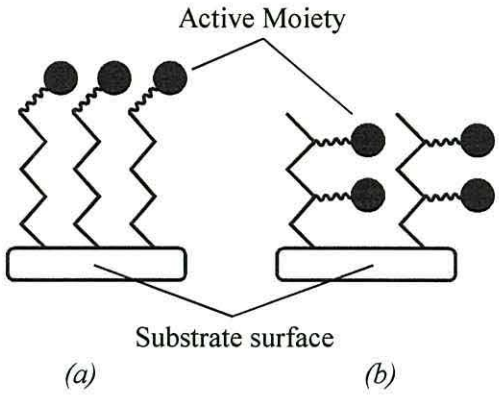

Figure 7.3 *Possible addition of active moieties, (a) surface macrostructure and (b) in-plane macrostructure.*

A common use for polymers which are polymerised using azobenzene units is in the production of liquid crystal displays. Polymers such as poly(acrylic acid) [192] and poly(methacrylates) [193] have been used in liquid crystal cells which consist of the azobenzene functionalised polymer on a suitable substrate, such as ITO, sandwiching the liquid crystal material between itself and another sheet of ITO [194]. The polymer chains are then used to align the liquid crystal and isomerisation of the azobenzene causes a switch between homeotropic and homogeneous alignment [195].

7.1 Polymer preparation

Acrylonitrile (**1**) and acrylic acid (**2**) (99 %, Aldrich chemicals, UK) were used without further purification. 2-Cyanoprop-1-en-3-ol (**3**) was supplied by the Department of Chemistry at the University of Hull after being synthesised using a procedure first described by Villieras and Rambaud [196]. The structure of (**3**) was confirmed by ^{1}H NMR (JEOL JNM-GX 270 MHz spectrometer), infrared spectroscopy (Perkin Elmer Model 783 Grating Spectrophotometer) and mass spectrometry (Finnegan-MAT 1020G/MS spectrometer). ^{1}H NMR ($CDCl_3$): δ 6.05 (s, 1H), 4.25 (s, 2H), 2.80-3.05 (s, broad, 1H); IR (KBr): 3100-3600, 2970, 2890, 2220, 1625, 1450, 1040, 950 cm^{-1}; m/Z: 83 (M^+), 66 (M-OH).

Solutions of acrylonitrile, acrylic acid and 2-cyanoprop-1-en-3-ol (approximately 0.4 M) were prepared in acetonitrile with tetraethylammonium perchlorate (TEAP, $5x10^{-2}$ M) as a supporting salt. Electropolymerisation was achieved

using the standard three electrode cell described previously except that the working electrode was formed by evaporating a silver film (100 nm thick) onto a glass substrate rather than using gold or ITO-coated glass.

The polymerisation and diode preparation used the same method as used previously for the semiconducting polymers, and growing conditions for both anodic and cathodic electropolymerisation are given in table 7.1.

Table 7.1 *Conditions used for growth of command surface polymers.*

	Nucleation step		Growth step	
Type of polymerisation	**Applied potential (V)**	**Time applied (s)**	**Applied potential (V)**	**Time applied (s)**
Anodic	2.8	10	1.8	1200
Cathodic	-2.8	10	-1.8	600

7.2 Polymer characteristics

Polymerisation of the monomers on the silver substrates was achieved giving stable, robust films between 0.2 and 0.4 μm thick under both anodic and cathodic conditions (table 7.2). Even though the time allowed for growth was some 50% greater for anodic polymerisation, the resulting films were 20-30% thinner than cathodically-produced films [199]. Films of poly(acrylic acid) showed the most rapid growth rates for both anodic and cathodic polymerisation. Taking acrylonitrile as the reference, these preliminary results indicate that replacing the *gem*-hydrogen has little effect on the rate of electropolymerisation. However, replacing the cyano group with another electron-withdrawing group produces a significant effect.

The strength of the polymer/metal bonding was tested by rinsing in dimethylformamide (DMF), tetrahydrofuran (THF) or dichloromethane (DCM) at room temperature. None of the films were removed and the vacuum-dried films also resisted attempts at removal with adhesive tape suggesting that they are strongly bonded to the silver surface.

AFM images of polyacrylonitrile produced under both anodic and cathodic conditions and given in figure 7.4 are typical of all three materials

Table 7.2 *Typical properties of the electropolymerised command surface polymer films grown from the monomers listed.*

Monomer	Thickness (nm)		RMS roughness 500 nm^2 area (nm)		Conductivity ($S\ m^{-1}$)	
	anodic	cathodic	anodic	cathodic	anodic	cathodic
Acrylonitrile	220	320	2.3	3.0	$1.45x10^{-3}$ $\pm 2.5x10^{-5}$	$2.28x10^{-3}$ $\pm 2.3x10^{-6}$
Acrylic acid	300	360	6.6	1.2	$1.54x10^{-3}$ $\pm 1.3x10^{-5}$	$2.13x10^{-3}$ $\pm 8.8x10^{-6}$
2-Cyanoprop-1-en-3-ol	230	310	1.5	2.2	$2.81x10^{-3}$ $\pm 8.5x10^{-6}$	$2.56x10^{-3}$ $\pm 1.1x10^{-4}$

investigated. Anodic films were exceptionally smooth and although punctuated by deep crevices (figure 7.4(b)) did not show the nodules projecting from the surface that are characteristic of the cathodic film (figure 7.4(a)). At higher magnification (figure 7.4(c) and 7.4(d)) the underlying surface morphologies differ only slightly with the rms roughness of all films in the range 1 - 6 nm (table 7.2).

Interestingly, films from the two cyano-containing compounds are smoother than those from acrylic acid which may well reflect the slower growth rate of the cyano-containing films (table 7.2). The presence of crevices suggests a more rigid film as expected when conjugated structures such as figure 7.1(b) or 7.1(c) are growing. AFM probing showed that the crevices found in the anodic polymer films did not penetrate the full depth of the layer. Depending on the type of tip used and the width of the crevice being probed, the AFM tip can probe to a depth of 1-2 μm [198]. As the films examined here are, at maximum, only 360 nm thick and the crevices are approximately 1 μm wide (see figure 7.4(b)) the full depth of the crevice should be examined.

The electrical conductivity of the sandwich structures was measured under ambient conditions using a Tektronix Model 571 Current/Voltage plotter revealing essentially linear characteristics over a 2 V range. The conductivities of the polymers ranged from $1.4x10^{-3}$ to $2.8x10^{-3}$ Sm^{-1} (Table 7.2). Despite their supposed conjugated

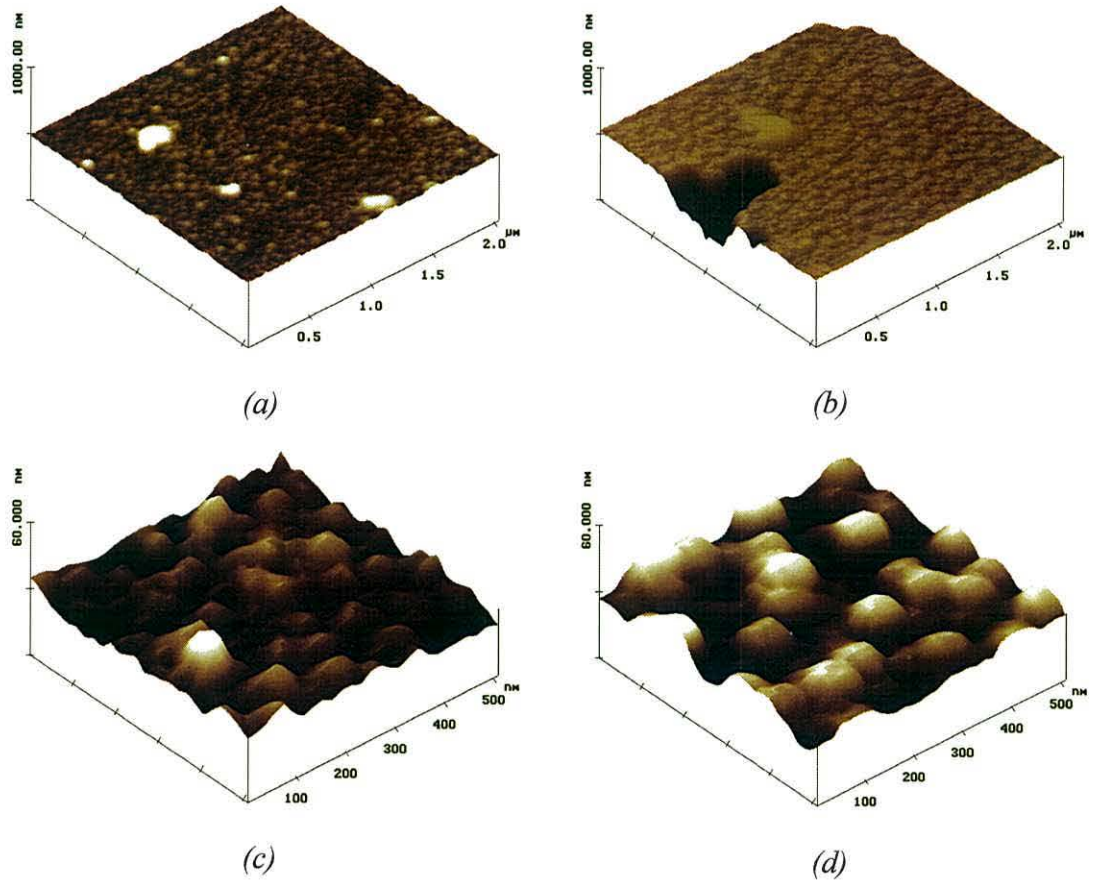

Figure 7.4 *AFM micrographs of cathodically, (a) and (c), and anodically, (b) and (d), polymerised acrylonitrile. In (a) and (b) the area is 2 x 2 μm and z-range is 500 nm/div, in (c) and (d) the area is 500 x 500 nm and z-range is 30 nm/div.*

structure, the anodically grown films were generally of lower conductivity than those produced cathodically. This provides some confirmation of the AFM observation that the crevices in the film did not penetrate the whole film and indeed had little effect on the electrical properties.

The Raman spectra for the three monomers and their respective polymers are shown in figures 7.5 to 7.7. Some areas are expanded and shown above the main spectra to make the detail clearer. All monomer spectra (labelled (c)) show the ν(CH=CH) peak at approximately 1620 cm^{-1} and the ν(C-H) peak of the CH=CH moiety just above 3000 cm^{-1}. The sharp band characteristic of ν(C≡N) is clearly visible at approximately 2225 cm^{-1} in both the acrylonitrile and 2-cyano-prop-1-en-3-ol, while in the latter material bands due to ν(C-H) in the CH_2 moiety are seen just below 3000 cm^{-1}.

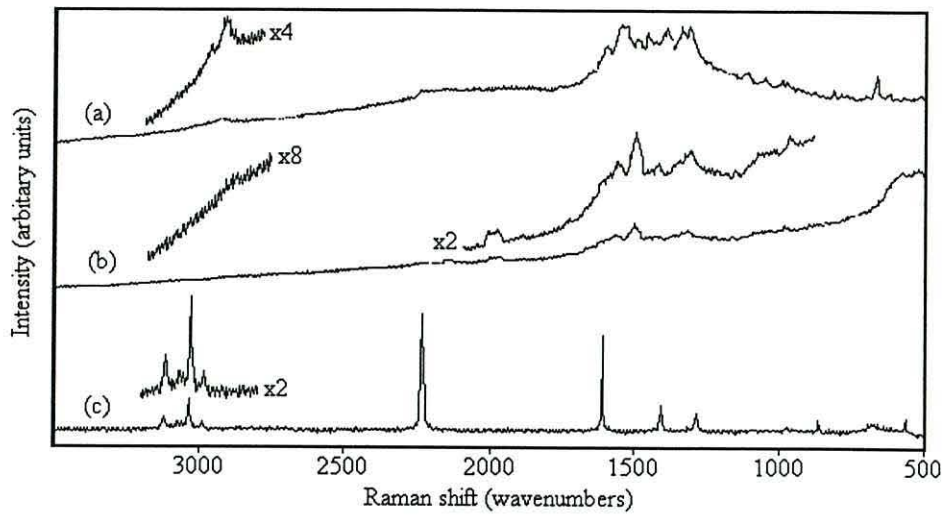

Figure 7.5 *Raman spectra of acrylonitrile (a) anodically polymerised, (b) cathodically polymerised and (c) monomer.*

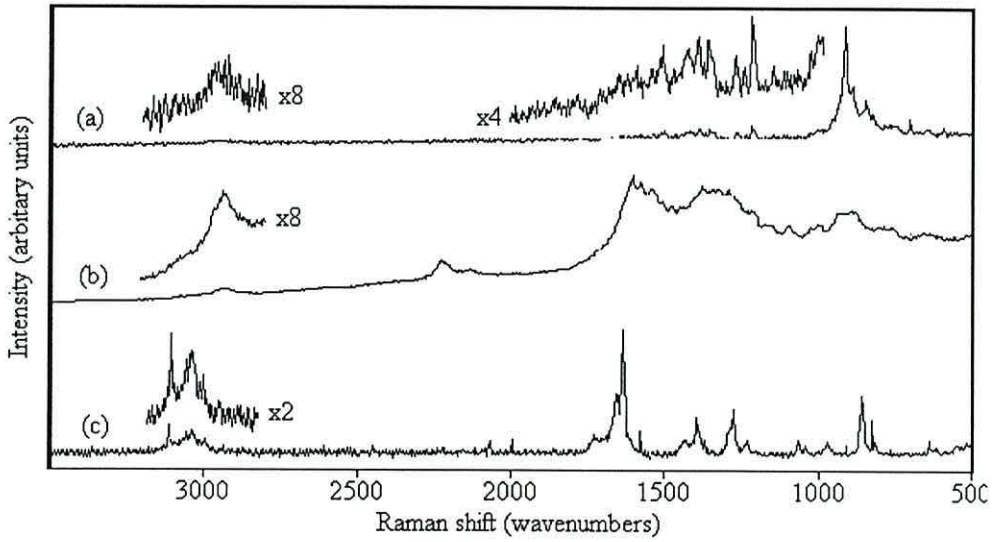

Figure 7.6 *Raman spectra of acrylic acid (a) anodically polymerised (b) cathodically polymerised and (c) monomer.*

The spectra obtained for the electrodeposited films show clear evidence for polymerisation. (a) The C-H stretch vibration of the CH=CH moiety above 3000 cm^{-1} has disappeared to be replaced by the C-H stretching vibration of the saturated CH-CH moiety just below 3000 cm^{-1}. (b) The appearance of a broad absorption band in the range 1200-1700 cm^{-1}. Interestingly, the detailed structure of the band in this region is different in the cathodic and anodic polymers consistent with the different polymerisation schemes in Figure 7.1.

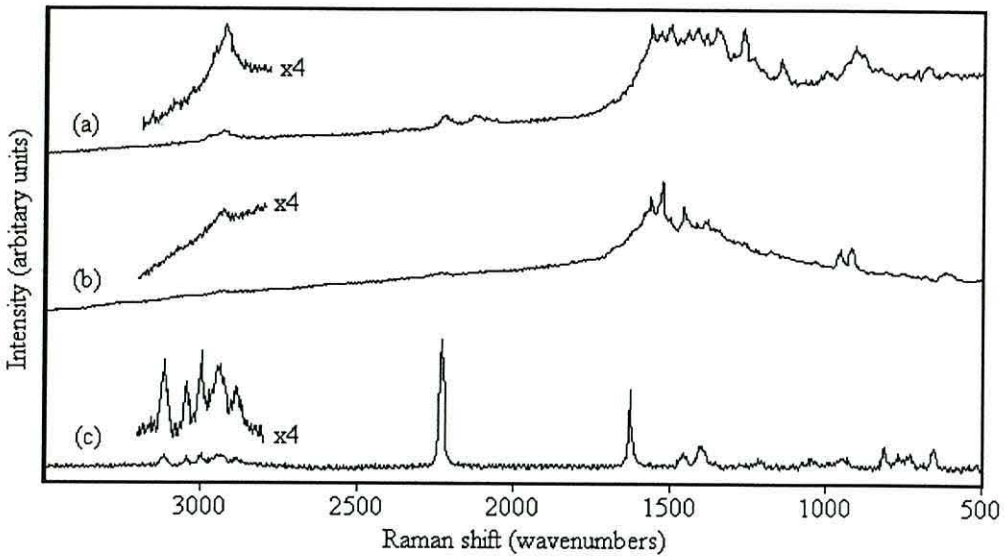

Figure 7.7 *Raman spectra of 2-cyanoprop-1-en-3-ol (a) anodically polymerised, (b) cathodically polymerised and (c) monomer.*

7.3 Summary

To summarise, a series of ethylene homopolymers has been prepared by both anodic and cathodic electropolymerisation. The rate of electropolymerisation (as judged by film thickness) was dependent on both the nature of the electropolymerisation and the structure of the monomer. Polymers grown under both anodic and cathodic conditions were found to be very smooth with an rms. roughness between 1 and 7 nm, however, the anodically grown films were found to contain crevices suggesting a rigid, conjugated polymer structure.

Polymerisation was confirmed using Raman spectroscopy to compare the spectra of the polymers with those of their respective monomers. The polymers all displayed peak broadening between 1200 and 1700 cm^{-1} indicative of polymerised C-C. Also the ν(C-H) band just above 3000 cm^{-1} (characteristic of CH=CH) was replaced by a new band just below 3000 cm^{-1} characteristic of the CH-CH moiety. In all cases the spectra of the cathodic and anodic polymers were different in detail consistent with different polymerisation schemes in the two cases. The polymers were found to have conductivities of approximately $2x10^{-3}$ Sm^{-1} which seemed to be independent of the presence of the crevice-like defects in the anodic films.

Functionalisation of the polymers with azobenzene groups, to which liquid crystal units can be attached, could lead to applications such as liquid crystal displays

(LCD). The production of the LCD can be achieved by sandwiching the LC between the azobenzene modified polymer and glass treated with lecithin which produces a homeotropic alignment.

8. Conclusions and further work

A physical and electrical characterisation of the carbon-bridged dithienyl polymers poly(4-dicyanomethylene-4H-cyclopenta[1,2-b;3,4-b']dithiophene (PCDM) and poly(7-benzo[1,3]dithiol-2-ylidine-7H-3,4-dithia-cyclopenta[a]pentalene (PBDT), and their respective monomers, has been undertaken. This has been achieved by examining electropolymerised films on ITO substrates and by testing diodes produced using these films.

The theory behind semiconducting polymers and the Schottky diode devices that can be formed using those polymers has been reviewed. Diode theory has also been covered with a description of ohmic contacts and Schottky barrier diodes, where the AC and DC behaviour of an ideal Schottky barrier was investigated. The polymeric diode was modelled by an equivalent circuit consisting of two RC circuits in parallel, describing the bulk and depletion layers in the polymer, and revealed a single dispersion in theoretical admittance curves. Modification of this model to include a small series resistance caused the appearance of a second dispersion, assigned to the presence of the resistance. The mathematical theory behind the modified circuits is given.

The conduction mechanisms within diodes were then studied with respect to the potential energy wells and barriers found in these systems. Four mechanisms for conduction were studied, namely, the Poole-Frenkel model, the Schottky effect, Fowler-Nordheim tunnelling theory and space charge limited current theory. A review of the literature concerning low band-gap polymers currently known, including some theoretical polymers and the polymers involved in this project, has been completed.

The results of this study can be separated into 3 parts, namely, physical and electrical characterisation of the low band gap polymers PCDM and PBDT, and the characterisation of command surface polymers based on ethylene homopolymers.

8.1 Physical characterisation

- Microscopic analysis of the substrate and polymer reveals different morphologies for the polymers studied here, PCDM and PBDT, when compared to a similar polymer, P3MeT. PCDM is generally smooth but the presence of larger aggregations of polymer could cause deviations from ideality during electrical characterisation. SEM images reveal that the PBDT had a much rougher surface, possibly suited to the production of polymeric batteries, with evidence for the formation of holes.

- FTIR and Raman spectroscopy has confirmed the polymerisation of PCDM and PBDT with the PCDM spectra being similar to those reported by Huang and Pickup. Both polymers are similar in the spectral region where the C-C polymerisation peaks occur. One year old samples of both CDM monomer and PCDM show no spectral changes suggesting "chemical" stability is high over this time period. The stability of the monomer is confirmed by the similarity of the NMR spectra.

- Raman mapping of the fluorescence of a PCDM sample has shown that the fluorescence in the spectra corresponds to the thickness of the polymer. Due to the growing conditions, the central area of the film was thought to be the most favourable region for testing electrical diodes.

- UV-visible spectra for PCDM is seen to be similar to that reported by Lambert and Ferraris, and also similar to that for the chemically similar PBDT. From the π-π^* transition, the band-gap of PCDM and PBDT were found to be 1.38 eV and 1.29 eV respectively which are lower than the corresponding values determined theoretically for monomers and dimers.

- The unit cell of crystalline CDM was determined, by XRD spectroscopy, to be triclinic. The monomer units layered in a similar way to graphite with the

possibility of π-orbital overlap. The unit cell dimensions and the monomer dimensions and volume could also be calculated.

- XPS measurements have revealed a large concentration of oxygen on the surface of the polymer due to adsorbed atmospheric oxygen. The presence of different conformations, such as aromatic and quinoid states within the polymer, or the presence of atmospheric nitrogen during the experiment has been used to explain extra forms of nitrogen and sulphur.

- The measurement of the valence band edge, also by XPS spectroscopy, has been used to produce preliminary band diagrams for metal/PCDM/ITO and metal/PBDT/ITO diodes suggesting that devices should rectify.

- Exposing PCDM to the Raman laser produces impressions in the polymer which lead to an increase (and blue shift) in the fluorescence intensity present in the Raman spectra. This is thought to be due to local melting of the polymer by the laser so that it is structurally rearranged from a semi-crystalline state to a more amorphous structure upon melting and then cooling.

Table 8.1 summarises the properties of CDM and PCDM deduced from physical measurements.

Table 8.1 *Properties of CDM and PCDM deduced from physical measurements.*

Property	Value
CDM unit cell description	triclinic
CDM volume	~2.28×10^{-28} m^3
RMS roughness of PCDM	28.28 nm (on ITO)
	51.79 nm (on Au)
PCDM band gap (E_g)	1.38 eV

8.2 Electrical characterisation

- RC circuits of ITO/PCDM/Al diodes have been used to model the dispersions in the admittance curves., at low and high frequencies, as a depletion layer and a bulk polymer region, with an additional finite electrode resistance. The dependence of device capacitance on applied voltage provided confirming evidence for the presence of a depletion region at the polymer/ITO interface but DC conduction through the device was too great to allow a definitive conclusion to be drawn. The effects of temperature, polymer film thickness and top contact material have also been investigated.

- The DC characteristics of the devices displayed little or no rectification. On the contrary the I-V plots were essentially independent of voltage polarity (except at the lowest voltages) but, surprisingly, were found to depend on the direction of the voltage sweep used to obtain the plots. Starting at + 5 V a form of trap-free SCLC was observed in which current, I, varied as V^3. With the sweep carried out in the opposite sense, a trap-modified SCLC was present with a trap-filled limit being reached at ~ 1 V from which a trap density and a trap depth were deduced. The appearance of this "hysteresis" has been explained as being due to configurational changes in the polymer around a trap or by the injection of a second conducting species with greater mobility.

- The lifetime of the conductance states, "high" and "low", have been investigated. The "low" state being stable for many months and the "high" state found to have lifetimes of approximately 2000 seconds when the device is tested at positive and negative bias.

Table 8.2 summarises the properties deduced from electrical measurements of ITO/PCDM/Al diodes with a 220 nm thick polymer film and a sample area of 2.5 mm^2.

Table 8.2 *Properties of a 200 nm thick PCDM film deduced from electrical measurements on ITO/PCDM/Al diodes. Sample area = 2.5 mm².*

Property	Value
Bulk capacitance (C_b)	$7x10^{-10}$ F
Depletion layer capacitance (C_d)	~$3.2x10^{-8}$ F
Relative permittivity (ε_r)	~7
Depletion layer width (W)	5 nm
Trap density (N_t)	$8x10^{21}$ m^{-3}
Activation energy (E_A)	~0.36 eV (complex impedance plot)
	0.45 eV (Arrhenius plot)

8.3 Command surface polymers

- A series of ethylene homopolymers has been prepared by both anodic and cathodic electropolymerisation. The rate of electropolymerisation (as judged by film thickness) was dependent on both the nature of the electropolymerisation and the structure of the monomer. Polymers grown under both anodic and cathodic conditions were found to be smooth with low RMS roughness, however, the anodically grown films were found to contain crevices suggesting a rigid, conjugated polymer structure.

- Polymerisation was confirmed using Raman spectroscopy to compare the spectra of the polymers with those of their respective monomers. The polymers all displayed peak broadening between 1200 and 1700 cm^{-1} indicative of polymerised C-C. In all cases the spectra of the cathodic and anodic polymers were different in detail consistent with different polymerisation schemes in the two cases.

Generally, a wide chemical and electrical characterisation of PCDM thin films, and to a lesser extent PBDT thin films, has been undertaken. Concurrently, a study of the growing conditions and physical properties of cathodically and anodically polymerised ethylene homopolymers has been completed. The results described above suggest that PCDM thin films have the potential for use in thin polymeric film

applications, such as the memory element described, and with careful design of the diode system, with respect to electrode choice and film quality, such applications as polymer LEDs.

PBDT appears to have too rough a topography to be useful for precision thin film devices but its large surface area and semiconducting properties could be used in the production of polymeric batteries and capacitors. The ability to grow ethylene homopolymers both cathodically and anodically has been found to produce polymers with different chemical conformations, useful for the generation of command surfaces.

8.4 Suggestions for further work

The electropolymerisation of PCDM has some drawbacks with respect to the surface morphology and homogeneity of the fabricated polymer thin films. A rough surface, as seen in the AFM micrographs, and the possibility of pin-hole formation are detrimental to the electrical characteristics of diodes subsequently formed using this polymer. The ability to solubilise the PCDM for use in thin film fabrication methods, such as spin coating would be advantageous. If the spin coating deposition could be controlled in such a manner to reduce the formation of pin-holes, this technique would give flat, homogeneous films with fewer possible experimental variables than electrpolymerisation, and hence more reproducible films.

Unfortunately PCDM is highly insoluble in organic solvents in its pristine state. However, some of the polymer modification methods suggested in section 3.1.2 could be used to aid in solublising the polymer. This could be achieved by two methods, addition of a solublising alkyl chain at the 3-position of the thiophene ring or by controlling the polymerisation to produce short chain oligomers;

1. Production of the alkyl substituted monomer could be realised using two different synthetic methods:

   Using 3-bromothiophene (1) as the starting product, the alkylthiophene (2) could be produced by nucleophilic substitution (Scheme 8.1). 3-bromo-4-alkylthiophene (3) can then be made by bromination of the alkylthiophene and the alkylated CDM

monomer (4) can then be produced using the synthetic method described in Appendix 1.

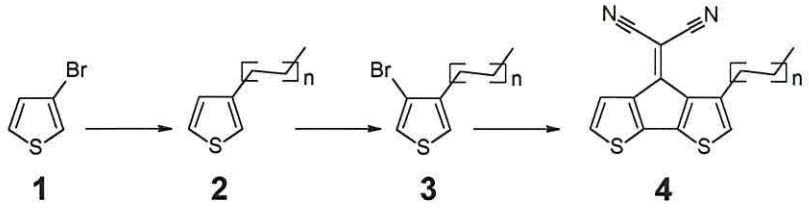

Scheme 8.1 *Synthesis of alkylated CDM* **4** *from 3-bromothiophene* **1**.

Alternatively, the alkylated monomer could be synthesised from CDT (1, Scheme 8.2). Bromination of the CDT gives 3-bromo-CDT (2) which could be converted 3-alkyl-CDT (3) and hence to alkylated CDM (4) as described in appendix 1 .

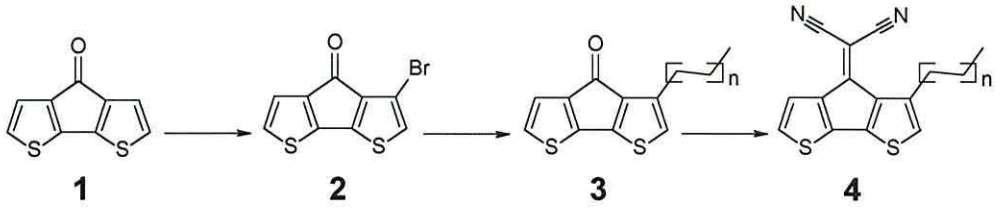

Scheme 8.2 *Synthesis of alkylated CDM* **4** *from CDT* **1**.

The synthetic route chosen will depend on the effect the presence of the alkyl chain has on the synthesis of the CDM monomer. The polymer can then be formed in solution and used in the fabrication of polymeric thin films.

2. Solubilisation of PCDM using short chain oligomers could be achieved by bromination of the CDM monomer in the 2-position (1, Scheme 8.3). Polymerisation can then be controlled by chemical means to give the dimer (2). Successive bromination steps of the of the 2-positions of the products can be used to produce the tetramer (3), hexamer etc. These short chain moieties can then be used for device fabrication which may have different characteristics to the long chain polymers already fabricated.

The soluble polymer could then be used for producing FET's as growing films across interdigitated electrodes, a process that has been found to be problematic by electropolymerisation [199], would now be possible. Short chain oligomers have also been found to possess interesting characteristics in their crystalline state. A similar

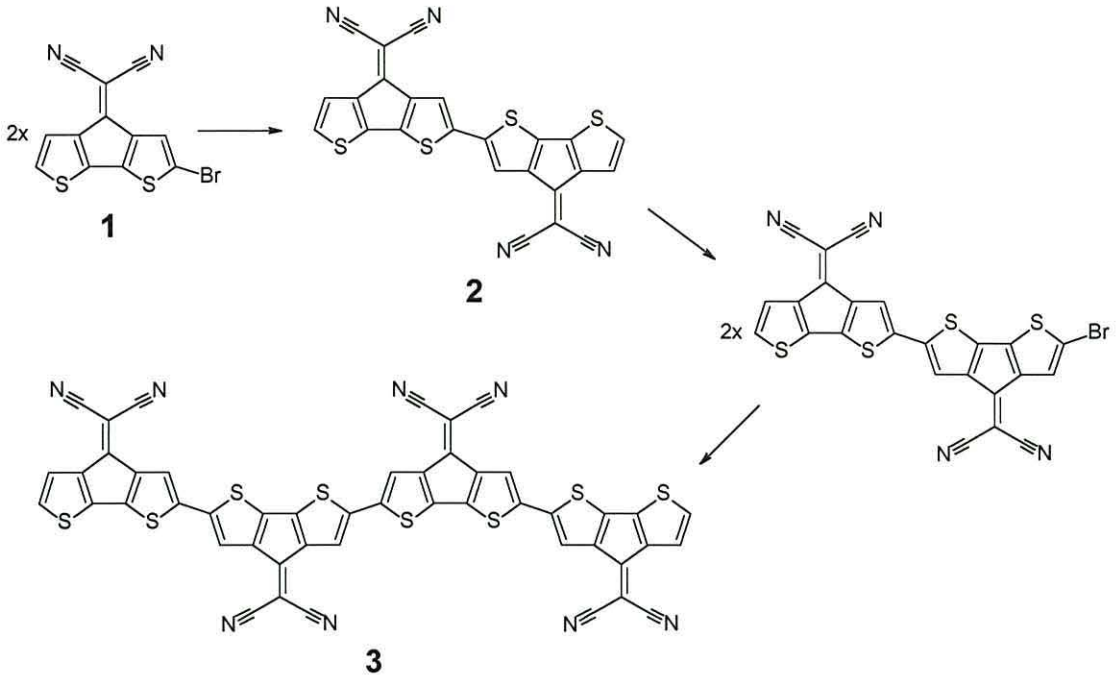

Scheme 8.3 *Synthesis of short chain oligomers of PCDM.*

oligomer, a-sexithiophene [200], has been used as the semiconducting channel between the source and drain electrodes in a flexible polymeric MISFET as described in section 3.4.2.2.

The discovery of switching behaviour in the PCDM polymeric diodes needs further investigation to try to understand the processes occurring when this phenomenon occurs, and to try to optimise the effect for possible use as a stable, low-voltage memory element. Possible investigations into temperature effects, the effect of exposure to light and the effect of altering the electrical measurement conditions, such as the magnitude of the initial applied voltage, could be carried out. Physical characterisation, similar to the initial results published here would have to be undertaken to identify whether there is any structural change in the polymer upon switching from one conducting state to another. Finally, the optimised device would need to be integrated into a viable circuit for use as a memory device.

Appendix 1. Chemical synthesis of CDM monomer

The synthesis of CDM monomer is given with the reaction scheme separated into sections for each reaction. NMR analysis is given for the major products of the reaction scheme.

A1.1 Reaction 1. Preparation of bis(3-thienyl)ketone

A1.1.1 Preparation of bis(3-thienyl)methanol

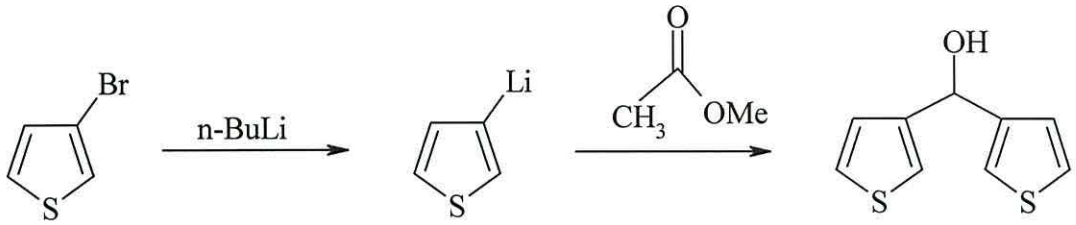

1 **2**

Scheme A1.1 *Production of bis(3-thienyl)methanol* **2**.

3-Bromothiophene **1** (0.184 M, 30 g) was dissolved in hexane (120 ml), by stirring under argon, and then cooled to -30 °C. N-butyllithium, BuLi, (2.35 M, 86 ml) was added to the solution and then tetrahydrofuran, THF, (20 ml) was added drop-wise. On addition of the THF the solution turned yellow and a white precipitate was formed. The reaction was allowed to warm to room temperature and the top layer was decanted under nitrogen. The solution was re-cooled to -30 °C and a solution of methyl formate (0.092 M, 5.66 ml) in THF (100 ml) added. The reaction mixture was then stirred continuously under argon for four hours.

Work up

Water (100 ml), saturated ammonium chloride, NH_4Cl, (100 ml) and ether (100 ml) were added to the reaction mixture in a separating funnel. The organic fractions were collected and the aqueous layers washed with ether.

Brine was added to the organic fraction, the solution was dried over magnesium sulphate, $MgSO_4$, and filtered. The organic fraction was then condensed by vacuum extraction and passed through a silica pad (30 g) washing with copious amounts of ether. The solvent was removed by vacuum extraction leaving a brown oil.

The oil was decolourised by adding activating charcoal and ether (20 ml) and heating the mixture. Petrol (20 ml) was added giving a precipitate which was decanted off. The decolourisation was repeated two more times.

1.1.2 Preparation of bis(3-thienyl)ketone

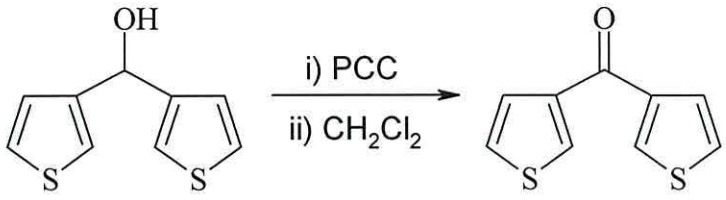

2 **3**

Scheme A1.2 *Production of bis(3-thienyl)ketone* **3**.

Dichloromethane (200 ml) was added to the bis(3-thienyl)methanol **2** (8.12 g) and cooled to 0 °C under argon. Pyridinium chlorochromate, PCC, (0.06 mM, 12.93 g) was added drop-wise and the solution stirred for 1 hour at 0 °C. The solution was then allowed to warm to room temperature and stirred overnight under argon.

Work up

The solution was worked up using a hexane column. The contents of the reaction mixture were added to the column and then eluted using a 50:50 ethyl acetate/petrol mixture. The yellow/orange filtrate was concentrated under vacuum and ethyl acetate added. The solvent was removed under vacuum extraction leaving a brown oil.

The oil was dissolved in ether (30 ml), activated charcoal added and the solution heated. Petrol (30 ml) was added to the solution and the liquid phase decanted. The decolourisation was repeated four more times, the solution evaporated to dryness under vacuum giving 3.6 g of product **3** (% yield = 44.79%). The NMR spectrum for the product is given in figure A1.1.

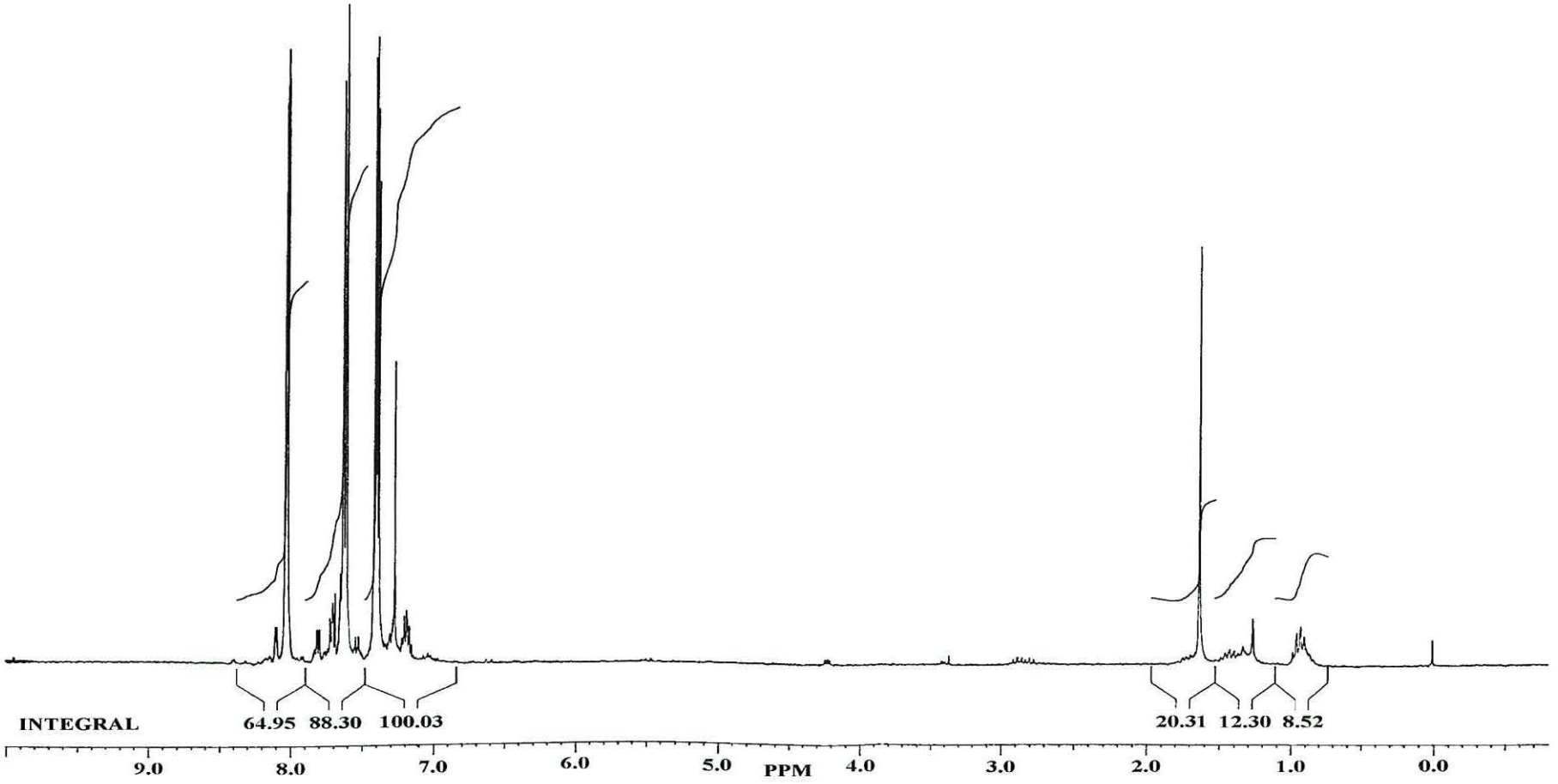

Figure A1.1 *NMR spectrum of bis(3-thienyl)ketone* **3.**

Reaction 1 was repeated a number of times to produce enough product to continue with the next step of the reaction. The successful products were combined and recrystallised in hexane. Activating charcoal was added and the solution heated. On filtration, the major fraction produced crystals, the remainder was passed through a column chromatograph to obtain **2**. 25.3 g of product **3** was obtained.

Table A1.1 gives the interpretation of the NMR spectrum shown in figure A1.1. The chemical shift (δ) is measured in parts per million (ppm). Also given are the peak type (multiplet, doublet, singlet) and the peak identification, whether it is due to the solvent, the reactants or the product. A list of the possible solvent contaminants is given and, for the less complicated spectra, the peaks are assigned to specific protons on the product.

Table A1.1 *NMR interpretation of figure A1.1.*

δ (ppm)	Peak type	Peak identification
0.9	multiplet	solvent peak
1.3	multiplet	solvent peak
1.6	singlet	solvent peak
7.25	singlet	product peak
7.4	quartet	product peak
7.6	doublet	product peak
8.05	quartet	product peak

Possible solvent contaminants : Petrol, Ether, Ethyl acetate, Hexane.

A1.2 Reaction 2. Preparation of 2,2-bis(3-thienyl)-1,3-dioxalan

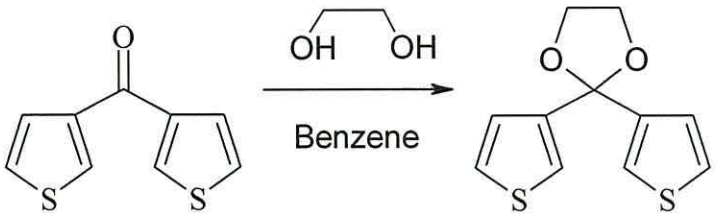

3 **4**

Scheme A1.3 *Production of 2,2-bis(3-thienyl)-1,3-dioxalan* **4**.

The ketone **3** (25.3 g) was added to three equivalents of ethylene glycol (0.39 M, 21.5 ml) and then 1 microspatula of toluene sulphonic acid (TSA) added. The solution was refluxed using Dean-Stark apparatus (Figure A1.2) for four days, removing water from the reaction vessel.

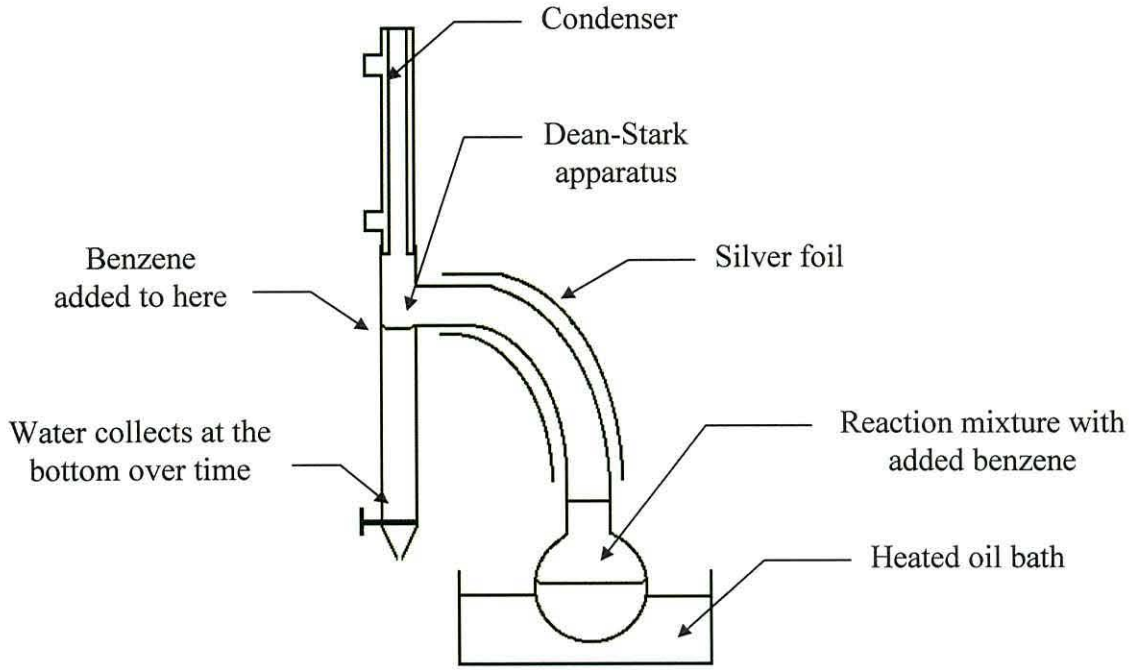

Figure A1.2 *Dean-Stark apparatus.*

Work up

The solution was recrystallised using ether (100 ml) and then redissolved, in a separating funnel, with ether (100 ml) and sodium hydrogen carbonate, $NaHCO_3$, (100 ml). The organic fraction was collected and the aqueous fraction washed with ether. The organic fraction was dried over $MgSO_4$, filtered and concentrated under vacuum.

The crude product was added to ether (100 ml) and heated under reflux conditions. Petrol (100 ml) was added and then small portions of dichloromethane were added until the crude product dissolved into solution. The solution was then allowed to recrystallise in a freezer overnight and the liquid decanted off. The pale yellow crystals of **4** were washed in petrol and dried. (thin layer chromatography: RF = 0.41 in 20% ether/petrol) (NMR: Figure A1.3(a) and (b)).

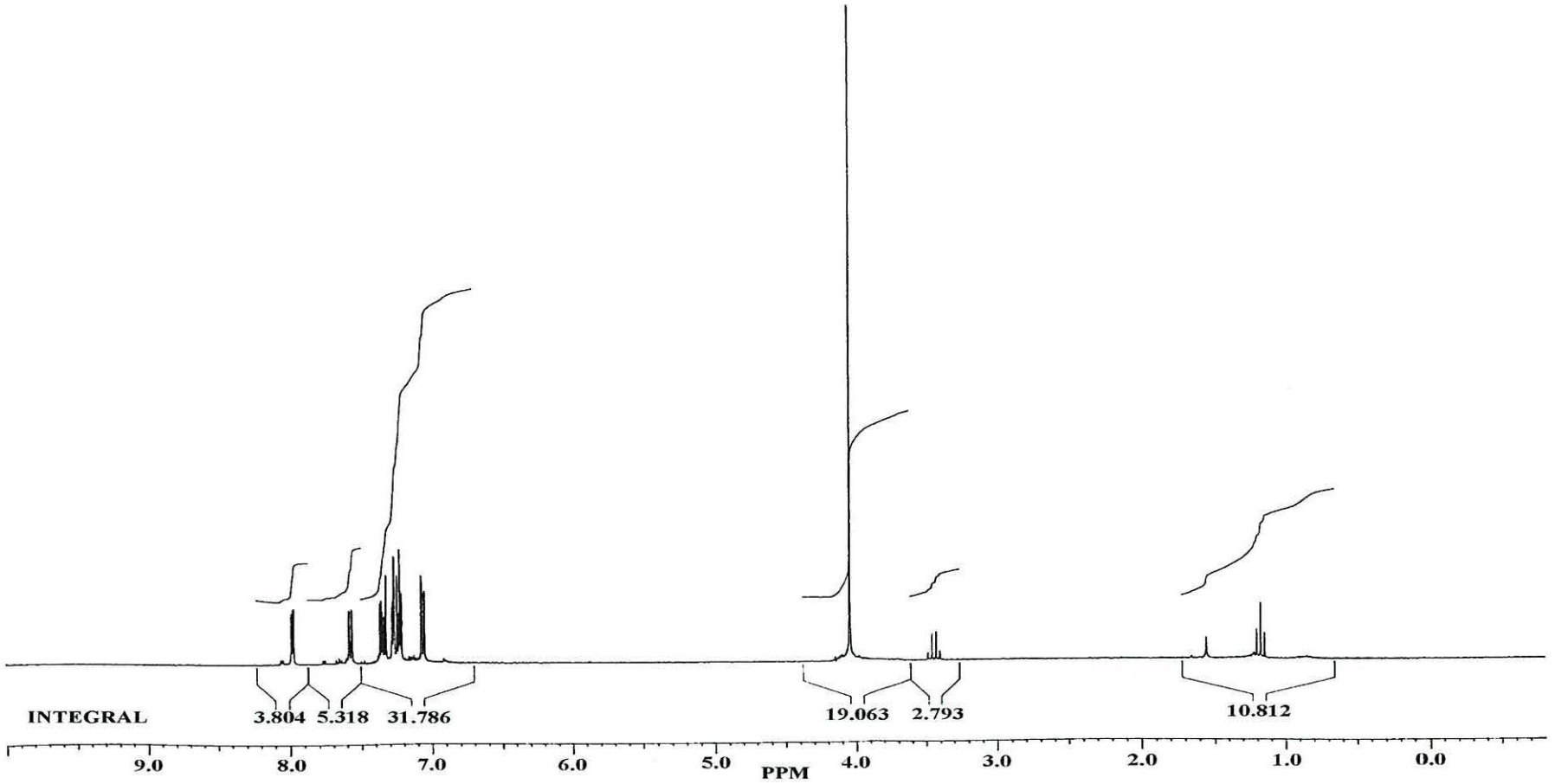

Figure A1.3(a) *NMR spectrum of 2,2-bis(3-thienyl)-1,3-dioxolan* **4** *showing peaks due to contaminants.*

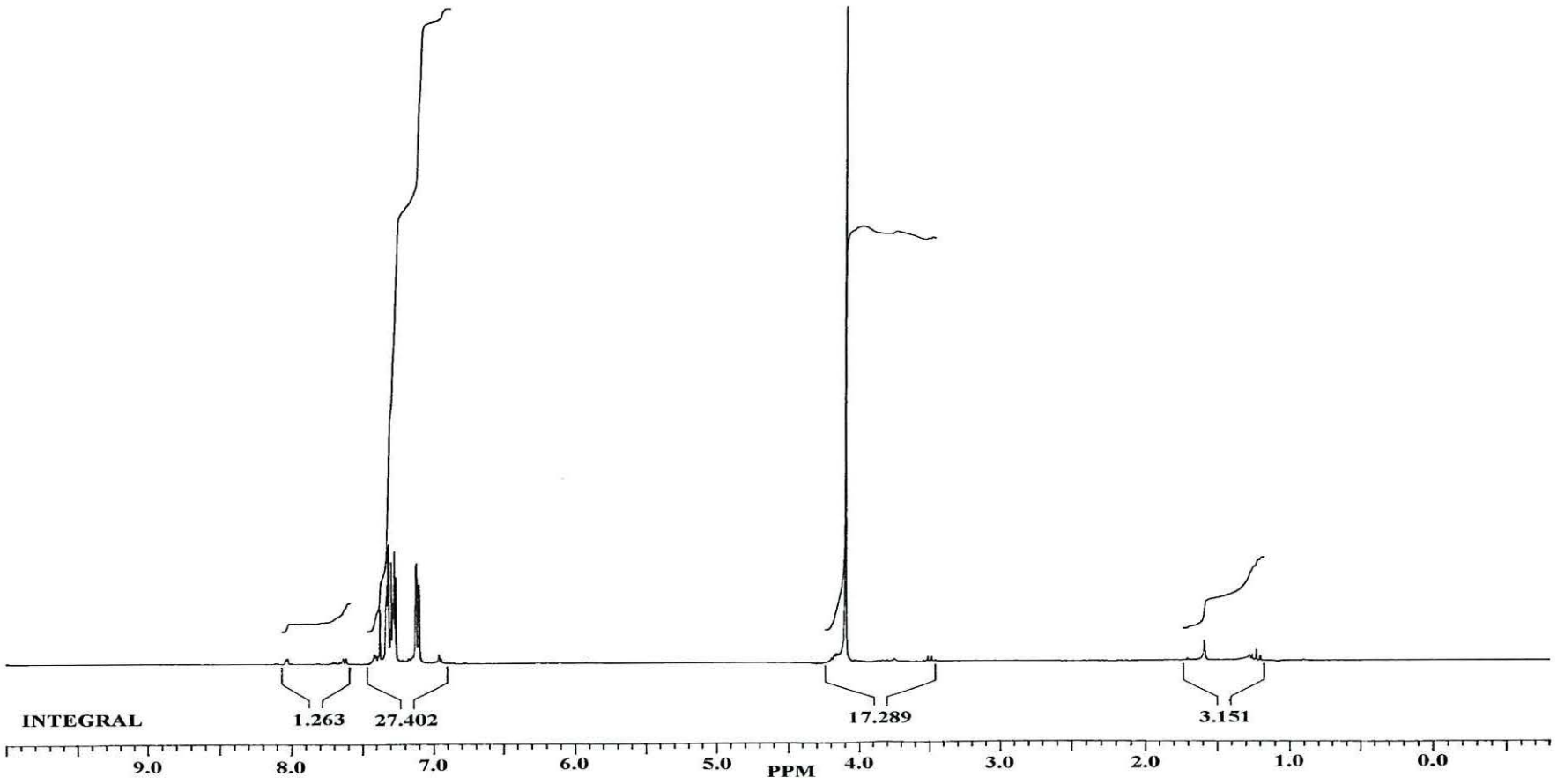

Figure A1.3(b) *Repeat NMR spectrum of 2,2-bis(3-thienyl)-1,3-dioxalan* **4.**

Table A1.2 *NMR interpretation of figure A1.3(a).*

δ (ppm)	Peak type	Peak identification
1.2	triplet	solvent peak
1.6	singlet	solvent peak
3.45	quartet	solvent peak
4	singlet	protecting group protons
7.1	multiplet	product peak
7.3	multiplet	product peak
7.4	multiplet	product peak
7.6	doublet	reactant peak
8	doublet	reactant peak

Possible solvent contaminants : Petrol, Dichloromethane, Ether.

Table A1.3 *NMR interpretation of figure A1.3(b).*

δ (ppm)	Peak type	Peak identification
1.4	triplet	solvent peak
1.6	singlet	solvent peak
3.5	quartet	solvent peak
4.15	singlet	protecting group protons
7.15	multiplet	product peak
7.3	multiplet	product peak
7.6	doublet	reactant peak
8	doublet	reactant peak

In figure A1.3(b), the reactant peaks are much smaller than in figure A1.3(a) suggesting that the reaction has proceeded to completion. Interpretation of the integrals for figure A1.3(b) is given in table A1.4. The chemical shift and corresponding integral height, measured by hand, are given. The integral values shown in the NMR spectra are not used because they tend to include the result for more than one set of proton signals. The number of protons is calculated from the integral heights using the equations,

$$x = \frac{\Sigma(\text{integral heights})}{\text{Number of protons on the molecule}}, \qquad \text{(A1.1)}$$

$$\text{Number of protons} = \frac{\text{integral height}}{x}, \qquad \text{(A1.2)}$$

The value calculated is rounded to the nearest integer and the proton type can be identified, the positioning of the protons on the molecule is then displayed in figure A1.4. This process is repeated for each of the NMR spectra.

Table A1.4 *Integral interpretation of figure A1.3(b).*

δ (ppm)	Integral height (mm)	Number of protons	Proton identification
4.15	122	4	protecting group protons
7.15	56	2	protons in 3-position on thiophene ring
7.3	129	4	protons in 2-position on thiophene ring

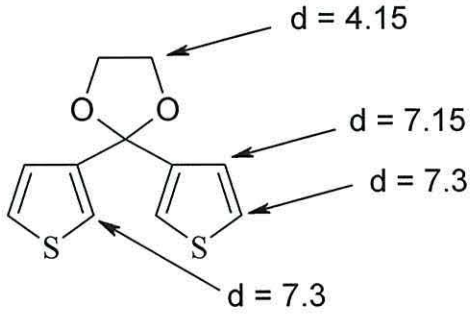

Figure A1.4 *Proton positions in 2,2-bis(3-thienyl)-1,3-dioxalan.*

A1.3 Reaction 3. Preparation of 2,2-bis(2-iodo-3-thienyl)-1,3-dioxalan

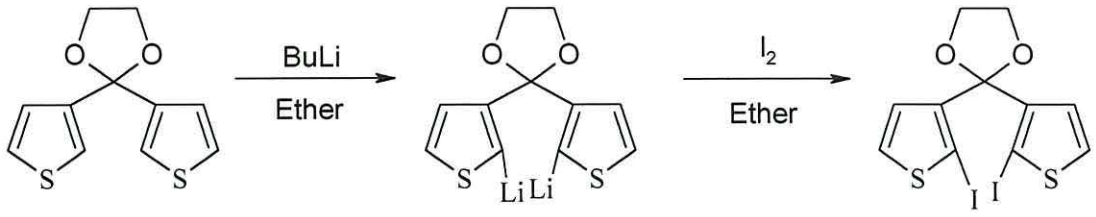

4 **5**

Scheme A1.4 *Production of 2,2-bis(2-iodo-3-thienyl)-1,3-dioxalan* **5**.

The dioxalan crystals **4** (0.042 M, 10.04 g) were suspended in ether (100 ml) and cooled to -40 °C. 2.2 equivalents of BuLi (0.09 M (1.66 M titrated in dry ether), 54.2 ml) was added drop-wise and stirred for 30 minutes. Iodine (26.67 g) was dissolved in ether (200 ml) and added drop-wise to the solution. The solution was then allowed to warm to room temperature and stirred for a further 1.5 hours.

Work up

Water (2 x 50 ml) and saturated sodium sulphate, $Na_2(S_2O_3)$, (2 x 50 ml) was added to the solution and the organic layer extracted twice. The organic layer was washed with brine (100 ml) and then ether, and subsequently dried over $MgSO_4$. The solvents were removed by vacuum.

After NMR analysis, it was found that this reaction had not proceeded to completion and was repeated using the end product as the repeat experiment start material, using the assumption that all of **4** was still present. This produced 18.28 g of crude product which was recrystallised using petrol (60-80 °C petrol fraction), ether and dichloromethane to give 9.5 g of crystallised product. (% yield = 56.58 % (NMR: Figure A1.5)).

Table A1.5 *NMR interpretation of figure A1.5.*

δ (ppm)	Peak type	Peak identification
0.9 - 1.8	multiplets	solvent peaks
3.2	triplet	solvent peak
4.1	singlet	protecting group protons
7	doublet	product peak
7.35	doublet	product peak

Possible solvent contaminants : Petrol, Ether.

The integral calculations for figure A1.5 verify that the protons at approximately 7.3 ppm are the 2-position protons as two of these protons are replaced by iodine going from 2,2-bis(3-thienyl)-1,3-dioxalan to 2,2-bis(2-iodo-3-thienyl)-1,2-dioxalan. The protons at the 2-position are further down-field than those in the 3-position due to a stronger inductive effect from the neighbouring, electropositive sulphur atom.

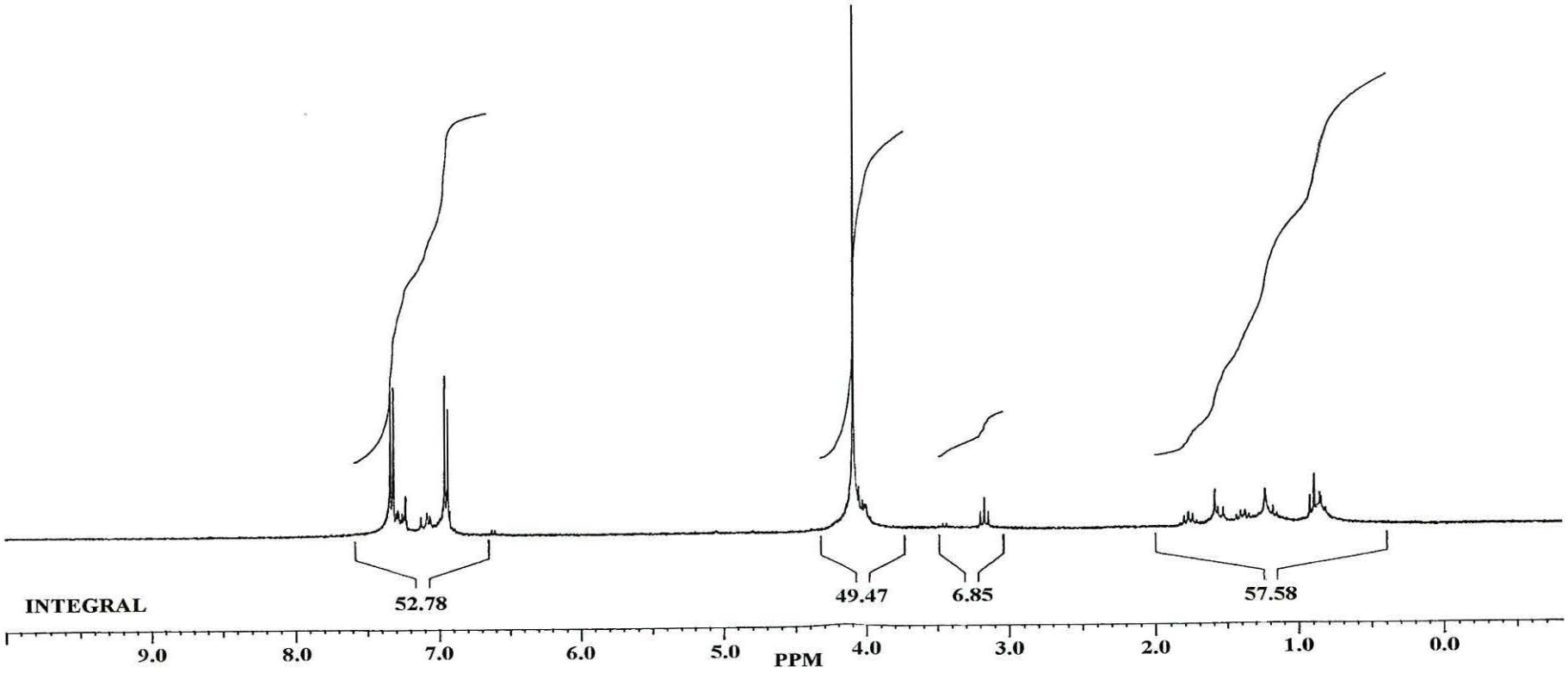

Figure A1.5 *NMR spectrum of 2,2-bis(2-iodo-3-thienyl)-1,3-dioxalan* **5.**

Table A1.6 *Integral interpretation of figure A1.5.*

δ (ppm)	Integral height (mm)	Number of protons	Proton identification
4.1	87	4	protecting group protons
7	43	2	protons in 3-position on thiophene ring
7.35	48	2	protons in 2-position on thiophene ring

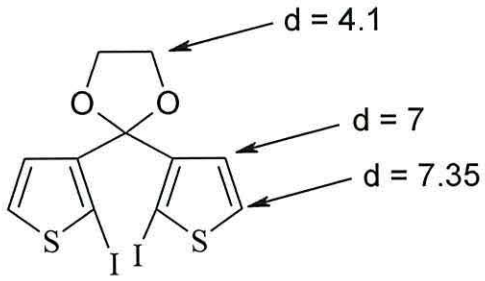

Figure A1.6 *Proton positions in 2,2-bis(2-iodo-3-thienyl)-1,3-dioxalan.*

A1.4 Reaction 4. Preparation of cyclopenta[2,1-b:3,4-b']dithiophen-7-one (CDT)

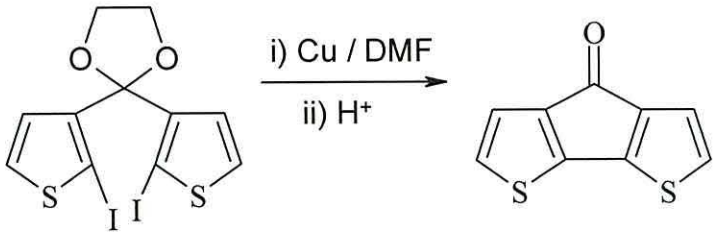

5 **6**

Scheme A1.5 *Production of cyclopenta[2,1-b:3,4-b']dithiophen-7-one (CDT)* **6.**

Copper powder (3.96 g) and the iododioxalan **5** (0.019 M, 9.5 g) were dissolved in dimethyl formamide, DMF, (80 ml) and refluxed in the absence of light for 24 hours at 150 - 160 °C. Concentrated hydrochloric acid (150 ml) was then added.

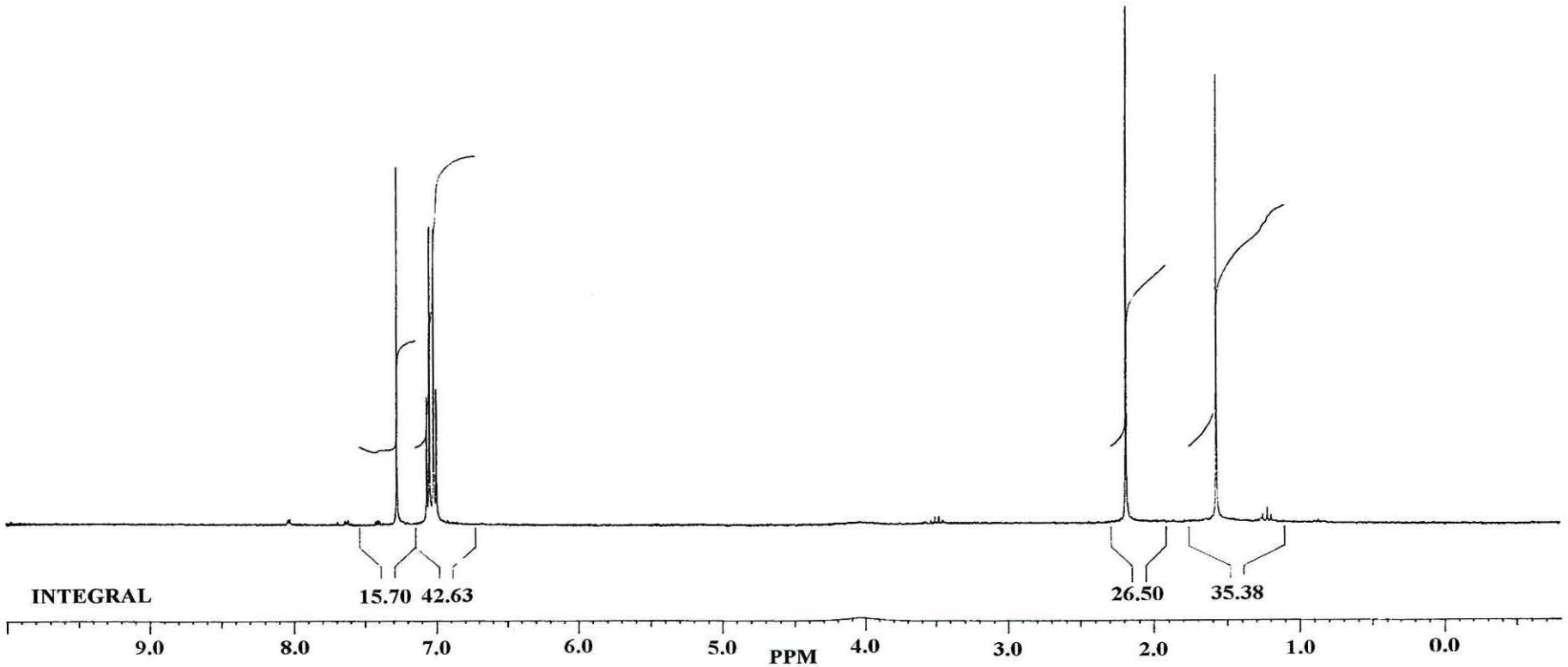

Figure A1.7 *NMR spectrum of CDT* **6.**

Work up

Water (500 ml) was added to the stirred solution and then transferred to a separating funnel and ether (200 ml) added. The organic layer was collected and the aqueous layer extracted with ether (2 x 200 ml). The organic layer was then washed with 2N-hydrochloric acid (2 x 100 ml) and aqueous sodium hydrogen carbonate added before drying over $MgSO_4$ and concentrating under vacuum.

Recrystallisation from ethanol and chloroform gave 2.22 g of crystallised product **6**. (% yield = 48.44 % (NMR: Figure A1.7)).

Table A1.7 *NMR interpretation of figure A1.7.*

δ (ppm)	Peak type	Peak identification
1.6	singlet	solvent peak
2.2	singlet	solvent peak
7	doublet	product peak
7.05	doublet	product peak
7.25	singlet	solvent peak

Possible solvent contaminants : Water, Ethanol, Chloroform.

The peaks at 7 ppm and 7.05 ppm in figure A1.7 can be considered as a pair of doublets in an A-B splitting pattern rather than a quartet corresponding to the protons in the 2- and 3- positions of the thiophene rings.

Table A1.8 *Integral interpretation of figure A1.7.*

δ (ppm)	Integral height (mm)	Number of protons	Proton identification
7	38	2	protons in 3-position on thiophene ring
7.05	37	2	protons in 2-position on thiophene ring

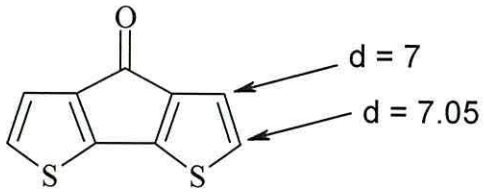

Figure A1.8 *Proton positions in CDT.*

A1.5 Reaction 5. Preparation of 4-dicyanomethylene-4H-cyclopenta[2,1-b:3,4-b']dithiophene (CDM)

Malonitrile (0.011 M, 0.726 g) was added to the CDT **6** (0.011 M, 2.22 g) and both dissolved in ethanol (60 ml). Piperidine (approximately 8 drops) was added and the solution stirred for four hours. The reaction was quenched with water (100 ml) and stirred. A brown precipitate was formed which was filtered out and washed with the filtrate.

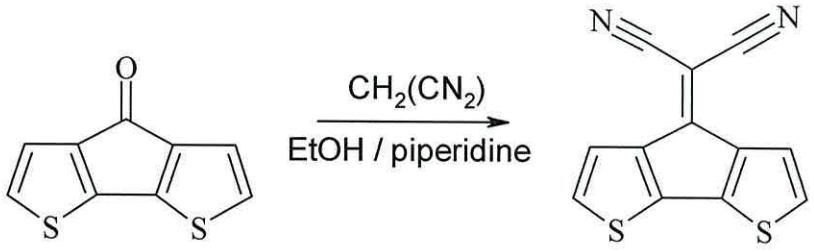

6 **7**

Scheme A1.6 *Production of 4-dicyanomethylene-4H-cyclopenta[2,1-b:3,4-b']dithiophene (CDM)* **7**.

Work up

The precipitate was recrystallised from acetonitrile and chloroform and removed from solution by filtration. 0.68 g of purple/brown crystals were obtained. (% yield = 24.5 % (NMR: Figure A1.9)).

The NMR spectrum for the new monomer (Figure A1.9) was compared to one of a CDM monomer sample produced one year previously (Figure A1.10).

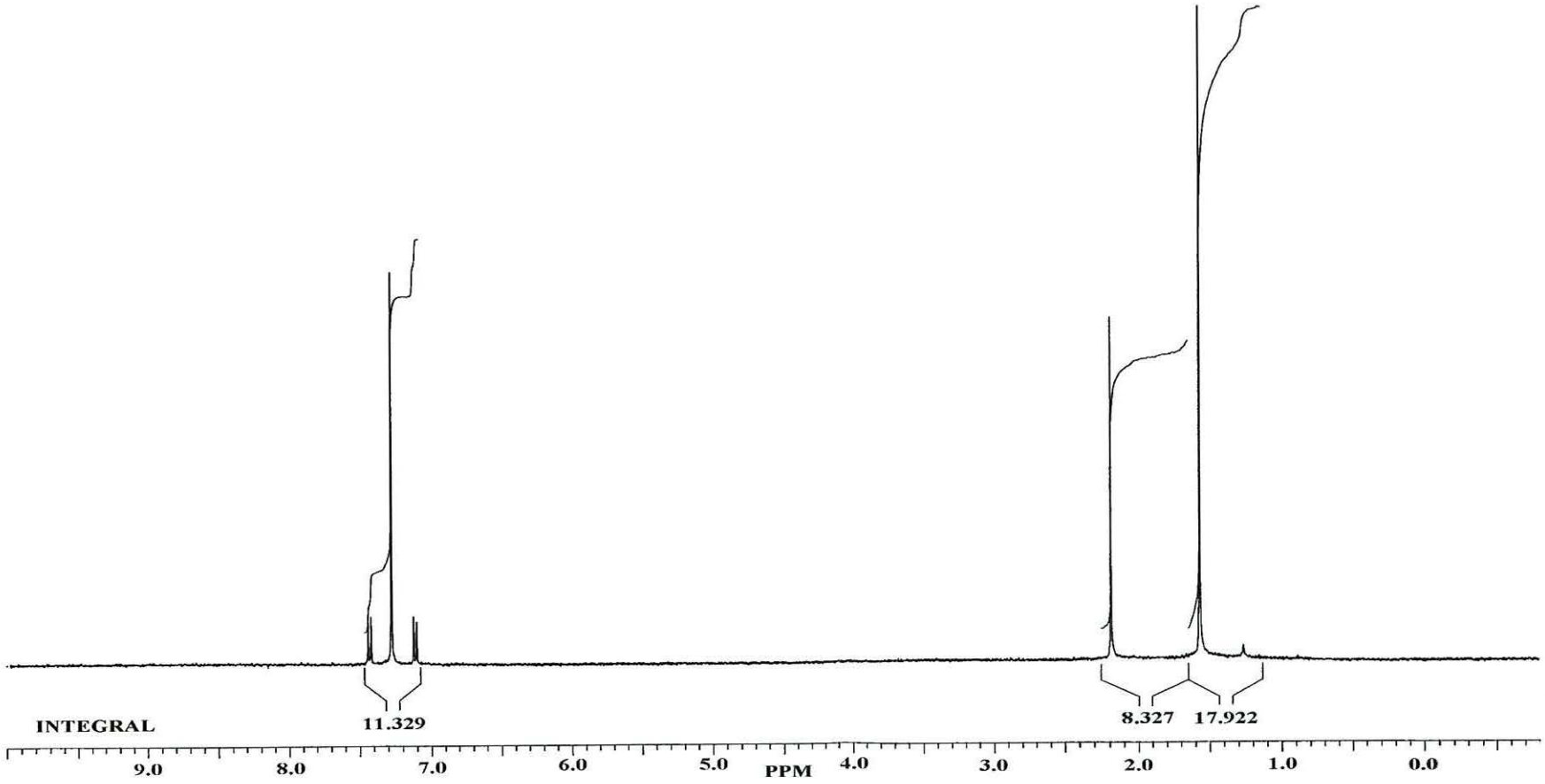

Figure A1.9 *NMR spectrum of CDM* **7.**

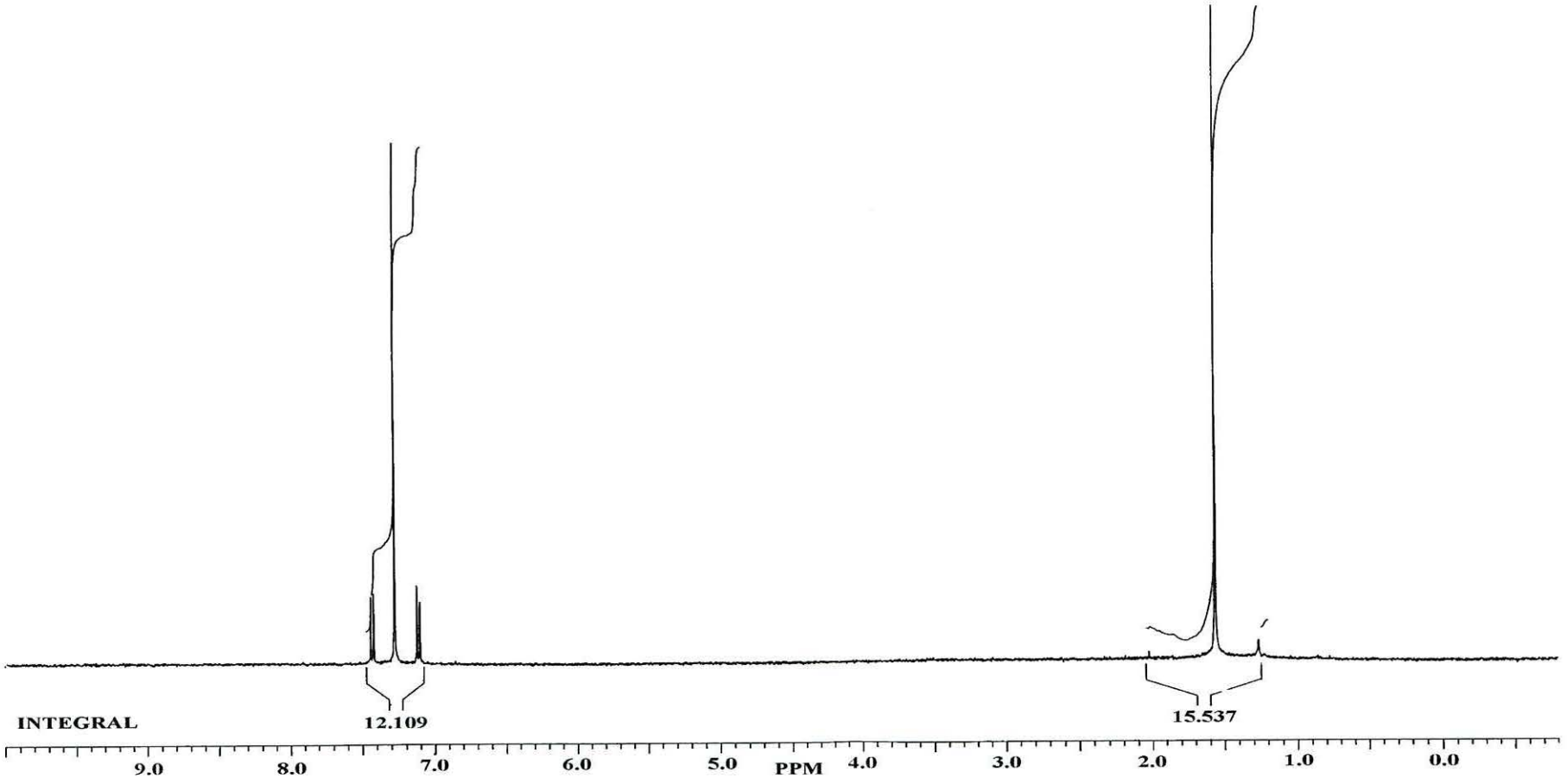

Figure A1.10 *NMR spectrum of a 1 year old sample of CDM showing the stability of the protons over this time.*

Table A1.9 *NMR interpretation of figure A1.9.*

δ (ppm)	Peak type	Peak identification
1.5	singlet	solvent peak
2.2	singlet	solvent peak
7.1	doublet	product peak
7.25	singlet	solvent peak
7.45	doublet	product peak

Possible solvent contaminants : Water, Ethanol, Acetone, Chloroform.

The proton peaks at 7 and 7.4 ppm are present in both complexes suggesting that the protons on the old CDM monomer are unchanged over time and that no contaminant protons are present. Differences occur only in the amounts of solvent present in the end product. The peak at approximately 1.5 ppm in both samples was due to atmospheric water vapour which could not be excluded from the NMR apparatus. At approximately 2.2 ppm in figure A1.7 is a peak due to the presence of acetone ($(CH_3)_2CO$) used during the synthesis to clean reaction vessels etc. This peak was found to disappear after the monomer had spent some time under vacuum and it is presumed that any of the volatile acetone in the solid sample evaporates over time. The peak at approximately 7.25 ppm, bisecting the monomer hydrogen peaks, was due to the solvent, trichloromethane ($CHCl_3$), used to dissolve the CDM prior to NMR analysis.

Table A1.10. *Integral interpretation of figure A1.9.*

δ (ppm)	Integral height (mm)	Number of protons	Proton identification
7.1	18	2	protons in 3-position on thiophene ring
7.45	18	2	protons in 2-position on thiophene ring

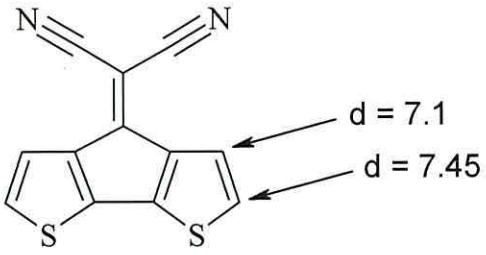

Figure A1.11 *Proton positions in CDM.*

Appendix 2. Mathematical modelling

To interpret the impedance and admittance data obtained for the PCDM plots, mathematical expressions were derived for the equivalent circuit given in figure 2.12.

A2.1 AC analysis of the polymer diode circuit

In view of the similarities between the present results and previous work on polymeric Schottky diodes [156] it will be assumed that the low-frequency admittance data can be modelled by a series-parallel combination of capacitances and resistances representing the depletion and bulk regions of the diode (figure A2.1(a)). The high frequency dispersion may then be accounted for by including a resistance R_S to represent the series resistance associated with an electrode [201] (figure A2.1(b)), probably the ITO substrate since the high frequency dispersion is absent when diodes are formed on gold.

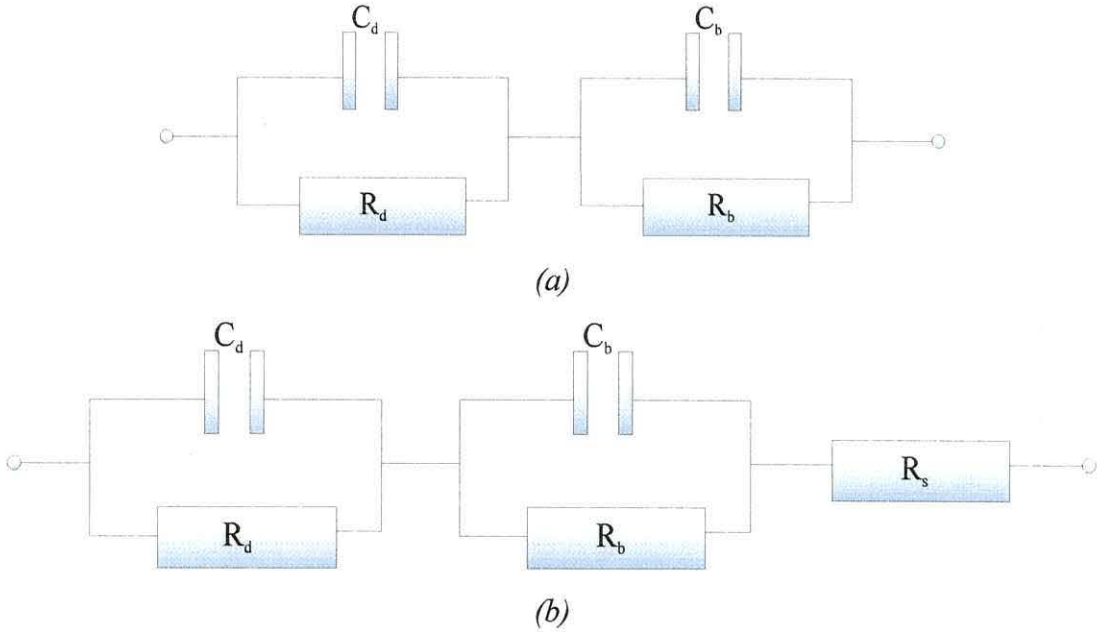

Figure A2.1. *Equivalent circuits for (a) a polymeric diode and (b) a diode with an additional series resistance.*

It is readily shown that the equivalent circuit in figure A2.1(a) may be represented by a capacitance C_P in parallel with a conductance G_P so that the

admittance Y_P of the diode can be written as

$$Y_P = G_P + j\omega C_P \tag{A2.5}$$

where

$$C_P = C_g + \frac{C_{LF} - C_g}{1+(\omega\tau_{LF})^2} \tag{A2.6}$$

$$G_P = G_{LF} + \frac{G_a}{1+(\omega\tau_{LF})^2}. \tag{A2.7}$$

Here $C_g = (C_dC_b/(C_d+C_b))$ is the series sum of the barrier and bulk capcitances, C_{LF} the effective low-frequency capacitance of the structure given by

$$C_{LF} = \frac{C_dR_d^2 + C_bR_b^2}{(R_d+R_b)^2} \tag{A2.8}$$

and G_{LF} the low frequency or DC conductance $(R_d+R_b)^{-1}$. The AC conductance, G_a is given by

$$G_a = \omega^2 \frac{R_dR_b(R_dC_d - R_bC_b)^2}{(R_d+R_b)^3} \tag{A2.9}$$

and τ_{LF} the circuit relaxation time by

$$\tau_{LF} = \frac{R_dR_b}{R_d+R_b}(C_d+C_b). \tag{A2.10}$$

Therefore, the circuit displays a Debye-like dispersion [202] and at low frequency, it is readily seen that so long as $R_d >> R_b$, then $C_P \sim C_d$ and $G_P \sim R_d^{-1}$. At high frequency $C_P = C_bC_d/(C_d+C_b)$ which reduces to $C_P \sim C_b$ if $C_d >> C_d$. In the presence of a series resistance, R_S, as in figure A2.1(b) the impedance of the series-parallel network is given by,

$$Z = \frac{1}{\frac{1}{R_d} + j\omega C_d} + \frac{1}{\frac{1}{R_b} + j\omega C_b} + R_s \tag{A2.11}$$

Multiplying the first and second terms by their respective resistances, R_d and R_b,

$$Z = \frac{R_d}{1+j\omega C_dR_d} + \frac{R_b}{1+j\omega C_bR_b} + R_s \tag{A2.12}$$

Rearranging equation A2.12 to produce a common denominator,

$$Z = \frac{R_d\left(1+j\omega C_b R_b\right)+R_b\left(1+j\omega C_d R_d\right)+R_s\left(1+j\omega C_b R_b\right)\left(1+j\omega C_d R_d\right)}{\left(1+j\omega C_b R_b\right)\left(1+j\omega C_d R_d\right)} \quad \text{(A2.13)}$$

The impedance is related to the admittance by the relationship,

$$Y = \frac{1}{Z} \quad \text{(A2.14)}$$

Therefore, substituting A2.13 into A2.14 and separating the real and imaginary parts of the equation gives,

$$Y = \frac{1}{\dfrac{R_b}{1+C_b^2R_b^2\omega^2}+\dfrac{R_d}{1+C_d^2R_d^2\omega^2}+R_s-j\left(\dfrac{C_bR_b^2\omega}{1+C_b^2R_b^2\omega^2}+\dfrac{C_dR_d^2\omega}{1+C_d^2R_d^2\omega^2}\right)} \quad \text{(A2.15)}$$

The admittance can also be related to the total capacitance (C_T) and conductance (G_T) of the system by the relationship,

$$Y = G_T + j\omega G_T \quad \text{(A2.16)}$$

After expanding equation A2.15, the conductance can then be expressed as,

$$G_T = \frac{C_d^2R_d^2\omega^2\left(C_b^2R_b^2R_s\omega^2+R_b+R_s\right)+}{C_d^2R_d^2\omega^2\left(C_b^2R_b^2R_s^2\omega^2+\left(R_b+R_s\right)^2\right)+}\Bigg\| \frac{C_b^2R_b^2\omega^2\left(R_d+R_s\right)+R_d+R_b+R_s}{2C_dC_bR_d^2R_b^2\omega^2+C_b^2R_b^2\omega^2\left(R_d+R_s\right)^2+\left(R_d+R_b+R_s\right)^2} \quad \text{(A2.17)}$$

Placing limits on equation A2.17, as $\omega \to 0$,

$$G_T \approx \frac{1}{R_d+R_b+R_s} \quad \text{(A2.18)}$$

Let $R_d = \infty$

$$G_T \approx 0 \quad \text{(A2.19)}$$

Dividing equation A2.11 by $\omega^4C_1^2R_1^2C_2^2R_2^2R_s$ and allowing $\omega \to \infty$,

$$G_T \approx \frac{1}{R_s} \quad \text{(A2.20)}$$

The capacitance can be expressed as,

$$C_T = \frac{C_d^2C_bR_d^2R_b^2\omega^2+}{C_d^2R_d^2\omega^2\left(C_b^2R_b^2R_s^2\omega^2+\left(R_b+R_s\right)^2\right)+}\Bigg\| \frac{C_dR_d^2\left(1+C_b^2R_b^2\omega^2\right)+C_bR_b^2}{2C_dC_bR_d^2R_b^2\omega^2+C_b^2R_b^2\omega^2\left(R_d+R_s\right)^2+\left(R_d+R_b+R_s\right)^2} \quad \text{(A2.21)}$$

Placing limits on equation A2.21, as $\omega \rightarrow 0$,

$$C_T \approx \frac{C_d R_d^2 + C_b R_b^2}{R_d^2 + R_b^2 + R_s^2 + 2R_d R_b + 2R_d R_s + 2R_b R_s} \quad \text{(A2.22)}$$

Let $R_d = \infty$

$$C_T \approx C_d \quad \text{(A2.23)}$$

Dividing equation A2.21 by $\omega^4 C_1^2 R_1^2 C_2^2 R_2^2 R_s$ and allowing $\omega \rightarrow \infty$,

$$C_T \approx 0 \quad \text{(A2.24)}$$

Equations A2.17 and A2.21 may be re-written, where,

$$C_T = \frac{C_P R_P^2}{\left(R_P + R_S\right)^2 + \omega^2 C_P^2 R_P^2 R_S^2}, \quad \text{(A2.25)}$$

$$G_T = \frac{\left(R_P + R_S\right) + \omega^2 C_P^2 R_P^2 R_S}{\left(R_P + R_S\right)^2 + \omega^2 C_P^2 R_P^2 R_S^2} \quad \text{(A2.26)}$$

and $R_P = G_P^{-1}$. Again, a Debye-like dispersion is expected though now modified by the frequency dependence of C_P and G_P. For two well-separated processes and so long as $R_S << R_P$ then the relaxation time, τ_{HF}, of this second, higher frequency dispersion is given by

$$\tau_{HF} = C_P R_S . \quad \text{(A2.28)}$$

A2.2 Impedance plots

The capacitance and loss data can be used to produce impedance data, in the form of real versus imaginary impedance, using the inverse relationship with admittance,

$$Z = \frac{1}{Y} = \frac{1}{G + j\omega C} \quad \text{(A2.1)}$$

Where, Z is the impedance, Y is the admittance, C_p and G_p are the capacitance and conductance respectively, ω is the angular frequency and j is an imaginary number. Multiplying out and separating the real and imaginary parts of equation A2.1 gives,

$$Z = \frac{G}{G^2 + \omega^2 C^2} - j\omega \frac{C}{G^2 + \omega^2 C^2} \quad \text{(A2.2)}$$

Therefore,

$$\text{Real impedance, } Z' = \frac{G}{G^2 + \omega^2 C^2} \tag{A2.3}$$

$$\text{Imaginary impedance, } Z'' = \frac{\omega C}{G^2 + \omega^2 C^2} \tag{A2.4}$$

Replacing C_p and G_p with their respective values and plotting Z' versus Z'' produces the impedance plot.

Appendix 3. Polymer displacement by laser exposure

The ability to shape polymers on the surface of substrates is necessary to produce polymeric circuitry and polymer based optoelectronics. Printing [203] and photolithography [204] have been used to this end but both can be lengthy processes. Post polymerisation etching of the polymer, using laser or UV light, could be used as an alternative. A review of the fundamentals of ablation and surface processing of polymers has been completed by various authors [205] and applications include machining of high surface quality, microscopic circuit parts [206, 207] and etching of sensing electrodes for electrochemical gas sensors [208]. Sputtering of polymer, from a substrate surface using laser radiation, for deposition on other surfaces, including other polymers, could also be possible [207].

A3.1 Polymer displacement

An interesting side effect of analysis of the PCDM polymer using Raman spectroscopy was an apparent colour change of the polymer exposed to the spectrometer laser. Local areas of the PCDM were exposed to a stationary red laser beam for increasing lengths of time to investigate the ablation and discoloration of the polymer underneath (Figure A3.1). The polymer was submitted to the laser for periods of 5, 10, 20, 30, 60, 120, 300, 600, 1200, 1800, 3600 and 7200 seconds, with the exposed areas separated at 20 μm intervals. With the laser set to 100% power, the colour of the polymer changed, during exposure to the laser, from a light red to a blue/white.

Figure A3.1 shows the pristine PCDM with the spots due to the laser-exposure for the increasing exposure time increments. The lighter, circular areas are the laser exposed polymer, whereas the irregular, dark areas are due to aggregations on the polymer surface. The spots due to the exposed areas are approximately 60 μm across for the 7200 s exposure time decreasing to approximately 5 μm for the 5 s exposure time. After the exposure, the sample was re-examined by scanning the laser, at low

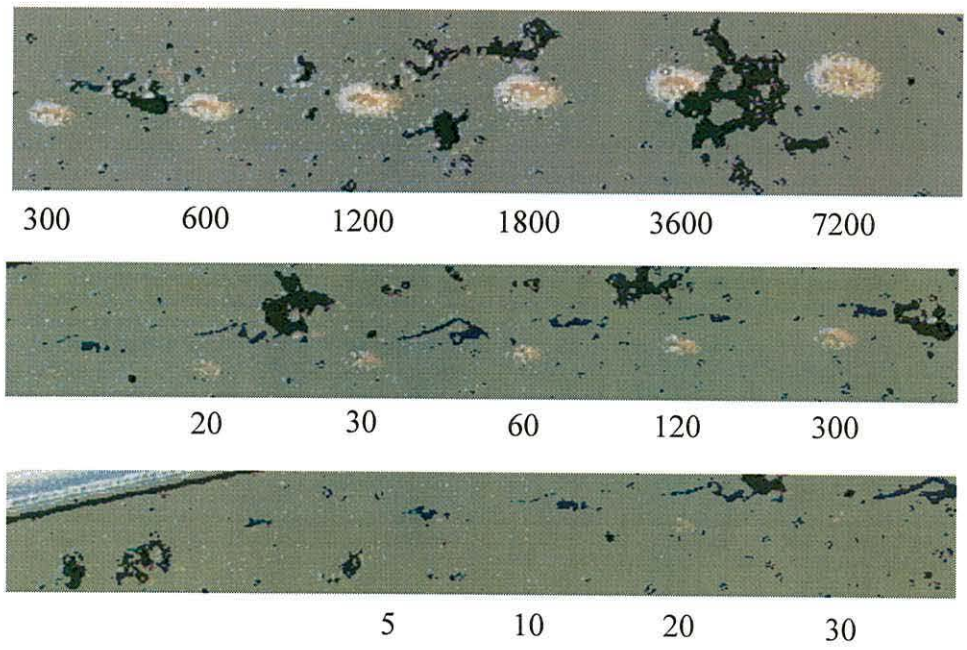

Figure A3.1 *Images of the surface of a PCDM film exposed to a red laser for decreasing exposure times between 7200 and 5 seconds. (Magnification : 2000x)*

power (1 %), along a line through the centres of the ablated holes (Figure A3.2). Thus the fluorescence intensity of the pristine polymer film, ablated polymer debris and the exposed polymer could be examined.

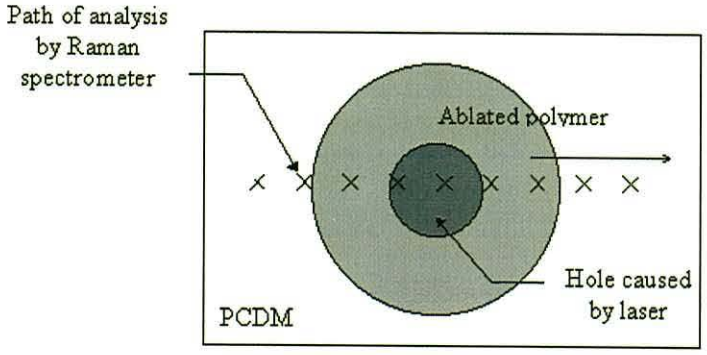

Figure A3.2 *Schematic diagram of Raman analysis across ablated areas on PCDM surface.*

The Raman spectra (Figure A3.3) show an increase in the background fluorescence in the areas where the polymer was exposed to the laser radiation, the fluorescence increasing with increasing exposure time. Between 3600 and 7200 seconds the spectrometer encountered a large aggregation of polymer (which can be seen in Figure A3.1) and this was recorded as a decrease in the amount of fluorescence

signal returned to the spectrometer. This enforces the statement about the reduction in signal seen at certain points in the fluorescence mapping experiment (Section 5.3.2.1).

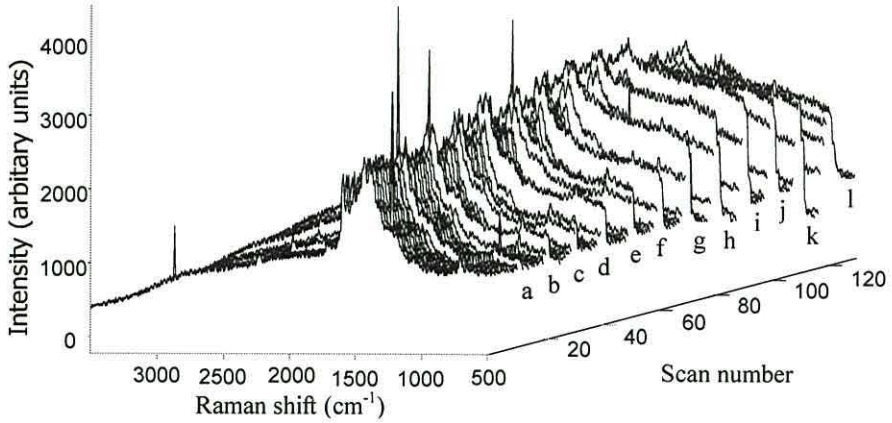

Figure A3.3 *Raman mapping across laser exposed PCDM where a to l correspond to the scans recorded in the laser exposed polymer. The letters correspond to the exposure times between 5 and 7200 s respectively. Note that the sharp peaks seen in different positions on different scans in figure A3.3 are due to the detection of cosmic rays by the spectrometer and are not due to the polymer sample.*

The Raman spectra either side of the laser exposed polymer areas show no difference to that in the pristine polymer suggesting that there is little debris, produced by the laser exposure, deposited in the locality of the indented polymer. A similar finding has been made for laser ablated polyanaline where the ablation craters had sharp contours and no debris was observed in the surrounding area [(206)].

Curve fitting was carried out on the individual Raman spectra to ascertain the wavelength at which the maximum fluorescence intensity occurred. The raw spectrum first had the laser filter line at 0 cm^{-1} removed, by beginning the x-axis at 200 cm^{-1}, so that the levelling step had a constant start point. The spectrum was then baseline levelled to zero and the CDM spectral lines removed to stop them interfering with the curve fit of the background fluorescence. The curve fitting was then calculated by the computer and the wavelength of the maximum fluorescence intensity found. A better curve fit could be achieved for spectra recorded on the pristine polymer than those recorded within the areas exposed to the laser but all error values, r^2, were greater than 0.9 .

A plot of the wavelengths of the fluorescence maximum revealed an increasing blue shift in the electromagnetic spectrum as the polymer was exposed to the laser for

increasing amounts of time (Figure A3.4), but all the values remained within the red region of the spectrum (650 to 750 nm). Again, the value for the 3600 second exposure was found to be low, possibly due to the close proximity of the polymer aggregation.

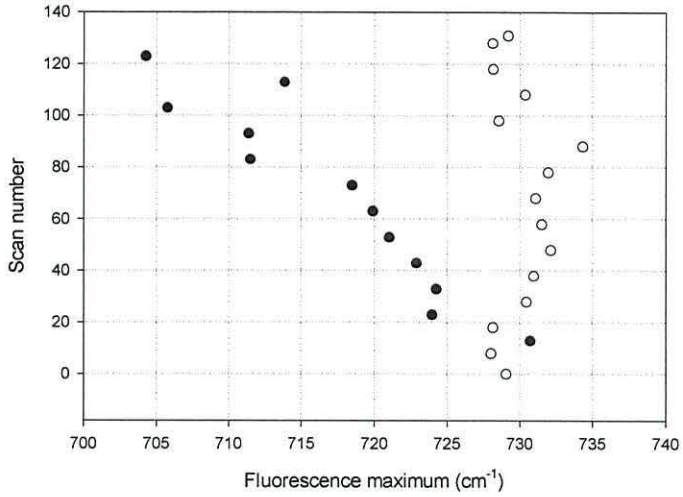

Figure A3.4 *Graph of maximum fluorescence wavelength showing the blue shift for laser exposed areas of the PCDM. Laser exposed polymer (●) and pristine polymer between exposed areas (○).*

AFM analysis of the holes produced by the laser exposure shows that the depth increases upon increasing exposure time (Figure A3.5). The thickness of the polymer was found by sectional analysis of a score line close to the measurement area (Figure A3.6). Comparison of the hole depths with the thickness of the polymer, 190 nm, shows that the holes produced by the laser did not penetrate the full depth of the polymer. This is supported by the appearance of an unchanged Raman PCDM spectra superimposed on top of the increased fluorescence.

Repeat experiments of the laser exposure on different polymer samples produced similar results, including the blue shift in the polymer fluorescence. However, comparison shows that the values vary, with deeper holes and a greater blue shift. These results show that the difference in the Raman fluorescence values for the exposed areas are solely due to a change in the polymer and not substrate effects

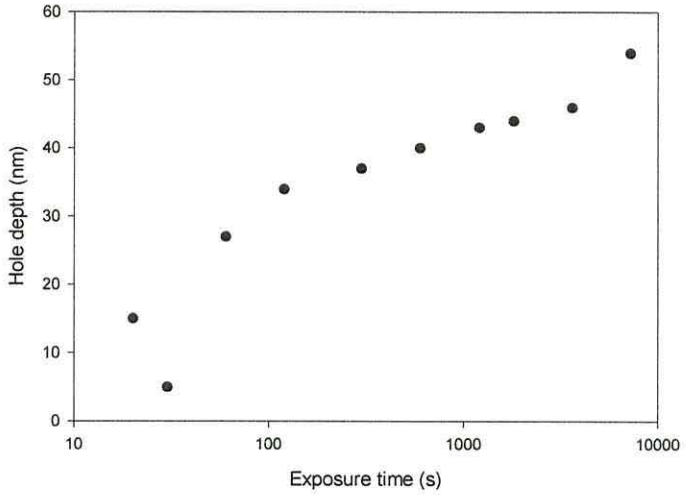

Figure A3.5 *Graph showing the depth of holes produced upon exposure PCDM to laser radiation showing increasing depth with increasing exposure times.*

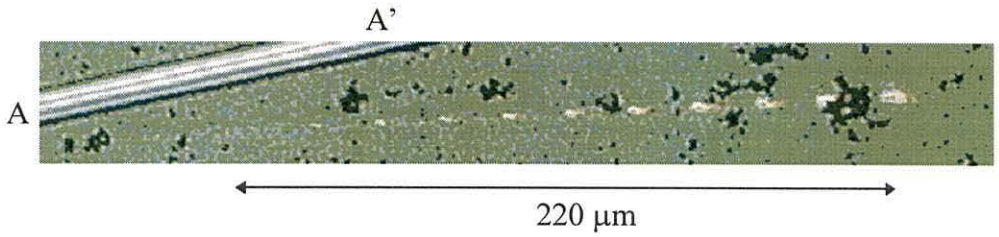

Figure A3.6 *Laser exposed PCDM. Sectional analysis score line for polymer thickness measurement shown (A to A'). (Magnification : 800x)*

because the sample film is thicker than the deepest hole in the exposed areas of polymer.

The changes could be due to the changes in thickness or crystallinity changes due to the laser exposure. Polymers crystallise, and gain the physical characteristics of crystals, by packing of the polymer chains in a regular fashion with respect to each other depending on the tacticity and lowest-energy conformation. A straight chain conformation is more likely to crystallise than a random coil. The crystallinity can be found by measuring the x-ray diffraction pattern where crystalline polymers give similar patterns to micro-crystalline solids. Some examples of crystalline polymers are given by Allcock and Lampe [209].

Jawhari and co-workers [210] suggested that laser ablated polyethylene terephthalate presented a lower degree of order, hence a higher amorphous character, in the laser exposed areas. The exposed area was thought to have melted causing the high

degree of disorder. They also found that more fluorescence was seen in the Raman spectra of the laser exposed areas which was thought to be due to impurities in the polymer or by degradation processes. Greenham and Friend [211] have also found that amorphous polymers recrystallise over periods of time in storage or during operation.

A combination of photochemically induced bond dissociation and photothermal processes are thought to occur in laser exposed areas [212] and chemical tailoring of polymers with photoliable groups can facilitate polymer decomposition upon irradiation with laser radiation of a specific wavelength [213]. This allows high resolution, photochemical etching of the polymer reducing thermal damage at the edges of the ablated areas.

Therefore it could be assumed that the pristine PCDM is originally semi-crystalline and that the polymer exposed to the laser melts and forms a more disordered polymer causing the Raman fluorescence to be blue shifted. The lack of change in the Raman spectra does not suggest that the polymer breaks up into fragments which would form new compounds detectable by the spectrometer. However, if the ablation of the PCDM film produced small PCDM particles, approximately the wavelength of the irradiating light, this could cause diffraction of the light and hence a shift in the measured radiation wavelength. Also, the shift in fluorescence could be due to the amount of crystallisation or a concentration of impurities in the ablated areas.

A3.2 Summary

The effect of exposing PCDM to the Raman laser for increasing amounts of time was investigated to explore the possibility of patterning the polymer for applications such as polymeric circuitry. AFM analysis has revealed that the laser did not penetrate the full extent of the polymer film even after exposure for 7200 s at full power. The production of impressions in the polymer by the laser was found to increase the fluorescence intensity present in the Raman spectra without altering the spectral peaks in the spectrum and hence, the chemical structure of the polymer. The fluorescence in the Raman spectra was found to be blue shifted as the laser exposure time increased and this, coupled with the increase in fluorescence, was thought to be due to local melting of the polymer by the laser so that it is structurally rearranged. The polymer

was thought to be semi-crystalline, originally, and changes to a more amorphous structure upon melting and then cooling.

Ablation of the polymer through to the substrate surface, which did not occur here, could be achieved by using a more powerful, pulsed laser which could be used to machine circuitry, electrode shapes or polymer gratings for various applications. The changes in crystallinity could be used in recordable media where the change in crystallinity is detected using a system similar to the spectrometer which detects changes in intensity of scattered laser light.

References

1 H. Sirikawa, E. J. Louis, A. G. MacDiarmaid, C. K. Chaing and A. J. Heeger, *J. Chem. Soc. Chem. Comm.*, (1977) 578.

2 "Organic displays", J. Kido, *Physics World*, **12 pt. 3** (1999) 27. "Polymer diodes", R. H. Friend, J. Burroughes and T. Shimoda, *Physics World*, **12 pt. 6** (1999) 35.

3 "Electronics put it on plastic", C. Scott, *Physics World*, **11 pt. 10** (1998) 21. "Plastic electronics", D. de Leeuw, *Physics World*, **12 pt. 3** (1999) 31.

4 "Fantastic Plastic", N. Jones, *New Scientist*, **168 pt. 2261** (2000) 14. "Roll up for the flexible transistor", J. Brown, *New Scientist*, **143 pt. 1944** (1994) 5. "Can multicolour diodes switch on flat screens?", C. Arthur, *New Scientist*, **144 pt. 1956** (1994) 24. "The electric plastic show", K. C. Fox, *New Scientist*, **141 pt. 1915** (1994) 33. "Polymers bring a glow to TV screens", D. Bradley, *New Scientist*, **133 pt. 1803** (1992) 19.

5 For example, "Roll up, roll up, for the worlds first flexible TV set", *The Daily Express*, Friday July 9th 1999, pp. 15.

6 "Semiconductors and Electronic Devices", 3rd edition, A. Bar-Lev, Prentice Hall International Ltd., UK, 1993.

7 "Handbook of conducting polymers", 2nd edition, T. A. Skotheim, R. L. Eisenbaumer and J. R. Reynolds (eds.), Marcel Dekker Inc., NY, 1998.

8 "Organic Chemistry", K. P. C. Volthardt, W. H. Freeman and Company, NY, 1987.

9 "Quantum Theory of Solids", R. E. Pieirls, Clarendon Press, Oxford, UK, 1955.

10 "Semiconductor Devices, Circuits and Systems", A. Moschwitzer, Clarendon press, Oxford, UK, 1991.

11 S. R. Forrest, *57th Annual Device Research Conference Digest*, (1999) 4.

12 A. Hasegawa, *Proceedings of the SPIE - The International Society for Optical Engineering*, **3666** (1999) 302.

13 "Organic Semiconductors", F. Gutmann and L. E. Lyons, John Wiley and Sons Ltd., 1967.

14 H. Stubb, E. Punkka and J. Paloheimo, *Mater. Sci. Eng.*, **10** (1993) 85.

15 "Advances in Synthetic Metals: Twenty Years of Progress in Science and Technology", P. Bernier, S. Lefrant and G. Bidan (eds.), Elsevier Science, Switzerland, 1999, Chapter 2, M. D. McGehee, E. K. Miller, D. Moses and A. J. Heeger.

16 D. D. Notte, *J. Appl. Phys.*, **85** (1999) 6259. A. Matsui, *J. Opt. Soc. America B: Opt. Phys.*, **7** (1990) 1615.

17 "Introduction to Semiconductor Materials and Devices", M. S. Tyagi, John Wiley and Sons, NY, 1991.

18 "Advances in Synthetic Metals: Twenty Years of Progress in Science and Technology", P. Bernier, S. Lefrant and G. Bidan (eds.), Elsevier Science, Switzerland, 1999, Chapter 1, D. Marsitzky and K. Mullen,.

19 D. M. Taylor and H. L. Gomes, *J. Phys. D: Appl. Phys,* **28**, 1995, 2554.

20 "Fundementals of Semiconductor Devices", E. S. Yang, M^{c}Graw-Hill Book Co., NY, 1978.

21 C. Wagner, *Phys. Z.*, **32** (1931) 641.

22 "Physics and Technology of Semiconductor Devices", A. S. Grove, John Wiley and Sons, NY, 1967.

23 G. Valincius and V. Reipa, *J. Electrochem. Soc.*, **147** (2000) 1459. N. F. Mott, *Proc. Royal Soc.*, **171** (1939) 27. W. Schottky, *Phys. Z.*, **113** (1939) 367.

24 I. Musa and W. Ecclestone, Synth. Met., 101 (1999) 598.

25 C. A. Mills, D. M. Taylor, A. Riul Jr., A. P. Lee, *Journal of Applied Physics* (submitted).

26 R. A. Street, G. Davies and A. D. Joffe, *J. Non. Cryst. Sol.*, **5**, 1971, 276.

27 "The New Penguin Dictionary of Electronics", E. C. Young, Penguin books, UK, 1979.

28 J. Frenkel, *Phys. Rev.*, **54**, 1938, 647.

29 R. I. Frank and J. G. Simmons, *J. Appl. Phys.*, **38** (1967) 832.

30 S. Sakthivel, B. Chander Shekar, D. Mangalaraj, SA. K. Narayandass, S. Venkatachalam, P.V. Prabhakaran, *Eur. Polym. J.*, **33**, 1997, 1747

31 "Electrical Conduction in Polymeric Films", D. M. Taylor, Ph.D. thesis, University of Wales, Bangor, UK, 1970.

32 I.D. Parker, *J. App. Phys.*, **75** (1994) 1656.

33 A.J. Heeger, I. D. Parker and Y. Yang, *Synth. Met.*, **67** (1994) 23.

34 "Electronic Processes in Ionic Crystals", N. F. Mott and R. W. Gurney, Oxford University Press, 1940.

35 M. A. Lampert, *Phys. Rev.*, **103** (1956) 1648.

36 P. Mark and W. Helfrich, *J. App. Phys.*, **33** (1962) 205.

37 P. W. M. Blom, M. J. M. de Jong and J. J. M. Vleggaar, *Appl. Phys. Lett.*, **68** (1996) 3308. I. Musa, S. J. Higgins and W. Ecclestone, *J. Appl. Phys.*, **81** (1997) 2288. I. Musa, W. Eccleston and S. J. Higgins, *J. App. Phys.*, **83** (1998) 5558.

38 For example: R. H. Friend, A. J. Heeger, J. Roncali, W. R. Salaneck, F. Garnier, J-L. Bredas.

39 L. J. Rothberg, M. Yan, F. Papadimitrakopoulos, M. E. Galvin, E. W. Kwok and T. M. Miller, *Synth. Met.*, **80** (1996) 41.

40 G. Yu and A. J. Heeger, *Synth. Met.*, **85** (1997) 1183.

41 Y. Yang, Q. Pei and A. J. Heeger, *J. App. Phys.*, **79** (1996) 934.

42 J. S. Kim, F. Cacialli, R. H. Friend, R. Daik and W. J. Feast, *Synth. Met.*, **102** (1999) 1065.

43 D. Braun and A. J. Heeger, *Appl. Phys. Lett.*, **58** (1991) 1982.

44 E. G. Staring, R. C. Demandt, D. Braun, G. L. Rikken, Y. A. Kessner, A. H. Venhuizen, M. M. von Knippenburg and M. Bouwmans, *Synth. Met.*, **71** (1995) 2179.

45 N. C. Greenham, S. C. Moratti, D. D. C. Bradley, R. H. Friend and A. B. Holmes, *Nature*, **365** (1993) 628.

46 D. R. Baigent, P. J. Hamer, R. H. Friend, S. C. Moratti and A. B. Holmes, *Synth. Met.*, **71** (1995) 2175.

47 S. C. Moratti, R. Cervini, A. B. Holmes, D. R. Baigent, R. H. Friend, N. C. Greenham, J. Gruner and P. J. Homer, *Synth. Met.*, **71** (1995) 2117.

48 M. Berggren, O. Inganas, G. Gustaffson, M. R. Andersson, T. Hjertberg and O. Wennerstrom, *Synth. Met.*, **71** (1995) 2185.

49 T. L. Lambert and J. P. Ferraris, *J. Chem. Soc. Chem. Comm.*, **11** (1991) 752. *J. Chem. Soc. Chem. Comm.*, **18** (1991) 1268.

50 M. Pomerantz and X. Gu, *Synth. Met.*, **84** (1997) 243.

51 J. M. Toussaint, B. Themans, J. M. Andre and J. L. Bredas, *Synth. Met.*, **28** (1989) C205.

52 E. E. Havinga, W. Hoeve and H. Wynberg, *Synth. Met.*, **55** (1993) 299.

53 J. L. Bredas, *Synth. Met.*, **17** (1987) 115.

54 J. M. Maud, M. E. Cooper, E. C. Bolton and D. M. Haynes, *Synth. Met.*, **71** (1995) 1935.

55 C. K. Chaing, C. R. Fincher Jr., Y. W. Park, A. J. Heeger, H. Sirikawa, E. J. Lous, S. C. Gau and A. G. MacDairmaid, *Phys. Rev. Lett.*, **39** (1977) 1098.

56 P. M. Grant, T. Tani, W. D. Gill, M Korunbi, T. C. Clarke, *J. Appl. Phys.*, **52** (1981) 869. F. Ebisawa, T. Kurokawa and S. Nara, *J. Appl. Phys.*, **54** (1983) 3255.

57 T. Ito, H. Sirikawa and S. Ikeda, *J. Polym. Sci. Polym. Chem. Ed.*, **12** (1974) 11.

58 H. Sirikawa, *Synth. Met.*, **69** (1995) 3.

59 J. H. Burroughs, D. D. C. Bradley, A. R. Brown, R. N. Marks, K. Makay, R. H. Friend, P. L. Burns and A. B. Holmes, *Nature*, **347** (1990) 539.

60 T. Granier, E. L. Thomas, D. R. Gagnon, F. E. Karasz and R. W. Lenz, *J. Polym. Sci. B.*, **24** (1986) 2793. D. D. C. Bradley, R. H. Friend, H. Linderberger and S. Roth, *Polymer*, **27** (1986) 1709.

61 D. A. dos Santos, C. Quattrocchi, R. H. Friend and J. L. Bredas, *J. Chem. Phys.*, **100** (1994) 3301.

62 D. Braun and A. J. Heeger, *Thin Solid Films*, **216** (1992) 96.

63 J. Cornil, D. Beljonne, D. A. dos Santos and J. L. Bredas, *Synth. Met.*, **76** (1996) 101. J. M. Toussaint, B. Themans, J. M. Andre and J. L. Bredas, *Synth. Met.*, **28** (1989) C205.

64 P. L. Burn, A. Kraft, D. R. Baigent, D. D. C. Bradley, A. R. Brown, R. H. Friend, R. W. Gymer, A. B. Holmes and R. W. Jackson, *J. Am. Chem. Soc.*, **115** (1993) 10117.

65 I. D. W. Samuel, B. Crystall, G. Rumbles, P. L. Burn, A. B. Holmes and R. H. Friend, *Chem. Phys. Lett.*, **213** (1993) 472.

66 R. W. Gymer, *Endeavour*, **20** (1996) 115. D. M. Collard and M. A. Fox, *J. Am. Chem. Soc.*, **113** (1991) 9414. S. A. Chen and J. M. Ni, *Macromol.*, **26** (1993) 3230. A. Pelter, M. Rowlands and I. H. Jenkins, *Tetrahedron*, **28** (1987) 5213.

67 "Aromatic Heterocyclic Chemistry", D. T. Davies, Oxford Chemistry Primers, Oxford Science Publications, Oxford, UK, 1993.

68 F. Wuld, M. Kobayashi and A. J. Heeger, *J. Org. Chem.*, **49** (1984) 3382.

69 J. Poplawski, E. Ehrenfreund, H. Schaffer, F. Wuld and A. J. Heeger, *Synth. Met.*, **28** (1989) C539.

70 S. A. Jenekhe, *Nature*, **322** (1986) 345.

71 I. Musa, D. A. I. Munindrasdasa, G. A. J. Amaratunga and W. Ecclestone, *Nature*, **395** (1998) 362. Y. Ohmori, N. Tada, M. Yoshida, A. Fujii and K. Yushino, *J. Phys. D.*, **29** (1996) 2983.

72 S. Y. Hong, S. J. Kwon and S. C. Kim, *J. Chem. Phys.*, **103** (1995) 1871.

73 J. D. Hong, D. Kim, K. Cha and J. I. Jin, *Synth. Met.*, **84** (1997) 815.

74 D. S. Boudreaux, R. R. Chance, R. L. Eisenbaumer, J. E. Frommer, J. L. Bredas and R. Silbey, *Phys. Rev. B.*, **31** (1985) 652.

75 J. M. Toussaint and J. L. Bredas, *Synth. Met.*, **61** (1993) 103.

76 M. Karikomi, C. Kitamura, S. Tanaka and Y. Yamashita, *J. Am.. Chem. Soc.*, **117** (1995) 6791. G. A. Satzing and J. R. Reynolds, *J. Chem. Soc. Chem. Comm.*, (1995) 703. J. L. Bredas, *Synth. Met.*, **17** (1987) 115. J. L. Bredas, *J. Chem. Phys.*, **82** (1985) 3808. J. L. Bredas, G. B. Street, B. Themans and J. M. Andre, *J. Chem. Phys.*, **83** (1985) 1323.

77 M. Fahlman, J. L. Bredas and W. R. Salaneck, *Synth. Met.*, **78** (1996) 237. C. L. Gettinger, A. J. Heeger, J. M. Drake and D. J. Pine, *J. Chem. Phys.*, **101** (1994) 1673.

78 M. Breggren, G. Gustafsson, O. Inganas, M. R. Anderson, O. Wennerstrom and T. Hjertberg, *Appl. Phys. Lett.*, **65** (1994) 1489. T. A. Chen and R. D. Rieke, *Synth. Met.*, **60** (1993) 175.

79 "Oxford Concise Science Dictionary", 3rd edition, A. Issacs, J. Daintith and E. Martin (eds.), Oxford University Press, Oxford, UK, 1996.

80 J. P. Ferraris and T. Lambert, *J. Chem. Soc. Chem. Comm.*, (1991) 1268.

81 H. Huang and P. G. Pickup, *Acta polymer.*, **48** (1997) 455.

82 H. Huang and P. G. Pickup, *Chem. mater.*, **10**, (1998) 2214.

83 H. Huang and P. G. Pickup, *Chem. mater.*, **11**, (1999) 1541.

84 S. R. Gunatunga, G. W. Jones, M. Kalaji, P. J. Murphy, D. M. Taylor and G. O. Williams, *Synth. Met.*, **84** (1997) 973.

85 Y. Dong, S. C. Bayliss and M. Parkinson, *Appl. Phys. Lett.*, **72** (1998) 1344.

86 A. Riul Jr., D. M. Taylor, C. A. Mills and P. J. Murphy, *Thin Solid Films*, **366** (2000) 249.

87 M. Kozaki, S. Tanaka and Y. Yamashita, *J. Chem. Soc. Chem. Comm.*, **16** (1992) 1137.

88 M. Kozaki, S. Tanaka and Y. Yamashita, *J. Org. Chem.*, **59** (1994) 442.

89 B. H. Cumpston and K. F. Jensen, *Synth. Met.*, **73** (1995) 195.

90 C. A. Mills, D. Lacey, G. Stevenson and D. M. Taylor, *J. Mater. Chem.*, **10** (2000) 1551.

91 M. Fahlman, C. Fauquet, K. Kaerijama, Y. Sonoda, Lazzaroni, J. L. Bredas and W. R. Salaneck, *Synth. Met.*, **67** (1994) 133.

92 Y. Ohmori, N. Tada, M. Yoshida, A. Fujii and K. Yushino, *J. Phys. D.*, **29** (1996) 2983.

93 K. L. Chopra, S. Major and D. K. Pandya, *Thin Solid Films*, **102** (1983) 1.

94 Y. Yang and A. J. Heeger, *App. Phys. Lett.*, **64** (1994) 1245.

95 J. Gao, A. J. Heeger, J. Y. Lee and C. Y. Kim, *Synth. Met.*, **82** (1996) 221.

96 S. Tasch, C. Brandstatter, F. Meghdadi, G. Leising and G. Froyer, *Adv. Mater.*, **9** (1997) 33.

97 F. Cacialli, R. H. Friend, N. Haylett, R. Daik, W. J. Feast, D. A. dos Santos and J. L. Bredas, *Appl. Phys. Lett.*, **69** (1996) 3794.

98 A. R. Brown, D. D. C. Bradley, J. H. Burroughes, R. H. Friend, N. C. Greenham, P. L. Burn, A. B. Holmes and A. Kraft, *Appl. Phys. Lett.*, **61** (1992) 2793.

99 G. Gustaffson, G. Cao Gustaffson, Y. Cao, G. M. Treacy, F. Klavelter, N. Calameri and A. J. Heeger, *Nature*, **357** (1992) 477.

100 F. Garnier, R. Hajlaoui, A. Vasser and P. Siwastava, *Science*, **265** (1994) 1684. Z. N. Bao, Y. Feng, A. Dodapalapur, V. R. Raju and A. J. Lovinger, *Chem. Mater.*, **9** (1997) 1299, C. J. Drury, C. M. J. Mutsaers, C. M. Hart, M. Matters and D. M. DeLeeuw, *Appl. Phys. Lett.*, **73** (1998) 108.

101 M. Hamaguchi, A. Fujii, Y. Ohmori and K. Yoshino, *Synth. Met.*, **84** (1997) 557. N. C. Greenham, A. R. Brown, D. D. C. Bradley and R. H. Friend, *Synth. Met.*, **55** (1993) 4134.Y. Ohmori, M. Uchida, K. Muro and K. Yoshino, *Solid St. Comm.*, **80** (1991) 605. A. R. Brown, D. M. de Leew, E. J. Lous and E. E. Havinga, *Synth. Met.*, **66** (1994) 93. L. M. Goldenburg, M. C. Petty and A. P. Monkman, *J. Electrochem. Soc.*, **141** (1994) 1573.

102 M. S. Weaver and D. D. C. Bradley, *Synth. Met.*, **83** (1996) 61.

103 E. G. J. Staring, D. Braun, G. L. J. A. Rikken, R. J. C. E. Demandt, Y. A. R. R. Kessener, M. Bouwmans and D. Broer, *Synth. Met.*, **67** (1994) 71.

104 A. V. Vannikov, A. R. Tameev, E. I. Mal'tsey, G. W. H. Milburn, A. J. Shand, A. R. Werninck and J. Wright, *Synth. Met.* **78** (1996) 79. W. Gebauer, C. Vaterlein,A. Soukopp, M. Sokolowski, R. Hock, H. Port, P. Bauerle and E. Umbach, *Synth. Met.* **87** (1997) 127. V. Papez and S. Brodska, *Sens. and Actu. B* **40** (1997) 143. S. J. Limb, C. B. Labelle, K. K. Gleason, D. J. Edell and E. F. Gleason, *App. Phys. Lett.* **68** (1996) 2810. F. Cacialli and P. Bruschi, *J. App. Phys.* **80** (1996) 70.

105 K. Isobe, T. Fukunaga, W. Takashima and K. Kaneto, *Synth. Met.*, **85** (1997) 1435.

106 D. G. Lidzey, M. A. Pate, M. S. Weaver, T. A. Fisher and D. D. C. Bradley, *Synth. Met.*, **82** (1996) 141. L. J. Rothberg, M. Yan, S. Son, M. E. Galvin, E. W. Kwok, T. M. Millar, H. E. Katz, R. C. Haddon and F. Papadimitrakopoulos, *Synth. Met.*, **78** (1996) 195.

107 M. Onada and K. Yoshino, *J. App. Phys.*, **78** (1995) 4456. L. Xiao-Chang, F. Cacialli, R. Cervini, A. B. Holmes, S. C. Moratti, A. C. Grimsdale and R. H. Friend, *Synth. Met.*, **84** (1997) 159. H. Hong, D. Davidov, M. Tarabia,

H. Chayet, I. Benjamin, E. Z. Faraggi, Y. Avny and R. Neumann, *Synth. Met.*, **85** (1997) 1265.

108 C. A. Mills, D. M. Taylor, P. J. Murphy, C. Dalton, G. W. Jones, L. M. Hall and A. V. Hughes, *Synth. Met.*, **102** (1999) 1000.

109 C. M. Chan, *Surface Science Reports* **24** (1996) 1. M. R. Wertheimer, H. R. Thomas, M. J. Perri, J. E. Klemburg-Sapieka and L. Martinu, *Pure and App. Chem.* **68** (1996) 1047. K. Endo and T. Tatsumi, *App. Phys. Lett.* **68** (1996) 3656. S. Gorwadker, G. K. Vinogradov, K. Senda and S. Morita, *J. App. Phys.* **78** (1995) 2242. K. Senda, G. K. Vinogradov, S. Gorwadker and S. Morita, *J. App. Phys.* **74** (1993) 6425. R. Nakamura, H. Muguruma, K. Ikebakuro, S. Sasaki, R. Nagata, I. Karube and H. Pedersen, *Anal. Chem.* **69** (1997) 4649. M. Tazaki, H. Aizawa and T. Homma, *Chem. Lett.* (1994) 1905. Z. S. Tong, T. S. Pu, M. Z. Wu, Z. Y. Zhang, J. Zhang, R. P. Jin, D. Z. Zhu and J. Q. Cao, *Synth. Met.* **79** (1996) 85. D. H. Shin, S. D. Lee, S. Y. Park, D. H. Choi and H. Kim, *Synth. Met.* **71** (1995) 2263. K. Tanaka, K. Yoshizawa, T. Takeuchi, T. Yamabe and A. Yamauchi, *Synth. Met.* **38** (1990) 107. X. Xie, J-U. Thiele, R. Stiener and P. Oelhafen, *Synth. Met.* **63** (1994) 221. K. Tanaka, Y. Matsuura, S. Nishio and T. Yamabe, *Synth. Met.* **65** (1994) 81. I. Sugimoto, M. Nakamura and H. Kuwano, *Sens. and Actu. B* **37** (1996) 163.

110 P.L. Burns, A. B. Holmes, A. Kraft, D. D. C. Bradley, A. R. Brown, R. H. Friend and R. W. Gymer, *Nature*, **356** (1992) 47. K. Kobayashi, T. X. Yang, K. Moruyama, M. Shimomura and S. Miyauchi, *Synth. Met.*, **69** (1995) 475.

111 M. R. Anderson, M. Berggen, O. Inganas, G. Gustaffson, J. C. Gustaffson-Cargberg, D. Selse, T. Hjertberg and O. Wennerstrom, *Macromol.*, **28** (1995) 7525.

112 F. Cacialli, R. N. Marks, R. H. Friend, R. Zamboni, C. Taliani, S. C. Moratti and A. B. Holmes, *Synth. Met.*, **76** (1996) 145. D. R. Baigent, R. N. Marks, N. C. Greenham, R. H. Friend, S. C. Morrati and A. B. Holmes, *Appl. Phys. Lett.*, **65** (1994) 2636.

113 T. Shimoda, M. Kimura, S. Seki, H. Kobyashi, S. Kanbe, S. Miyashita, R. H. Friend, J. H. Burroughes, C. R. Towns and I. S. Millard, *International electron devices meeting 1999*, Technical digest (Cat. No. 99CH36318), 107.

114 R. Neale, *Electr. Eng.*, **71** (1999) 20.

115 G. Kranzelbinder and G. Leising, *Reports on Progress in Physics*, **63** (2000) 729.

116 G. Wegmann, H. Giessen, R. F. Mahrt, *Proceedings of the third international conference on excitonic processes in condensed matter EXCON '98*, (1998) 53.

117 M. D. McGehee, R. Gupta, E. K. Miller and A. J. Heeger, *Synth. Met.*, **102** (1999) 1030. Y. Kawabe, C. Speigelberg, A. Schulzgen, M. F. Nabor, B. Kippelen, E. A. Mash, P. M. Allemand, M. Kuwata-Gonokami, K. Takeda and N. Peyghambarian, *Appl. Phys. Lett.*, **72** (1998) 141.

118 S. Stagira, M. Zavelani-Rossi, M. Nisoli, S. De Silvestri, G. Lanzani, C. Zenz, P. Mataloni and G. Leising, *Summeries of the papers presented at the conference on lasers and electro-optics CLEO '99*, (1999) 466.

119 W. J. Wadsworth, I. T. McKinnie, A. D. Woolhouse and T. G. Haskell, *Summeries of the papers presented at the conference on lasers and electro-optics CLEO '99*, (1999) 549. S. M. Giffen, I. T. McKinnie, W. J. Wadsworth, A. D. Woolhouse, G. J. Smith and T. G. Haskell, Optics Comms., 161 (1999) 163.

120 S. V. Frolov, M. Shkunov, A. Fujii, K. Yoshino and Z. V. Vardeny, *IEEE Journal of Quantum Electronics*, **36** (2000) 2. A. Fujii, D. Chinn, M. N. Shkunov, S. V. Frolov, Z. V. Vardney and K. Yoshino, *Synth. Met.*, **102** (1999) 1010.A. Schutzgen, C. Speigelberg, M. M. Morrell, S. B. Mendes, P. Allemand, Y. Kawabe, M. Kuwata-Gonokami, S. Hokanen, B. Kippelen and N. Peyghambarian, *Optical Eng.*, **37** (1998) 1149.

121 C. Kallinger, M. Hilmer, A. Haugeneder, M. Perner, W. Spirkl, U. Lemmer, J. Feldmann, U. Scherf, K. Mullen, A. Gombert and V. Wittwer, *Adv. Mater.*, **10** (1998) 920.

122 G. Yu, C. Zang and A. J. Heeger, *Appl. Phys. Lett.*, **64** (1994) 1540.

123 G. Yu, J. Gao, J. C. Hummelen, F. Wuld and A. J. Heeger, *Science*, **270** (1995) 1789. S. Morita, T. Akashi, A. Fujii, M. Yoshida, Y. Ohmori, K. Yoshimoto, T. Kawai, A. A. Zakhidov, S. B. Lee and K. Yoshino, *Synth. Met.*, **69** (1995) 433.

124 K. Pakbaz, G. Yu and A. J. Heeger, *Appl. Phys. Lett.*, **64** (1994) 3422.

125 G. Yu, *Synth. Met.*, **80** (1996) 143.

126 Q. Pei, G. Yu, C. Zhang, Y. Yang and A. J. Heeger, *Science*, **269** (1995) 1086.

127 L. Holzer, B. Winkler, F. P. Wenzel, S. Tasch, L. Dai, A. W. H. Mau and G. Leising, *Synth. Met.*, **100** (1999) 71.

128 G. Yu, J. Gao, J. C. Hummelen, F. Wuld and A. J. Heeger, *Science*, **270** (1995) 1789.

129 K. Yoshino, K. Tada, M. Hirohata, H. Kajii, Y. Hironaka, N. Tada, Y. Kaneuchi, M. Yoshida, A, Fujii, M. Hamaguchi, H. Araki, T. Kawai, M. Ozaki, Y. Ohmori, M. Onada and A. A. Zakhidov, *Synth. Met.*, **84** (1997) 477.

130 Y. Yang and A. J. Heeger, *Nature*, **372** (1994) 344.

131 A. J. Heeger, D. J. Heeger, J. Langan and Y. Yang, *Science*, **270** (1995) 1642.

132 Y. Cao, N. Colaneri, A. J. Heeger and P. Smith, *Appl. Phys. Lett.*, **65** (1994) 2001.

133 "Electroactive Polymer Materials, State of the art review of conductive polymers", Technomic publishing Co. Inc., Lancaster, PA.

134 M. Kalaji, P. J. Murphy and G. O. Williams, *Synth. Met.*, **102** (1999) 1360, M. Kalaji and G. O. Williams, *EESAT (Electrical Energy Storage Systems Applications and Technologies) '98 International conference proceedings*, (1998) 167.

135 M. Kalaji, P. J. Murphy and G. O. Williams, *Synth. Met.*, **101** (1999) 123.

136 A. R. Brown, A. Pomp, D. M. de Leew, D. B. M. Klaasen, E. E. Havinga, P. Herwig and K. Mullen, *J. App. Phys.*, **79** (1996) 2136.

137 D. M. Taylor, H. L. Gomes, A. E. Underhill, S. Edge and P. I. Clemenson, *J. Phys. D.*, **24** (1991) 2032.

138 A. R. Brown, A. Pomp, C. M. Hart and D. M. de Leew, *Science*, **270** (1995) 972.

139 H. Sirringhaus, R. J. Wilson, R. H. Friend, M. Inbasekaran, W. Wu, E. P. Woo, M. Grell and D. C. C. Bradley, *Appl. Phys. Lett.*, **77** (2000) 406.

140 F. Garnier, R. Hajlaoni, A. Yasser and P. Sirastava, *Science*, **265** (1994) 1684.

141 Jasowicz M., *Analyst*, **120** (1995) 1019.

142 Musio F., Ferrara M.C., *Sens. and Act. B*, **41** (1997) 97.

143 Barker P.S., Monkman A.P., Petty M.C., Pride R., *IEEE Proc Circuits Devices Syst.*, **144** (1997) 111.

144 Ohsawa T., Kaneto K., Yoshino K., *J. J. App. Phys.*, **23** (1984) L663.

145 Grate J.W., Martin S.J., White R.M., *Anal. Chem.*, **65** (1993) 940A and 978A.

146 Grate J.W., Patresh S.J., Abraham M.H., *Anal. Chem.*, **67** (1995) 2162.

147 Sugimoto I., Nakamura M., Kuwano H., *Sens. and Act. B*, **37** (1996) 163.

148 Dominguez M.E., Li J., Curiale R.L., Poziomek E.J., Quere A., *Anal. Lett*,. **28** (1995) 945.

149 Chang Q., Lahowicz J.R., Rao G., *Analyst*, **122** (1997) 173. Xu W., Kneas K.A., Demas J.N., DeGraff B.A., *Anal. Chem.*, **68** (1996) 2605. Xu W., McDonough R.C., Luingsdorf B., Demas J.N., DeGraff B.A., *Anal. Chem.*, **66** (1994) 4133.

150 Abdelghani A., Chovelon J.M., Jaffrezie-Renault N., Viella C., Gaguaire H., *Anal. Chim. Acta*, **337** (1997) 225.

151 Nakamura R., Muguruma H., Ikebukuro K., Sasaki S., Nagata R., Karube I., Pedersen H., *Anal. Chem.*, **69** (1997) 4649.

152 Yoshino K., Hayashi S., Kohno Y., Kaneto K., Okabe J., Mariya T., *J. J. App. Phys.*, **23** (1984) L198.

153 Gringov B.V., Andryashchenko L.A., Budakovski S.V., Raigorodski I.M., Sotnikov V.T., *IEEE Trans. Nuc. Sci.*, **42** (1995) 361. Bowen M., Majewski S., Pettey D., Walker J., Wojcik R., Zorn C., *IEEE Trans. Nuc. Sci.*, **42** (1995) 361.

154 P. Jordans, G. Rawson and H. Wynberg, *J. Chem. Soc. Chem. Comm.*, (1970) 273.

155 J. Roncali, A. Yasser and F. Garnier, *J. Chem. Phys.*, **86** (1989) 85.

156 For example, D. M. Taylor and H. L. Gomes, *J. Phys. D: Appl. Phys.*, **28** (1995) 2554.

157 "Fundementals of Analytical Chemistry", D. A. Skoog, D. M. West and F. J. Holler, 7th Edition, Saunders College Publishing, USA, 1996.

158 "Principles of Instrumental Analysis", D. A. Skoog and J. J. Leary, 4th Edition, Saunders College Publishing, USA, 1992.

159 "X-Ray and Absorption Wavelengths and Two Theta Tables", E.W. White and G. G. Johnson Jr., 2nd edition, American society for testing and materials, ASTM data series DS 37A, USA, 1970.

160 R. Beyer, M. Kalaji, G. Kingscote-Burton, P. J. Murphy, V. M. S. C. Pereira, D. M. Taylor, G. O. Williams, *Synth. Met.*, **92** (1998) 25.

161 "Organic Polymers and Solid State Fabrication", G. W. Jones, PhD thesis, University of Wales, Bangor, UK, 1999.

162 G. W. Jones, D. M. Taylor, P. J. Murphy, C. A. Mills, A. Riul Jr., B. Laks and J. Del Nero, (in preparation).

163 MOPAC program version 6 (QCEP 455)

164 Ridley and M. C. Zerner, *Theor. Chim. Acta*, **53** (1979) 21, J. D. Head and M. C. Zerner, *Chem. Phys. Lett.*, **122** (1985) 264 and **131** (1986) 359, W. P. Anderson, W. D. Edwards and M. C. Zerner, *Inorg. Chem.*, **25** (1986) 2728, W. D. Edwards and M. C. Zerner, *Chim. Acta*, **72** (1987) 347.

165 T. L. Lambert and J. P. Ferraris, J. Chem. Soc. Chem. Comm., (1991) 752.

166 "Conducting Polymers, Fundementals and Applications. A Practical Approach", P. Chandrasekhar, Kluwer Academic Publishers, Boston, USA, 1999.

167 S. Evans, R. G. Pritchard and J. M. Thomas, *J. Electr. Spec. Rel. Phen.*, **14** (1978) 341. J. M. Adams, S. Evans, P. I. Reid, J. M. Thomas and M. J. Walters, *Anal. Chem.*, **49** (1977) 2001. S. Evans, R. G. Pritchard and J. M. Thomas, *J. Phys. C.*, **10** (1977) 2483.

168 "CRC Handbook of Chemistry and Physics", 54th edition, R. C. Weast (ed.), CRC Press, Cleveland, 1973.

169 "Polymer Light Emitting Diodes: Anode Surface Conditioning and Device Preparation", J. S. Kim, PhD Thesis, University of Cambridge, 2000.

170 "International Tables for Crystallography, Volume C: Mathematical, Physical and Chemical Tables", A. J. C. Wilson (ed.), Kluwer Academic Publishers, Dordrecht, NL, 1995.

171 "Organic Chemistry", K. P. C. Vollhardt, W. H. Freeman and company, NY, 1987.

172 K. S. Cole and R. H. Cole, *J. Chem. Phys.*, **9** (1941) 341.

173 "Metal-Semiconductor Contacts", E. H. Rhoderick, Oxford University Press, Oxford, UK, 1978.

174 H. Reil, W. Brutting, T. Beierlein, E. Haskal, P. Muller and W. Rieß, *Synth. Met.*, **111** (2000) 303.

175 A. Beck, J. G. Bednorz, Ch. Gerber, C. Rossel and D. Widmer, *Appl. Phys. Lett.*, **77** (2000) 139.

176 P. W. M. Blom and M. J. M. DeJong, *IEEE J. Sel. Top. Quantum Electron.*, **4** (1998) 105.

177 "Physical Chemistry", 3rd Ed, P.W. Atkins, Oxford University Press, Oxford, UK, 1986.

178 R. H. Parmenter and W. Rupel, *J. Appl. Phys.*, **30** (1959) 1548.

179 D. M. Taylor and C. A. Mills, *J. Appl. Phys.* (submitted).

180 H. L. Gomes and D. M. Taylor, *IEE Proc.-Circuits Devices Syst.*, **144** (1997) 117. H. L. Gomes, G. W. Jones and D. M. Taylor, *Synth. Met.*, **85** (1997) 1351.

181 F. Garten, J. Vrijmoeth, A. R. Schlatmann, R. E. Gill, T. M. Klapwijk and G. Hadziioannou, *Synth. Met.*, **76** (1996) 85.

182 G. Lecayon, C. LeGressus and A. LeMoel, Eur. Patent, N°. 0038244, 1981. G. Lecayon, Y. Bouizem, C. LeGressus, C. Reynaud, C. Bioziau and C. Jurer, *Chem. Phys. Lett.*, **91** (1982) 506. G. Lecayon, P. Viel, C. LeGressus, C. Boiziou, S. Leroy, J. Perreau and C. Reynaud, *Scanning Microscopy*, **1** (1987) 85.

183 R. Jerome, M. Mertens and L. Martinot, *Adv. Mater.*, **7** (1995) 807. N. Baute, P. Teyssie, L. Martinot, M. Mertens, P. Dubois and R. Jerome, *Eur. J. Inorg. Chem.*, (1998) 1711.

184 M. Mertens, C. Calberg, L. Martinot and R. Jerome, *Macromol.,* **29** (1996) 4910.

185 V. M. Geskin, R. Lazzaroni, M. Mertens, R. Jerome and J. L. Bredas, *J. Chem. Phys.*, **417** (1996) 175, X. Crispin, C. Bureau, V. M. Geskin, R. Lazzaroni, W. R. Salaneck and J. L. Bredas, *J. Chem. Phys.*, **111** (1999) 3237.

186 C. Carlberg, M. Mertens, N. Baute, R. Jerome, V. Carlier, M. Sclavons and R. Legras, *J. Polym. Sci. - Pt. B, Polym. Phys.*, **36** (1998) 543.

187 C. Bureau, G. Deniau, F. Valin, M-J. Buittet, G. Lecayon and J. Delhalle, *Surface Science,* **355** (1996) 177, X. Crispin, R. Lazzaroni, V. Geskin, N. Baute, P. Dubois, R. Jerome and J. L. Bredas, *J. Am. Chem. Soc.*, **121** (1999) 176.

188 N. Baute, L. Martinot and R. Jerome, *J. Electroanal. Chem.*, **472** (1999) 83.

189 T. Seki, K. Tanaka and K. Ichimura, *Mol. Cryst. Liq. Cryst. Sci. Tech. Sect. A - Mol. Cryst. Liq. Cryst.*, **297** (1997) 511. T. Seki, K. Tanaka and K. Ichimura, *Adv. Mater.*, **9** (1997) 561.

190 L. Martinot, M. Mertens, L. Lopes, C. Calberg, P. Faack, M. Krausch, J. Guillaume, G. Ghitti, J. Marien, J. Riga, R. Jerome and J. Schrijnemackers, *Radiochim. Acta.*, **75** (1996) 111.

191 A. Curulli, S. Kelly, C. O. O'Sullivan, G. G. Guilbault and G. Palleschi, *Biosens. Bioelect.*, **13** (1998) 1245. M. Situmorang, J. J. Gooding, D. B. Hibbert and D. Barnett, *Biosens. Bioelect., 13* (1998) 953. S. Cosnier, L. Allien, L. Coche-Guerente, C. Innocent, P. Labbe and P. Mailley, *Sens. and Mater.*, **8** (1996) 169.

192 S. Furumi, M. Nakagawa, S. Morino and K. Ichimura, *J. Mater. Chem.*, **10** (2000) 833.

193 C. Ruslim and K. Ichimura, *Macromol.*, **32** (1999) 4254.

194 L. Cui, P. Xie, R. B. Zhang and T. H. Yang, *Liq. Cryst.*, **26** (1999) 1541. Y. Majima, K. Kato, M. Iwamoto and K. Ichimura, *IEICE Trans. Electron.*, **E81C** (1998) 1070. D. F. Gu, C. Rosenblatt and Z. L. Li, *Liq. Cryst.*, **19** (1995) 489.

195 Z. H. Lu, H. H. Deng and Y. Wei, *Supramol. Sci.*, **5** (1998) 649. M. Buchel, B. Weichart, C. Minx, H. Menzel and D. Johannsmann, *Phys. Rev. E*, **55** (1997) 455.

196 J. Villeras and M. Rambaud, *Synthesis*, (1982) 924.

197 J. Tanguy, G. Deniau, G. Zalczer and G. Lecayon, *J. Electroanal. Chem.*, **417** (1996) 175.

198 "Multimode™ Scanning Probe Microscope Instruction Manual", Version 4.31ce, Digital Instruments Inc., 1996-97.

199 "Preparation and Characterisation of the low band gap polymer PCDM", C. Dalton, M. Sc. dissertation, University of Wales, Bangor, 1998.

200 L. Torsi, A. Dodabalapur, L. J. Rothberg, A. W. P. Fung and H. E. Katz, *Phys. Rev. B.: Condensed Matter*, **57** (1998) 2271.

201 R. A. Street, G. Davies and A. D. Yoffe, *J. Non. Cryst. Sol.*, **5** (1971) 276

202 "Dielectric Materials and Applications", A. R. Von Hippel, Artech House, Boston, USA, 1995.

203 For example, T. R. Hebner, C. C. Wu, D. Marcy, M. H. Lu and J. C. Sturm, *Appl. Phys. Lett.*, **72** (1998) 519. J. Bharathan and Y. Yang, *Appl. Phys. Lett.*, **72** (1998) 2660. T. R. Hebner and J. C. Sturm, *Appl. Phys. Lett.*, **73** (1998) 1775. G. Percin, T. S. Lundgren and B. T. Kuhri-Yakub, *J. Appl. Phys.*, **73** (1998) 2375.

204 For example, M. J. Lee, C. P. Judge and S. W. Wright, *Solid-St. Electr.*, **44** (2000) 1431. O. Prucker, M. Schimmel, G. Tovar, W. Knoll and J. Ruhe, Adv. Mater., 10 (1998) 1073. T. Miyashita, M. Nakaya and A. Aoki, *Thin Solid Films*, **328** (1998) 833.

205 "Advances in Laser Ablation, Symposium", Eds. R. K. Singh, D. H. Lowndes, D. B. Chrisey, E. Fogarassy and J. Narayan, Mater. Res. Soc, San Francisco, 1998.

206 A. Slocombe and L. Li, *Appl. Surf. Sci.*, **154** (2000) 617.

207 A. Yabe, J. Wang and H. Niino, *Proceedings of the SPIE - The International Society for Optical Engineering*, **3550** (1998) 276.

208 "Proceedings of the International Conference on Lasers '98", Z. Qui, Z. Yang, X. Lu, Y. Wang, T. He, L. Quin, Q. Wang and Y. Zhang, Soc. Opt. and Quantum Elecron., USA, 1998, 929.

209 "Contemporary Polymer Chemistry", H. R. Allcock and F. W. Lampe, Prentice-Hall Inc., NJ, 1981

210 T. Jawhari, J. C. Merino and J. M. Pastor, *Polymer Bulletin*, **34** (1995) 71.

211 N. C. Greenham and R. H. Friend, *Solid State Phys.*, **49** (1995) 1.

212 A. A. Serafetinides, C. D. Skordoulis, M. I. Makropoulou and A. K. Kar, *Appl. Surf. Sci.*, **135** (1998) 276.

213 T. Lippert, *Proceedings of the SPIE - The International Society for Optical Engineering*, **3274** (1998) 204.

Bibliography

- "Semiconductors and Electronic Devices", 3rd edition, A. Bar-Lev, Prentice Hall International Ltd., UK, 1993.
- "Semiconductor Devices, Circuits and Systems", A. Moschwitzer, Clarendon press, Oxford, UK, 1991.
- "Introduction to Semiconductor Materials and Devices", M. S. Tyagi, John Wiley and Sons, NY, 1991.
- "Fundementals of Semiconductor Devices", E. S. Yang, M^{c}Graw-Hill Book Co., NY, 1978.
- "Physics and Technology of Semiconductor Devices", A. S. Grove, John Wiley and Sons, NY, 1967.
- "Metal-Semiconductor Contacts", H. Rhoderick, Oxford University Press, Oxford, UK, 1978.
- "Dielectric Materials and Applications", A. R. Von Hippel, Artech House, Boston, USA, 1995.

- "Handbook of conducting polymers", 2nd edition, T. A. Skotheim, R. L. Eisenbaumer and J. R. Reynolds (eds.), Marcel Dekker Inc., NY, 1998.
- "Quantum Theory of Solids", R. E. Pieirls, Clarendon Press, Oxford, UK, 1955.
- "Organic Semiconductors", F. Gutmann and L. E. Lyons, John Wiley and Sons Ltd., 1967.
- "Advances in Synthetic Metals: Twenty Years of Progress in Science and Technology", P. Bernier, S. Lefrant and G. Bidan (eds.), Elsevier Science, Switzerland, 1999.
- "Electronic Processes in Ionic Crystals", N. F. Mott and R. W. Gurney, Oxford University Press, 1940.
- "Electroactive Polymer Materials, State of the art review of conductive polymers", Technomic publishing Co. Inc., Lancaster, PA.
- "Conducting Polymers, Fundementals and Applications. A Practical Approach", P. Chandrasekhar, Kluwer Academic Publishers, Boston, USA, 1999.

- "Contemporary Polymer Chemistry", H. R. Allcock and F. W. Lampe, Prentice-Hall Inc., NJ, 1981

- "Organic Chemistry", K. P. C. Vollhardt, W. H. Freeman and company, NY, 1987.
- "Physical Chemistry", 3rd Ed, P.W. Atkins, Oxford University Press, Oxford, UK, 1986.
- "Fundementals of Analytical Chemistry", D. A. Skoog, D. M. West and F. J. Holler, 7th Edition, Saunders College Publishing, USA, 1996.
- "Principles of Instrumental Analysis", D. A. Skoog and J. J. Leary, 4th Edition, Saunders College Publishing, USA, 1992.

- "Electrical Conduction in Polymeric Films", D. M. Taylor, Ph.D. thesis, University of Wales, Bangor, UK, 1970.
- "Organic Polymers and Solid State Fabrication", G. W. Jones, PhD thesis, University of Wales, Bangor, UK, 1999.
- "Polymer Light Emitting Diodes: Anode Surface Conditioning and Device Preparation", J. S. Kim, PhD Thesis, University of Cambridge, 2000.
- "Preparation and Characterisation of the low band gap polymer PCDM", C. Dalton, M. Sc. dissertation, University of Wales, Bangor, 1998.

Papers published during the course of this work

- "Investigations into a low band gap, semiconducting polymer", C. A. Mills, D. M. Taylor, P. J. Murphy, C. Dalton, G. W. Jones, L. M. Hall and A. V. Hughes, *Synthetic Metals*, **102** (1999) 1000.
- "The electrical characteristics of a heterojunction diode formed from an analine oligomer LB-deposited onto poly(3-methylthiophene)", Antonio Riul Jr., Christopher A. Mills and D. Martin Taylor, *Journal of Materials Chemistry*, **10** (2000) 91.
- "Langmuir and Langmuir-Blodgett (LB) films of 4-dicyanomethylene,4H-cyclopenta[2,1-b,3,4-b']dithiophene", A. Riul Jr., D. M. Taylor, C. A. Mills and P. J. Murphy, *Thin Solid Films*, **366** (2000) 249.
- "The preparation and characterisation of polymeric macrostructures (command surfaces) using electropolymerisation", Christopher A. Mills, David Lacey, Gary Stevenson and D. Martin Taylor, *Journal of Materials Chemistry*, **10** (2000) 1551.

Also,

- "A memory effect in the current-voltage characteristic of a low-bandgap conjugated polymer", D. M. Taylor and C. A. Mills, submitted to the Journal of Applied Physics.
- "Preparation and electrical characterisation of a low band gap, semiconducting polymer film based on a carbon bridged dithienyl monomer", C. A. Mills, D. M. Taylor, A. Riul Jr. and A. P. Lee, submitted to the Journal of Applied Physics.
- "Theoretical modelling and optical characterisation of low band-gap organic polymers", G. W. Jones, D. M. Taylor, P. J. Murphy, C. A. Mills, A. Riul Jr., B. Laks and J. Del Nero, in preparation.

ELSEVIER

Synthetic Metals 102 (1999) 1000–1001

SYNTHETIC METALS

Investigations into a low band gap, semiconducting polymer

C. A. Mills, D. M. Taylor, P. J. Murphy, C. Dalton, G. W. Jones, L. M. Hall, A. V. Hughes
Institute of Molecular and Biomolecular Electronics, University of Wales, Dean Street, Bangor, Gwynedd, LL57 1UT, UK.

Abstract

A low bandgap polymer based on a carbon-bridged dithienyl monomer has been prepared by potentiostatic electrodeposition. Microscopic analysis of the polymer revealed a generally smooth morphology with scattered features protruding from the surface. Raman mapping shows the presence of a thickness dependent fluorescence in the film. Al/polymer/ITO Schottky diodes based on this new polymer show a small degree of rectification.

Keywords: Electrochemical polymerisation, semiconducting films, low-bandgap conjugated polymers.

1. Introduction

Low-bandgap semiconducting polymers have potential applications in photonic devices and sensors. In addition to ease of processing and improved mechanical properties compared with their inorganic counterparts, the characteristics of semiconducting polymers may also be influenced by slight changes to their chemistry. Already many studies have been carried out on oligomers and polymers [1] based on the thiophene molecule. In this paper we present new results from an on-going investigation of a low-band-gap polymer based on CDM, a carbon-bridged dithiophene.

2. Experimental

4H-cyclopenta [1, 2-b ; 3, 4-b'] dithiophene-4-one (CDT) **1** was synthesised using a method described previously [2]. 4-dicyanomethylene-4H-cyclopenta [1,2-b;3,4-b']dithiophene (CDM) **2** was then fabricated from CDT using a piperidine catalysed Knoevenagel condensation [3] (Figure 1).

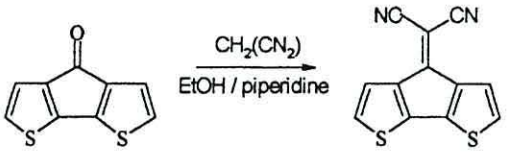

1 **2**

Figure 1. CDM monomer synthesis.

The polymer was potentiostatically grown onto gold coated microscope slides or indium tin oxide (ITO) glass using a three electrode polymerisation cell controlled by a Princeton Applied Research EG&G potentiostat/galvanostat Model 273. The cell consisted of a platinum foil secondary electrode, a silver wire reference electrode and contained a solution of CDM monomer (0.01 mol dm^{-3}) and tetrabutylammonium tetrafluoroborate (TBATFB, 0.1 mol dm^{-3}) in nitrobenzene.

Polymer films were grown at +1.6 V (vs Ag/Ag^+) for 600s following a nucleation step at 1.7V (vs Ag/Ag^+) for 10s, the potentials previously established by voltammetry. The electrodeposited films were removed from the solution, rinsed with acetone and dried under a stream of nitrogen. Subsequently, films were placed in a turbomolecular pumped evaporator and 100 nm thick aluminium films evaporated at 10^{-5} mbar onto the surface through a mask to form an array of circular devices, 1 mm^2 in area. The DC characteristics of the devices were obtained under vacuum (10^{-3} mbar) using a Hewlett-Packard 4140B pA meter/DC voltage source. Microscopic analysis of the polymer was undertaken using a Digital Instruments Nanoscope 3A atomic force microscope (AFM) and an International Scientific Instruments ISI-40 scanning electron microscope (SEM). Spectroscopic analysis of the monomer was completed using a Bruker AC 250 MHz nuclear magnetic resonance (NMR) spectrometer. Both the monomer and polymer were examined using a Renishaw Ramascope 1000 Raman Microscope with a He/Ne excitation laser (633 nm).

3. Results and discussion

Proton NMR studies (Table 1) show no change in the main spectral lines of a monomer sample immediately after synthesis and after storage for 1 year in the dark under vacuum. The slight differences in intensities arose from differences in the concentrations of the samples. This is confirmed by the Raman spectra of the samples where the background counts were similar but the spectral lines of the older sample were less intense. It is concluded therefore that, the monomer is stable for long periods under the storage conditions indicated.

SEM and AFM investigation of polymer film grown on gold-coated glass slides, revealed a generally smooth, pinhole-free morphology with larger aggregates up to ~0.2μm high scattered over the surface (Figure 2).

Raman mapping of the polymer surface (Figure 3) showed the presence of vibrational modes superimposed on a changing background fluorescence. Interestingly, at the top edge of the

PII: S0379-6779(98)01170-9

film where the thickness tapers to zero, the fluorescence intensity grows from about 2000 counts over the bulk film to >6000 counts midway along the taper before falling away to zero at the extreme edge of the film. This result shows that control of film thickness and/or doping concentration may be important in maximising the efficiency of electroluminescence from light emitting diodes formed from this polymer.

The I-V characteristics of an Al/polymer/ ITO diode is shown in Figure 4. A small degree of rectification is apparent with, strangely, the higher currents flowing when the ITO electrode is negatively biased.

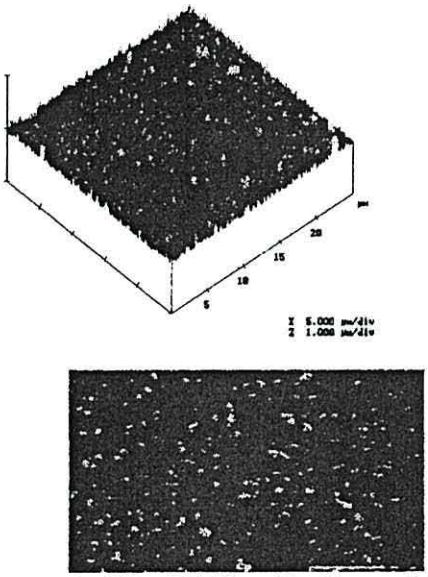

Figure 2. AFM and SEM (bar = 10 μm) images of a CDM polymer film on gold coated glass.

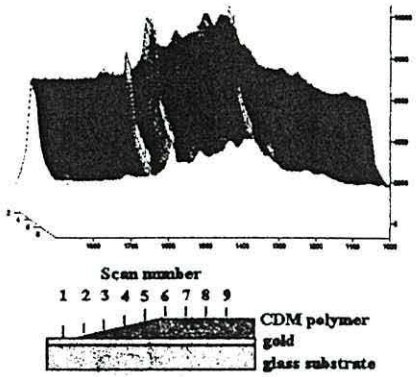

Figure 3. Raman map from a CDM polymer film (x-axis : wavenumbers, y-axis : Raman counts, z-axis : scan number (shown diagrammatically).

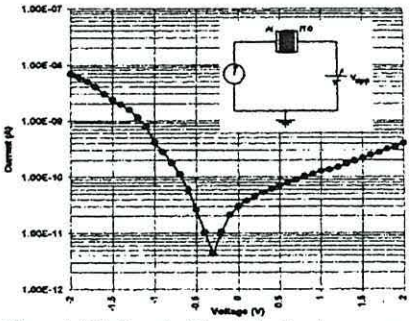

Figure 4. I-V characteristic obtained under vacuum at T = 293K.

4. Conclusions

Results from a microscopic, spectroscopic and electrical characterisation of the low band-gap semiconducting polymer CDM are presented. The electrodeposited polymer has a smooth surface morphology with small, scattered aggregates protruding from the surface. Raman maps show background fluorescence dependent on film thickness. The I-V characteristics show some rectification but opposite in direction to that normally observed for an Al/polymer Schottky diode

Acknowledgements

The authors would like to thank EPSRC and BNFL for supporting this work.

References

[1] Handbook of conducting polymers, T. A. Skotheim, Marcell Dekker, NY.,1986, and references within.
[2] P. Jordans, G. Rawson, H. Wynburg, *J. Chem. Soc. Chem. Comm.* (1970) 273.
[3] J. P. Ferraris, T. Lambert, *J. Chem. Soc. Chem. Comm.* (1991) 1268.

Table 1.
NMR spectral data for CDM monomer immediately after synthesis and approximately one year later.

new monomer		1 year old monomer		multiplicity	description
δ (ppm)	intensity (arb. units)	δ (ppm)	intensity (arb. units)		
1.56	5.85	1.56	17.69	singlet	atmospheric water vapour
7.10	6.96	7.10	6.12	doublet	protons in 3-position on CDM
7.12	7.59	7.12	7.01		
7.27	15.12	7.27	27.31	singlet	chloroform (NMR solvent)
7.41	7.55	7.41	6.85	doublet	protons in 2-position on CDM
7.43	6.91	7.43	6.27		

JOURNAL OF Materials CHEMISTRY

The electrical characteristics of a heterojunction diode formed from an aniline oligomer LB-deposited onto poly(3-methylthiophene)†

Antonio Riul Jr., Christopher A. Mills and D. Martin Taylor*

Institute of Molecular and Biomolecular Electronics, University of Wales, Dean Street, Bangor, Gwynedd, UK LL57 1UT. E-mail: martin@sees.bangor.ac.uk

Received 24th May 1999, Accepted 13th August 1999

Organic heterojunction diodes have been formed by depositing a Langmuir–Blodgett (LB) multilayer of 16-mer polyaniline and stearic acid (1 : 1) onto films of poly(3-methylthiophene) electropolymerised onto gold electrodes. The diode was completed by depositing small, circular gold counterelectrodes onto the LB film. The devices thus formed show weak rectification. In forward bias it is argued that all the applied field appears across the LB layer. At high applied fields the resulting current follows the Richardson–Schottky equation indicative of electrode limitation, though it is not clear whether the rate limiting step is electron emission from the gold electrode or hole emission from the polymer into the LB film. In reverse bias it is argued that part of the applied voltage appears across the depletion region formed at the interface between the polymer and the LB film resulting in a smaller reverse current for a given applied voltage. The frequency dependence of capacitance and loss for the diode structure is reminiscent of a Maxwell–Wagner dispersion normally associated with a two-layer structure. However, reasonable agreement between experimental data and theoretical modelling is only possible if a third layer, *i.e.* the depletion region at the interface of the two organic films, is included in the model. This is confirmed by the reverse-bias capacitance–voltage curve which suggests that the device behaves as a Metal–Insulator–Semiconductor (MIS) structure driven into depletion/inversion. In forward bias, when the LB/polymer interface is in accumulation, the capacitance again decreases as the bias voltage increases. While this effect could be ascribed to the presence of a second depletion layer in the device, it is argued that this behaviour arises from the increase in conductance of the LB multilayer shunting the LB layer capacitance.

1 Introduction

Thiophenes and polyanilines are two important classes of conducting polymers owing to their stability in the neutral state. As such they have been investigated for a range of electronic applications. For example, Schottky diodes exhibiting high rectification ratios have been fabricated from electropolymerized poly(3-methylthiophene) (P3MeT) over the last ten years using aluminium or molybdenum as the rectifying contact.[1–8] The currents flowing through these devices were found to be sensitive to both the thickness and the doping concentration in the P3MeT film, while thermal annealing was found to improve the rectification ratio.[1,3] The electrical characteristics were strongly affected by the exposure of P3MeT film to oxygen and water vapour which changed drastically the rectification ratio of the diodes[1,8] presumably by changing the concentration of electronegative dopants in the polymer. At high forward bias, conduction through the devices appeared to be determined by a space-charge-limited-current (SCLC) regime involving an exponential distribution of traps.[8] Some evidence has also been given[5] for the presence of minority carriers in this normally p-type material.

Schottky barriers have been fabricated from polyaniline (PANi) using electropolymerization,[9,10] solvent casting[11–13] and Langmuir–Blodgett (LB) deposition,[14] vacuum deposited films[15] and pellets[16] of the organic layer. Acid doping of the polyaniline in these devices led to an increase in the rectification ratio, a decrease in the barrier height and a decrease in the width of the depletion region.[12,13]

Pani has also been successfully employed as an intermediate layer between ITO and MEH-PPV in light emitting diodes (LEDs), improving device performance through better hole injection from the ITO.[17–19] Such an effect was also reported[20] for insulating cadmium stearate films LB-deposited onto gallium phosphide where an enhanced electroluminescence was tentatively ascribed to increased hole injection from the metal electrode but could also have arisen from the formation of localised defects in the insulating layer at the high device currents employed.

Heterojunctions formed between organic semiconducting materials of different bandgaps offer the possibility of developing device structures with unique electrical properties. P3MeT and PANi with bandgaps of 2.0 eV[7] and 3.14 eV[15] respectively are potential candidates for forming such junctions. The present paper reports some recent results obtained during an on-going investigation of an organic heterojunction prepared by the LB deposition of a mixed stearic acid–PANi oligomer (16-mer) (1 : 1 wt/wt) onto P3MeT films prepared by electrodeposition onto gold substrates. Using the LB technique to deposit the 2nd layer gives the possibility of interposing an ultrathin layer of controlled thickness and composition between the polymer and the counterelectrode. Since the LB layer is expected to be relatively insulating (the 16-mer is undoped) the structure acts essentially as a Metal–Insulator–Semiconductor (MIS) diode, thus enabling a systematic study of the effects of an interfacial layer on charge injection from electrodes into the polymer. As a result, a range of techniques well-known in the study of inorganic interfaces becomes available for investigating the electronic properties of the polymer.

The present experiments differ from those on bilayer polymer films described by Murray and co-workers in the 1980s[21–24] in that the latter were carried out in electrolytic solutions to monitor redox activity in polymer films containing redox active species. Such interactions are not expected in the present work, since our measurements were carried out on 'dry' films so that solid state charge transport processes are expected to be more relevant.

†Basis of a presentation given at Materials Chemistry Discussion No. 2, 13–15 September 1999, University of Nottingham, UK.

2 Experimental procedures

All devices were prepared in a class 10000 clean room. Microscope slides were cleaned with DECON90 and chromic acid, followed by a thorough rinse with ultrapure water (Millipore SuperQ System). A gold film ~30 nm thick was vacuum evaporated, in a Balzers (TSH 170) turbosystem at pressures less than 10^{-6} Torr, onto the slides which had been precoated with a thin chrome layer to aid adhesion. Substrates free of visual defects were then selected for the deposition of P3MeT.

Electrodeposition was carried out in a conventional three-electrode cell connected to a Princeton EG&G, model 273, potentiostat/galvanostat following techniques which have been shown by Taylor and Gomes to result in the growth of films of reproducible thickness and morphology.[4] Briefly, a rectangular sheet of platinum foil 2.5 cm × 3 cm acted as the counter-electrode and a clean silver wire as the quasi-reference electrode. One of the gold-coated glass slides, dipped to a depth of 2.5 cm into the electrolyte solution, formed the working electrode. Electropolymerization was effected by anodic oxidation at room temperature in a 0.05 M solution of 3-methylthiophene monomer (Aldrich) dissolved in propylene carbonate (HPLC grade) using 0.1 M of tetrabutylammonium tetrafluoroborate (TBATFB) as the supporting salt. Nitrogen was bubbled through the solution for at least 20 minutes prior to starting the electrodeposition. The nitrogen flux was moderate to avoid both solvent and monomer evaporation. The P3MeT was grown by applying a 2.3 V (*vs.* Ag) pulse to the working electrode for 3 s after which the potential was reduced to 1.8 V (*vs.* Ag) and maintained constant until a film of the desired thickness had been grown. Under these experimental conditions, the film grows uniformly over the central area of the working electrode (~1 cm^2) at a rate of about 0.6 μm min^{-1}.[25] The films were electrochemically dedoped by reducing the potential of the working electrode to 0.0 V (*vs.* Ag) until the current had decreased to ~2.4 μA cm^{-2}. Afterwards, the films were washed with acetone (Aldrich) to remove residual electrolytic solution and dried in a stream of dry-nitrogen.

The monodisperse 16-mer PANi used in this work was synthesised chemically from the tetramer in the leucoemeraldine oxidation state following the procedures of Zhang *et al.*[26] A sample of the 16-mer PANi was mixed with camphorsulfonic acid, dissolved in *m*-cresol and added to a solution of stearic acid dissolved in chloroform (HPLC) to form a 1:1 (wt/wt) PANi–stearic acid spreading solution. Earlier work[27] had established that films of this composition were stable at the air–water interface and deposited with good deposition ratio. Mixed LB films of the 16-mer PANi and stearic acid were deposited onto the P3MeT films following procedures fully reported elsewhere.[27] Briefly, an aliquot of the final solution was spread over the surface of a pure water subphase and 5 min allowed for solvent evaporation before the monolayer was compressed to 25 mN m^{-1}. The P3MeT-coated slides were dipped vertically through the monolayer at a rate of 2 mm min^{-1}. Deposition occurred on both the up- and down-stroke with deposition ratios close to unity. To aid later comparisons, the LB films were deposited in staircase fashion so that three different thicknesses, namely 5, 15 and 41 monolayers, of the 16-mer PANi were accommodated on the same P3MeT layer. The diodes were completed by placing the films in the turbopumped vacuum chamber and evaporating circular gold or aluminium counterelectrodes, 0.8 mm^2 in area, onto the free surface of the 16-mer PANi. Electrical connections to the metal electrodes were made using fine gold wire and silver dag.

The electrical characteristics of the diodes were measured both under vacuum (0.12 mbar) and in ambient atmosphere using a HP 4041B pA meter/DC source. The AC characteristics were measured over the range 20 Hz to 1 MHz using an HP 4284A Precision LCR meter. In both cases, the data were logged automatically by computer.

3 Results

The morphology of the electropolymerised P3MeT film was similar to that reported by Taylor and Gomes[4] *i.e.* the 0.3 μm films were dense with a nodular structure as seen in the AFM micrographs in Fig. 1. Even in the worst case, the rms roughness over a 25 × 25 $μm^2$ area was less than 24 nm. At higher magnification, the films appeared much smoother with an rms roughness of ~15 nm over a 0.5 × 0.5 $μm^2$ area.

3.1 DC characteristics

Fig. 2 shows the dependence of current density, *J*, on applied voltage for diodes with LB films of three different thicknesses, (a) 5, (b) 15 and (c) 41 monolayers, deposited onto the same P3MeT layer and furnished with gold counterelectrodes.The diodes exhibit a weak rectification with the higher currents (forward bias) corresponding to hole injection from the lower gold electrode into the P3MeT layer. For both polarities, the device current increased superlinearly with increasing applied voltage. Except for a small difference in reverse bias, it was immaterial whether the device characteristics were measured in air or under vacuum.

Curve (d) in Fig. 2 was obtained for a diode incorporating a 15-layer LB film but furnished with an aluminium counter-electrode. Again the device displays a weak rectification but the striking features is that the currents for *both* polarities of applied voltage are ~4 orders of magnitude smaller than for the diode with the gold counterelectrode.

For both polarities of applied voltage in the absence of the LB layers, device currents measured in air with a gold counterelectrode were orders of magnitude greater than the currents reported in Fig. 2. Under vacuum, currents measured in these 'pure' P3MeT diodes were much reduced owing to a reduced degree of oxygen doping of the P3MeT[1] but still remained significantly greater than those reported in Fig. 2 for the heterojunction devices.

3.2 AC characteristics

Fig. 3 shows the experimentally-measured dependence of the diode capacitance and loss on frequency. The capacitance (curve (o)) displays a strong dispersion between 10^3 and 10^5 Hz. The corresponding maximum in the AC loss curve (*) is apparently swamped by the presence of a low-frequency loss that rises rapidly as the frequency decreases.

Fig. 4 gives the dependence of device capacitance on applied voltage. Interestingly and unexpectedly, the capacitance is a maximum at zero applied bias and decreases for increasing bias in both forward and reverse directions. For reverse bias ($-V$), however, the capacitance eventually tends to a constant value at the highest applied voltage but decreases throughout the measurement range with increasing forward bias.

4 Discussion

It is well-known that a gold electrode is a good hole injector into P3MeT.[4] Furthermore, as indicated above, the forward bias current is significantly reduced in the heterojunction diodes compared with Au/P3MeT/Au diodes for the same magnitudes of applied voltage. Clearly, then, transport through the LB layers appears to be the rate limiting step. That device characteristics were almost independent of whether the measurements were carried out in ambient air or under vacuum provides further confirmation for the controlling influence of the LB layer. In forward bias, polarisation of the

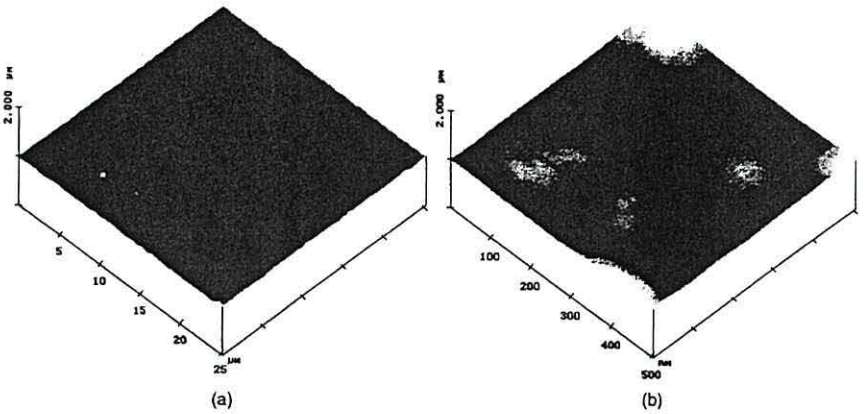

Fig. 1 AFM micrographs showing the morphology of a typical P3MeT film ~0.3 μm thick at different magnifications: (a) 25 × 25 μm; (b) 0.5 × 0.5 μm. In both cases the *z*-scale is 1 μm per division.

P3MeT film will occur with holes accumulating at the P3MeT/LB film interface causing the field in the polymer to collapse. Thus, to a first approximation at least, all the applied voltage may be assumed to appear across the LB layer.

Replotting the data in Fig. 2 for the device with gold counterelectrodes in order to show the explicit dependence of device currents on the applied field, E, appearing in the LB layers yields the characteristics in Fig. 5. (The field E is calculated assuming the LB layer to have a thickness of 25 nm per monolayer).[28] In forward bias (Fig. 5(a)) the currents appear to follow a square-law dependence on field at high fields suggesting space-charge limitation. In such a regime it is expected that[29] eqn. (1) holds,

$$J = \frac{9}{8}\varepsilon\varepsilon_0\theta\mu\frac{V^2}{d^3} \tag{1}$$

where ε is the relative permittivity of the material, ε_0 the permittivity of free space, θ the ratio of free to trapped carriers and d the film thickness. From eqn. (1) it is readily deduced that when space-charge-limitation is present, the forward currents at a given applied field in Fig. 5(a) should be inversely proportional to the thickness of the LB layer. This is clearly not the case. All the data appear to fall more or less onto the same general curve. It is likely, therefore, that emission either of holes across the P3MeT/LB film interface or electrons from the gold counterelectrode into the LB film is the rate limiting step.

When the electrode emission is controlled by thermal emission over a field-lowered, image-law barrier, so-called Schottky emission, the dependence of current on applied field is given by the Richardson–Schottky equation[29] generally written as the high field approximation eqn. (2),

$$J = A * T^2 \exp\left(-\frac{(\phi_b - e\beta_S E^{1/2})}{kT}\right) \tag{2}$$

where A^* is the Richardson constant, T the absolute temperature, ϕ_b the height of the barrier to thermal emission, e the electronic charge, β_S the Schottky coefficient and k Boltzmann's constant. For emission into a semiconductor or insulator eqn. (3) holds,

$$\beta_S = \left(\frac{e}{4\pi\varepsilon_\infty\varepsilon_0}\right)^{1/2} \tag{3}$$

where ε_∞ is the high frequency relative permittivity of the semiconductor or insulator.[29] (At lower fields the exponential term in eqn. (2) is replaced by the more correct sinh function.)

In Fig. 6 the data from Fig. 2 are replotted to test for

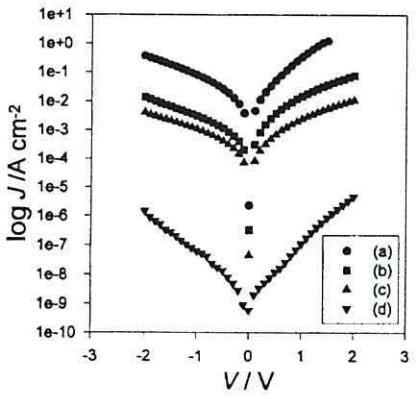

Fig. 2 Log J *vs.* V for Au/P3MeT/16-mer/Au heterojunctions in air for diodes incorporating (a) 5, (b) 15 and (c) 41 monolayers of LB deposited films of PANi–stearic acid. Curve (d) is for a Au/P3MeT/16mer/Al diode incorporating a 15-monolayer LB film.

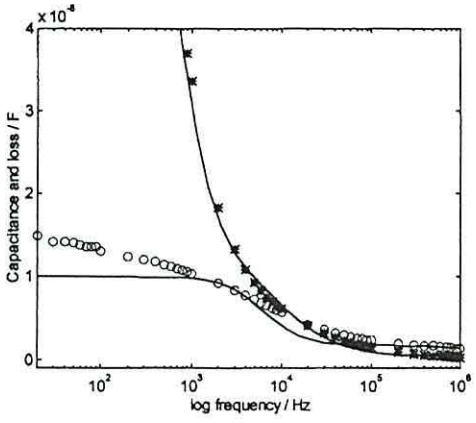

Fig. 3 Experimentally measured capacitance (o) and loss (*) as a function of frequency for a diode incorporating a 15-monolayer LB film and a gold counterelectrode. The theoretical response (—) of the three element RC equivalent circuit in Fig. 8 for which it is assumed that $R_1 = 50\ \Omega$, $R_2 = 1.6\ k\Omega$, $R_d = 3.8\ k\Omega$, $C_1 = 0.2$ nF, $C_2 = 2.0$ nF and $C_d = 20$ nF.

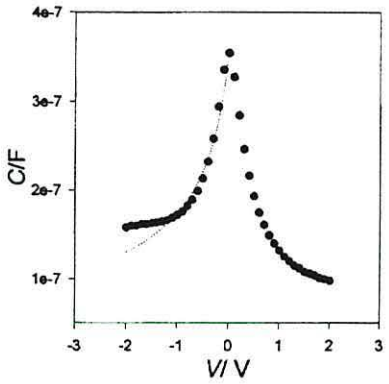

Fig. 4 Capacitance–voltage (C–V) plot for a diode incorporating a 15-monolayer LB film and furnished with a gold counterelectrode. The dotted curve is a theoretical plot based on eqn. (11) for which it has been assumed that $C_{LB}=3.6\times10^{-7}$ F cm^{-2}, $\varepsilon=5$ and $N_A=1.1\times10^{18}$ cm^{-3}.

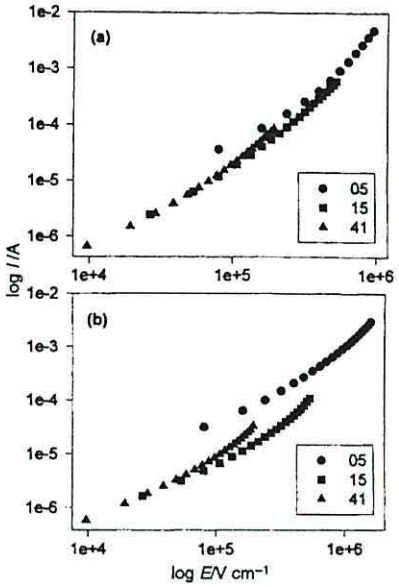

Fig. 5 Log I *vs.* log E for Au/P3MeT/16-mer/Au diodes with 5, 15 and 41 LB monolayers in (a) forward and (b) reverse bias. The fields were calculated by assuming that all the applied voltage appears across the PANi LB layer.

Schottky emission. As can be seen, for forward bias (Fig. 6(a)) all three curves asymptote to the same linear dependence at the highest fields. That the forward characteristics at high fields are independent of the LB layer thickness is good evidence for the integrity of the LB layers and, more importantly, supports the notion of an electrode limited process. From the gradient at high fields and assuming $T=300$ K, β_S is estimated to be 1.8×10^{-5} (V m)$^{-1/2}$ from which it is deduced that $\varepsilon_\infty=4.5$ for the mixed stearic acid–16-mer layer. In total some 40 devices on seven different P3MeT films were studied. While some differences were observed in the actual magnitude of the currents flowing at a particular applied field, the functional relationship was identical with values estimated for ε_∞ falling in a narrow range from 2.6 to 4.5. This compares with values of 2.71, the reported relative permittivity of stearic acid,[30] and 5.6 when the LB layer was formed from the pure 16-mer polyaniline.

The general behaviour seen in Fig. 6(a) coupled with the eminently reasonable range of values estimated for ε_∞ provides strong evidence for Schottky emission. This begs the question as to whether the current is an electron emission from the gold counterelectrode or hole emission from the P3MeT into the LB film. Aluminium has a smaller workfunction than gold, and so should favour electron emission. However, from Fig. 2 it is seen that an aluminium counterelectrode reduces both the forward and reverse currents by several orders of magnitude. While this may be taken as evidence against electron emission occurring from the gold counterelectrode, it is known that aluminium forms a Schottky barrier to PANi[11,15] and may also have an associated, highly insulating interfacial layer. Therefore no definitive conclusion as to the origin of the barrier to thermal emission in the diode is possible without carrying out further investigations.

In reverse bias the situation is even less clear. At low fields the currents are ohmic but quickly become superlinear as the applied field increases (Fig. 5(b)). Some dependence on the thickness of the LB layer is seen but not that expected from eqn. (1). In any case, since the reverse currents are lower than for forward bias then, *de facto*, the former cannot be space-charge-limited, unless a different carrier of lower mobility now dominates charge transport. When replotted in Fig. 6(b) a good linear dependence indicating Schottky emission is again seen but in contrast with forward bias β_S now depends on the thickness of the LB layer so that values calculated for ε_∞ range from 1.8 to 11.

It is notable that, for both forward and reverse bias applied to the device with the thinnest LB layer, extrapolating the I–V plots suggests that the currents flowing at low fields would be greater than expected if low-field transport was dominated by ohmic conduction through the film. If indeed, as suggested, an image-law barrier dominates transport, then it is not surprising that the five-layer film behaves differently to the others. This layer will be sufficiently thin (~12.5 nm) to cause an overlap of the image law barriers from both interfaces so that even with zero applied field the barrier height is reduced by an amount $\Delta\phi_b=2(q^2/16\pi\varepsilon\varepsilon_0x_0^2)$ where $2x_0$ is the thickness of the LB layer. Assuming $\varepsilon=4.5$ and a film thickness of 12.5 nm, then $\Delta\phi_b=0.013$ eV, which is sufficient to increase thermal emission currents by a factor 3 or so above that expected in a wider barrier at the same applied field. At high fields, the maximum in the potential barrier moves close to one electrode so that the influence of the second electrode becomes negligible and the dependence on film thickness is lost.

With fields approaching 1 MV cm^{-1} in a thin barrier, tunnelling may also become a possibility. Parker[31] has shown that the DC characteristics of thin PPV films follow the Fowler–Nordheim law,[29] eqn. (4),

$$J=AE^2\exp\left(-\frac{B\cdot\phi_b^{3/2}}{E}\right) \quad (4)$$

where A and B are constants. In Fig. 7 the forward bias data from Fig. 2 are replotted as ln I/E^2 *vs.*, $1/E$. Only the diode with the five-layer LB film shows the steep, negatively sloping plot indicative of tunnelling. Following Parker's analysis, ϕ_b is estimated to be 0.003 eV which is unreasonably small. Clearly, measurements would need to be carried out to much higher fields before tunnelling was significant when, presumably, a much steeper slope would be observed and a more realistic barrier height deduced.

The dispersion in capacitance observed in Fig. 3 appears to follow the behaviour expected from a capacitor composed of two homogeneous layers. The equivalent circuit of such an arrangement is the series-parallel RC circuit shown in Fig. 8(a) where C_1 and R_1 represent the properties of the P3MeT layer while C_2 and R_2 represent the stearic acid–16-mer layer. It is

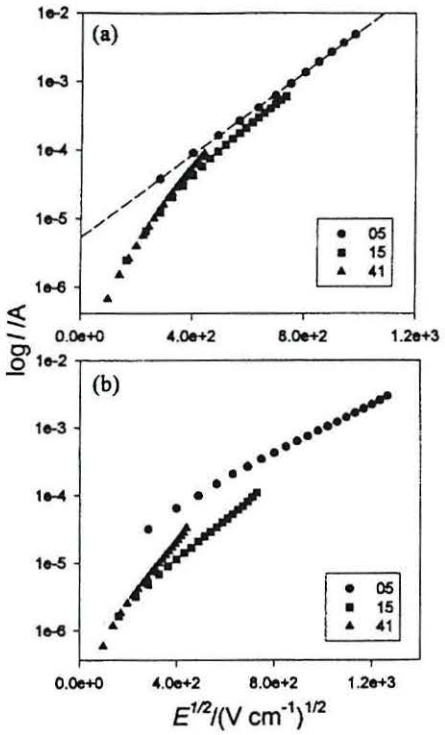

Fig. 6 The data in Fig. 5 replotted as log I *vs.* $E^{1/2}$ to test for Schottky emission in (a) forward bias and (b) reverse bias.

readily shown that the admittance of such a circuit is given by[4] eqn. (5),

$$Y = G + j\omega C \tag{5}$$

where ω is the angular frequency, eqn. (6a)

$$C = C_g + \frac{C_{LF} - C_g}{1 + (\omega\tau)^2} \tag{6a}$$

and eqn. (6b).

$$G = G_{LF} + \frac{G_a}{1 + (\omega\tau)^2} \tag{6b}$$

Here, G_{LF} is the low frequency conductance $(R_1 + R_2)^{-1}$, and eqn. (7)–(10) hold.

$$C_g = \frac{C_1 C_2}{C_1 + C_2} \tag{7}$$

$$C_{LF} = \frac{C_1 R_1^2 + C_2 R_2^2}{(R_1 + R_2)^2} \tag{8}$$

$$G_a = \omega^2 \frac{R_1 R_2 (R_1 C_1 - R_2 C_2)^2}{(R_1 + R_2)^3} \tag{9}$$

$$\tau = \frac{R_1 R_2}{(R_1 + R_2)} (C_1 + C_2) \tag{10}$$

These equations describe the so-called Maxwell–Wagner effect and predict that the device should display Debye-like behaviour. This is certainly true of the capacitance (o) in Fig. 3 but the expected maximum in the loss term, $G\omega^{-1}$ (*) cannot be discerned. Presumably this could be because it is swamped by the DC term, $(R_1 + R_2)^{-1}$ in eqn. (6b), which would manifest itself as an ω^{-1} dependence in Fig. 3. However, no combination of resistances and capacitances in the equivalent circuit in Fig. 8(a) can reproduce the experimental plots, indicating that additional processes must be occurring in the devices. This is further confirmed by the experimental data presented in Fig. 4. Here it is seen that, for both polarities, the effective device capacitance decreases with increasing magnitude of applied bias. This result may be explained by considering the device to be a Metal–Insulator–Semiconductor (MIS) structure in which the insulating layer displays a moderate conductance. This is not an unreasonable assumption. Ram *et al.*[32] have shown that a metal/cadmium stearate/polypyrrole structure behaves as a classic MIS device showing a transition from accumulation to depletion and then inversion as the bias is swept from negative to positive values. In the present case, the undoped 16-mer PANi incorporated into the stearic acid layer should also be insulating although the presence of the 16-mer may increase the transport rate through the layer above that expected for a pure stearic acid film.

In reverse bias, positive voltage applied to the gold counterelectrode, holes are repelled from the P3MeT/LB layer interface creating a depletion region in the P3MeT composed of negatively charged acceptor ions. Consequently, an additional parallel RC element, R_d/C_d must be introduced into the equivalent circuit to represent the depletion region (see Fig. 8(b)). Upon increasing the reverse bias, the depletion region grows while the associated capacitance C_d and hence the overall device capacitance falls[33] in a manner described by eqn. (11),

$$C = \frac{C_{LB}}{\sqrt{1 + \frac{2C_{LB}^2}{eN_A\varepsilon\varepsilon_0} V}} \tag{11}$$

where C_{LB} is the capacitance per unit area of the LB layer, N_A the concentration of acceptor ions in the semiconducting P3MeT and ε the relative permittivity of P3MeT. The dotted curve in Fig. 4 represents the best fit of eqn. (11) to the experimental data assuming $\varepsilon = 5$[4] and $C_{LB} = 3.6 \times 10^{-7}$ F cm^{-2} from which it is deduced that $N_A = 1.1 \times 10^{18}$ cm^{-3}, a value at the top end of the range quoted by Taylor and Gomes[4] for electropolymerised P3MeT.

In conventional inorganic MIS devices, when a threshold voltage is reached the semiconductor surface inverts, at which point the device capacitance attains a constant value, a trend seen in Fig. 4. Depletion/inversion at the P3MeT/LB film interface could explain the poor fit of the reverse bias characteristics to the Richardson–Schottky equation. Part of the applied bias will now appear across the depletion region thus reducing the field across the LB layer and hence the current flowing through the device at a given applied voltage.

Assuming now that a depletion region is present at the

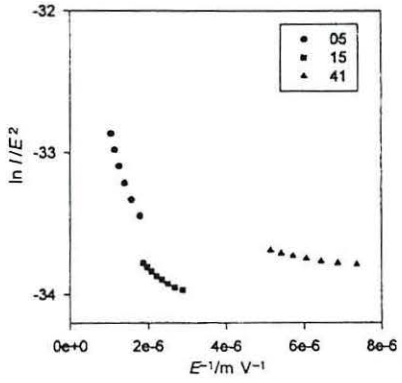

Fig. 7 The data from Fig. 5(a) replotted as ln I/E^2 *vs.* $1/E$.

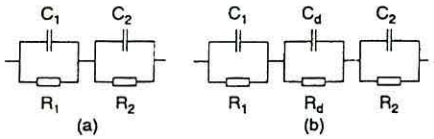

Fig. 8 (a) Equivalent circuit of a diode structure composed of two homogeneous layers. R_1 and C_1 represent the P3MeT layer while R_2 and C_2 represent the LB deposited 16-mer PANi film. In (b) an additional element R_d/C_d has been included to represent the presence of a depletion region at the interface between the two layers.

P3MeT/LB film interface and that the equivalent circuit in Fig. 8(b) applies, a further attempt was made to fit the experimental data in Fig. 3. The results shown by the continuous curves in Fig. 3 were obtained using the parameter set given in the caption and show reasonable agreement with experiment albeit with the latter displaying a wider frequency dispersion than the former. Although this is a 6 parameter fit, the need to reproduce both the capacitance and loss curves simultaneously places severe restrictions on the values that may be adopted for each parameter in the set, otherwise the quality of the fit deteriorates rapidly. Thus each parameter may be deduced within tightly defined ranges.

The theoretical fitting indicates that there are two main dispersions in the system, one in the range 10^3 to 10^4 Hz which coincides with that seen in Fig. 3 and the other at 10^9 Hz which is inaccessible using the present equipment. The low-frequency capacitance is determined in the main by the depletion region capacitance C_d but will depend to some extent on the values of the other components in the circuit. As the signal frequency increases a dispersion occurs with the measured capacitance decreasing to a value determined mainly by the capacitance of the LB layer but again influenced by the relative magnitudes of the other components. Finally at frequencies exceeding those used here a further decrease in capacitance would be expected to a value corresponding to the capacitance of the bulk P3MeT.

From the fit in Fig. 3, the depletion capacitance is deduced to be 20 nF and assuming that $\varepsilon \sim 5$ for P3MeT the width of the depletion region, d_d ($=\varepsilon\varepsilon_0 A/C_d$), is estimated to be ~ 1.8 nm. This is orders of magnitude lower than the thickness of ~ 300 nm measured for the bulk P3MeT layer using the AFM and a value of ~ 180 nm deduced from $C_1 = 0.2$ nF used to obtain the best fit in Fig. 3. The best fit value for the capacitance of the 15-layer LB films, $C_2 = 2.0$ nF, yields a *low-frequency* relative permittivity of ~ 10.6 which is approximately twice the *high-frequency* relative permittivity deduced from the Schottky plots in Fig. 6.

Returning now to Fig. 4, in forward bias the decrease in capacitance with voltage is readily explained by the 'lossy' nature of the LB layer. In this polarity, the depletion region at the interface is replaced by an accumulation layer, and the device equivalent circuit reverts to that in Fig. 8(a). As the bias increases, the LB-layer becomes more conductive, R_2 decreases and begins to shunt C_2, the capacitance of the LB layer, so that the measured capacitance will tend to C_1, the capacitance of the P3MeT layer.

5 Conclusions

A heterojunction diode has been formed by the controlled LB deposition of a 1 : 1 (wt/wt) mixture of stearic acid and 16-mer polyaniline onto electropolymerised P3MeT. Although the dependence of capacitance on voltage indicates the presence of a depletion region in the structure and rectification, albeit weak, is observed, the diodes are examples of MIS devices, in which most of the applied voltage appears across the LB layer.

The *I–V* characteristics in forward bias follow closely the Richardson–Schottky equation yielding a high-frequency relative permittivity in the range 2.6–4.5 for the LB-deposited layer. There is insufficient evidence to determine whether the current is an electron emission from the gold electrode or a hole emission from the P3MeT into the LB film. In reverse bias, Schottky emission is again believed to be the dominant conduction mechanism. However, agreement with theory is not as good, probably because part of the applied potential appears across the depletion/inversion layer present on the P3MeT side of the heterojunction.

At first sight, the AC characteristics appear to follow the simple Maxwell–Wagner model for a two-layer capacitor. However, only when a third RC element representing the depletion region is added to the equivalent circuit is it possible to obtain good agreement between theory and experiment.

In reverse bias the capacitance–voltage plot exhibits the behaviour of a classic MIS structure from which the doping density in the P3MeT is estimated to be 1.1×10^{18} cm^{-3}.

Acknowledgements

The authors are pleased to acknowledge the financial support provided by the Engineering and Physical Sciences Research Council and BNFL (CASE studentship to CAM) and are grateful to FAPESP for the award of the Research Fellowship to AR.

References

1 D. M. Taylor, H. L. Gomes, A. E. Underhill, S. Edge and P. I. Clemenson, *J. Phys. D: Appl. Phys.*, 1991, **24**, 2032.
2 H. L. Gomes and D. M. Taylor, *Mol. Cryst. Liq. Cryst.*, 1993, **236**, 151.
3 H. L. Gomes, D. M. Taylor and A. E. Underhill, *Synth. Met.*, 1993, **55**, 4076.
4 D. M. Taylor and H. L. Gomes, *J. Phys. D: Appl. Phys.*, 1995, **28**, 2554.
5 G. W. Jones, D. M. Taylor and H. L. Gomes, *Synth. Met.*, 1997, **85**, 1341.
6 H. L. Gomes, G. W. Jones and D. M. Taylor, *Synth. Met.*, 1997, **85**, 1351.
7 S. Tagmouti, A. Ouriagli, A. Outzourhit, M. Khaidar, L. Ameziani El, A. Yassar, H. K. Youssoufi and F. Garnier, *Synth. Met.*, 1997, **87**, 109.
8 S. Tagmouti, A. Ouriagli, A. Outzourhit, M. Khaidar, L. Ameziani El, A. Yassar, H. K. Youssoufi and F. Garnier, *Synth. Met.*, 1997, **88**, 109.
9 S. S. Pandey, S. C. K. Misra, B. D. Malhotra and S. Chandra, *J. Appl. Polym. Sci.*, 1992, **44**, 911.
10 Y. Renkuan, Y. Hong, Z. Zheng and Z. Youdou, *Synth. Met.*, 1991, **41**, 731.
11 C. Li, Y. Wang, M. Wan and S. Li, *Synth. Met.*, 1990, **39**, 91.
12 S.-A. Chen, Y. Fang and H.-T. Lee, *Synth. Met.*, 1993, **55**, 4082.
13 S.-A. Chen and Y. Fang, *Synth. Met.*, 1993, **60**, 215.
14 M. K. Ram, R. Gowri and B. D. Malhotra, *J. Appl. Polym. Sci.*, 1997, **63**, 141.
15 S. C. K. Misra, M. K. Ram, S. S. Pandey, B. D. Malhotra and S. Chandra, *Appl. Phys. Lett.*, 1992, **61(10)**, 1219.
16 S. S. Pandey, M. K. Ram, V. R. Srivastava and B. D. Malhotra, *J. Appl. Polym. Sci.*, 1997, **65**, 2745.
17 A. J. Heeger, I. D. Parker and Y. Yang, *Synth. Met.*, 1994, **67**, 23.
18 Y. Yang and A. J. Heeger, *Appl. Phys. Lett.*, 1994, **64(10)**, 1245.
19 Y. Yang, E. Westerweele, C. Zhang, P. Smith and A. J. Heeger, *J. Appl. Phys.*, 1995, **77(N2)**, 694.
20 J. Batey, G. G. Roberts and M. C. Petty, *Thin Solid Films*, 1983, **99**, 283.
21 H. D. Abruña, P. Denusevich, M. Umaña, T. J. Meyer and R. W. Murray, *J. Am. Chem. Soc.*, 1981, **103(1)**, 1.
22 P. Denisevich, K. W. Willman and R. W. Murray, *J. Am. Chem. Soc.*, 1981, **103**, 4727.
23 P. G. Pickup, W. Kutner, C. R. Leidner and R. W. Murray, *J. Am. Chem. Soc.*, 1984, **106**, 1991.
24 P. G. Pickup and R. W. Murray, *J. Electrochem. Soc.: Electrochem. Sci. Technol.*, 1984, **131(4)**, 833.
25 A. Pennarun, *Organic Systems for non-linear Optical Applications*, MPhil Thesis, School of Electronic Engineering and Computer Systems, University of Wales (UK), 1997.

26 W. J. Zhang, J. Feng, A. G. MacDiarmid and A. J. Epstein, *Synth. Met.*, 1997, **84**, 119.
27 A. Dhanabalan, A. Riul Jr. and O. N. Oliveira Jr., *Langmuir*, 1997, **13**, 4882.
28 A Riul Jr., A. Dhanabalan, L. H. C. Mattoso, L. M. de Souza, E. A. Ticianelli and O. N. Oliveira Jr., *Thin Solid Films*, 1998, **329**, 576.
29 J. G. Simmons, in *DC Conduction in Thin Films*, J. Gordon Cook, London, 1971.
30 G. Roberts, in *Langmuir-Blodgett Films*, Plenum Press, New York, 1990.
31 I. D. Parker, *J. Appl. Phys.*, 1994, **75(3)**, 1656.
32 M. K. Ram, S. Annapoorni and B. D. Malhotra, *J. Appl. Polym. Sci.*, 1996, **60**, 407.
33 M. S. Tyagi, in *Introduction to Semiconductor Materials and Devices*, John Wiley and Sons, Singapore, 1991.

Paper a904112e

ELSEVIER

Thin Solid Films 366 (2000) 249–254

thin solid films

www.elsevier.com/locate/tsf

Langmuir and Langmuir–Blodgett (LB) films of 4-dicyanomethylene,4H-cyclopenta[2,1–b,3,4–b′]dithiophene

A. Riul Jr., D.M. Taylor*, C.A. Mills, P.J. Murphy

Institute of Molecular and Biomolecular Electronics, University of Wales, Dean Street, Bangor, Gwynedd, LL57 1UT, UK

Received 26 July 1999; received in revised form 10 January 2000; accepted 10 January 2000

Abstract

Attempts at forming Langmuir monolayers and Langmuir–Blodgett (LB) multilayer films of 4-dicyanomethylene-4H-cyclopenta[2,1–b,3,4–b′]dithiophene (CDM), a low bandgap polymer precursor, are reported for the first time. The CDM was rendered soluble in different mixtures of common organic solvents with acetonitrile (CH_3CN). Highly condensed monolayers of both the CDM monomer and mixed films with stearic acid were obtained on ultrapure water, and transferred by vertical dipping onto glass, ITO (indium tin oxide-coated glass) and gold surfaces with good visual uniformity. The LB films were characterized by UV–vis and Raman spectroscopy, atomic force microscopy (AFM), and DC electrical conductivity (σ) measurements. AFM images show that deposited films are composed of microscopic crystallites, indicating that microcrystallites of CDM are formed during spreading and/or compression on the subphase surface. Comparing the average film thickness with the unit cell dimensions deduced from X-ray diffraction supports this view. The in-plane conductivity of pure CDM LB film was found to be $\sim 2 \times 10^{-9}$ S/cm.

Keywords: Atomic force microscopy; Conductivity; Raman spectroscopy; Langmuir–Blodgett films

1. Introduction

Recently, several new, low bandgap polymers have been designed [1–7] with promising potential for applications in electronics both as devices, e.g. Schottky diodes [8], and as polymeric contacts to devices [9–11]. It is possible also that such materials may find applications in thermal and chemical sensing. Unfortunately, poor processability militates against the use of many polymers and resort has to be made to the pre-processing of films prior to conversion to the final form. An example is the thermal conversion of a spin-coated film of PPyV monomer [12]. It is expected that the structure of the pre-converted layer will have some influence on the structure and morphology of the final film. In this context, the Langmuir–Blodgett (LB) technique should prove useful since it has been employed successfully for building up uniform multilayer of organic materials and has been applied to polymers. For example, polymers can be pre-formed at the air/water interface [13] or multilayers films can be polymerized after LB deposition [14,15]. Another advantage offered by the LB technique is the excellent control over architecture and thickness, enabling the fabrication of mixed multilayers analogous to bandgap engineering achieved by molecular beam epitaxy with inorganic compounds. Moreover, the use of more soluble oligomeric materials of polyaniline, for example, resulted in LB films having similar properties to those from high molecular weight polymers [16,17]. Although poor molecular organisation has been observed in Langmuir films of conducting polymers [18–20], the presence of surface irregularities during multilayer deposition [21–23] need not impede the fabrication of polymeric devices [24–28].

We have reported previously [8] on the preparation and electrical properties of electropolymerized films of the monomer 4-dicyanomethylene-4H-cyclopenta [2,1–b,3,4–b′]dithiophene (CDM). Dong et al. [11] recently reported the incorporation of this material into LEDs based on porous silicon for tuning the wavelength of the light output. Although it was reported that this material plays an important role in stable light emission, it should be noted that these workers are likely to have worked with the monomer material (CDM) since the polymer (PCDM) is highly insoluble in all normal organic solvents and, therefore, would be unsuitable for use in spin coating or self-assembly. Thin films formed from small organic molecules, e.g. pentacene [29], and end-capped sexithiophene [30] are also being investigated as the active semiconducting layers for device applications.

As part of a longer-term investigation into the electrical

* Corresponding author.

0040-6090/00/$ - see front matter
PII: S0040-6090(00)00743-4

and optical properties of thiophene-based compounds we have investigated the use of LB deposition for preparing thin films of CDM monomer.

2. Experimental

2.1. Preparation of CDM spreading solutions

As described previously [8], CDM was synthesized following the route first reported by Ferraris and Lambert [2]. The material was found to dissolve to differing extents (0.08–0.2 mg/ml) in acetonitrile (CH_3CN) (GLC grade, BDH Laboratory Supplies) and in 1:1 mixtures of CH_3CN with dichloromethane (CH_2Cl_2) (HPLC grade, CBS Biologicals), chloroform ($CHCl_3$) (HPLC grade, Aldrich) or diethyl ether ($CH_3CH_2OCH_2CH_3$) (analytical grade, Aldrich). Prior to use, the solutions were placed in an ultrasound bath for 30 min to ensure dissolution of the CDM. Mixed solutions of different mole percentages of CDM and stearic acid (SA) were also prepared. For these mixtures, CH_2Cl_2/CH_3CN (1:1 by volume) was used as the solvent. Although the monolayer behaviour of all solutions was examined, LB films were only deposited from monolayers spread from mixtures of CH_2Cl_2/CH_3CN.

2.2. Preparation of Langmuir and Langmuir–Blodgett films

Monolayers of CDM were prepared on the surface of ultrapure water in a sliding barrier PTFE trough located in a Class 10 000 clean room. Ultrapure water was supplied by a Milli-RO60 Reverse Osmosis cartridge feeding a Milli-Q system comprising of an activated carbon ion exchange prefilter, organex and 0.2 μm filter cartridges. The water system is automatically re-circulated hourly. Aliquots of the CDM solutions, typically 500 or 1000 μl were spread onto the water surface and approximately 10 min allowed for solvent evaporation prior to compressing the film to the deposition pressure, at a rate of 1.38 cm^2/s, which corresponds to 1.7×10^{-2} nm^2/min per molecule for pure CDM films and 3.9×10^{-2} nm^2/min per molecule for pure stearic acid monolayers. Mixed films of CDM with stearic acid have compression rates between these two values, depending on the mole % of the constituents used in each mixture. The surface pressure was monitored using a Wilhelmy plate connected to a microbalance.

LB films were deposited by vertical dipping onto three different substrates, in order of decreasing hydrophilicity: (i) hydrophilic glass; (ii) a gold film vacuum evaporated onto glass precoated with a thin keying layer of chromium; and (iii) indium tin oxide coated glass (ITO). The hydrophobic or hydrophilic character of the surface was tested by viewing the contact angle of a water droplet placed on each surface. The substrates were dipped vertically through the subphase surface at a speed of 2 mm/min while maintaining the surface pressure constant at 25 mN/m during film transfer.

2.3. Optical, morphological and electrical characterization

The UV-visible spectra of the spreading solutions and of the deposited LB films were obtained using a double beam, Hitachi U2000 spectrophotometer. The baselines were acquired by averaging two scans from the pure solvent, or ITO in the case of the LB films, as a reference. Deposited films were further investigated using Raman spectroscopy (Renishaw Model 1000 Raman microscope) employing a 633 nm red He/Ne laser. Film morphology was investigated using a Digital Instruments, Nanoscope IIIA atomic force microscope (AFM) in the tapping mode. The electrical properties were measured by depositing films over a pair of parallel gold finger electrodes formed on a glass microscope slide. Such an arrangement avoids the problem of pinholes, which are ever present in sandwich structures. In the present case, the interelectrode gap was 1 mm and the effective length of the electrodes 10 mm. Film conductance was measured automatically using the HP 4041B *I–V* plotter in increments of 0.1 V in the range −1 to +1 V, allowing 20 s between each measurement. The measurements were made in air at room temperature.

3. Results and discussion

The UV-visible spectra of all the spreading solutions were identical, except for the low wavelength cut-off (below ~200 nm) where differences arising from the different solvents was evident. Curve (a) in Fig. 1, obtained for CDM dissolved in a mixture of CH_2Cl_2 and CH_3CN (1:1), is typical of the spectra obtained. As can be seen, there are two main absorption bands. The first is a broad band in the region from ~200 to ~400 nm arising from the overlap of π–π^* transitions in the molecule. The second, centred at 600 nm, is the charge transfer band arising from the interaction of the sulphur (electron donor) and the CN (electron acceptor) groups (see Fig. 2), which gives rise to the blue colour of the CDM solutions. That the relative strengths of the two bands were identical in all solutions was taken as good evidence for the absence of any significant solvent effects.

The room temperature surface pressure–area (π–A)

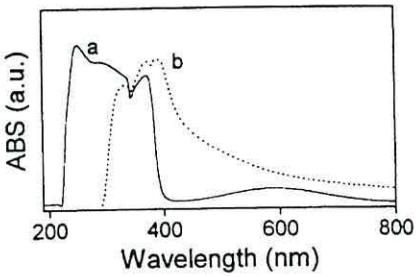

Fig. 1. UV-vis spectra of CDM: (a) in solution, 0.08 mg/ml in (1:1) mixture of CH_2CL_2 and CH_3CN as solvents, and (b) as LB deposited multilayer.

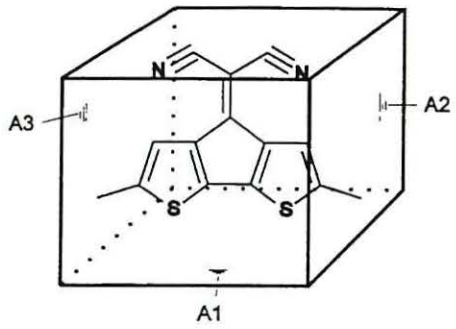

Fig. 2. Size of CDM molecule as determined from Cerius 2 (version 3.5, Molecular Simulations Inc). A1 = 21.2 Å^2 (bottom area), A2 = 15.8 Å^2 (lateral area), A3 = 51.8 Å^2 (front area).

isotherms of monolayers spread using the various solvent systems were similar to that in Fig. 3, obtained using the (1:1) CH_2Cl_2/CH_3CN mixture. At the low compression rate used (1.65×10^{-2} nm^2/min per molecule) the monolayer could be compressed into a condensed high surface pressure phase. No evidence was seen in the isotherm of the characteristic inflexion that heralds the onset of collapse. Yet, the area per molecule at the highest surface pressures (>50 mN/m) is considerably smaller than expected from the dimensions of the CDM molecule (Fig. 2) suggesting that collapse or dissolution had occurred. Upon opening the barriers, little hysteresis was observed and an isotherm obtained subsequently, followed the first closely. Dissolution in the subphase may be discounted as the reason for the small area per molecule in the condensed phase owing to the insolubility of CDM in water. Rather, the visible formation of aggregates on the water surface suggests that the monomer crystallizes on the subphase surface.

When using different solvents, the main difference seen was in the values measured for the extrapolated area per monomer in the condensed phase, which ranged from 4.5 to 10.2 Å^2/molecule. For all solvents investigated, expansion–compression cycles displayed little hysteresis in the isotherm. The likely explanation is that as the solvent evaporates, the monomer aggregates into small crystallites whose average dimensions define the observed 'extrapolated area'. The condensed 'monolayer' is likely, therefore, to consist of a tightly packed assembly of these aggregates, which readily disperse upon opening the barriers. Such behaviour has been observed previously in polymeric systems [18–20] where aggregation is difficult to avoid.

Nevertheless, transfer of the pure material was attempted and found to occur onto hydrophilic glass slides only during the upstroke, a characteristic of Z-type LB films. In this case the meniscus always pointed upwards, even during immersion of the substrate into the liquid subphase. On the other hand, with ITO or gold substrates transfer occurred during both the up and the downstroke, a characteristic of Y-type films. For gold and ITO the transfer ratio was close to unity (~0.9), with good visual uniformity, for the first few cycles but slowly decreased with increasing film thickness.

In an attempt to improve the dispersion of the CDM, mixed monolayers with stearic acid were investigated. Fig. 4 shows the effect on the stearic acid isotherm, at room temperature, of adding an increasing mole percentage

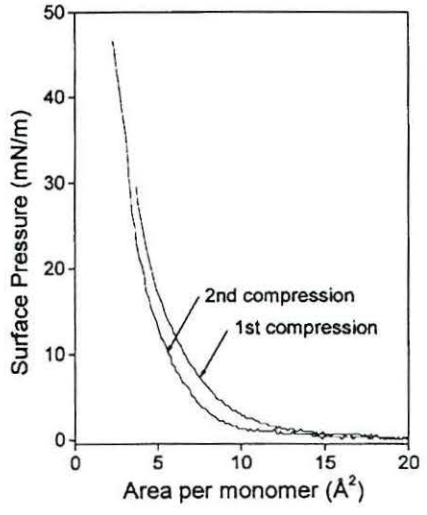

Fig. 3. π–A isotherm of CDM at 20°C processed with CH_2Cl_2 and CH_3CN (0.2 mg/ml). The spread volume was 1000 µl. The first two compression curves follow each other closely with little hysteresis. The extrapolated areas from the first and second compressions are 6.0 and 5.5 Å^2, respectively.

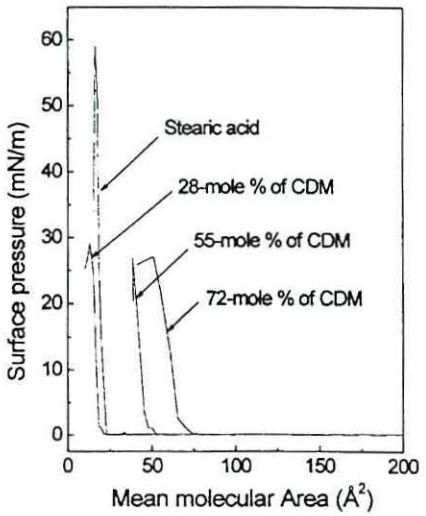

Fig. 4. π–A isotherm of mixed monolayers, at 20°C, containing different mole percentage of CDM and stearic acid. The mean molecular area was calculated considering only the stearic acid molecules.

of CDM. Initially, a small reduction in area per stearic acid molecule occurs followed by a rapid increase as the concentration of CDM increases. As can be seen the presence of the CDM induces an early collapse of the host stearic acid monolayer (collapse pressure reduced to <30 mN/m). Very little hysteresis was observed during a compression–expansion cycle and successive isotherms were again reproducible, discounting any possibility of material dissolution into the liquid subphase.

From the data in Fig. 4, the area per molecule occupied by CDM in each of the mixed monolayers may be calculated as a function of the mole % of CDM in the monolayer. This was achieved by subtracting the area of a stearic acid molecule (~20 Å^2) from the extrapolated area for each isotherm in Fig. 4, and dividing by the ratio of CDM to stearic acid molecules in the mixture. The results of the calculation are shown in Fig. 5. Up to about 40-mole%, the area occupied by CDM is insignificant. The initial negative values are probably caused by a slight collapse of the stearic acid monolayer, with the CDM aggregates acting as nucleating centres for collapse. Between 40 and 60-mole%, the area occupied by CDM molecules increases to a maximum of ~18 Å^2/molecule before falling to the values seen in pure CDM films (~7 Å^2/molecule) upon further increasing the CDM concentration.

While in some cases changing the subphase temperature has improved film quality, we do not believe this would be the case with CDM. Lower subphase temperatures are known to result in more rigid films, i.e. more solid-like behaviour. At higher temperatures, solvent evaporation would occur more rapidly leading to poor dispersion of the CDM.

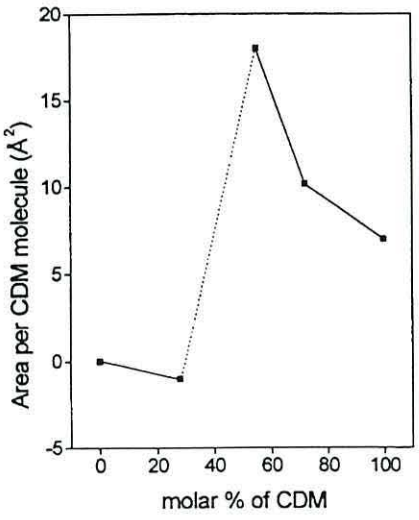

Fig. 5. Limiting mean molecular area of CDM vs. the molar ratio of CDM in the mixed monolayers.

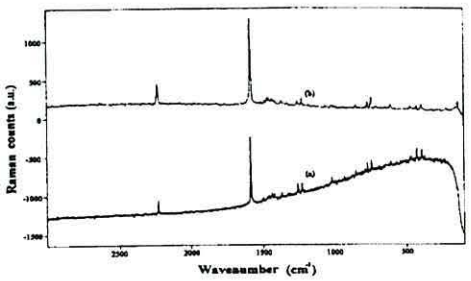

Fig. 6. Raman spectra of: (a) CDM LB film (15 layers) deposited onto gold, (b) crystals of pure CDM.

Curve (b) in Fig. 1 is the UV-vis spectrum obtained for a 16-layer LB film of pure CDM deposited onto ITO. An identical spectrum was obtained for a film deposited onto glass, and for a mixed film (55-mole % of CDM) deposited onto ITO. The low wavelength π–π^* band observed in solution shows a bathochromic shift in the LB film and is also modified by the strong absorption of the ITO glass below ~300 nm. Another significant difference is the loss of the charge transfer band at 600 nm owing to the depolarizing effect of intermolecular interactions on the S-CN dipole.

Spectroscopic analysis using Raman microscopy confirms the presence of the monomer structure in the LB film cf. spectra (a) and (b) in Fig. 6. In both, characteristic vibrations are seen at 3000 cm^{-1} (CH stretch), 2236 cm^{-1} (C≡N stretch), 1589 cm^{-1} (probably CC stretch), 1512 cm^{-1} (C_α=C_β stretch), 1446 cm^{-1} (C_α=C_β stretch), 1389 cm^{-1} (C_α–C_β stretch), 1200 (C=S stretch), 702 cm^{-1} (C–S defm) and 500 cm^{-1} (C-S defm). Exposure of the pure CDM film to UV radiation from a deuterium lamp for 24 h produced no detectable polymerization or any change in the visual appearance of the film as observed using optical microscopy. This latter observation is not surprising since AFM images (Fig. 7) show that the LB film surface is rough, probably hiding any changes in surface structure. Microscopic needle-like crystallites are clearly seen in both the pure (Fig. 7a) and mixed (Fig. 7b) films confirming the interpretation of the π–A isotherms. In the pure CDM film the average width of the crystallites is ~150 nm. The average surface roughness in a 9 μm^2 area increases with increasing number of deposited layers in the pure CDM films, from 24 nm in a 9-layer film to 73 nm in a 42-layer film. In a 6-layer mixed film (55-mole % of CDM) the average roughness was 58 nm. A transversal score in the samples indicates an average height of 100 nm for the 9-layer pure CDM film, 309 nm for the 42-layer pure CDM film, and 71 nm for the mixed film.

X-ray diffraction shows that the crystalline structure of CDM is triclinic (Fig. 8a–d) with an interlayer distance of 6.48 Å. If monolayer molecules adopt a flat orientation on the subphase surface as in Fig. 8b, the area per molecule in a true monolayer would be expected to be 72.5 Å^2, a value

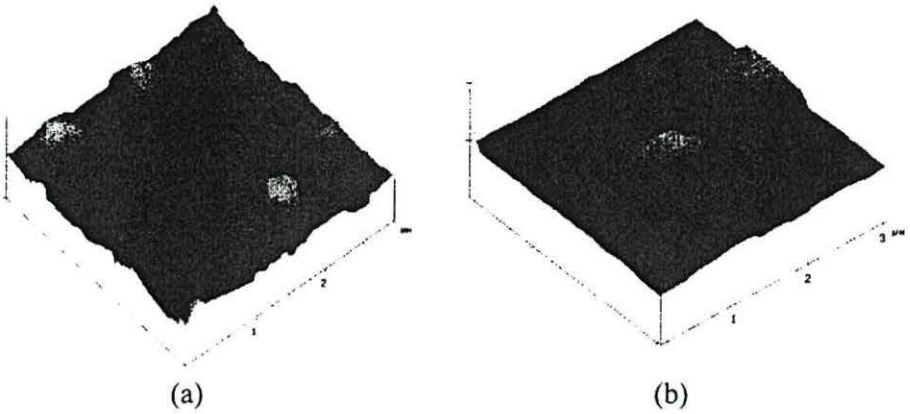

Fig. 7. AFM micrographs of CDM: (a) pure monomer, (b) mixed film (55-mole % of CDM) with stearic acid. Z axis scale = 1 μm/div.

which is some ten times greater than that obtained from the π–A isotherms. This difference may be explained by assuming that the 'monolayer' is composed of ten-layer thick aggregates in which molecules are stacked on top of each

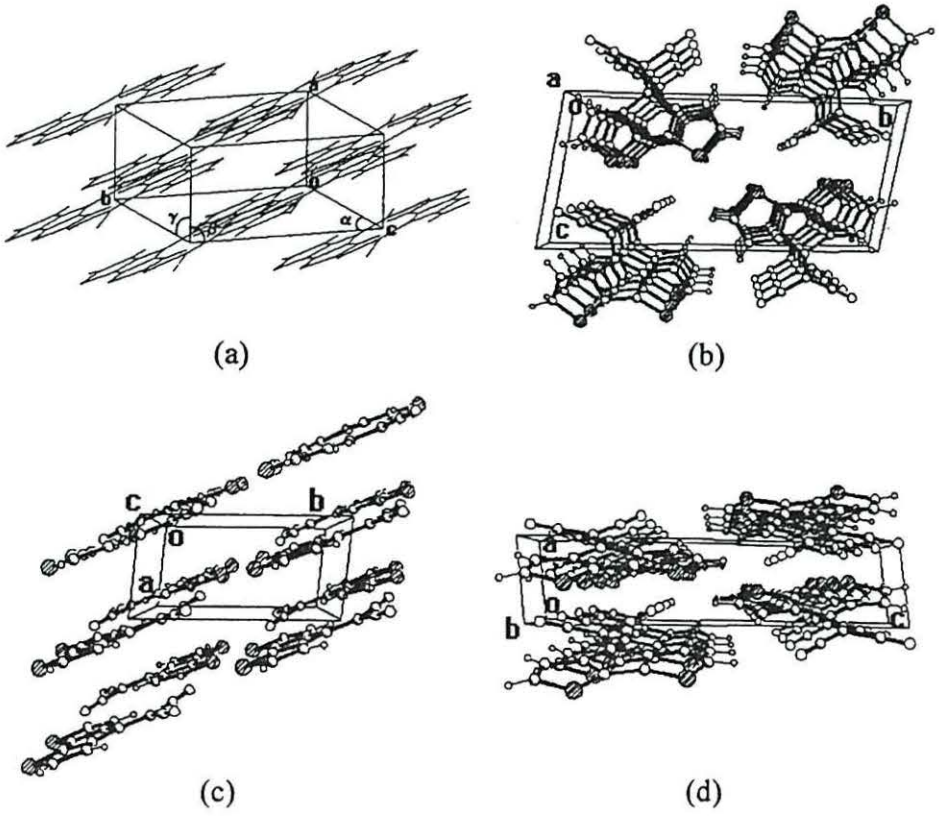

Fig. 8. Schematic structure of the unit cell of CDM: (a) triclinic unit cell (oa ≠ ob ≠ oc, and $\alpha \neq \beta \neq \gamma$), (b) top view (plane ocb), (c) lateral view (plane oac) and, (d) front view (plane oab).

other with the orientation shown in Fig. 8b. In such an arrangement the 'monolayer' thickness would be expected to be some ten times greater than the interlayer distance, i.e. 67.1 Å, which is close to the average thickness per deposited 'monolayer' (73.5 Å) deduced from AFM measurements for pure CDM. The origin of the film roughness is seen then to be due to an irregular packing of multilayer aggregates since the monolayers are composed of almost randomly oriented crystallites. That the monolayer is composed of a collection of aggregates may also explain the lack of hysteresis in the isotherms. Compression and expansion cycles will simply act on islands of solid material.

The current–voltage (I–V) characteristic of a 9-layer pure CDM measured using the finger electrodes was linear and independent of polarity for electric fields less than 10^5 V/cm. Based on the average film thickness and noting that the surface roughness of the film was ~25% of the average film thickness, film conductivity was estimated to be $(2.0 \pm 0.5) \times 10^{-9}$ S/cm. The intrinsic conductivity of the polymer formed from CDM has been estimated to be $\sim 10^{-8}$ S/cm [31] and similar, therefore, to polycrystalline films of the monomer.

4. Conclusions

Pure CDM as well as mixtures of CDM with stearic acid display poor monolayer behaviour at the air–water interface yielding areas per molecule that were significantly smaller than expected. Nevertheless, it proved possible to LB deposit 'monolayers' onto solid supports, with good visual uniformity. However, AFM investigation showed that both the pure and mixed films were composed of crystalline aggregates. Drawing together the unit cell dimensions, deduced from X-ray diffraction data, the average film thickness measured by AFM and the area per molecule from the π–A isotherms, it was argued that a condensed CDM 'monolayer' is a collection of aggregates some ten layers thick. The presence of aggregates can also be inferred by the absence of the 600 nm charge transfer band in the UV-visible spectra of deposited films. No change was observed in the Raman or UV-visible spectra of the films by prolonged UV exposure confirming the stability of the molecule. The lateral conductivity of the pure CDM film was estimated to be $\sim 2 \times 10^{-9}$ S/cm.

Acknowledgements

The authors are pleased to acknowledge the assistance of Louise Hall (University of Wales, Bangor) with the synthesis of CDM, Thomas Gelbrich (Southampton University) for the XRD results and Dr Osvaldo Novais de Oliveira Jr., Dr Don Marshall, Dr Arwel Hughes, Dra Debora T. Balogh, and Dra Sarita V. Mello for discussions. They are also grateful to BNFL and FAPESP for financial support of this work.

References

[1] T.A. Skotheim, R.L. Elsenbaumer, J.R. Reynolds, Handbook of Conducting Polymers, 2nd ed., Marcel Dekker, New York, 1998.
[2] J.P. Ferraris, S. Rodriguez, D.A. Torres, Abstr. Pap. Am. Chem. Soc. 207 (1994) 37.
[3] Q. Pei, G. Zuccarello, M. Ahlskog, O. Inganäs, Polymer 35 (1997) 1347.
[4] R. Kiebooms, A. Aleshin, K. Hutchison, F. Wudl, J. Phys. Chem. B 101 (1997) 11037.
[5] N. Sakmeche, E.A. Bazzaoui, M. Fall, S. Aeiyach, M. Jouini, J.C. Lacroix, J.J. Aaron, P.C. Lacaze, Synth. Met. 84 (1997) 191.
[6] R. Corradi, S.P. Armes, Synth. Met. 84 (1997) 453.
[7] J.R. Reynolds, A. Kumar, J.L. Reddinger, B. Sankaran, S.A. Sapp, G.A. Sotzing, Synth. Met. 85 (1997) 1295.
[8] S.R. Gunatunga, G.W. Jones, M. Kalaji, P.J. Murphy, D.M. Taylor, G.O. Williams, Synth. Met. 84 (1997) 973.
[9] M. Granström, M. Berggren, O. Inganäs, Synth. Met 76 (1996) 141.
[10] K.Z. Xing, M. Fahlman, X.W. Chen, O. Inganäs, W.R. Salaneck, Synth. Met. 89 (1997) 161.
[11] Y. Dong, S.C. Bayliss, M. Parkinson, Appl. Phys. Lett. 72 (1998) 1344.
[12] X-C. Li, F. Cacialli, R. Cervini, et al., Synth. Met. 84 (1997) 159.
[13] R.S. Duran, H.C. Zhou, Polymer 33 (1992) 4019.
[14] I. Watanabe, K. Hong, M.F. Rubner, Langmuir 6 (1990) 1164.
[15] R.B. Rosner, M.F. Rubner, Chem. Mater. 6 (1994) 581.
[16] A. Dhanabalan, A. Riul Jr., L.H.C. Mattoso, O.N. Oliveira Jr., Langmuir 13 (1997) 4882.
[17] A. Dhanabalan, A. Riul Jr., O.N. Oliveira Jr., Supramol. Sci. 5 (1998) 75.
[18] S.V. Mello, L.H.C. Mattoso, R.M. Faria, O.N. Oliveira Jr., Synth. Met. 71 (1995) 2039.
[19] L.H.C. Mattoso, S.V. Mello, A. Riul Jr., O.N. Oliveira Jr., R.M. Faria, Thin Solid Films 244 (1994) 714.
[20] A. Dhanabalan, A. Riul Jr., C.J.L. Constantino, O.N. Oliveira Jr., Synth. Met. 101 (1999) 690.
[21] A. Riul Jr, L.H.C. Mattoso, G.D. Telles, et al., Thin Solid Films 284/285 (1996) 177.
[22] A. Riul Jr., A. Dhanabalan, M.A. Cotta et al., Synth. Met. 101 (1999) 830.
[23] T.L. Porter, D. Thompson, M. Bradley, Thin Solid Films 288 (1996) 268.
[24] O. Österbacka, A.J. Pal, H. Stubb, Thin Solid Films 327 (1998) 668.
[25] T. Östergård, J. Paloheimo, A.J. Pal, H. Stubb, Synth. Met. 88 (1997) 171.
[26] J. Paloheimo, P. Kuivalainen, H. Stubb, E. Vuorimaa, P. Yli-Lahti, App. Phys. Lett. 56 (1990) 1157.
[27] A.J. Pal, R. Österbacka, K.-M. Källman, H. Stubb,, Appl. Phys. Lett. 70 (1997) 2022.
[28] T. Ostergard, A.J. Pal, H. Stubb, Thin Solid Films 329 (1998) 712.
[29] H. Clauk, D.J. Gundlach, J.A. Nichols, T.N. Jackson, IEEE Trans. Electron. Devices 46 (1999) 1258.
[30] C. Väterlein, H. Neureiter, W. Gebauer, B. Ziegler, M. Sokolowski, P. Bäurle, E. Umbach, J. Appl. Phys. 82 (1997) 3003.
[31] H. Huang, P.G. Pickup, Chem Mater. 11 (1999) 1541.

JOURNAL OF Materials CHEMISTRY

The preparation and characterisation of polymeric macrostructures (command surfaces) using electropolymerisation

Christopher A. Mills,*[a] David Lacey,[b] Gary Stevenson[b] and D. Martin Taylor[a]

[a]*Institute of Molecular and Biomolecular Electronics, University of Wales, Dean Street, Bangor, Gwynedd, UK LL57 1UT. E-mail: cmills@sees.bangor.ac.uk*
[b]*Department of Chemistry, Faculty of Science and the Environment, University of Hull, Hull, UK HU6 7RX*

Received 17th January 2000, Accepted 14th April 2000
Published on the Web 21st June 2000

Polymeric films of acrylonitrile, acetic acid and 2-cyanoprop-1-en-3-ol have been electrodeposited to a thickness of ~300 nm onto silver electrodes, using a 2-step polymerisation method, under both cathodic and anodic conditions. Raman microscopy was used to confirm (i) that polymerisation had occurred and (ii) that anodic and cathodic conditions produced different polymeric structures. AFM analysis showed the films to be microscopically smooth (RMS roughness 1–6 nm) but characterised by deep crevices when produced anodically. The polymers have the potential to be used as a command surface for the attachment of surface moieties.

1. Introduction

In 1981, Lecayon and co-workers showed that polymers can be grafted electrochemically onto a metal surface,[1] for example, the electropolymerisation of acrylonitrile led to the formation of a thin film of poly(acrylonitrile) on nickel and platinum surfaces.[2,3] Of particular interest is the difference in the nature of the metal/polymer interface depending on whether cathodic or anodic polymerisation is used. When the substrate metal (nickel or platinum) acts as a cathode it behaves as a basic initiator for anionic polymerisation through a 1,4 Michael-type addition from the metallic surface to the vinylic carbons to form a polymeric structure as shown in Fig. 1(a). However, when the metal substrate is made an anode, it acts as a Lewis acid towards the acrylonitrile molecules, resulting in either (i) a 1,2 nucleophilic addition on the nitrile groups which affords a 'conjugated' structure [Fig. 1(b)] or (ii) the formation of a cumulene type structure *via* the 1,4-addition of the nitrile group to the vinyl carbon [Fig. 1(c)]. Thus by changing the nature of the metallic surface either end of the acrylonitrile (and also the methacrylonitrile[4]) molecule may be chemically bonded to the metal surface.

Recent work by Jerome and co-workers[5] has shown that it is possible also to 'debond' the grafted poly(acrylonitrile) by increasing the cathodic potential beyond that required for bonding. This is an exciting development since it suggests a means of producing thin, free-standing polymeric membranes.

Furthermore, the work to date indicates that acrylonitrile-based polymer films may well be suited to the preparation of functionalised macrostructures or command surfaces which could be useful in sensor or optical applications. Although much is already known about the electropolymerisation process, there is still some doubt as to the actual mechanism of polymerisation and little is known about either (a) the tacticity of the polymer or (b) the effects of functional groups on the polymerisation process.

In this paper we present the preliminary results of an investigation into the cathodic and anodic polymerisation of the three monomers shown in Fig. 2. Electropolymerisation of monomers **2** and **3** will result in a command surface, *i.e.* a surface functionalised polymeric macrostructure. In a subsequent step (not investigated here) such a surface should allow the attachment of different types of active moieties, for example a sensor unit, NLO chromophore or a liquid crystal unit, as shown in Fig. 3.

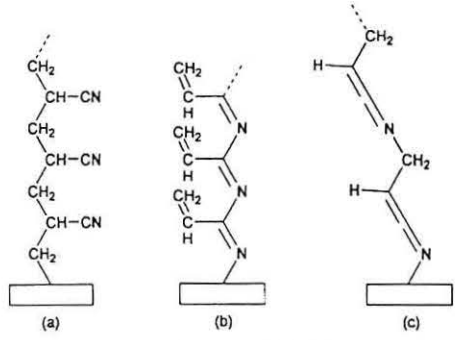

Fig. 1 Polymer structure when synthesised by (a) Michael-type addition, (b) 1,2 nucleophilic addition on the nitrile group and (c) 1,4 addition through the nitrile group and the vinyl carbon.

2. Experimental procedures

Acrylonitrile (**1**) and acrylic acid (**2**) were purchased from Aldrich and used without further purification.

2-Cyanoprop-1-en-3-ol (**3**) was synthesised using a procedure first described by Villeras and Rambaud.[6] Diethyl cyanomethyl phosphate (50 g, 0.282 mol) was added to formaldehyde solution with rapid stirring at room temperature. Saturated potassium carbonate solution (68 g) was added slowly over 45 minutes while maintaining the temperature below 30 °C. The solution was stirred for a further 2.5 hours at room temperature. Saturated ammonium chloride solution (125 mL) was added with effervescence. The product was extracted into diethyl ether (3 × 125 mL) and the combined

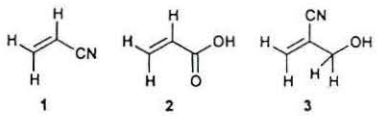

Fig. 2 Monomers used for polymerisation, acrylonitrile **1**, acrylic acid **2** and 2-cyanoprop-1-en-3-ol **3**.

DOI: 10.1039/b000450m

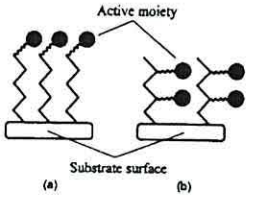

Fig. 3 Possible addition of active moieties: (a) surface macrostructure and (b) in-plane macrostructure.

ethereal extracts were then dried ($MgSO_4$). The diethyl ether was removed by distillation under reduced pressure (water pump) to leave a slightly viscous, yellow liquid. The product was purified by distillation under reduced pressure (water pump) to afford (3) as a pale yellow liquid. The product, collected in the range 110–120 °C with a 56% yield (13.2 g), gave a single spot on thin layer chromatography (silica gel, 1 : 1 mixture of diethyl ether and dichloromethane).

The structure of (3) was confirmed by ^{1}H NMR (JEOL JNM-GX 270 MHz spectrometer), infrared spectroscopy (Perkin Elmer Model 783 Grating Spectrophotometer) and mass spectrometry (Finnegan-MAT 1020G/MS spectrometer). ^{1}H NMR ($CDCl_3$): δ 6.05 (s, 1H), 4.25 (s, 2H), 2.80–3.05 (s, broad, 1H); IR (KBr): 3100–3600, 2970, 2890, 2220, 1625, 1450, 1040, 950 cm^{-1}; *m/z*: 83 (M^+), 66 (M−OH).

Solutions of acrylonitrile, acrylic acid and 2-cyanoprop-1-en-3-ol (approximately 0.4 M) with supporting salt (tetraethylammonium perchlorate, 5×10^{-2} M) were prepared in acetonitrile. Electropolymerisation was achieved by placing 40 mL of solution in a standard three electrode cell connected to a potentiostat/galvanostat (EG+G Model 273A). The working electrode was formed by evaporating a silver film (100 nm thick) onto a glass microscope slide precoated with a keying layer of chromium (20 nm thick). During film growth, approximately 30 mm^2 of the electrode was immersed into the monomer solution. The counter electrode was formed from a thin platinum foil 7 mm^2 in area with a clean silver wire used as a pseudo-reference electrode. Prior to polymerisation, the monomer solution was de-aerated by purging with nitrogen for 20 minutes.

Polymerisation followed the two-step technique suggested initially by Garnier and co-workers[7] and adapted by Taylor and Gomes[8] for poly(3-methylthiophene), in which a high potential was applied for a short time to nucleate the growth followed by a lower potential for a longer time during which most of the film was grown. The growth conditions for both anodic and cathodic electropolymerisation are given in Table 1. At the end of the growth stage, polymer-coated substrates were retrieved from the cell, washed with acetone to remove residual monomer solution, dried under a gentle stream of bottled nitrogen and stored under vacuum prior to characterisation.

Raman spectra, covering the range 500–3500 cm^{-1}, were obtained for all the monomers and for polymer films grown both cathodically and anodically, using a Renishaw Ramascope 1000 Raman spectrometer fitted with a 633 nm helium–neon laser. To measure the electrical properties of the deposited films circular aluminium electrodes approximately 2.5 mm^2 in area were evaporated onto the free surface of the films in a turbomolecular pumped evaporator. The electrical conductivity of the sandwich structures was measured under ambient conditions using a Tektronix Model 571 Current/Voltage plotter revealing essentially linear characteristics over a 2 V range. The morphology of the deposited films was studied by Atomic Force Microscopy (Digital Instruments, Nanoscope IIIA) operating in tapping mode. The AFM was also used to measure film thickness by scoring and peeling away part of the polymer using a sharp blade.

3. Results

All three monomers were electropolymerised successfully onto the silver substrates giving stable, robust films between 0.2 and 0.4 μm thick (Table 2) under both anodic and cathodic conditions. Film growth was much more rapid under cathodic conditions. Even though the time allowed for growth was some 50% greater for anodic polymerisation, the resulting films were 20–30% thinner than those produced cathodically. Films of poly(acrylic acid) showed the most rapid growth rates for both anodic and cathodic polymerisation. Taking acrylonitrile as the reference, these preliminary results indicate that replacing the *gem*-hydrogen has little effect on the rate of electropolymerisation. However, replacing the cyano group with another electron-withdrawing group produces a significant effect.

None of the deposited films could be washed off the silver surfaces by rinsing in dimethylformamide (DMF), tetrahydrofuran (THF) or dichloromethane (DCM) at room temperature. Furthermore, the vacuum-dried films resisted attempts at removal with adhesive tape suggesting that they are strongly bonded to the silver surface.

AFM images of polyacrylonitrile produced under both anodic and cathodic conditions and given in Fig. 4 are typical of all three materials investigated. Anodic films were exceptionally smooth and although punctuated by deep crevices [Fig. 4(b)] did not show the nodules projecting from the surface that are characteristic of the cathodic film [Fig. 4(a)]. At higher magnification [Fig. 4(c) and 4(d)] the underlying surface morphologies differ only slightly with the RMS roughness of all films in the range 1–6 nm (Table 2).

Interestingly, films from the two cyano-containing compounds are smoother than those from acrylic acid, which may well reflect the slower growth rate of the cyano-containing films (Table 2). The presence of crevices are suggestive of a more rigid film expected when conjugated structures such as Fig. 1(b) or 1(c) are growing. AFM probing showed that the crevices found in the anodic polymer films did not penetrate the full depth of the layer.

The conductivities of the polymers ranged from 1.4×10^{-3} to 2.8×10^{-3} S m^{-1} (Table 2). Despite their supposed conjugated structure, the anodically grown films were generally of lower conductivity than those produced cathodically. This provides some confirmation of the AFM observation that the crevices in the film did not penetrate the whole film and indeed had little effect on the electrical properties.

The Raman spectra for the three monomers and their respective polymers are shown in Figs. 5–7. All monomers [curves labeled (c)] show the ν(CH=CH) peak at approximately 1620 cm^{-1} and the ν(C–H) peak of the CH=CH moiety just above 3000 cm^{-1}. The sharp band characteristic of ν(C≡N) is clearly visible at approximately 2225 cm^{-1} in both acrylonitrile and 2-cyanoprop-1-en-3-ol, while in the latter material bands

Table 1 Conditions used for polymer growth

	Nucleation step		Growth step	
Type of polymerisation	Applied potential/V	Time applied/s	Applied potential/V	Time applied/s
Anodic	2.8	10	1.8	1200
Cathodic	−2.8	10	−1.8	600

Table 2 Typical properties of the electropolymerised films grown from the monomers listed

	Thickness/nm		RMS roughness 500 nm^2 area/nm		Conductivity/S m^{-1}	
Monomer	anodic	cathodic	anodic	cathodic	anodic	cathodic
Acrylonitrile	220	320	2.3	3.0	$1.45\times10^{-3}\pm2.5\times10^{-5}$	$2.28\times10^{-3}\pm2.3\times10^{-6}$
Acrylic acid	300	360	6.6	1.2	$1.54\times10^{-3}\pm1.3\times10^{-5}$	$2.13\times10^{-3}\pm8.8\times10^{-6}$
2-Cyanoprop-1-en-3-ol	230	310	1.5	2.2	$2.81\times10^{-3}\pm8.5\times10^{-6}$	$2.56\times10^{-3}\pm1.1\times10^{-4}$

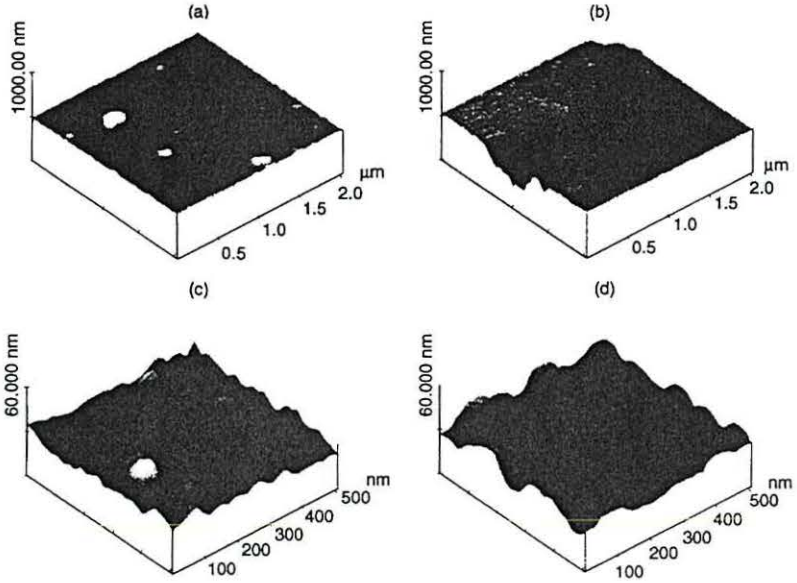

Fig. 4 AFM micrographs of cathodically, (a) and (c), and anodically, (b) and (d), polymerised acrylonitrile. [In (a) and (b), area = 2 × 2 µm, z-range = 500 nm div^{-1}; in (c) and (d), area = 500 × 500 nm, z-range = 30 nm div^{-1}.]

due to ν(C–H) in the CH_2 moiety are seen just below 3000 cm^{-1}.

The spectra obtained for the electrodeposited films show clear evidence for polymerisation: (a) the C–H stretch vibration of the CH=CH moiety above 3000 cm^{-1} has disappeared to be replaced by the C–H stretching vibration of the saturated CH–CH moiety just below 3000 cm^{-1}; (b) the appearance of a broad absorption band in the range 1200–1700 cm^{-1}. Interestingly, the detailed structure of the band in this region is different in the cathodic and anodic polymers, consistent with the different polymerisation schemes in Fig. 1.

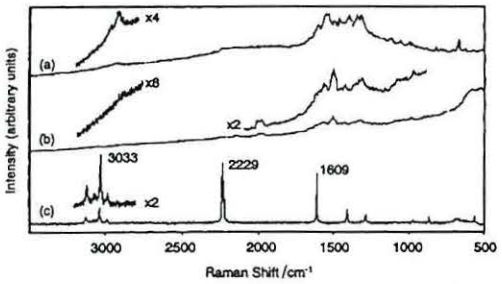

Fig. 5 Raman spectra of acrylonitrile (a) anodically polymerised, (b) cathodically polymerised and (c) monomer. (Expanded regions above main spectra show detail for that area.)

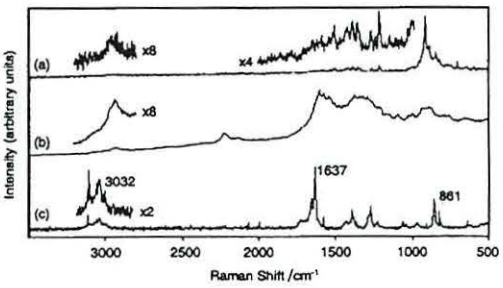

Fig. 6 Raman spectra of acrylic acid (a) anodically polymerised (b) cathodically polymerised and (c) monomer. (Expanded regions above main spectra show detail for that area.)

4. Conclusions

For the first time, a series of ethylene homopolymers has been prepared by both anodic and cathodic electropolymerisation. The rate of electropolymerisation (as judged by film thickness) was dependent on both the nature of the electropolymerisation and the structure of the monomer. Polymers grown under both anodic and cathodic conditions were found to be very smooth with an RMS roughness between 1 and 7 nm, however, the anodically grown films were found to contain crevices suggesting a rigid, conjugated polymer structure.

Polymerisation was confirmed using Raman spectroscopy to compare the spectra of the polymers with those of their respective monomers. The polymers all displayed peak broad-

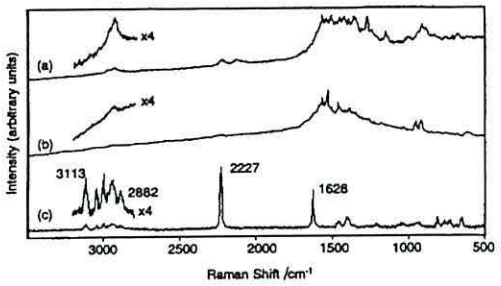

Fig. 7 Raman spectra of 2-cyanoprop-1-en-3-ol (a) anodically polymerised, (b) cathodically polymerised and (c) monomer. (Expanded regions above main spectra show detail for that area.)

ening between 1200 and 1700 cm^{-1} indicative of polymerised C–C. Also the ν(C–H) band just above 3000 cm^{-1} (characteristic of CH=CH) was replaced by a new band just below 3000 cm^{-1} characteristic of the CH–CH moiety. In all cases the spectra of the cathodic and anodic polymers were different in detail consistent with different polymerisation schemes in the two cases.

The polymers were found to have conductivities of approximately 2×10^{-3} S m^{-1} which seemed to be independent of the presence of the crevice-like defects in the anodic films.

References

1 G. Lecayon, C. LeGressus and A. LeMoel, *Eur. Pat.*, No. 0038244, 1981; G. Lecayon, Y. Bouizem, C. LeGressus, C. Reynaud, C. Bioziau and C. Jurer, *Chem. Phys. Lett.*, 1982, **91**, 506; G. Lecayon, P. Viel, C. LeGressus, C. Boiziou, S. Leroy, J. Perreau and C. Reynaud, *Scanning Microscopy*, 1987, **1**, 85.

2 R. Jerome, M. Mertens and L. Martinot, *Adv. Mater.*, 1995, **7**, 807.

3 N. Baute, P. Teyssie, L. Martinot, M. Mertens, P. Dubois and R. Jerome, *Eur. J. Inorg. Chem.*, 1998, 1711.

4 C. Bureau, G. Deniau, F. Valin, M.-J. Buittet, G. Lecayon and J. Delhalle, *Surf. Sci.*, 1996, **355**, 177.

5 M. Mertens, C. Calberg, L. Martinot and R. Jerome, *Macromolecules*, 1996, **29**, 4910.

6 J. Villeras and M. Rambaud, *Synthesis*, 1982, 924.

7 F. Garnier, G. Horowitz and D. Fichou, *Synth. Met.*, 1989, **28**, C275; J. Roncali, A. Yasser and F. Garnier, *J. Chem. Phys.*, 1989, **86**, 85.

8 D. M. Taylor, H. L. Gomes, A. E. Underhill, S. Edge and P. I. Clemenson, *J. Phys. D: Appl. Phys.*, 1991, **24**, 2032; D. M. Taylor and H. L. Gomes, *J. Phys. D: Appl. Phys.*, 1995, **28**, 2554.